SPIN- AND ANGLE-RESOLVED PHOTOEMISSION STUDY OF TOPOLOGICAL BAND INVERSIONS WITHIN A SINGLE ORBITAL MANIFOLD

Oliver Jon Clark

A Thesis Submitted for the Degree of PhD
at the
University of St Andrews

2019

Identifiers to use to cite or link to this thesis:

DOI: https://doi.org/10.17630/10023-17458
http://hdl.handle.net/10023/17458

Spin- and angle-resolved photoemission study of topological band inversions within a single orbital manifold

Oliver Jon Clark

University of
St Andrews

This thesis is submitted in partial fulfilment for the degree of

Doctor of Philosophy (PhD)

at the University of St Andrews

January 2019

Candidate's declaration

I, Oliver Jon Clark, do hereby certify that this thesis, submitted for the degree of PhD, which is approximately 55,000 words in length, has been written by me, and that it is the record of work carried out by me, or principally by myself in collaboration with others as acknowledged, and that it has not been submitted in any previous application for any degree.

I was admitted as a research student at the University of St Andrews in September 2015.

I received funding from an organisation or institution and have acknowledged the funder(s) in the full text of my thesis.

Date Signature of candidate

Supervisor's declaration

I hereby certify that the candidate has fulfilled the conditions of the Resolution and Regulations appropriate for the degree of PhD in the University of St Andrews and that the candidate is qualified to submit this thesis in application for that degree.

Date Signature of supervisor

Permission for publication

In submitting this thesis to the University of St Andrews we understand that we are giving permission for it to be made available for use in accordance with the regulations of the University Library for the time being in force, subject to any copyright vested in the work not being affected thereby. We also understand, unless exempt by an award of an embargo as requested below, that the title and the abstract will be published, and that a copy of the work may be made and supplied to any bona fide library or research worker, that this thesis will be electronically accessible for personal or research use and that the library has the right to migrate this thesis into new electronic forms as required to ensure continued access to the thesis.

I, Oliver Jon Clark, confirm that my thesis does not contain any third-party material that requires copyright clearance.

The following is an agreed request by candidate and supervisor regarding the publication of this thesis:

Printed copy

Embargo on all of print copy for a period of 2 years on the following ground(s):

- Publication would preclude future publication

Supporting statement for printed embargo request

Some of the research presented in this thesis is part of ongoing, unpublished works.

Electronic copy

Embargo on all of electronic copy for a period of 2 years on the following ground(s):

- Publication would preclude future publication

Supporting statement for electronic embargo request

Thesis contains ongoing, unpublished research.

Title and Abstract

- I agree to the title and abstract being published.

Date Signature of candidate

Date Signature of supervisor

Underpinning Research Data or Digital Outputs

Candidate's declaration

I, Oliver Jon Clark, understand that by declaring that I have original research data or digital outputs, I should make every effort in meeting the University's and research funders' requirements on the deposit and sharing of research data or research digital outputs.

Date Signature of candidate

Permission for publication of underpinning research data or digital outputs

We understand that for any original research data or digital outputs which are deposited, we are giving permission for them to be made available for use in accordance with the requirements of the University and research funders, for the time being in force.

We also understand that the title and the description will be published, and that the underpinning research data or digital outputs will be electronically accessible for use in accordance with the license specified at the point of deposit, unless exempt by award of an embargo as requested below.

The following is an agreed request by candidate and supervisor regarding the publication of underpinning research data or digital outputs:

Embargo on all of electronic files for a period of 2 years on the following ground(s):

- Publication would preclude future publication

Supporting statement for embargo request

Thesis contains ongoing, unpublished research.

Date Signature of candidate

Date Signature of supervisor

List of Papers

The research presented in this thesis has directly led to the following publications:

1. **Ubiquitous formation of bulk Dirac cones and topological surface states from a single orbital manifold in transition-metal dichalcogenides**
   M. S. Bahramy*, O. J. Clark*, B.-J. Yang, J. Feng, L. Bawden, J. M. Riley, I. Marković, F. Mazzola, V. Sunko, D. Biswas, S. P. Cooil, M. Jorge, J. W. Wells, M. Leandersson, T. Balasubramanian, J. Fujii, I. Vobornik, J. Rault, T. K. Kim, M. Hoesch, K. Okawa, M. Asakawa, T. Sasagawa, T. Eknapaul, W. Meevasana and P. D. C. King.
   *equal contribution
   Nature Materials, **17,** 23-27 (2018)

2. **Fermiology and superconductivity of topological surface states in $PdTe_2$**
   O. J. Clark, M. J. Neat, K. Okawa, L. Bawden, I. Marković, F. Mazzola, J. Feng, V. Sunko, J. M. Riley, J. Fujii, I. Vobornik, T. K. Kim, M. Hoesch, T. Sasagawa, P. Wahl, M. S. Bahramy and P. D. C. King.
   Physical Review Letters, **120,** 156401 (2018)

3. **Dual quantum confinement and anisotropic spin splitting in the multi-valley semimetal $PtSe_2$**
   O. J. Clark, F. Mazzola, J. Feng, V. Sunko, I. Marković, L. Bawden, T. K. Kim, P. D. C. King and M. S. Bahramy
   Physical Review B, **99,** 045438 (2019)

4. **A general route to form topologically-protected surface and bulk Dirac fermions along high-symmetry lines**
   O. J. Clark, F. Mazzola, I. Marković, J. M. Riley, J. Feng, B.-J. Yang, K. Sumida, T. Okuda, J. Fujii, I. Vobornik, T. K. Kim, K. Okawa, T. Sasagawa, M. S. Bahramy and P. D. C. King
   Electronic Structure, **1,** 014002 (2019)

Research conducted during the study of this degree, but which did not contribute to the work discussed in this thesis, has resulted in the following publications:

5. **Highly Anisotropic electronic structure of ReS_2**
   D. Biswas, A. Ganose, R. Yano, J. M. Riley, L. Bawden, O. J. Clark, J. Feng, L. Collins-McIntyre, W. Meevasana, T. K. Kim, M. Hoesch, J. Rault, T. Sasagawa, D. O. Scanlon and P. D. C. King.
   Physical Review B **96,** 085205 (2017)

6. **Maximal Rashba-like spin splitting via kinetic energy-driven inversion symmetry breaking**
   V. Sunko, H. Rosner, P. Kushwaha, S. Khim, F. Mazzola, L. Bawden, O. J. Clark, J. M. Riley, D. Kasinathan, M. W. Haverkort, T. K. Kim, M. Hoesch, J. Fujii, I. Vobornik, A. P. Mackenzie, and P. D. C. King.
   Nature **549,** 492-496 (2017)

7. **Electronic Structure and Enhanced Charge-Density Wave Order of Monolayer VSe_2**
   J. Feng*, D. Biswas*, A. Rajan*, M. D. Watson, F. Mazzola, O. J. Clark, K. Underwood, I. Marković, M. McLaren, A. Hunter, D. M. Burn, L. B. Duffy, S. Barua, G. Balakrishnan, F. Bertran, P. Le Fevre, T. K. Kim, G. Van der Laan, T. Hesjedal, P. Wahl, P. D. C. King
   *equal contribution
   Nano Letters **18,** 7, 4493-4499 (2018)

8. **Itinerant ferromagnetism of the Pd-terminated polar surface of $PdCoO_2$**
   F. Mazzola, V. Sunko, S. Khim, H. Rosner, P. Kushwaha, O. J. Clark, L. Bawden, I. Marković, T. K. Kim, M. Hoesch, A. P. Mackenzie, and P. D. C. King.
   PNAS, **115,** 12956 (2018)

9. **k_z-selective hybridisation of Se 4p and Ti 3d states at the charge density wave transition of $TiSe_2$**
   M. D. Watson, O. J. Clark, F. Mazzola, I. Marković, V. Sunko, T. K. Kim, K. Rossnagel, P. D. C. King
   Physical Review Letters, **122,** 076404 (2019)

10. **Probing spin correlations using angle resolved photoemission in a coupled metallic/Mott insulator system**
    V. Sunko*, F. Mazzola*, S. Kitamura*, S. Khim, P. Kushwaha, O. J. Clark, M. D. Watson, I. Marković, D. Biswas, L. Pourovskii, T. K. Kim, T.-L. Lee, P. K. Thakur, H. Rosner, A. Georges, R. Moessner, T. Oka, A. P. Mackenzie, P. D. C. King
    *equal contribution
    arXiv:1809.08972

Abstract

The isolation of graphene in 2004 and the subsequent characterisation of its many remarkable properties marked the start of an intense and ongoing research effort into other systems hosting so-called *Dirac cones* within their electronic band structures.

This thesis focuses on two classes of Dirac materials in particular. Dirac semimetals are essentially three-dimensional analogues of graphene, hosting spin-degenerate Dirac cones within their bulk band structure. Topological insulators are characterised by 'topological surface states' which are spin-polarised, surface-localised Dirac cones, essentially enclosing an otherwise insulating material in a highly conductive outer shell.

In both cases, the formation of the Dirac cone requires the crossing of bands within the bulk electronic band structure. In the vast majority of experimental realisations to date, these two bands derive from different atomic and orbital manifolds. Through spin- and angle-resolved photoemission, we establish that Dirac cones arising instead from a single-orbital manifold are both commonplace and advantageous. A mechanism allowing for the simultaneous formation of bulk Dirac cones and topological surface states is introduced, requiring only a discrepancy in bandwidths of a single, crystal field-split orbital manifold along a rotationally-symmetric axis.

Unlike in the conventional cases, the Dirac cones populating the resulting 'topological ladders' are not easily destroyed by changes to the relative energetics of orbital manifolds, caused by deformations to a lattice, for example. Instead, lattice deformations can be used to tune the position along the rotationally-symmetric axis where the crossings occur, but the states themselves are extremely robust. Indeed, we demonstrate that topological ladders of a common origin exist in six transition metal dichalcogenide (TMD) compounds, despite their disparate bulk properties and ground states. Moreover, the underlying mechanism driving the formation of topological ladders is expected to be applicable to many other compound classes, suggesting that single-orbital manifold topological phenomena is prevalent in nature.

Acknowledgements

This work would not have been possible without the guidance and support from Phil King and the other members of the King group, both past and present. I thank Lewis Bawden in particular, who invested a lot of effort in my early months integrating me into the group and the town, and then a lot more effort derailing anything resembling productivity after that. I also thank Federico Mazzola for helping me both to rationalise frequent work-related anxiety, and to develop a severe caffeine dependency.

I also acknowledge numerous collaborations: M. Saeed Bahramy (RIKEN & Uo Tokyo) contributed a large amount to the original research presented within this thesis in the form of DFT calculations and scientific discussions, and for that I am thankful. I additionally thank T. Sasagawa (Tokyo Institute of Tech.) for a large quantity of the samples used in this work, and Matt Neat (Wahl group, St Andrews) for his expertise in both STM and brew-making.

Finally I thank Rebecca Mekler, for reminding me that there is more to life than physics.

This work was supported by the EPSRC [Grant No. EP/K503162/1].

Research data underpinning this thesis are available at:
https://doi.org/10.17630/eed8dad8-836b-40e7-8e57-89c8dabed070

for Phil and Julie Clark

Contents

List of Abbreviations

2DEG	**Two**-**D**imensional **E**lectron **G**as
ARPES	**A**ngle-**R**esolved **P**hoto**e**mission **S**pectroscopy
B/AB or BA	**B**onding/**A**nti-**B**onding
BDP	**B**ulk **D**irac **P**oint
CDW	**C**harge **D**ensity **W**ave
CFS	**C**rystal **F**ield **S**plitting
CL	**C**ircular **L**eft (polarised)
CR	**C**ircular **R**eft (polarised)
(C)CW	(**C**ounter) **C**lock**w**ise
CBM	**C**onduction **B**and **M**inimum
DFT	**D**ensity **F**unctional **T**heory
DSM	**D**irac **S**emi**m**etal
EDC	**E**nergy **D**istribution **C**urve
GGA	**G**eneralised **G**radient **A**pproximations
IBG	**I**nverted **B**and **G**ap
IS	**I**nversion **S**ymmetry
LDA	**L**ocal-**D**ensity **A**pproximation
MDC	**M**omentum **D**istribution **C**urve
QHE	**Q**uantum **H**all **E**ffect
QSR	**Q**uantised **S**urface **R**esonance
QSS	**Q**uantised **S**urface **S**tate
SOC	**S**pin-**O**rbit **C**oupling
SS	**S**urface **S**tate
STM	**S**canning **T**unnelling **M**icroscopy
STS	**S**canning **T**unnelling **S**pectroscopy
TBG	**T**rivial **B**and **G**ap
TBM	**T**ight **B**inding **M**odel
TI	**T**opological **I**nsulator
TMD	**T**ransition **M**etal **D**ichalcogenide
TRIM	**T**ime-**R**eversal **I**nvariant **M**omenta
TRS	**T**ime-**R**eversal **S**ymmetry
TSS	**T**opological **S**urface **S**tate
UHV	**U**ltra-**H**igh **V**acuum
VBM	**V**alence **B**and **M**aximum
WSM	**W**eyl **S**emi**m**etal

Chapter 1

Introduction

1.1 Motivation

Silicon-based electronic devices have almost reached their limits. For decades, Moore's law, stating that the number of transistors on an integrated circuit chip doubles approximately every two years, has held true, commensurate with the ever growing demand for smaller, faster and more capable electronics (Fig. 1.1). There are now close to 20 billion transistors on a standard chip in a typical device, with their separation on the order of a few nanometers.

In order to sustain the current rates of advancement in device functionality, there must be a major upheaval in the operational principles behind how subsequent devices will work as well as the materials that will form them. The origin of this fast approaching limitation is two-fold. Firstly, with increasing transistor density, the management of the heat-load from thermal losses becomes both more crucial and more difficult [1], effectively imposing a maximum density to a conventional transistor array. Secondly, as the size of the transistors themselves approach the quantum limit, tunnelling effects become significant causing them to fail. 'Next-generation' electronics need therefore to exploit quantum mechanical effects, rather than trying to circumvent them.

One approach to bypass these heat loss limitations is to build devices with operational principles capable of exploiting new materials which are better conductors of electronic charge. Superconductors, which develop zero resistivity below some transition temperature, are of course excellent candidates. However, since the discovery of the first superconducting phase in 1911 [3], the record transition temperature achieved is only 203 K in sulphur hydride (H_2S) when under pressures in excess of 200 GPa [4], with a Ba-Ca-Cu-O system holding the current maximum transition temperature (133 K) at atmospheric pressure [5]. The lack of a superconductor with a transition temperature close to room temperature, and the risk of "nearly instant death" [6] when exposed to the current record holder, suggests that superconductors are unlikely the solution needed to prevent the stagnation of device development.

Two-dimensional systems such as graphene are arguably more likely candidates. Graphene, an allotrope of carbon successfully isolated in 2004 [7], possesses so-called *Dirac cones* within its electronic structure. The electronic structure is essentially a rule-book for how electrons can behave within a given solid, and electrons described by these Dirac cones are analogous

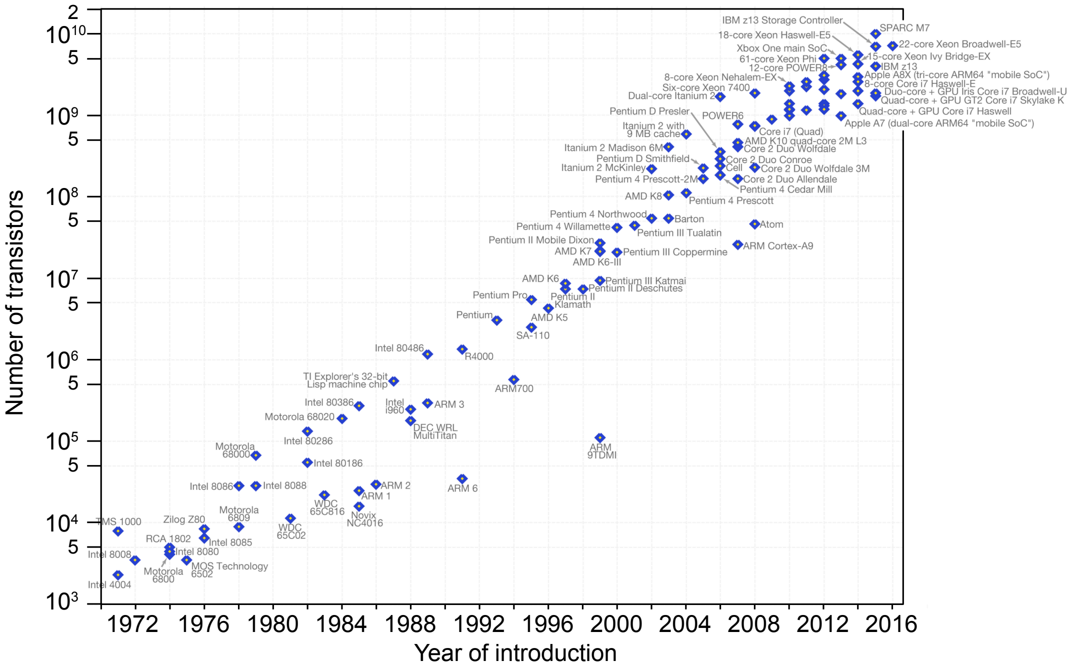

FIGURE 1.1: **Demonstration of Moore's law.** Graphic is adapted from [2].

to massless Dirac fermions theorised in high-energy physics; possessing extremely high mobilities and therefore providing graphene with a lower resistivity at room temperature than any elemental metal [8–10].

The work in this thesis focusses predominantly on two subsequent classes of Dirac materials that have been discovered within the last decade. The first of these is 'Dirac semimetals', essentially three-dimensional analogues of graphene [11], with 'bulk' Dirac cones potentially permitting electrons to move with high mobilities in three dimensions rather than two.

The second is the class of 'topological insulators'. Determining the topology of an object simply requires counting the number of holes. A mug and a ball are topologically distinct owing to the handle of the former. A mug and a donut however, are the same. Whilst this sounds like little more than needless characterisation, finding a compound with an electronic structure which is topologically distinct from that of the vacuum enforces electrons localised to the surface of this material to behave as massless Dirac fermions, essentially forming a highly conductive shell around an otherwise insulating bulk material [12]. These 'topological surface states' also present an opportunity to develop devices not requiring charge transfer at all. At the surfaces of topological insulators (and equivalently at the surfaces of 'Rashba'-compounds), electrons with spin 'up' and spin 'down' can behave differently under an external stimulus [13], opening routes to use spin as the information carrier, rather than charge.

The study of Dirac materials beyond graphene is only a decade old, but forms one of the most prominent research areas in condensed matter physics. Many compounds hosting Dirac cones of some form have been found to exist, but for the most part they are scattered, seemingly random subsets of only a few material families. Both topologically 'non-trivial' phases and

Dirac semimetal phases, collectively referred to as topological phenomena in this thesis, require crossings between two or more electronic bands. When these two bands originate from different constituent atoms, as is true for the majority of realisations to date, any slight perturbation to the crystal structure can alter the relative energetics of these bands, often destroying the electronic state of interest. Not only is this the origin of the apparent randomness in host materials, but it also greatly confines the design and development of any potential device utilising them. Only a few suitable candidates can be used, and the scope for tuning the behaviour of the topological phase itself is extremely limited.

This work instead searches for instances of both bulk and surface-localised Dirac cones formed within a single orbital manifold, originating from a single constituent atomic species of the unit cell. This thesis will show, that with a very minimal set of starting prerequisites concerning the rotational symmetry of the crystal structure and the delocalisation of electrons across the unit cell, it is possible to stabilise arrays of coexisting bulk Dirac cones and topological surface states within a single compound. More importantly, once a compound is found to host single-orbital manifold topological phenomena, the entire material family to which it belongs is likely host to the same physics. The states formed by this novel mechanism can be expected to be robust to extremely large perturbations, therefore lending themselves to a rich parameter space in which their energetic positions and fine-details can be tuned. The underlying mechanism behind this work therefore greatly bolsters the arsenal of potential candidates for next-generation electronic and spintronic devices, and creates new mechanisms by which potential devices may operate.

This will be demonstrated via spin- and angle-resolved photoemission studies predominantly into the transition-metal dichalcogenide family, a materials system already in the spotlight for its diverse properties in both bulk and single-layer forms.

1.2 Outline of Thesis

Chapter 2 begins with a theoretical overview of the bulk and surface electronic structures of a solid. Spin-orbit coupling and other relativistic effects are introduced from the Dirac equation. The importance of global lattice symmetries is emphasised with a discussion of spin-polarised electronic states which may only exist when inversion and/or time-reversal symmetries are lifted. Dirac materials and non-trivial band topology are introduced starting from a simplified tight-binding model of graphene. A discussion of how to protect three-dimensional Dirac cones from spin-orbit coupling and other perturbations is given, before discussing how topological surface states can occur in the cases where the crossing points are not protected.

Angle-resolved photoemission spectroscopy (ARPES) is the main experimental tool used for all work within this thesis. The underpinning theory as well as some practical considerations are discussed in Chapter 3. The basic operational principles behind spin-resolved ARPES are also provided. The experimental Chapters in this thesis (Chapters 4, 5 and 6) each include complementary density functional theory (DFT) based calculations provided by collaborators. As such, a working understanding of the main underlying principles behind DFT is demonstrated here.

Chapter 4 begins with an overview of the properties of transition-metal dichalcogenides (TMDs). A mechanism by which k_z-mediated topological surface states and bulk Dirac cones can be simultaneously formed is discussed. A 'topological ladder' of this origin is demonstrated to exist within the group-X superconducting TMD, 1T-PdTe$_2$, as well as the 'strongly spin-orbit coupled' semiconductor, 2H-WSe$_2$, despite the different symmetries, ground states and properties of these two compounds.

Chapter 5 concentrates primarily on the tunability of topological ladders formed within the TMDs, as well as their practical potential. The possibility of altering both the number and types of topological band crossings is discussed in part through a detailed comparison of the group-X TMDs PdTe$_2$ and PtSe$_2$. A brief overview of a scanning-tunnelling microscopy study into the possible role of topological surface states in the surface superconductivity of PdTe$_2$ is also given.

Chapter 6 continues to show the potential of the relatively understudied group-X TMDs. It is shown how, by Rb dosing the surface of PtSe$_2$, a two-dimensional electron gas (2DEG) can be stabilised which exhibits an 'enhanced' Rashba-splitting relative to what is typically achieved in 2DEGs with semiconducting systems as the basis. The Chapter shows how the 2DEG is confined by an unusual 'dual' form of a band bending potential, enhancing Rashba spin splitting, and likely generic to semimetallic systems.

Concluding remarks are given in Chapter 7 along with a discussion of the validity of the underlying mechanism driving the formation of topological phases to systems outside of the TMD family, and on the additional properties that could arise as a result. Specifically, single-orbital manifold topology in systems with different crystal structures, rotational lattice symmetries and ground state properties are overviewed, with a focus primarily on ferroelectric SnTe.

Chapter 2

Scientific Background

2.1 Electronic structure

The electronic structure is a strict rulebook for the behaviour of electrons within a solid. Its basis is an intertwined band network, the *electronic band structure*. Each band is populated by electrons, setting their energy-momentum relationship within the solid. The shape taken by the full electronic structure, also encompassing charge, spin and quasiparticle correlations, informs many physical properties of a solid, from charge carrier mobilities to magnetic structure. Understanding the fine details of the electronic structures of novel materials is a crucial prerequisite to the development of next-generation devices harnessing their properties.

An isolated atom has a set of discrete, well-defined electronic energy levels described by the set of quantum numbers (n, l, m_l, m_s). The relative energetics of electrons occupying a given energy level is described by n, and their real space probability distribution is set by the orbital type (l, m_l) with each orbital able to contain two electrons with opposite spin, m_s. When forming the unit cell of a solid, atomic orbitals overlap to produce bonding and anti-bonding sets of molecular energy levels, $E_{0,i}$, where the corresponding molecular orbitals are indexed by i. The periodic potential associated with bringing many of these unit cells together transforms each of these energy levels into quasi-continuous k-dependent bands, $E_i(\boldsymbol{k}) = E_{0,i} + f_i(\boldsymbol{k})$, where $\boldsymbol{k}$ is a position in momentum space and i now the band index.

The extent of the k-dependence of a band, or equivalently its bandwidth, is determined by the localisation of the occupying electrons to a given lattice site. In general, the most tightly bound electrons of the constituent atoms (lowest n) retain their atomic-like k-independent descriptions even within the solid. In contrast, the most loosely bound valence electrons lie in orbitals which can overlap across lattice sites. The extent of relative orbital overlaps within a unit cell, or equivalently the *hopping strengths*, directly determine the relative dispersions of bands of a particular orbital character. The final result is a spaghetti like network of interlocking bands.

The crystal structure is therefore ultimately responsible for shaping the electronic structure. Not only is its periodicity directly adopted by the electronic structure, but the geometric arrangement of orbitals within the unit cell sets both the initial energetics, $E_{0,i}$, of bands, as well as the relative orbital overlaps that determine the details of their k-dependence, $f_i(\boldsymbol{k})$.

2.1.1 Crystal field splitting

Solids are held together by the bonding of electrons across atomic sites. One or more pairs of electrons may be ‘shared’ across sites (covalent bonding), or electrons can be fully transferred between sites creating strong Coulombic forces between the resulting ions (ionic bonding)[1]. In either case, the shape of the unit cell is set such that the chemical bonds required to hold the solid together are formed, whilst the overall Coulomb repulsion of all ions and electrons, both bonding and non-bonding, in the system is minimised. Depending on the symmetry of the resultant unit cell, subsets of orbitals belonging to a given orbital manifold (s, p, d or f for $l = 0, 1, 2$ or 3) can experience disparate degrees of orbital overlap, lifting degeneracies within. This is *crystal field splitting*.

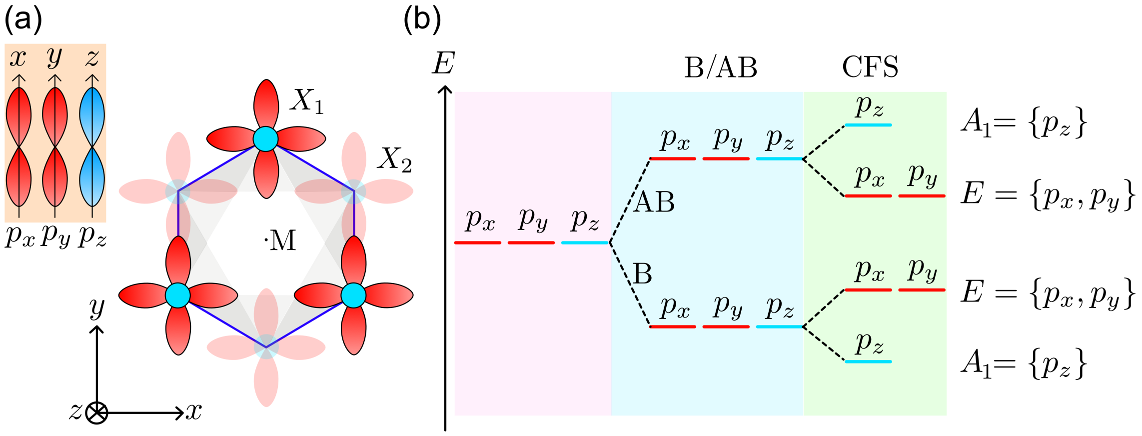

FIGURE 2.1: **Crystal field splitting (CFS) in the chalcogen p-orbitals of an octahedral crystal structure.** (a) Schematic illustration of the p-orbitals at the chalcogen sites of an octahedron collapsed onto a two dimensional plane. (b) Energetic degeneracy lifting of the $p_{x,y,z}$ orbitals when forming a unit cell (bonding/anti-bonding (B/AB)), and with the CFS.

This thesis will focus largely on transition metal containing compounds. These systems are held together predominantly by covalent bonds formed between the d-orbitals of the transition metal (M) and the p-orbitals of a chalcogen (X={O, S, Se, Te}) [14]. An octahedral unit cell often results in order to minimise the Coulomb repulsion between these p- and d-orbitals [15]. The metal is positioned at the centre of the octahedron, with repulsive electron clouds from the chalcogen atoms positioned at each corner.

In this geometry, both the d- and p-orbital manifolds experience a crystal field splitting. A schematic of the unit cell as viewed along the c-axis ($\parallel z$) is shown schematically in Fig. 2.1(a), with the valence p-orbitals of the chalcogen included. This demonstrates how there is a greater orbital overlap of $p_{x,y}$ orbitals than p_z orbitals, therefore raising the energy of the former set (A_1) relative to the latter (E).

---

[1] Further intermolecular forces also contribute. Dipoles deriving from an uneven distribution of charge across a chemical bond can interact with other dipoles and ions. These interactions can involve ‘permanent’ dipoles (e.g. dipole-dipole interactions, hydrogen bonding) or ‘instantaneous’ dipoles induced by charge fluctuations (e.g. van der Waals forces).

Since all valence d-orbitals within the system are localised to a single atomic site here, the crystal field splitting for the metal d-orbital manifold is set by relative overlaps with the chalcogen p-orbitals: d-orbitals which maximally avoid the p-orbital lobes at the corners ($t_{2g} = \{d_{xy}, d_{yz}, d_{xz}\}$) are lowered in energy, whilst those with significant overlap ($e_g = \{d_{x^2-y^2}, d_{z^2}\}$) are raised in energy.

2.1.2 Calculating the electronic band structure

Fortunately, it is not required to consider the interactions of every electron with every other electron on each atomic site within the lattice to obtain a good approximation of the electronic structure, at least for simple systems. Instead, by assuming that electron dynamics are much faster than lattice dynamics, one can effectively combine the interaction of each electron with the lattice into a single potential, $V(\boldsymbol{r})$ [16, 17]. That is, any motion of the nuclei will be accompanied by an almost instantaneous shift of the electrons without any energy cost. The interaction of an electron with all the other electrons can also be included within this same term by assuming that the main contribution of electron-electron interactions is to screen the nuclear charge from the atom. $V(\boldsymbol{r})$ is therefore the potential felt by a single electron from electronically screened nuclear charges [16, 17].

The Hamiltonian of interest is then the time independent Schrödinger equation with a periodic potential:

$$\hat{H}(\boldsymbol{r}) = -\frac{\hbar^2}{2m}\boldsymbol{\nabla}^2 + V(\boldsymbol{r}); \quad V(\boldsymbol{r}) = V(\boldsymbol{r} + \boldsymbol{r}_n), \tag{2.1}$$

where m is the electron mass and $\boldsymbol{r}_n$ is some linear combination of the basis lattice vectors for the relevant crystal structure. The eigenfunctions for this problem also must contain information about the underlying lattice. In particular, they must satisfy the Bloch condition, which enforces periodicity:

$$\Psi(\boldsymbol{r} + \boldsymbol{r}_n) = e^{i\boldsymbol{k}\boldsymbol{r}_n}\Psi(\boldsymbol{r}). \tag{2.2}$$

Typically one of two approaches are used to find the corresponding eigenstates. Either the potential, $V(\boldsymbol{r})$, is treated as a small perturbation as in the nearly-free electron model, or one can do the opposite, as will be discussed below.

The tight-binding model (TBM)

Within the tight-binding model, electrons are assumed to be sufficiently tightly bound to the lattice that the single particle Hamiltonian of a crystal is the same for that of the isolated atom, but with an extra periodic potential, $V(\boldsymbol{r})$:

$$\hat{H}_{\text{atom}} + V(\boldsymbol{r}) = \hat{H}_{\text{crystal}}. \tag{2.3}$$

The contribution to $V(\boldsymbol{r})$ from an atom at site n is a maximum exactly at that lattice site, i.e on top of that atom, and zero a real space distance $\boldsymbol{r}_n = r_1$ away at site $n+1$, where $\boldsymbol{r}_1$ is a nearest-neighbour lattice spacing. $V(\boldsymbol{r})$ is therefore at a minimum midway between atomic sites.

The atomic wavefunctions $|\phi_i\rangle$ are eigenstates of $\hat{H}_{\text{atom}}$,

$$\hat{H}_{\text{atom}}|\phi_i\rangle = \epsilon_i|\phi_i\rangle, \tag{2.4}$$

where ϵ_i is the i^{th} energy level. When transitioning to an ordered crystal, atomic wavefunctions, $|\phi_i\rangle$, overlap, meaning that they are no longer eigenstates of the atomic Hamiltonian. In order to satisfy the Bloch condition, it is necessary to construct linear combinations of these starting atomic wavefunctions,

$$\Psi_i = \sum_n c_{i,n}|\phi_{n,i}\rangle, \tag{2.5}$$

where the summation is over the lattice sites, n, each a lattice vector $\boldsymbol{r}_n$ apart. The subscript, i, is now a band label. The more atomic orbitals included in the problem, the more solutions to the Schrödinger equation (Eqn. 2.1) and the more accurately the band structure will be captured. To get a good qualitative approximation, however, it is usually sufficient to include only the least-bound orbitals which contribute bands to the electronic structure near E_F, the Fermi level. In the most simple cases, it is possible to go simpler still and enforce that orbitals on each site are orthogonal such that $\langle\phi_{n,i}|\phi_{m,i}\rangle = \delta_{n,m}$ [2].

Considering only one orbital, inserting these wavefunctions into the Schrödinger equation and multiplying from the left by $\langle\phi_n|$ produces the following set of simultaneous equations for each n:

$$\sum_m H_{nm}c_m = Ec_n; \quad H_{nm} = \langle\phi_n|\hat{H}|\phi_m\rangle; \quad c_m = \frac{\mathrm{e}^{i\boldsymbol{k}\boldsymbol{r}_m}}{\sqrt{N}}. \tag{2.6}$$

The eigenvalues, $E(\boldsymbol{k})$, then provide the electronic band structure.

In order to highlight general key features of band dispersions in real materials, the 2D honeycomb carbon allotrope, graphene, will be considered as a simple example.

---

[2] This assumption is not true in general. It is possible to construct *Wannier orbitals* however, which are centred on lattice sites and are orthogonal across sites by definition. See Chapter 3.3.

2.1.3 Graphene

The crystal structure of graphene is shown in Fig. 2.2. Its unit cell is composed of two inequivalent carbon atoms, producing a global ‘honeycomb’ lattice structure. The honeycomb structure shown here is not a Bravais lattice however, since the vector connecting an A site to a B site is not a lattice translation vector. It is therefore necessary to consider this structure as two intersecting triangular sub-lattices composed of A and B lattice sites, respectively. The bonding in graphene is predominantly σ-type, deriving from the in-plane $2p_{x,y}$ orbitals. The band nearest the Fermi level is then p_z derived. Considering only the p_z orbitals therefore, the trial wavefunction is

$$c_m\phi_m = \frac{1}{\sqrt{N}}\Big[c_A e^{i\boldsymbol{k}(\boldsymbol{d}_A+\boldsymbol{r}_m)}\rho_m^A + c_B e^{i\boldsymbol{k}(\boldsymbol{d}_B-\boldsymbol{r}_m)}\rho_m^B\Big], \tag{2.7}$$

where $c_{A,B}$ are complex coefficients setting the size of the wavefunction at each lattice site on each the A and B sub-lattices. $\boldsymbol{d}_A = -\boldsymbol{d}_B$ is a vector connecting the A site to the origin, taken to be midway between an A and B lattice site (see Fig. 2.2). $\boldsymbol{r}_m$ is the set of linear combinations of $\boldsymbol{a}_{1,2,3}$ which map, for example, a lattice point on the A sub-lattice, to the surrounding lattice points on the B sub-lattice (i.e $\boldsymbol{R}_m^{A,B} = \pm\boldsymbol{r}_m + \boldsymbol{d}_{A,B}$ are vectors mapping the origin to a lattice point). $\rho_m^{A,B}$ are the wavefunctions for a given lattice site, m, on the A and B sub-lattices.

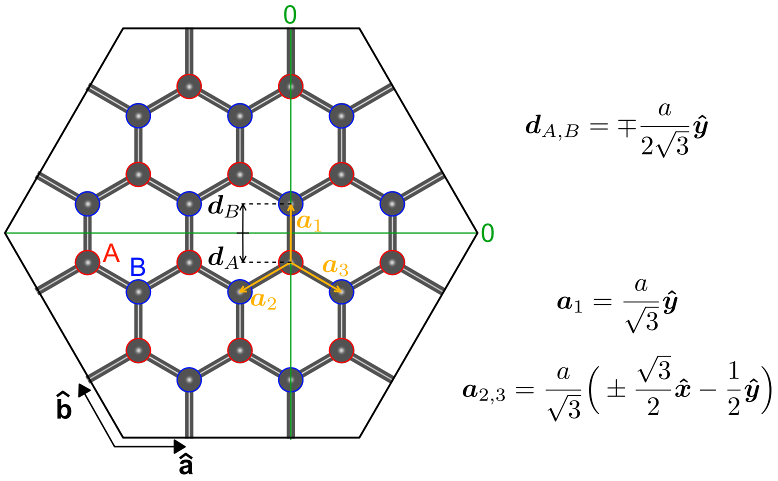

FIGURE 2.2: **Crystal structure of graphene.** The honeycomb lattice structure of graphene is shown, with the A and B sub-lattices labelled. Relevant vectors for the discussion are drawn and displayed.

Considering only nearest neighbour hopping ($\boldsymbol{r}_m \in \{0, \boldsymbol{a}_1, \boldsymbol{a}_2, \boldsymbol{a}_3\}$) and assuming that wavefunctions on neighbouring sites are orthogonal:

$$\langle\rho_n^A|\rho_m^B\rangle = 0; \quad \langle\rho_n^A|\rho_m^A\rangle = \delta_{nm}, \tag{2.8}$$

one can insert wavefunctions of the form of that in Eqn. 2.7 into the Schrödinger equation to obtain the following:

$$\sum_{m=0}^{3}\frac{1}{\sqrt{N}}\Big[c_A e^{i\boldsymbol{k}(\boldsymbol{d}_A+\boldsymbol{a}_m)}\hat{H}|\rho_m^A\rangle + c_B e^{i\boldsymbol{k}(\boldsymbol{d}_B-\boldsymbol{a}_m)}\hat{H}|\rho_m^B\rangle\Big]$$

$$= E(\boldsymbol{k})\sum_{m=0}^{3}\frac{1}{\sqrt{N}}\Big[c_A e^{i\boldsymbol{k}(\boldsymbol{d}_A+\boldsymbol{a}_m)}|\rho_m^A\rangle + c_B e^{i\boldsymbol{k}(\boldsymbol{d}_B-\boldsymbol{a}_m)}|\rho_m^B\rangle\Big]. \quad (2.9)$$

By defining both the hopping strength between p_z orbitals on neighbouring sites as

$$\langle\rho_n^A|\hat{H}|\rho_m^B\rangle = \begin{cases} -t_{p_z} & |\boldsymbol{R}_n^A - \boldsymbol{R}_m^B| = \frac{a}{\sqrt{3}} \\ 0 & \text{otherwise} \end{cases}$$

and the on-site energy for the A and B sub-lattice as

$$\langle\rho_n^{\{A,B\}}|\hat{H}|\rho_m^{\{A,B\}}\rangle = \begin{cases} E_{\{A,B\}} & n=m \\ 0, & \text{otherwise} \end{cases}$$

one can multiply Eqn. 2.9 from the left by $\langle\rho_0^{A,B}|$ to obtain an eigenvalue relation from which one can extract the dispersion relation $E(\boldsymbol{k})$:

$$\hat{H}\begin{pmatrix} c_A \\ c_B \end{pmatrix} = \begin{pmatrix} E_A & t_{p_z} f(\boldsymbol{k}) \\ t_{p_z} f(\boldsymbol{k})^* & E_B \end{pmatrix}\begin{pmatrix} c_A \\ c_B \end{pmatrix} = E(\boldsymbol{k})\begin{pmatrix} c_A \\ c_B \end{pmatrix};$$

$$E(\boldsymbol{k}) = \frac{E_A+E_B}{2} \pm \sqrt{\Big(\frac{E_A-E_B}{2}\Big)^2 + t_{p_z}^2|f(\boldsymbol{k})|^2}, \quad (2.10)$$

where

$$f(\boldsymbol{k}) = 1 + \exp(i\boldsymbol{k}(-\boldsymbol{a}_2+\boldsymbol{a}_1)) + \exp(i\boldsymbol{k}(-\boldsymbol{a}_3+\boldsymbol{a}_1))$$

$$= 1 + 2\exp\Big(\frac{iak_y\sqrt{3}}{2}\Big)\cos\Big(\frac{ak_x}{2}\Big). \quad (2.11)$$

Figure 2.3 shows the resultant band dispersion of graphene, where $E_A = E_B$. The bandwidth, dependent on the degree of overlap between neighbouring orbitals and therefore on the probability of hopping $t = t_{p_z}$, is also indicated along with the shape of the Brillouin zone.

Here, the band structure, $E(\boldsymbol{k})$, has only two bands, simply because only two inequivalent atoms per unit cell with one orbital each were included in the problem. The higher energy band ($E_\Gamma = E_0 + 3t$) at the Γ point is the anti-bonding solution, and the lower one ($E_\Gamma = E_0 - 3t$) the bonding solution. This simple one-orbital approximation in a 2D system captures the near-E_F π bands of graphene well, but more sophisticated approaches are required for more complex

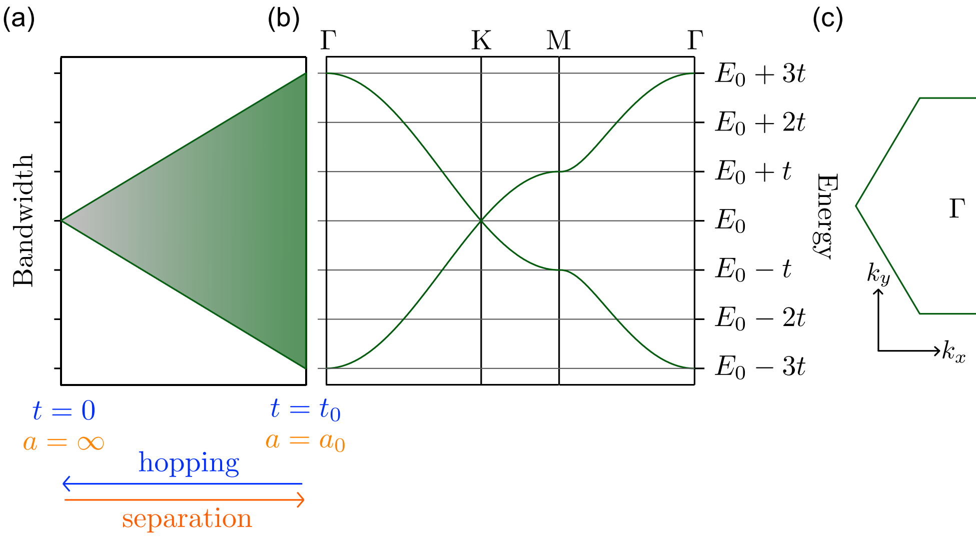

FIGURE 2.3: **Electronic structure of graphene.** (a) Bandwidth of the p_z-derived bands in graphene as a function of hopping strength, where $t = 0$ corresponds to infinitely separated atoms ($a = \infty$). (b) Electronic structure of the π bands along a Γ-K-M-Γ path in momentum space. (c) Brillouin zone with high symmetry points and directions indicated.

multi-orbital and higher dimensional systems [18]. Despite this, some properties of this band structure are true in general, at least in the non-interacting limit.

1. The band structure is symmetric in $\boldsymbol{k}$ about the time-reversal invariant momenta (TRIM), here Γ and M, to ensure periodicity across Brillouin zones.
2. The bandwidth of a band derived from a given orbital character is dependent solely on the size of the hopping strength, t, for that orbital. If this was extended to three dimensions, the resulting dispersion relation, $E(k_x, k_y, k_z)$, has a dependence on k_x, k_y and k_z, where the dispersion along each of these directions would be set by hopping strengths along the corresponding axis in real space.
3. The band minimum or maximum around the zone centre is usually approximately parabolic: $E(k) \propto \cos(k) \approx 1 - \frac{1}{2}k^2$.

Two-dimensional Dirac cones in graphene

The band structure obtained from the simple two-orbital tight binding model, shown in Fig. 2.3, exhibits linear crossing points at the K points. These linearly dispersing bands together form a two-dimensional *Dirac cone*, with the crossing point a *Dirac point*. These Dirac cones are almost solely responsible for the surge in interest of graphene in recent years, and the subsequent interest in so-called *Dirac semimetals* and *topological insulators*, discussed in Section 2.2 and relevant to the work in this thesis.

In the vicinity of the K points $(\pm\frac{4\pi}{3a}, 0)$ where the Dirac cones reside, $f(\boldsymbol{k})$ can be rewritten as

$$f(\boldsymbol{k}' = \boldsymbol{k} - K_\zeta) = 1 + 2\exp\left(\frac{iak_y\sqrt{3}}{2}\right)\cos\left(\frac{a(k_x - K_\zeta)}{2}\right)$$
$$\approx \frac{\sqrt{3}a}{2}(\zeta k_x - ik_y) = \frac{\sqrt{3}a}{2\hbar}(\zeta p_x - ip_y), \quad (2.12)$$

where $\boldsymbol{p} = \hbar\boldsymbol{k}$ and $\zeta = \pm 1$ defines the *valley index*, describing electrons at K or −K. Keeping the onsite energies inequivalent for generality ($E_A \neq E_B$), the Hamiltonian in Eqn. 2.10 becomes

$$\hat{H} = \begin{pmatrix} E_A & -\frac{\sqrt{3}t_{p_z}a}{2\hbar}(\zeta p_x - ip_y) \\ \frac{\sqrt{3}t_{p_z}a}{2\hbar}(\zeta p_x + ip_y) & E_B \end{pmatrix} = v(\zeta p_x\sigma_x + p_y\sigma_y) + m\sigma_z, \quad (2.13)$$

where $v = \frac{\sqrt{3}at_{p_z}}{2\hbar}$ is the Fermi velocity, and $E_A = -E_B = m$.

When written in this form, the Hamiltonian demonstrates the presence of a spin-like quantity, allowing it to be rewritten in terms of the Pauli matrixes, $\sigma_{x,y,z}$. The band structure of graphene is spin degenerate, however. Instead, the pseudospin quantity here describes the coupling between the A and B sub-lattices [19]. The corresponding dispersion relation is displayed in Eqn. 2.14.

$$E(\boldsymbol{k}') = \begin{cases} \pm\sqrt{m^2 + v^2(p_x^2 + p_y^2)} & E_A = -E_B = m \\ \pm\sqrt{v^2(p_x^2 + p_y^2)} & E_A = E_B \end{cases} \quad (2.14)$$

The case for graphene ($E_A = E_B$) can be compared directly to the eigenvalues for plane-wave solutions of the Dirac Hamiltonian (Eqn. 2.15). The Dirac Hamiltonian, discussed further in Section 2.1.5, describes relativistic spin-$\frac{1}{2}$ fermions, with its eigenvalues therefore providing their total relativistic energy.

$$E(\boldsymbol{p}) = \pm\sqrt{m_0^2c^4 + \boldsymbol{p}^2c^2} \quad (2.15)$$

For zero rest mass ($m_0 = 0$), Eqn. 2.15 produces a linear dispersion in momentum. The linear crossing points in the band structure of graphene are therefore considered to be condensed matter realisations of massless Dirac fermions in high energy physics. Whilst this is in itself provides routes to study analogues of massless Dirac fermions in a laboratory environment, their presence in graphene and any other compounds in which they are found has extremely useful implications for devices made from those materials. Dirac cones are naturally associated with extremely high mobility carriers and low resistivity. Indeed, electron and hole mobilities in graphene are found to be higher than InSb, the previous record holder for carrier mobilities [20], on the order of 10^5 cm^{2}V^{-1}s^{-1} [9], corresponding to a resistivity of $\approx 10^{-6}\ \Omega$ cm, smaller than all elemental metals at room temperature [10]. This, coupled with extremely high thermal conductivities [21], makes graphene one particularly attractive candidate material for efficient next-generation electronics devices, which are currently limited in size by thermal dissipation [1]. Graphene also possesses an unconventional integer quantum Hall effect as a direct consequence of its Dirac cones [22, 23], and its two-dimensional atomically thin nature opens up potential for applications requiring flexible and/or transparent conductors, in solar cells for example [24].

This array of remarkable properties in graphene can be attributed as a direct consequence of the simplicity of its crystal structure. More specifically, *sub-lattice symmetry* is crucial for the formation of Dirac points. By referring back to Eqn. 2.14, it is clear that the Dirac cones do not exist when $E_A \neq E_B$. As an example, hexagonal boron nitride (BN) shares a near-identical crystal structure to graphene, but since B and N occupy the A and B sub-lattices respectively, there are no Dirac points within its electronic structure [25]. The asymmetry of atomic species on neighbouring lattice sites is just one inhibitor to Dirac cone formation in graphene-like 2D materials. Another is *spin-orbit coupling* (SOC), which will be overviewed below in the context of symmetry breaking at the surface of a solid.

2.1.4 Surface states

The above provides an origin and simple description of the bulk electronic band structure of a material. In those discussions, the k-dependence of a given electronic band is defined by the periodicity of the potential, $V(\boldsymbol{r})$. At the surface of a solid, this periodicity is lost, and therefore the surface electronic structure need not be equivalent to that of the bulk.

The Bloch plane wave solutions to the Schrödinger equation possess a real k-vector, extending infinitely into the bulk ($z < 0$). At the surface the periodicity of $V(\boldsymbol{r})$ is lost, instead changing discontinuously to match the constant vacuum potential, $V(\boldsymbol{r})_{z>0} = V_{\text{vac}}$. Bulk solutions must obey the following boundary conditions which relate their wavefunctions inside (i) the crystal to the wavefunctions outside (o), into the vacuum [26, 27]:

$$\psi_o(z=0) = \psi_i(z=0); \quad \frac{d\psi_o}{dz}|_{z=0} = \frac{d\psi_i}{dz}|_{z=0}. \tag{2.16}$$

The wavefunction in vacuum must take the following form,

$$\psi_o \propto \exp[-\sqrt{\frac{2m}{\hbar^2}(V_{\text{vac}} - E)z}]; \quad E < V_{\text{vac}}, \tag{2.17}$$

found simply by solving the Schrödinger equation (Eqn. 2.1) for $V(\boldsymbol{r}) = V_{\text{vac}}$ [26]. Every bulk solution to the Schrödinger equation is matched onto an exponential tail of this form. The lack of an imaginary component here requires that both incident and reflected plane waves

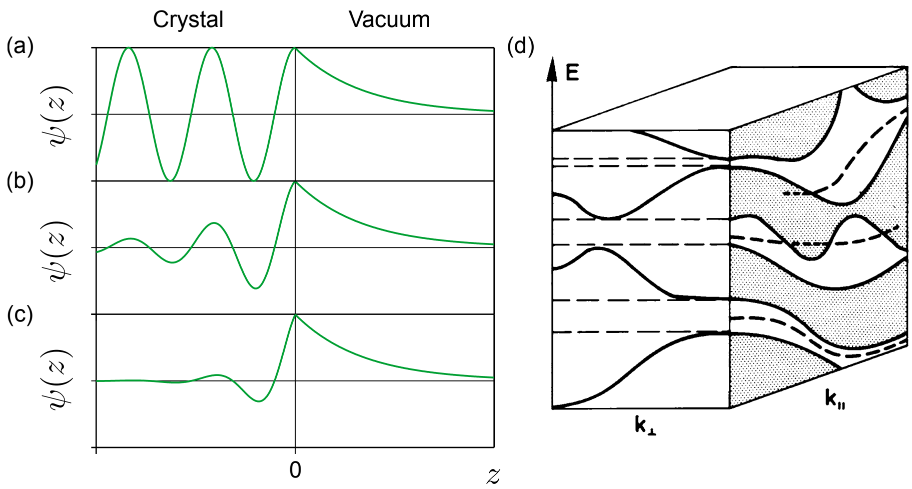

FIGURE 2.4: **Electronic wavefunctions at a sample surface.** (a-c) Electronic wavefunctions for a bulk band (a), a surface resonance (b) and a surface state (c). $z < 0$ corresponds to a crystal, $z > 0$ is the vacuum. (d) Schematic illustration of bulk-surface wavefunction overlap in a three dimensional band structure, adapted from [26]. Shaded areas along the $k_\parallel$ axis indicate the $k_\perp = k_z$ projected bulk band structure. Surface solutions which do not become degenerate with this area for all $k_\parallel$ are surface states (bottom), otherwise they are surface resonances (top and middle).

must be considered on the crystal side of the potential barrier to ensure that the continuity conditions can be fulfilled [26, 27].

These continuity conditions could also be satisfied for a single plane wave with a complex wavevector, such that the wavefunction inside the crystal $\propto \exp(ik_z z)$ is also real. Solutions of this form are *surface state* solutions, which correspond to additional real eigenvalues. Surface states possess Bloch-like wavefunctions parallel to the sample surface (in the x-y plane), but with exponentially decaying amplitudes in the z direction, both into the crystal and into the vacuum.

Their complex wave vector prohibits degeneracies with bulk solutions which have strictly real k-vectors, and as such, surface states exist within bulk band gaps. A band dispersion, $E(\boldsymbol{k})$, can only share the dimensionality of the underlying system. Surface states, localised to the two-dimensional surface plane, therefore do not disperse in k_z. However, whilst surface states are enforced to exist in local bulk band gaps, they are insensitive to k_z and therefore can become resonant with bulk bands at some k_z. The result is a *surface resonance* which possesses a wavefunction that is more spatially delocalised than that of a 'true' surface state existing within a k_z-projected bulk band gap [26]. Figure 2.4 illustrates wavefunction localisation for a bulk state, a surface resonance and a surface state, as well as schematic surface-derived solutions within a three-dimensional band structure.

In a tight-binding picture, every distinct orbital involved in the chemical bonding can give rise to one surface state. c-axis hopping for the topmost layer of a crystal is only possible with the layer directly below, and so the energy contribution from a near-surface layer is smaller than an otherwise equivalent layer deeper in the bulk. To first order, the surface electronic structure therefore mimics the $k_{||}$-dependence of the bulk solutions, tracing the bulk manifold along the full Brillouin zone, but with an energetic separation between the bulk and surface solutions set by the strength of the perturbation caused by the surface itself. This is maximised in, for example, 'rock-salt'-type crystals wherein significant bonding along the c-axis results in prominent surface states associated with the left over 'dangling bonds' [26]. Conversely, in van der Waals bonded layered systems, where there is neither strong bonding along the c-axis ($t_c \ll t_{a,b}$) or the possibility of surface charge build up, surface state solutions are not common, or at least, they are indistinguishable from the bulk band structure along which they trace.

2.1.5 Spin-orbit coupling and the Rashba effect

The previous Sections underline the origins of both the bulk and surface electronic structures of a solid. This is not a complete picture, however, as the Schrödinger equation does not capture relativistic effects. The *spin-orbit interaction* is one such effect missed, and although it offers only small energetic corrections, it underpins the entirety of the work within this thesis, and a significant proportion of modern day research in condensed matter systems.

Spin-orbit coupling can be considered as an *internal Zeeman effect*. The Zeeman effect is the energetic splitting of an electron system in a magnetic field by an amount $\pm\boldsymbol{\mu}\cdot\boldsymbol{B}$ depending on the electron spin, where $\boldsymbol{\mu}$ is the magnetic moment and $\boldsymbol{B}$ is the magnetic field. This analogy becomes intuitive when considering the oversimplified quasi-classical picture of an electron orbiting a nucleus. The electron has velocity $\boldsymbol{v} = \boldsymbol{p}/m$, and experiences an electric field, $\boldsymbol{E}(\boldsymbol{r})$, from the positive Coulomb potential of the nucleus. In the rest frame of the orbiting electron, the Lorentz transformation of $\boldsymbol{E}(\boldsymbol{r})$ is the effective field experienced. Hence, the electron experiences a magnetic field of the form $\boldsymbol{B} = -\boldsymbol{v} \times \frac{\boldsymbol{E}(\boldsymbol{r})}{c^2}$, and its Zeeman-like energy shift is

$$-\boldsymbol{\mu}\cdot\boldsymbol{B} = -\frac{\hbar e}{m^2c^2}\boldsymbol{\sigma}\cdot(\boldsymbol{E}\times\boldsymbol{p}), \tag{2.18}$$

where $\boldsymbol{\sigma}$ is the set of Pauli matrices. Although oversimplified, this picture is sufficient to see that spin-orbit coupling will readily produce a k-dependent spin mixed term when operating on a two component (for spin) plane wave wavefunction. Its strength is dependent both on the electron mass, m, and on the size of the electric field within a solid.

More formally, the Dirac Hamiltonian provides a complete relativistic description of quantum mechanics, containing spin-orbit coupling and other relativistic effects intrinsically:

$$\hat{H}_{\text{Dirac}} = c\tilde{\boldsymbol{\alpha}}\cdot\boldsymbol{p} + \tilde{\beta}mc^2 + V(\boldsymbol{r}), \tag{2.19}$$

where

$$\alpha_i = \begin{pmatrix} 0 & \tilde{\sigma}_i \\ \tilde{\sigma}_i & 0 \end{pmatrix}; \quad \tilde{\beta} = \begin{pmatrix} \tilde{I}_2 & 0 \\ 0 & -\tilde{I}_2 \end{pmatrix},$$

and $i \in \{x, y, z\}$. By taking the non-relativistic limit of this ($mc^2 \rightarrow m_0c^2$), by the method outlined by Foldy and Wouthuysen in [28], one reobtains the Schrödinger equation complete with relativistic corrections.

$$\hat{H}_{\mathrm{FW}} = \frac{\boldsymbol{p}^2}{2m_0} + V(\boldsymbol{r}) + \frac{e\hbar}{2m_0}\boldsymbol{\sigma}\cdot\boldsymbol{B} - \frac{e\hbar\boldsymbol{\sigma}\cdot\boldsymbol{p}\times\boldsymbol{E}}{4m_0^2c^2} - \frac{e\hbar^2}{8m_0^2c^2}\boldsymbol{\nabla}\cdot\boldsymbol{E} + O\Big(\frac{1}{m_0^3c^2}\Big) \tag{2.20}$$

Here, $\boldsymbol{B}$ and $\boldsymbol{E}$ are the applied magnetic and electric fields respectively. The first two terms on the right hand side are the kinetic energy and potential term of the Schrödinger equation, the third term is the Zeeman energy correction and the fourth term is the spin-orbit coupling correction seen in Eqn. 2.18 with an amended coefficient from Thomas Precession[3] [29]. The remaining terms are the Darwin correction, describing changes in electron-nucleus interactions due to quantum oscillations of the electrons, and higher order corrections to kinetic and Zeeman terms.

More insight into the effect of the spin-orbit interaction is gained when considering the case of a spherically symmetric electric field, $\boldsymbol{E}(\boldsymbol{r}) = \frac{1}{\epsilon}\frac{1}{\boldsymbol{r}}\frac{\partial V}{\partial r}\hat{r}$, applicable for a hydrogen-like atom, for example. The fourth term on the right hand side of Eqn. 2.20 then becomes [30]:

$$\hat{H}_{\mathrm{SOC}} = \frac{\mu_B}{\hbar m_e e c^2}\frac{1}{\boldsymbol{r}}\frac{\partial V(\boldsymbol{r})}{\partial r}\boldsymbol{L}\cdot\boldsymbol{S}; \quad \boldsymbol{L}\cdot\boldsymbol{S} = \frac{\hbar^2}{2}(j(j+1) - l(l+1) - s(s+1)), \tag{2.21}$$

where $\boldsymbol{S} = \frac{1}{2}\hbar\boldsymbol{\sigma}$. Writing in terms of the spin and angular momentum operators in this way explicitly shows the coupling of spin and orbital angular momentum quantum numbers. Spin-orbit coupling therefore promotes orbital character mixing and the lifting of spin degeneracy. In addition to the *atomic* spin-orbit coupling approximated in Eqn. 2.21, any further intrinsic or extrinsic electric fields in a real solid will contribute a further spin-orbit correction. Independent of the exact form of $\boldsymbol{E}(\boldsymbol{r})$, some key features always hold true.

1. In general, the valence electrons of heavier atoms experience larger spin-orbit corrections. The potential, $V(\boldsymbol{r})$, in this atomic picture goes as Z^4, for example [30].
2. The larger l, the larger the spin orbit correction, meaning that bands derived from d- and p-orbitals can experience larger spin orbit corrections than s-orbitals, for example.
3. Degeneracies of electrons with $m_s = \pm\frac{1}{2}$ can be lifted, if permitted by global lattice symmetries.

Following on from the final point, there must also be a breaking of either *inversion symmetry* (IS) or *time-reversal symmetry* (TRS) in order to lift spin degeneracy.

---

[3] The discrepancy in the coefficient between equations 2.18 and 2.20 originates from the failure to consider the temporal component of the electromagnetic field 4-vector when switching frames in the semi-classical derivation [29].

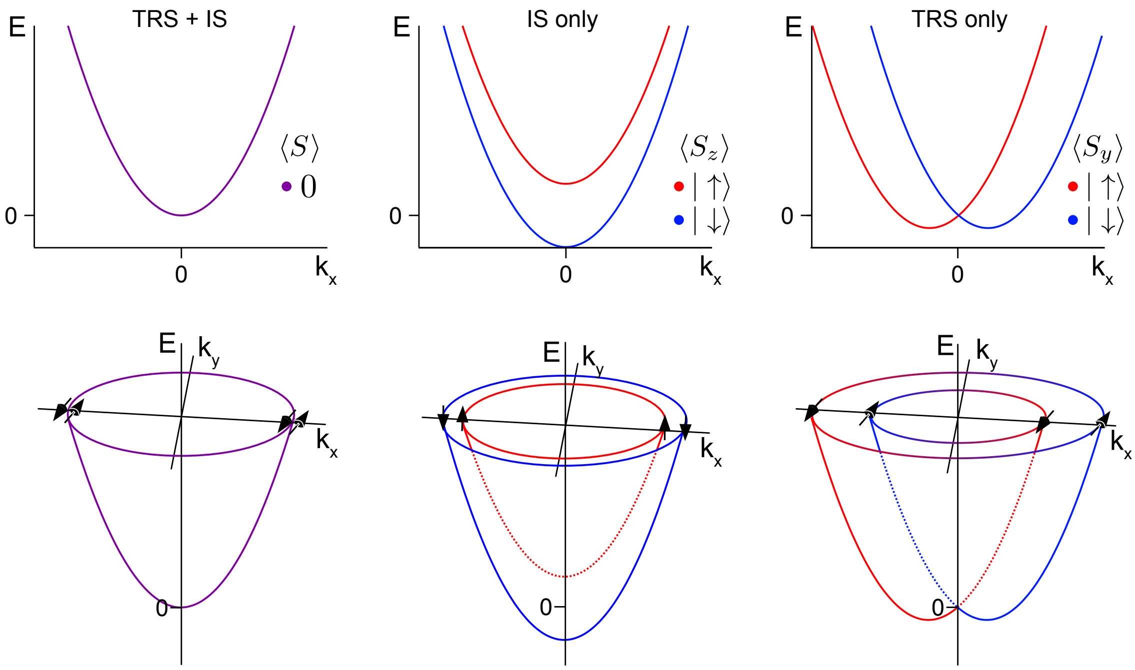

FIGURE 2.5: **Effect of TRS and IS breaking on the band structure of a free-electron gas.** A free electron band dispersion (left), can lose spin degeneracy by the violation of TRS (middle) or IS (right). In the latter case, inversion symmetry is lost along the z-axis (Rashba-type SOC).

In systems with IS, there exists a centre of inversion about which the system is unchanged following the transformation $-\boldsymbol{r} \rightarrow \boldsymbol{r}$ where $\boldsymbol{r}$ is some real space position in the crystal. The effect of IS on the electronic structure, $E(\boldsymbol{k})$, is as follows:

$$\boldsymbol{r} \rightarrow -\boldsymbol{r}: \quad E(\boldsymbol{k},\uparrow) = E(-\boldsymbol{k},\uparrow). \tag{2.22}$$

i.e. IS enforces that the band structure is symmetric about $\boldsymbol{k} = 0$, and therefore that the spin polarisation of a band at $\boldsymbol{k}$ is the same as the band at $-\boldsymbol{k}$. This constraint only permits spin splittings of a Zeeman type, where a spin degeneracy is lifted by offsetting the spin 'up' and spin 'down' electrons in energy (Fig. 2.5), seen in the electronic structures of magnetic materials. In that case, a spin degeneracy lifting is permitted since the magnetic field violates TRS.

TRS can be written as follows:

$$t \rightarrow -t: \quad E(\boldsymbol{k},\uparrow) = E(-\boldsymbol{k},\downarrow). \tag{2.23}$$

A band within a time-reversal symmetric electronic structure is enforced to switch sign of spin polarisation from $+\boldsymbol{k}$ to $-\boldsymbol{k}$, and thus the net spin polarisation at $\boldsymbol{k} = 0$ must be zero.

By combining equations 2.22 and 2.23, it becomes apparent that spin-orbit coupling is unable to create a spin splitting within environments that are simultaneously time-reversal and inversion symmetric. An electric field, and therefore spin-orbit coupling, cannot break TRS.

This thesis will focus entirely on non-magnetic (and hence time-reversal symmetric) materials, and therefore any spin-splittings shown are derived from a breaking of inversion symmetry alone. When $\boldsymbol{E}(\boldsymbol{r})$ is such that inversion symmetry is broken, spin-orbit coupling offsets two spin species in momentum, in accordance with TRS. A schematic of one possible resulting spin texture from SOC-derived spin degeneracy lifting is shown in Fig. 2.5. This *Rashba*-type spin-splitting, named after its discoverer [31], will be explored in some detail below.

Rashba spin-splitting in quasi-2DEGS

Consider a two-dimensional electron gas; a sea of free electrons not subjected to the periodic potential of any underlying lattice, in the x-y plane. The appropriate wavefunction describes a free electron in the x-y plane, but with confined motion in z and with two components allowing for spin. This has the form of Eqn. 2.24:

$$\psi = A\begin{pmatrix} a \\ b \end{pmatrix} \exp\left(i(k_x x + k_y y)\right) \sin\left(k_z z\right). \tag{2.24}$$

Such a wavefunction is applicable when an external or internal electric field, $\boldsymbol{E}(\boldsymbol{r})$, is applied to a free electron gas, orientated $\parallel \hat{\boldsymbol{z}}$, acting to confine electron motion to a two-dimensional plane. The applied electric field breaks inversion symmetry along the z-axis. Eqn. 2.20, with $\boldsymbol{E}(\boldsymbol{r}) = E_0\hat{\boldsymbol{z}}$ and $\boldsymbol{B} = 0$ reduces to

$$\hat{H}_R = \frac{-\hbar^2}{2m}\nabla^2 + \alpha_R(\boldsymbol{\sigma} \times \boldsymbol{p}) \cdot \hat{\boldsymbol{z}} = \frac{-\hbar^2}{2m}\nabla^2 + \alpha_R(p_x\sigma_y - p_y\sigma_x); \quad \alpha_R = \frac{E_0 e\hbar^2}{4m^2c^2}. \tag{2.25}$$

Inserting Eqn. 2.24 into Eqn. 2.25 produces the following dispersion relation:

$$E = \frac{\hbar^2 k_{\parallel}^2}{2m} + \frac{\hbar^2 k_z^2}{2m} \pm \alpha_R k_{\parallel}. \tag{2.26}$$

Here, $k_{\parallel} = \sqrt{k_x^2 + k_y^2}$. The third term on the right hand side is the Rashba term. Although the exact form of the Rashba coefficient, α_R, will vary in a real system, the direct proportionality with the applied electric field strength in this example suggests a route to directly tune of the magnitude of Rashba spin-splitting. This tunability is key to the functionality of many proposed and realised spintronic devices, including the 'Datta-Das'-style spin field effect transistor [32–34], and underpins the interest in compounds hosting spin-orbit coupling mediated spin degeneracy lifting. The second term in Eqn. 2.25 enforces that the momentum is locked perpendicular to the spin, producing entirely in-plane chiral spin textures for the case where $\boldsymbol{E} \parallel \hat{\boldsymbol{z}}$, depicted in Fig. 2.5[4].

---

[4] In general, spin degeneracy is only lifted in the dimensions perpendicular to the direction of the applied electric field. For the case of the 2DEG confined in z, applying an in-plane electric field $\boldsymbol{E}(\boldsymbol{r}) = E_0\hat{\boldsymbol{x}}$, produces a Rashba splitting $\propto \alpha_R k_y$, i.e. a case where there is full spin degeneracy when $k_y = 0$, with Rashba spin-splitting developing only for $k_y \neq 0$. This is predicted in the ferroelectric monolayer SnTe, for example [35].

Eqn. 2.26 also has a term in k_z. However, the electronic structure must match the dimensionality of the system. For a quasi-2D system with dimensions $L_x, L_y \gg L_z$,

$$k_z \propto \frac{n_z}{L_z} \gg k_{x,y} \propto \frac{n_{x,y}}{L_{x,y}}. \tag{2.27}$$

Therefore, the term in k_z does not provide continuous array of $E(k_z)$, like for the in-plane momenta, but it is instead discrete, providing multiple copies of the in-plane electronic structure stacked in energy. In the limit $L_z \to 0$ where the system is entirely two dimensional (such as a sample surface), the energy required to transition from $n_z = i$ to $n_z = i + 1$ is infinite, and so the electronic structure is entirely two-dimensional.

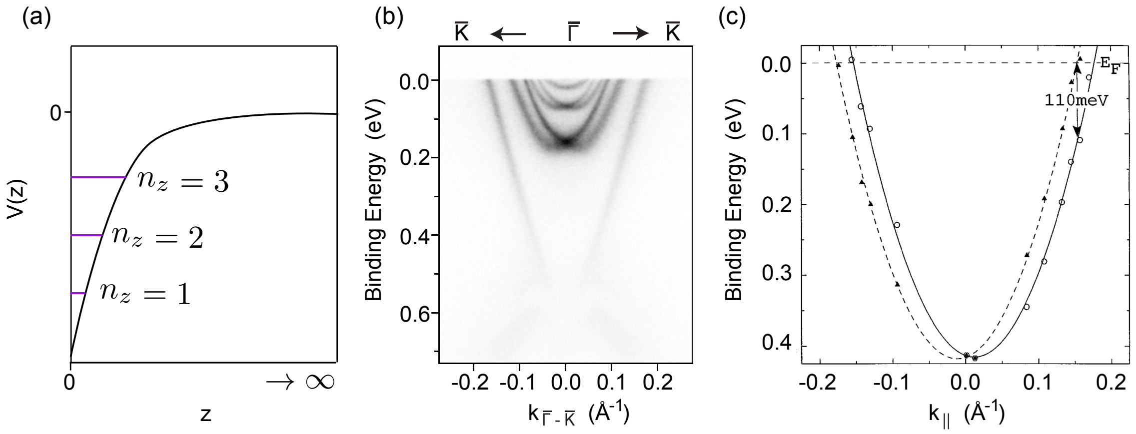

FIGURE 2.6: **Rashba splitting in real systems.** (a) Schematic quantised subbands originating from charge accumulation. (b) Experimental realisation of multiple Rashba split quantum confined 2DEGs, from [36]. (c) Experimental realisation of Rashba splitting in the surface state of Au(111), adapted from [37].

There are experimental conditions in which the near-surface electronic structure is only quasi-two dimensional however. Near-surface band bending effects, caused by charge accumulation in the sub-surface layers of a solid, can act as effective quantum wells capable of quantum confining sub-band copies of the electronic structure. There is some depth, z, to the potential well, and so two or more copies of the electronic structure corresponding to multiple n_z values can be realised. Experimentally, quantised sub-band states are often found in systems with residual surface charge [36, 38–41], at the interface between two materials (e.g. between ABO_3-type perovskite oxides) [42, 43], or on gated charge-neutral systems such as van der Waals bonded layered compounds [44, 45]. In each case, there is near-surface charge accumulation to screen the surface charge. A schematic of sub-bands within a quantum well, and the experimental realisation of multiple Rashba-split sub-band states deriving from the near-surface layers of Bi_2Se_3, is shown in Fig. 2.6(a-b) [36]. The quantum confinement of 2DEGs will be revisited in Chapter 6 for the case of the gated semimetal, $PtSe_2$.

Rashba spin splitting at the surfaces of bulk compounds

The confined two-dimensional electron gases discussed above are Rashba split even when the underlying crystal structure is inversion symmetric. The effective electrostatic potential normal to the surface naturally provides the loss of inversion symmetry required by Rashba-type spin-orbit coupling. The band structures of these confined sub-bands therefore mimic the bulk, but they can do so without the constraints imposed by inversion symmetry. Of course, a similar picture is true for surface-localised states in *all* compounds, not just those with accumulated surface charge. Inversion symmetry is naturally broken at the surface of a compound, and so anything with a surface could exhibit Rashba spin-splitting in its surface electronic structure.

In 1996, a Rashba-type spin splitting of the surface state of inversion symmetric Au(111) was demonstrated by angle-resolved photoemission (ARPES) [37], the result of which is shown in Fig. 2.6(c). Subsequently, similar Rashba type spin-splittings have been observed on the surfaces of other noble metals including silver and copper [46, 47], with the magnitude of spin-splitting correlating with the reducing atomic mass.

Rashba spin splitting of bulk band structures

Rashba-type spin-orbit coupling can also lift bulk spin degeneracies in compounds lacking inversion symmetry within their crystal structure. A clear example of this can be seen in bands belonging to the bulk electronic structure of BiTeI [41, 48–50] which exhibit a large spin-momentum locked, in-plane spin polarisation oweing to an intrinsic electric dipole orientated along the out-of-plane c-axis. Similarly, monolayer transition metal dichalcogenides, such as 1H-WSe_2 and 1H-MoS_2, exhibit an out-of-plane spin splitting due to an effective in-plane dipole within a single layer of their van der Waals-bonded crystal structures [51, 52].

Bulk systems lacking an inversion centre can also exhibit *Dresselhaus*-type spin-splitting [53]. Like Rashba-type SOC, Dresselhaus-type SOC will transform a single free-electron like parabola into a spin-polarised pair offset from one-another in momentum in accordance with TRS. Here though, the spin is not locked perpendicular to the momentum ($\langle \boldsymbol{k} \cdot \boldsymbol{S} \rangle = 0$). Instead, the form of the effective $\boldsymbol{E}(\boldsymbol{r})$ results in a spin texture satisfying $\langle \boldsymbol{k} \cdot \boldsymbol{S} \rangle = \pm 1$ [54]. Dresselhaus-type SOC is most often associated with ‘zinc-blende’ type crystal structures [53].

2.2 Dirac cones and non-trivial band topology

The previous Section demonstrates the tendency of spin-orbit coupling to lift degeneracies, naturally preventing gapless crossing points between spin-degenerate bands in the electronic structure of a compound. This Section focusses on the desirable physics that arise with maintaining gapless crossings within the electronic structure, and describes how to protect them against spin-orbit coupling.

2.2.1 Dirac cones

Two-dimensional Dirac cones without topological protection

The tight-binding result for the electronic structure of the π bands of graphene discussed in Section 2.1.3 produces two-dimensional Dirac cones at the K points. The presence of Dirac fermions in a band structure as simple as this may suggest that Dirac cones are prevalent in nature. In reality, although band crossings are extremely common, spin-orbit coupling removes the vast majority of would-be Dirac points by overlapping wavefunctions, therefore hybridising band crossings to make band gaps. Indeed, whilst the Dirac cones in graphene are responsible for many of its remarkable properties, they are not truly gapless, despite the apparent sub-lattice symmetry inherent to graphene's crystal structure.

The presence of both the σ_x and σ_y Pauli matrices in the graphene Hamiltonian presented in Eqn. 2.13 ($m = 0$) means that any perturbation containing those operators can be compensated for, and the gapless crossing can be retained. However, a perturbation proportional to the third Pauli matrix will break the sub-lattice symmetry protecting graphene's Dirac cones. Spin-orbit coupling is one such perturbation. Indeed, when incorporating $\boldsymbol{L}\cdot\boldsymbol{S}$ type spin-orbit coupling, a term proportional to $\lambda\zeta\sigma_z s^z$ is added to the Hamiltonian in Eqn. 2.13 [52, 55], where λ is the spin-orbit coupling strength and s^z the z-component spin operator. This inclusion essentially replaces m with $m+m_{\mathrm{SOC}}$ in the dispersion relation in Eqn. 2.14, and therefore generates a spin-orbit induced band gap on the order of 10^{-3} meV at the K points of graphene's Brillouin zone [56]. This gap is small, owing to the small atomic spin orbit coupling strength of carbon $2p$-orbitals and so the properties bestowed on graphene by its Dirac cones are therefore unaffected.

Graphene has other limitations, however. The sub-lattice symmetry of graphene is only possessed within a single monolayer (neglecting SOC), with Dirac cones absent in bilayer and few layer graphene [57]. Even in the limit of a monolayer, substrate interactions play a crucial role, including limiting electron mobilities [8, 9]. Devices exploiting properties relying on a true freestanding monolayer are inherently fragile, motivating the search for instances of Dirac materials in higher dimensions.

Critical three-dimensional (bulk) Dirac cones

One route to achieving truly gapless Dirac cones is to increase the dimensionality by one, such that there is already a σ_z term in the Hamiltonian. Consider a three dimensional analogue to the Dirac cones at the K points in graphene described by the Hamiltonian in Eqn. 2.13. Now, as well as having linear dispersions in k_x and k_y, there is also a linear dispersion in k_z. We can rewrite the Hamiltonian in the vicinity of this hypothetical Dirac point as [11]:

$$\hat{H}(\boldsymbol{k}) = v_{ij}k_i\sigma_j; \quad \det[v_{ij}] \neq 0. \tag{2.28}$$

Since all Pauli matrices are present in the ungapped Hamiltonian, this in principle could describe truly gapless Dirac points in three dimensional systems. However, to realise this, there must be some mechanism by which these crossings do not naturally hybridise.

So-called *critical 3D Dirac fermions* exploit the high symmetry behaviour of the time-reversal invariant momenta (TRIM-points). The TRIM points are necessarily spin degenerate in the absence of magnetism, and are subject to more symmetries possessed by the crystal structure than any other point in momentum space. A critical Dirac semimetal phase can be invoked at a TRIM point by finely tuning the mass parameters such that spin-orbit coupling is only sufficient to exactly compensate for any real mass term within the dispersion relation.

Consider a generalised solution to Eqn. 2.28, describing a three-dimensional electronic band dispersion in the vicinity of an appropriate TRIM point, consisting of a conduction and valence band separated by a small[5] band gap, either side of the Fermi level ($E_F = 0$):

$$E(k_x, k_y, k_z) = \pm\sqrt{(m + m_{\mathrm{SOC}})^2 + \hbar^2 v^2 (k_x^2 + k_y^2 + k_z^2)}, \tag{2.29}$$

where k_i are referenced to the TRIM point in question, and $m' = m + m_{\mathrm{SOC}}$ contains the 'real' mass and the mass term contributed by spin-orbit coupling. Upon reducing m', the gap shrinks eventually reaching a gapless Dirac semimetal phase at $m' = 0$. Although this produces a true bulk Dirac crossing, there is no mechanism by which the mass term is enforced to be zero. Achieving this requires fine tuning [58, 59], and any small change in the effective mass, via e.g. strain, would reopen a gap. This critical Dirac semimetal phase is therefore not stable [60].

Lattice symmetry protected bulk Dirac cones

All experimental realisations of stable Dirac semimetals do not rely on the fine-tuning of a mass term to zero. Instead, they rely on offsetting all mass-like terms with a real momentum, and employ an intrinsic lattice symmetry to protect the band crossing along that momentum direction.

Again with reference Eqn. 2.29, consider a bulk Dirac point (BDP) formed between two bands at a position $(k_x, k_y, k_z) = (0, 0, \frac{m'}{\hbar v})$ in a system where hybridisation of those two bands is forbidden along the k_z-axis. This hypothetical crossing produces a three-dimensional Dirac cone, with linearly dispersing bands in all three momentum directions away from the position of the Dirac point, protected against any perturbation, including spin orbit coupling. Any change to the mass terms can change the position in momentum space where the Dirac point occurs, but a gap cannot be opened.

---

[5] Although the single-orbital tight binding model in Section 2.1.2 suggested that extrema at TRIM points ought to be approximately parabolic, in real systems inter-orbital mixing contributes a $\boldsymbol{k} \cdot \boldsymbol{p}$ term to the Hamiltonian. This adds a linear term to the dispersion relation which can become dominant over the parabolic term when the separation of the conduction and valence bands becomes small [36].

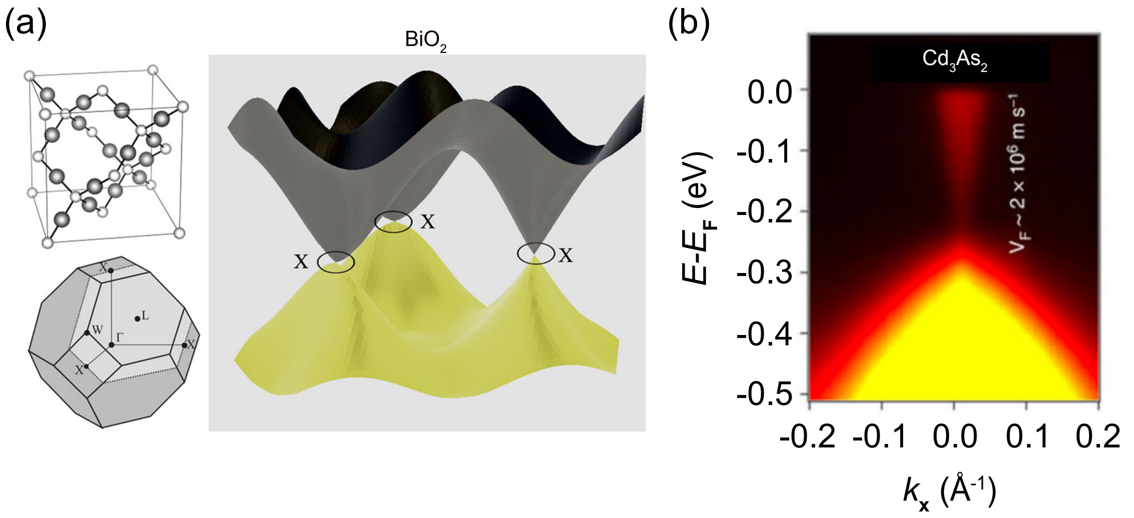

FIGURE 2.7: **Realisation of lattice symmetry protected BDPs.** (a) Predicted BDPs at the X points of rock-salt structured BiO_2, from [11]. The unit cell and Brillioun zone are shown in the inset. (b) Experimental realisation of a lattice symmetry protected BDP in Cd_2As_3, from [61].

Rotational lattice symmetries can provide this protection. The rotational symmetry operators, $\hat{C}_n$ ($n \in \{2,3,4,6\}$), preserve the information contained within a wavefunction, $|\psi\rangle$, upon rotation. They are therefore unitary operators and so their eigenvectors are necessarily orthogonal. Therefore, if wavefunctions $|\psi_1\rangle$ and $|\psi_2\rangle$ describe bands 1 and 2 respectively, and they give different eigenvalues under the operation of $\hat{C}_n$, then they are orthogonal and the hybridisation matrix element between them is equal to zero:

$$\langle\psi_1|\psi_2\rangle = 0; \quad \langle\psi_1|\hat{H}|\psi_2\rangle = 0. \tag{2.30}$$

Any crossing points between bands 1 and 2 along an axis where $\hat{C}_n$ is applicable will therefore remain gapless, not susceptible to a change in the mass term in $\hat{H}$. These crossing points are bulk Dirac points protected by the C_n lattice symmetry.

The careful consideration of all possible realisations of a Dirac semimetal phase for all space groups is beyond the scope of this thesis, but is presented in [60] for systems possessing both time-reversal and inversion symmetries. For $n = 2,4,6$, a single BDP can be realised at any TRIM point other than Γ. For $n = 3,4,6$, pairs of BDPs can be produced, symmetric about Γ along any axis adhering to $\hat{C}_n$ rotational symmetry. Despite this relatively broad series of alternate prerequisites for realising robust BDPs, experimental realisations are still relatively sparse. The first predicted example was in BiO_2 [11] which has BDPs protected by $\hat{C}_4$-symmetry at the X points of its rock-salt type Brillouin zone. Since then, Cd_2As_3 and Na_3Bi have been experimentally shown to host symmetric BDPs along their respective k_z axes, protected by $\hat{C}_4$ and $\hat{C}_3$ symmetries respectively [61–64].

2.2.2 Topological surface states

2D Dirac cones with topological protection

The final case of protected Dirac crossings that will be discussed here are those of *topological surface states*. Although two-dimensional, these are fundamentally different to the two-dimensional Dirac cones in graphene. They are a product of the bulk material, and as such can only exist on the surface of a three-dimensional system[6]. Unlike in graphene, the two branches of the Dirac cone are not spin degenerate, but instead possess chiral spin textures, with the direction of the spin locked in-plane and perpendicular to momentum (Fig. 2.8(b)). In the absence of magnetism, the Dirac point of a topological surface state is a Kramers degeneracy, completely protected against hybridisation by time-reversal symmetry.

This framework shares similarities to that for Rashba-split surface states. Rashba surface states too possess a Kramers degeneracy, and have a chiral spin texture (Fig. 2.8(a)). However, unlike Rashba spin-split bands, which are isolated within a band gap, topological surface states form connections between otherwise disconnected bulk bands across a band gap. Whilst a Rashba surface state may be destroyed by the passivation of a dangling bond, for example, topological surface states are product of the bulk crystal, and as such have some level of resilience against damage to a material surface. This is a consequence of their *topological protection*.

Topological protection

In geometry, the field of topology can be reduced to essentially counting the number of holes within an object. The classic example compares a sphere (an object with no holes), to a donut or a mug (which both have one hole). A mug and a sphere are topologically distinct, because one object cannot be smoothly moulded into the other without removing or cutting holes, whereas a mug and a donut are topologically equivalent. The topological nature of an object is characterised by the *topological invariant*, an integer quantity counting these holes. Objects are topologically distinct if the evaluation of their topological invariant yields different results.

In the context of electronic structure, the *Chern number* is a topological invariant of a two-dimensional electron system [12, 65]. The Chern number and the discussion of topology as a whole draws close parallels to that of classical magnetism. An electron populating a band described by a Bloch wavefunction experiences spatial variations within a unit cell and hence experiences an effective vector potential in k-space, $\boldsymbol{A}_k = \langle\psi_k| - i\boldsymbol{\nabla}_k|\psi_k\rangle$ [66]. The *Berry curvature*, given by $\boldsymbol{\nabla}_k \times \boldsymbol{A}_k$, can therefore be interpreted as a magnetic field in k space [66]. The Chern number, n_m, is then given as follows

$$n_m = \frac{1}{2\pi}\int_{BZ} (\boldsymbol{\nabla}_k \times \langle\psi_k| - i\boldsymbol{\nabla}_k|\psi_k\rangle)_m \, \mathrm{d}^2k, \tag{2.31}$$

---

[6] In analogy to the following discussions, one-dimensional topological *edge states* can exist at the edges of a two-dimensional material.

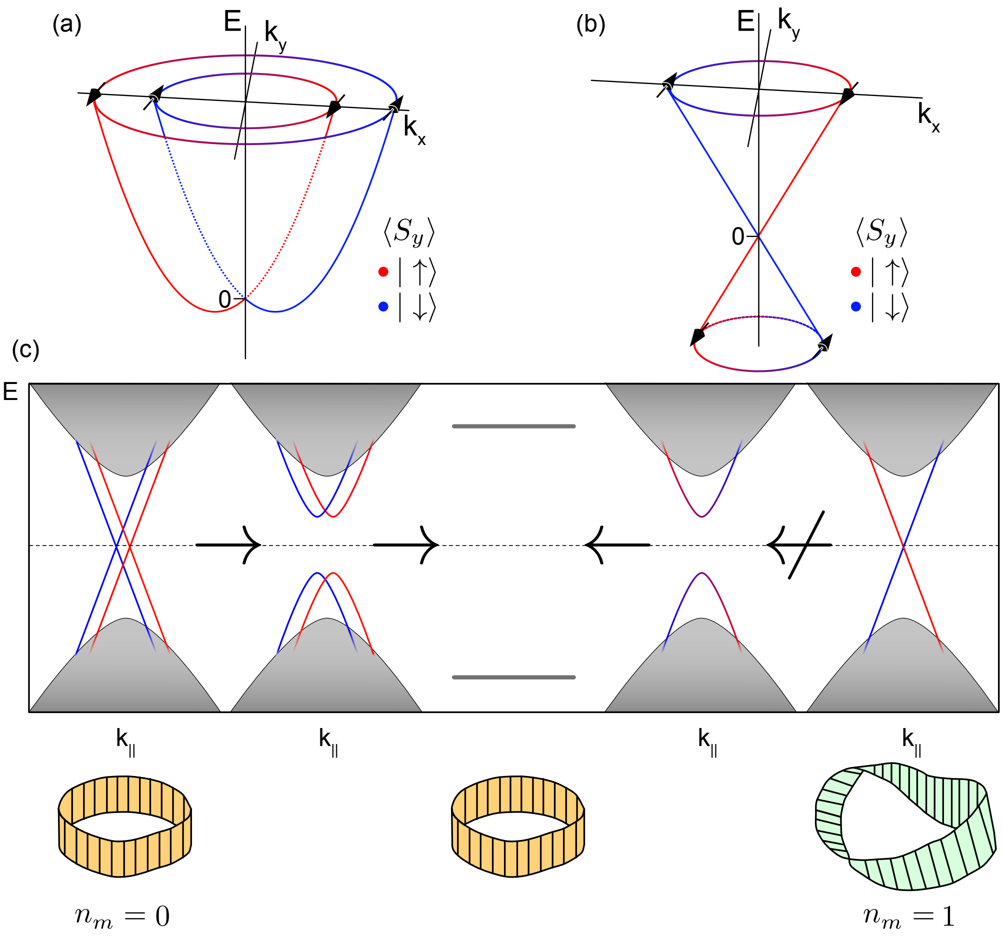

FIGURE 2.8: **Topological inequivalence of systems hosting Rashba and topological surface states.** (a-b) Spin-momentum locked in-plane spin texture of a Rashba (a) and topological (b) surface state. (c) Schematic demonstration that band structures containing Rashba and topological surface states are topologically distinct. From right to left, a band structure with a single Dirac cone bridging between bulk bands cannot be continuously deformed into the atomic limit, and as such is topologically district from it. This is not the case for a two such Dirac cones (left to right). An analogous statement can be made for a loop of paper with no twists and a a Möbius strip.

where the integrand is the Berry curvature and ψ_k is the wavefunction for band m, where the integration is taken over the Brillouin zone. The Chern number therefore characterises the curvature of an object in k-space. This same index characterises the quantum Hall effect, where discrete, k-independent 'Landau' energy levels of a 2DEG are created when a magnetic field is applied normal to its axis, with an energy spectrum given by $E_n = \hbar\omega_c(n + \frac{1}{2})$ [12][7]. In three dimensions, there are four such topological invariants, belonging to the group $\mathbb{Z}_2$ and therefore each taking a value of 0 or 1.

Although this description is complex, whether or not a system is topologically 'non-trivial' is defined by whether or not it is topologically distinct from the 'trivial' case of the atomic limit. Therefore the topological invariants can be inferred by evaluating if it is possible to

---

[7] Indeed, in analogy to edge and surface states on two and three dimensional topological insulators respectively, a quantum Hall state for $n \neq 0$ is associated with chiral 'skipping' modes localised to the edge of the system.

continuously deform an electronic structure back to the k-independent atomic limit. Below, it will be argued that a surface Dirac cone is a hallmark of a topologically non-trivial band structure, before discussing exactly how the surface Dirac cones themselves are formed.

Fig. 2.8(c) shows schematic $E(k_{||})$ dispersions for surface Dirac cones existing within a three-dimensional band structure. Two (or any even number of) spin-polarised surface Dirac cones spanning across a band gap can always be transformed through hybridisation into electron- and hole-like Rashba-split surface states separated by a band gap, and so the band structure can be continuously deformed back into the atomic limit without 'cutting' holes within the band structure. For a single (or any odd number of) spin-polarised surface Dirac cones, an analogous argument cannot be made. A spin-polarised Dirac cone can be interpreted as a pair of oppositely spin-polarised electrons each forming counter-rotating spin-polarised currents around the perimeter of a system. A 'hybridised Dirac cone' in a time-reversal symmetric environment therefore describes a pair of half-electrons forming counter rotating spin currents. This is unphysical, and so the Dirac point of a topological surface state is protected by time-reversal symmetry, preventing a smooth deformation to the atomic limit.

More generally, it is therefore possible to determine whether or not a system is topologically non-trivial by counting the number of bands one intersects if a straight line is drawn from the surface Brillouin zone centre to a neighbouring TRIM point, at the edge of the surface Brillouin zone. If the number is odd, then the compound is *topologically non trivial*, and if even, *topologically trivial*. In order to generate topological surface states, one must change to the topology of the bulk system via a *topological phase transition*.

Generating topological surface states

A topological phase transition requires inverting the band ordering relative to the atomic limit. This can be seen explicitly by again tuning the mass term in the prototypical Dirac dispersion relation, displayed again below.

$$E(k_x, k_y, k_z) = \pm\sqrt{(m + m_{\mathrm{SOC}})^2 + v^2(p_x^2 + p_y^2 + p_z^2)} \tag{2.32}$$

$m' = m + m_{\mathrm{SOC}}$ again contains all mass-like terms. As in the previous discussions, reducing this mass term from a finite positive value, by for example, offsetting a real mass with spin-orbit coupling, can create a critical 3D Dirac semimetal phase. The mass term can continue to shrink, however. Fig 2.9 illustrates the transition from a two-band system with a band gap ($m' > 0$) through to a regime of negative mass $m' < 0$, via a critical bulk Dirac semimetal phase ($m' = 0$).

For the negative mass regime, the band gap is *inverted* (IBG). A finite band gap exists, but the conduction and valence bands now possess regions of the other band's character. If the two bands have the same parity eigenstate (top row in Fig 2.9), then the inverted band gap is topologically trivial. If the two bands have opposite parity (bottom row), then the sign

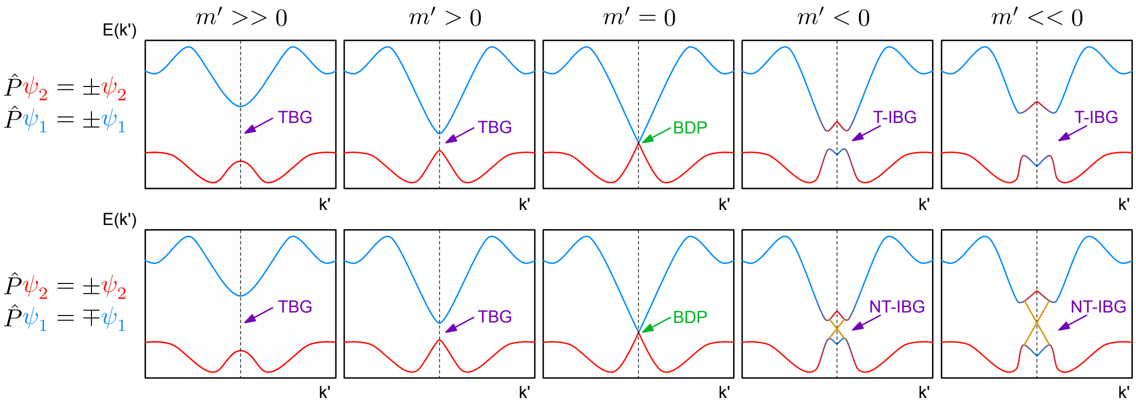

FIGURE 2.9: **Topological phase transition via a critical DSM phase.** Top: Topological phase transition for the case where $|\psi_1\rangle$ and $|\psi_2\rangle$ have the same parity eigenvalue. Bottom: Equivalent transition for the case where $|\psi_1\rangle$ have opposite parity eigenvalues. In both cases a critical Dirac semimetal is formed at $m' = 0$.

switching of m' is a topological phase transition: The host system is now topologically non-trivial.

The presence of a topological non-trivial inverted band gap (NT-IBG) within a material is sufficient to generate a topological surface state when interfaced with another medium which is topologically distinct. Without the gap-closing interface state, continuity across the boundary is not possible. Equivalently, one cannot smoothly deform a mug into a sphere without closing the hole in the mug. The 'hole closing' is provided by the topological surface state which exists at the interface between the two materials.

The significance of the band parity when forming a topologically non-trivial inverted band gap is as follows: If both bands are described by even or both by odd wavefunctions (i.e. they have the same parity), then it is still possible to write down non-zero continuous wavefunctions obeying boundary conditions at the interface between the band inverted system and a trivial medium. If the two bands have a parity switch, then this is not possible and a topological surface state is required.

Indeed, in systems hosting both time-reversal and inversion symmetry, the four $\mathbb{Z}_2$ topological invariants, $\nu_0; (\nu_1, \nu_2, \nu_3)$, can be directly calculated if the parity eigenvalues of each band in the bulk electronic structure are known [67]. At each TRIM point, Γ_i, a quantity, δ_i, is defined from which the invariants can be calculated.

$$\delta_i = \prod_{m=1}^{N} P_{2m}(\Gamma_i) \tag{2.33}$$

$P_{2m}(\Gamma_i)$ is the parity eigenstate of the $2m^{\text{th}}$ occupied band at Γ_i. The product is over the N occupied bands which are not related by the combination of time reversal and inversion symmetry (half of the total bands). The four invariants are then calculated from the product of δ_i over a subset of the eight Γ_i in the bulk Brillouin zone.

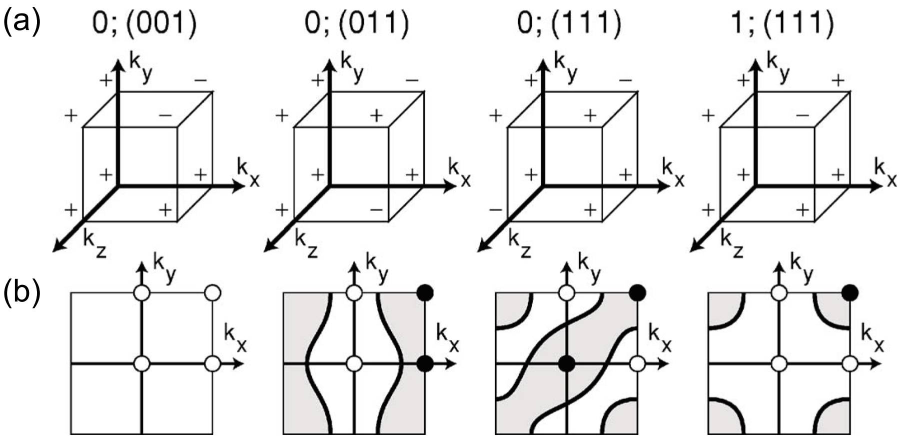

FIGURE 2.10: **Weak vs strong topological insulators.** Adapted from [67]. (a) δ_i at the eight Γ_i of the bulk Brillouin zone (only the first octant of a cubic Brillouin zone is shown) for various combinations of topological indices, $\nu_0; (\nu_1, \nu_2, \nu_3)$. (b) The surface Brillouin zone is shown. Filled and open circles indicate even and odd δ_i for the surface TRIM points, calculated by the product of δ_i along k_z. Possible Fermi surfaces of topological surface states are shown. Only in the 'strong' case is there an odd number of surface bands between all pairs of neighbouring surface TRIM points.

An odd number of surface bands are only intersected when drawing a line between two neighbouring TRIM points with different δ_i on the *surface* Brillouin zone, determined by the product of δ_i for the two Γ_i which k_z-project onto the same point in the surface zone.

Of the four topological indices, three ($\nu_{1,2,3}$) are calculated from the product of δ_i over four neighbouring Γ_i which define a 2D plane within the 3D Brillouin zone. A non-trivial result for any or all three of these indices characterises only a *weak topological insulator*, as the number of Dirac crossings between any two surface TRIM points is dependent both on the experimental 'cleavage' plane on which the surface structure is defined, as well as the pair of surface TRIM points being considered. Any resultant surface Dirac cones are *not* considered to be topologically protected. This is illustrated in Fig. 2.10 for a cubic Brillouin zone.

The fourth topological invariant, ν_0, however characterises a *strong* topological phase. ν_0 is calculated considering all TRIM points of the three-dimensional Brillouin zone.

$$(-1)^{\nu_0} = \prod_i \delta_i \tag{2.34}$$

Here, the product runs over all eight Γ_i. For $\nu_0 = 1$, topological surface states are enforced to exist at all surfaces, and an odd number of crossing points is intersected between any two neighbouring surface TRIM points.

It should be noted that the result of the procedures outlined above are only strictly applicable to 'true' topological insulators, wherein the Fermi level lies within the parity inverted band gap. Topological surface states are enforced to exist in any band gap with a parity inversion across it, regardless of the energetic position within the electronic structure. The topological nature of a band gap below E_F can be evaluated by considering only electronic bands below the band gap in the calculation of δ_i.

Topologically protected two-dimensional Dirac cones exist at the interface between two topologically distinct systems. The vacuum can be considered as infinitely separated atoms, and therefore it is topologically equivalent to the atomic limit. Therefore, as implied above, topological surface states must additionally exist at the surface of any single compound containing a parity inverted band gap, with the topological surface state falling energetically within.

Properties and uses of topological surface states

Perhaps the most well-known instance of a topological insulator is Bi_2Se_3, hosting a 'prototypical' topological surface state at the $\overline{\Gamma}$ point of its surface Brillouin zone. Here, the topological phase transition is mediated by the spin-orbit coupling strength. The formation of this state is schematised in Fig. 2.11(a). Under the influence of the crystal field, both the Bi and Se-derived p-orbital manifolds undergo a degeneracy lifting. For the Bi (Se) p-orbital manifold, the p_z derived band is lifted to a lower (higher) energy than the still-degenerate $p_{x,y}$ pair. Spin-orbit coupling further modifies this picture by lifting the remaining degeneracy (neglecting spin) of the $p_{x,y}$ pair, whilst modifying the energetic positions of the p_z-derived bands. Now, the Se and Bi p_z derived bands are inverted. Since the Bi and Se p-orbital manifolds have opposite parities, this inverted band gap is topologically non-trivial, and so a topological surface state is enforced to exist at the surface of Bi_2Se_3, energetically located within this inverted band gap.

This topological surface state shows clear signatures in angle-resolved photoemission (ARPES) experiments sensitive to the surface electronic structure (Fig. 2.11(b), [68]). When the spin-orbit coupling strength is reduced, the p_z-derived bands can unwind. This is clearly seen in sister compound Sb_2Se_3, wherein spin-orbit coupling is insufficient to drive a band inversion, rendering bulk band structure topologically trivial and therefore without topological surface states (Fig. 2.11(c-d)).

Topologically protected Dirac cones on the surfaces of three dimensional materials can be expected to exhibit many of the same properties as graphene. Indeed, Bi_2Se_3 has extremely high surface electron mobilities and an associated anomalous quantum Hall effect [70], not unlike graphene. In practise, this means that a highly conductive shell is formed around an otherwise insulating bulk band insulator, and their topological protection permits high surface mobilities even when exposed to atmospheric conditions, or in non ideal bulk crystals [71–74].

The purview of topological surface states is potentially much larger than that of graphene, however. Firstly, their Dirac crossings cannot be gapped, as the branches of topological surface states need be fully spin polarised, and their Dirac crossing is protected by time-reversal symmetry. This opens up potential for the exploitation of topological surface states in spintronics applications which require non degenerate band structures [75]. Their conic chiral spin texture is resistant to back scattering, as this always requires a spin flip [76] (unlike Rashba states where scattering vectors linking the inner and outer branches are allowed) opening the

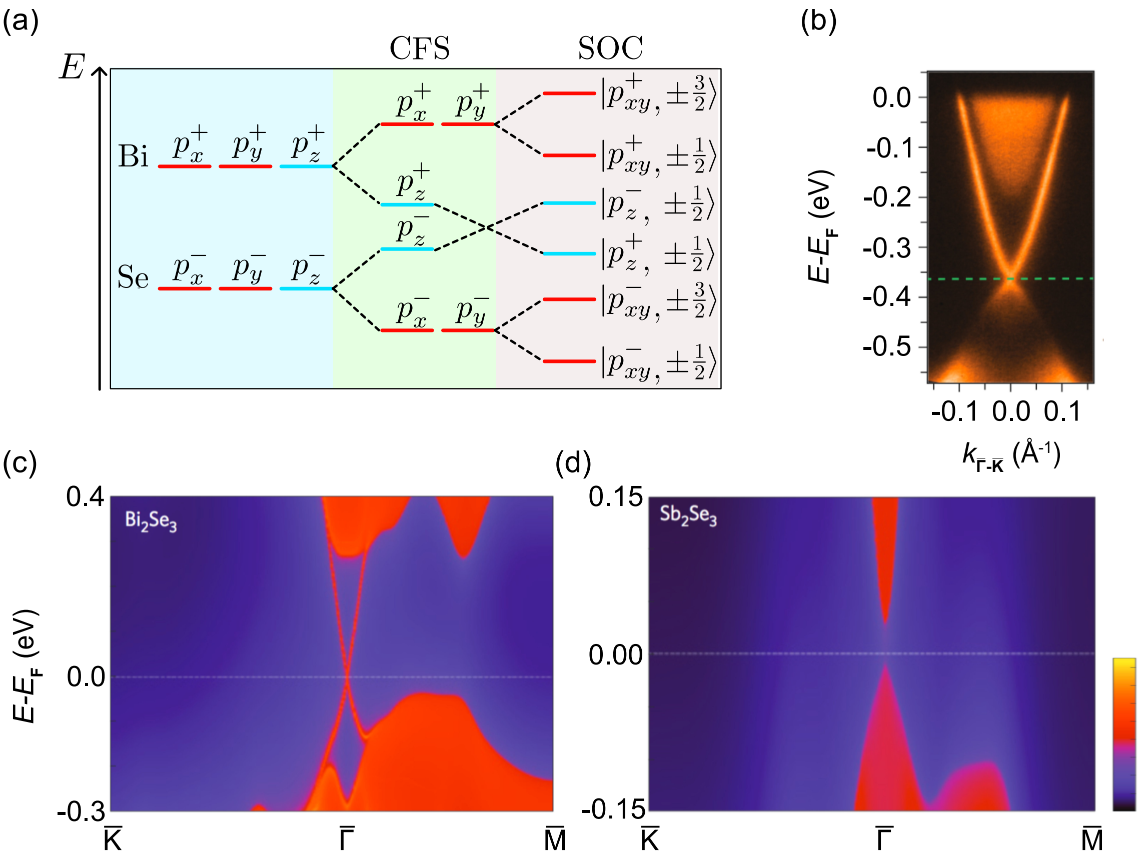

FIGURE 2.11: **Topological surface states (TSS) in the Bi_2Se_3 family.** (a) Modification of the Bi and Se derived p-orbital manifolds under the influence of the crystal field and spin orbit splitting. A band inversion is realised between the p_z derived bands. (b) Experimental realisation of a TSS in Bi_2Se_3 by angle-resolved photoemission (ARPES), from [68] (c-d) adapted from [69], shows density functional theory based slab calculation predicting a topological surface state in Bi_2Se_3 (b), but not sister compound Sb_2Se_3 (c).

potential for their use in quantum computing and in devices requiring coherent spin transport [34, 77]. Moreover, topological phase transitions can be traversed via chemical doping and strain, for example. For instance, the 'giant Rashba' semiconductor BiTeI becomes topologically non trivial if pressure is applied, via a critical Dirac semimetal phase [48, 49], opening routes for a binary switch for surface electron mobility in real devices.

2.2.3 Hexagonal warping

The framework in which both Rashba and topological surface states are introduced above permits only that these states form circular Fermi surfaces. In many cases this is not true. Even the prototypical topological surface state in Bi_2Se_3 has significant hexagonal warping, reflecting the global crystalline symmetries of the underlying bulk system [36, 78]. To see this, further higher order corrections to the Hamiltonians [36, 78–80] are required. Inserting a Bloch wavefunction $\propto \exp(i\boldsymbol{k}\cdot\boldsymbol{r})u_k$, where u_k is a two component spinor, into the Foldy-Wouthuysen Hamiltonian (Eqn. 2.20, $\boldsymbol{B}=0$) returns the following eigenvalue equation [81]:

$$\left[\frac{\boldsymbol{p}^2}{2m}+V(\boldsymbol{r})+\frac{\hbar}{4m^2c^2}\boldsymbol{\sigma}\cdot(\boldsymbol{\nabla}V\times\boldsymbol{p})+\frac{\hbar}{m}\boldsymbol{k}\cdot\boldsymbol{p}+\frac{\hbar^2}{4m^2c^2}\boldsymbol{\sigma}\cdot(\boldsymbol{\nabla}V\times\boldsymbol{k})\right]u_k=E(\boldsymbol{k})u_k. \quad (2.35)$$

The first two terms on the left hand side are the kinetic and potential energy terms respectively. The third and fifth terms are the atomic orbital and crystal momentum derived spin-orbit coupling terms respectively [82]. At $\boldsymbol{k}=0$, the fourth term, $\propto \boldsymbol{k}\cdot\boldsymbol{p}$, vanishes. As $\boldsymbol{k}$ becomes larger, this $\boldsymbol{k}\cdot\boldsymbol{p}$ term can be treated as a perturbation. Work by Fu [36, 78] shows how the Hamiltonian to third order for a system with C_3 rotational symmetry can be rewritten as follows:

$$H=E_0(\boldsymbol{k})+v'(k_x\sigma_y-k_y\sigma_x)+\frac{\lambda}{2}(k_+^3+k_-^3)\sigma_z;\quad k_\pm=k_x\pm ik_y. \quad (2.36)$$

$E_0(\boldsymbol{k})$ describes band dispersion in the absence of spin degeneracy lifting, modified away from a free electron description by higher order $\boldsymbol{k}\cdot\boldsymbol{p}$ terms [36]. The second term on the right hand side is the Rashba term allowing for spin-polarised Dirac and Rashba surface states with an in-plane spin-momentum locking, as discussed in the previous sections. However, its prefactor, $v'\propto v(1+k^2)$, includes a higher order term [78]. The third, cubic term in Eqn. 2.36 is the higher order $\boldsymbol{k}\cdot\boldsymbol{p}$ correction to the Rashba Hamiltonian. Unlike the previous terms, this term is only three-fold rotational symmetric and therefore is solely responsible for the warping of otherwise circular Fermi surfaces away from circular geometry. λ characterises the strength of warping. This has the following eigenstates [78]:

$$E_\pm(\boldsymbol{k})=E_0(\boldsymbol{k})\pm\sqrt{v^2\boldsymbol{k}^2+\lambda^2\boldsymbol{k}^6\cos^2 3\alpha}, \quad (2.37)$$

where α is the azimuthal angle defined as being zero for a line intersecting $\overline{\Gamma}$ and $\overline{\mathrm{K}}$, where $\overline{\Gamma}$ is the centre of rotation. This Hamiltonian acts to leave the $\overline{\Gamma}$-$\overline{\mathrm{M}}$ directions unaltered, whilst causing a curving effect in-between, evolving a circular constant energy contour into one with a 'snowflake'-like appearance' as λ increases in size. λ very often found to be non-zero in Rashba surface state and TSS containing systems [36, 48, 78, 80, 83], with some examples shown in Fig. 2.12 [80].

Eqn. 2.36 also suggests that the higher order $\boldsymbol{k}\cdot\boldsymbol{p}$ corrections permit small deviations from a fully in-plane and momentum-locked spin texture. Consider an amended Rashba Hamiltonian of $H_R=\alpha\boldsymbol{k}+\beta\boldsymbol{k}^2+\gamma\boldsymbol{k}^3+\delta\boldsymbol{k}^4+\epsilon\boldsymbol{k}^5\ldots$ in a C_3-symmetric system. TRS enforces $\beta=\delta=0$, but a combination of C_3 and time-reversal symmetries allow a non-zero out of plane spin component along the $\overline{\Gamma}$-$\overline{\mathrm{K}}$ directions on the now-hexagonal Fermi surfaces. However, the out-of-plane spin component, $\langle S_z\rangle$, is odd with respect to the Γ-M mirror line and therefore must remain zero exactly along the $\overline{\Gamma}$-$\overline{\mathrm{M}}$ direction. The out-of-plane 'spin canting' described here opens further

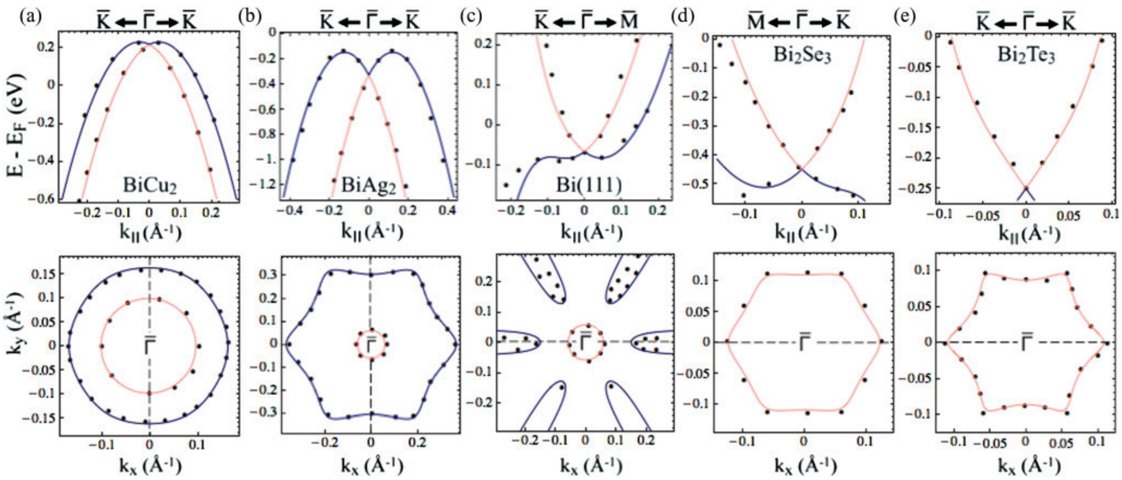

FIGURE 2.12: **Hexagonally warped surface states.** Adapted from [80].

scattering channels of topological and Rashba systems, potentially complicating the search for ideal materials for use in devices with functional properties relying on low-scatter spin-transport.

2.2.4 Fermi arcs between Dirac and Weyl points

Topological surface states of the form introduced above are not the only types of surface states in Dirac systems. Lattice symmetry protected Dirac cones are often associated with their own surface states. For the cases where bulk Dirac points are formed partway along the rotationally symmetric axis, as discussed in Section 2.2.1 and [60], the band crossing is often between two bands with different parity eigenvalues. In those cases, the system undergoes a topological phase transition as a function of a momentum, e.g. k_z. Therefore, exactly one of the time-reversal symmetric planes defined by $k_z = 0$ and $k_z = \frac{\pi}{c}$ have within them a parity inverted band gap and possess a non-trivial Chern number. Two *Fermi arc* surface states then form a closed loop between Dirac points, observable on a surface plane parallel to the rotationally symmetric axis [60]. This is schematised in Fig. 2.13(b). The presence of these surface states has been experimentally verified in all Dirac semimetal systems mentioned above [61–63]. However, since the protection of bulk Dirac points is governed by bulk lattice symmetries which are not shared by all possible choices of the surface Brillouin zone, surface localised Fermi arcs between bulk Dirac points, like topological surface states in weak topological insulators, are not considered to be topologically protected [84].

A bulk Dirac point is a four-fold degenerate point at the crossing of two spin-degenerate pairs of bands. It can therefore be transformed via the breaking time-reversal or inversion symmetry into two momentum separated, spin-polarised *Weyl cones.* The Weyl points at the crossing points of the Weyl cones no longer require a protective lattice symmetry, owing to their spin polarisation.

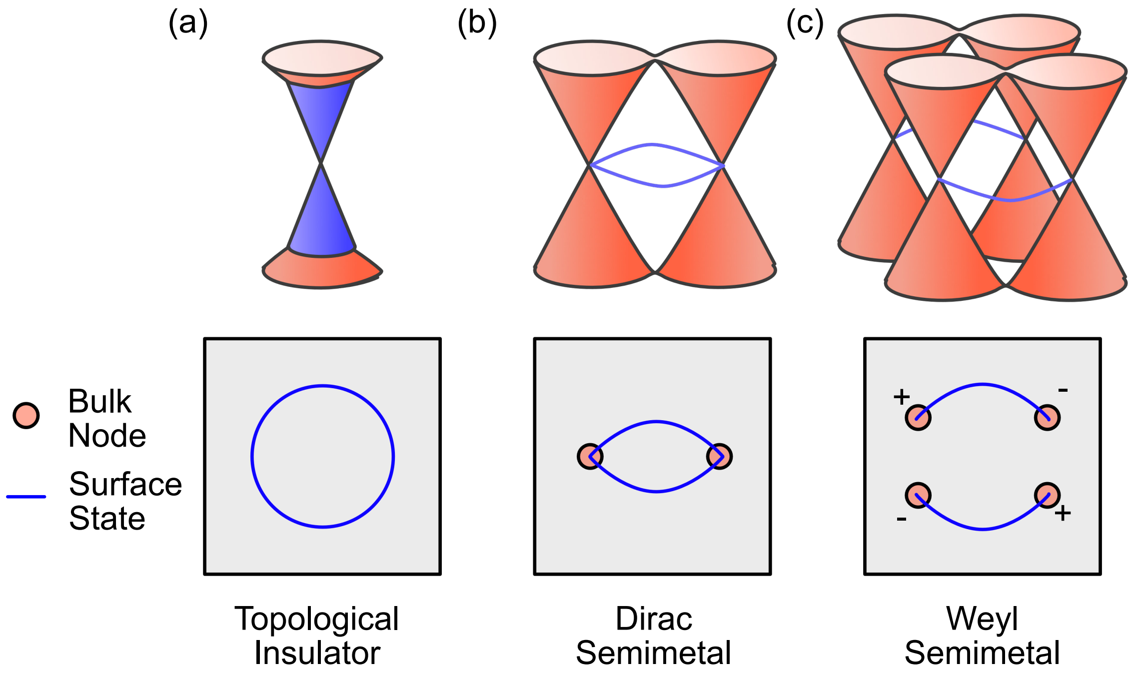

FIGURE 2.13: **Surface states in topological insulators (TI), Dirac semimetals (DSM), and Weyl semimetals (WSM).** Schematic representations of bulk (orange) and surface (blue) states of, from left to right, TI, DSM and WSM. The top panels shows the band dispersion $E(k_x, k_y)$, the bottom panels show schematised $k_x - k_y$ contours.

Weyl cones are of fundamental interest because the Weyl points themselves behave as magnetic monopoles in momentum space [85], similar to the emergent quasiparticles in frustrated 'spin ice' systems [86, 87]. A contour integral of the Berry curvature enclosing one single Weyl point produces a non-zero *chiral charge* equal to $\chi = \pm 1$. This is shown in the following equation:

$$\frac{1}{2\pi} \oint_{FS} F(\boldsymbol{k}) \cdot \mathrm{d}S(\boldsymbol{k}) = \chi, \tag{2.38}$$

where $F(\boldsymbol{k})$ is the Berry curvature [66]. The above equation is analogous to Gauss' law in classical electromagnetism, requiring the total chiral charge, χ of a system to be zero. Weyl nodes are therefore enforced to strictly live in pairs with the two halves of a pair of Weyl points having opposite chiral charges, with one Weyl point acting as a source of Berry curvature, and the other as a drain. In the case of Weyl nodes, their chiral charge and their Chern number are proportional [66]. A pair of Weyl points are therefore topologically distinct from each other. A Weyl semimetal is therefore always associated with topologically protected Fermi arcs originating and terminating between the Weyl points ([85] and Fig. 2.13(c)). TaAs and TaP were amongst the first Weyl semimetals experimentally verified, with Fermi arcs resolved clearly with electronic probes sensitive to the surface electronic structure [88–90][8].

---

[8] The persistence of Fermi arcs even in the presence of TRS and IS becomes intuitive when considering a lattice symmetry protected Dirac point as a superposition of two Weyl fermions. Therefore a pair of Fermi arcs can be expected to bridge between any pair of momentum separated Dirac cones in the surface Brillouin zone.

2.2.5 Topological superconductivity

A third emergent quasiparticle, the Majorana fermion, can be realised in so-called *topological superconductors* [91]. For certain choices of $\tilde{\boldsymbol{\alpha}}$ and $\tilde{\beta}$, the Dirac equation in Eqn. 2.19 is real, giving two coupled solutions describing spin $\frac{1}{2}$ neutral particles [92]. These permitted real solutions to the Dirac equation (Eqn. 2.19) do not distinguish between particle and antiparticle. These are Majorana fermions.

Superconductivity is the pairing of electrons to form *Cooper pairs*, creating a gap in the density of states, centred at the Fermi level. The symmetry of the superconducting gap is determined by the orbital component, χ of the Cooper pair wavefunction $|\Psi_{\mathrm{CP}}\rangle \propto \chi|\sigma_1, \sigma_2\rangle$, which needs to be overall antisymmetric under the exchange of electrons forming the pair. In 'conventional' superconductors, the pairing mechanism combines electrons with opposite spins to create an antisymmetric spin component of the wavefunction (e.g. $|\uparrow\downarrow\rangle - |\downarrow\uparrow\rangle$). The orbital component is then necessarily even. For $l = 0$, so-called s-wave superconductors have a symmetric, k-independent superconducting gap [93].

In p-wave, or equivalently topological, superconductors, the spin component of the wavefunction must be symmetric ($|\downarrow\downarrow\rangle$, $|\uparrow\downarrow\rangle + |\downarrow\uparrow\rangle$ or $|\uparrow\uparrow\rangle$) [93]. In this case the bulk system is topologically non-trivial [94] and the Majorana fermions which result benefit from a topological protection against decoherence, with potential applications in quantum computing [92].

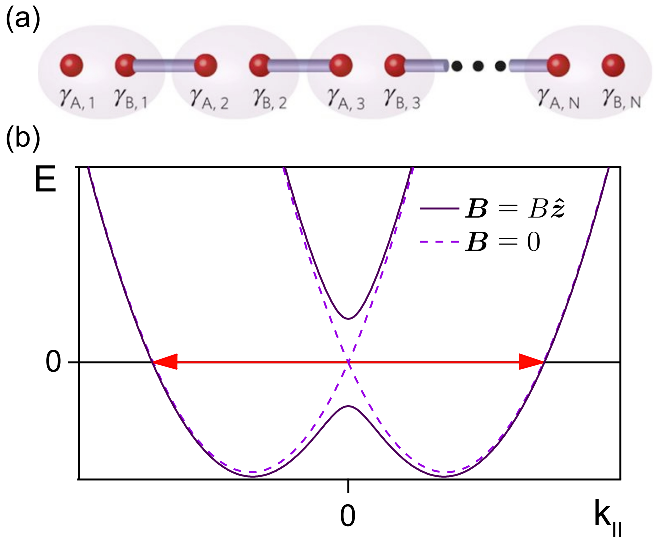

FIGURE 2.14: **Majorana fermions from spin-polarised surface states.** (a) Superconducting pairing of a 1D chain of spinless fermions, adapted from [95] (b) Evolution of a Rashba surface when a magnetic field, $\boldsymbol{B}$, is applied normal to the sample surface.

The possibility of realising Majorana fermions is easily seen, in one-dimension at least, by considering a chain of spin-polarised fermions with p-wave superconducting pairing [92, 96] depicted in Fig. 2.14. Simply, the idea is that by describing each fermion as two superimposed Majorana fermions, the superconducting pairing mechanism always leaves behind unpaired

Majorana fermions at each end of the chain, which remain as zero-energy modes within the superconducting gap [92, 95, 96].

This scenario is applicable to superconducting systems with spin-polarised surface states at the Fermi level [91, 94, 97–100]. Spin-orbit coupling, necessary for the formation of spin-polarised surface states without magnetism, promotes the mixing of orbital and spin degrees of freedom therefore providing the possibility for odd-parity pairing mechanisms. For example, applying a magnetic field normal to an s-wave superconductor with Rashba surface states at its Fermi level well approximates the toy-model. The magnetic field lifts the Kramers degeneracy such that the Fermi level only intersects a single Rashba branch at $\pm k$ (Fig. 2.14(b)). An overall odd-parity pairing is possible between electrons populating the Rashba split band to create topological superconductivity [92, 94]. Similarly, inducing superconducting pairing between branches of a topological surface state produces the same result, without the need for magnetism. In each case, Majorana fermions are bound within vortex cores [94].

Experimental probes of the surface density of states, such as scanning tunnelling spectroscopy (STS), can in principle observe Majorana zero modes, although this has proven to be controversial endeavour. In 'one-dimensional' systems, zero bias peaks were observed in strongly spin-orbit coupled InSb wires when interfaced with a s-wave superconductor and when a magnetic field is applied [101], although the effects of disorder have been shown to give indistinguishable results [102]. In higher-dimensions, there have been attempts to induce pairing between the branches of a topological surface state by interfacing a topological insulator with a conventional superconductor with some success [103–107] . Similarly, doping Cu into the topological insulator Bi_2Se_3 drives the formation of a superconducting phase, but the studies into the realisation of Majorana fermions are inconclusive, with groups obtaining incompatible results [108–110].

This search is hindered by the small number of compounds which are both intrinsic superconductors in their pristine form, and possess topological surface states crossing the Fermi level. In Chapter 5, the transition-metal dichalcogenide $PdTe_2$ will be shown to be one such example, with the possibility of Majorana fermions in that system explored.

More generally, research into the details of the surface electronic structures of compounds requires a surface sensitive probe. In the following chapter, angle-resolved photoemission spectroscopy (ARPES) will be overviewed, a direct probe of electronic structure.

Chapter 3

Methods

3.1 Angle-resolved photoemission spectroscopy

This Chapter provides an overview of the main experimental technique employed for the results presented in this thesis, angle-resolved photoemission spectroscopy (ARPES). In each of Chapters 4, 5 and 6, density functional theory (DFT) calculations are provided by collaborator M. S. Bahramy (RIKEN & University of Tokyo) for complementary insight to that provided by the experimental data. As such, a brief discussion of the underlying principles behind DFT will also be given in this Chapter.

3.1.1 Principles of photoemission

Although the tight-binding model introduced in Chapter 2 was able to give an accurate overview of graphene, even when neglecting relativistic effects, it is an independent particle picture not appropriate for even modestly correlated systems. In contrast, ARPES is a direct experimental probe of the electronic structure of a solid, and so naturally captures many-body effects. ARPES can provide information on the electronic band structure of a solid, as well as additional information including coupling to bosons, photohole lifetimes and orbital character. This Section draws heavily from [111].

The underlying principle behind photoemission is the *photoelectric effect*: The maximum kinetic energy for a photoelectron is given by $E_{\text{kin, max}} = h\nu - \varphi_f$, and, more completely

$$E_{\text{kin}} = h\nu - \varphi_f - |E_B|, \tag{3.1}$$

where E_B is the binding energy of the electron in the solid, before excitation. φ_f is the *work-function*, the minimum energy required to overcome the energy barrier at the crystal surface to excite the most loosely bound electrons into the vacuum. In the context of ARPES, φ_f is the minimum energy required for a photoelectron to travel from the sample surface to a detector, on the order of 4.5 eV. It therefore changes slightly between laboratories utilising different analysers but not often between samples.

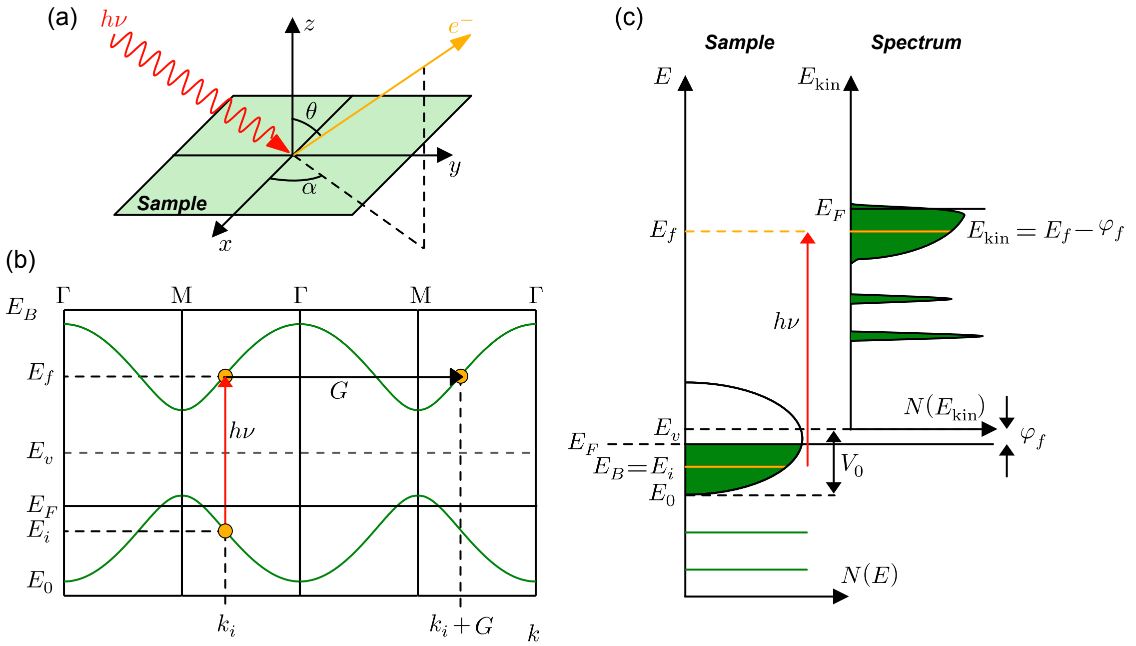

FIGURE 3.1: **Kinematics of photoemission.** (a) A photon of energy $h\nu$ is incident on a sample with a surface lying in the x-y plane. A photoelectron is emitted at a polar angle, θ, to the out-of-plane z-direction and an azimuthal angle, α, to an in-plane (here x) direction. (b) Tight binding band structure of the Γ-M direction of graphene, with a Fermi level shifted down corresponding to an electron deficient sample. Energies and momenta defined in the text are shown. (c) The relation between the density of states $N(E)$, $N(E_{\text{kin}})$ in a sample and an ARPES spectrum is shown. Similar Figures can be found in [111].

This is a very simple basis, but the understanding of exactly how ARPES works and the precise information encoded in an ARPES dataset is more complex. A complete description of ARPES, described by the *one-step model*, must treat photon absorption, electron removal and electron detection as a single coherent process. The transition probabilities between an initial state many-body wavefunction and one of many possible final state wavefunctions, where each is boundary matched to an appropriate solution in vacuum, requires the simultaneous consideration of the bulk crystal along with both its surface and the vacuum.

In practice, many assumptions are made to simplify this problem substantially, separating the process into several independent parts. In either case, the conservation of energy and momentum, shown in Eqn. 3.2, provide the basis of any model describing ARPES.

$$E_f^N - E_i^N = h\nu; \quad k_f^N - k_i^N = k_{h\nu} \approx 0 \tag{3.2}$$

Here, $E_{i,f}^N$ and $k_{i,f}^N$ are the energies and momenta for the initial and final states of the N electron system encompassing the electron undergoing excitation as well as the $N-1$ electrons which do not. The initial and final state energies are separated by exactly the photon energy, $h\nu$, and the initial and final state momenta by the photon momentum, $k_{h\nu}$. The first simplification is to assume the photon momentum is negligible. This is a reasonable approximation for photon energies below 100 eV, but is generally used even for much higher photon energies.

An ARPES spectrum can provide information only on the properties of the detected photoelectrons. Photoelectrons in vacuum are described in terms of their kinetic energies (E_{kin}) and momenta ($K = p/\hbar$). The momentum can be separated into its three spatial components, where the sample surface lies in the x-y plane (see Fig. 3.1(a)):

$$K_x = \frac{1}{\hbar}\sqrt{2mE_{\mathrm{kin}}}\sin\theta\cos\alpha; \quad K_y = \frac{1}{\hbar}\sqrt{2mE_{\mathrm{kin}}}\sin\theta\sin\alpha; \quad K_z = \frac{1}{\hbar}\sqrt{2mE_{\mathrm{kin}}}\cos\theta. \tag{3.3}$$

Here, θ is the polar angle, and α the azimuthal angle, depicted schematically in Fig. 3.1(a). In order to recreate the band structure of the crystal from the detected photoelectrons, it is necessary to relate E_{kin} to E_B and K to the momentum inside the crystal, k, before excitation. This former relation is given already by the photoelectric effect in Eqn. 3.1.

Whilst the photon provides an electron with all the energy required to get from the initial state to a final state, in the limit of $k_{h\nu} = 0$, the crystal potential, $V(\boldsymbol{r})$, is the only available source of momentum for electrons making the transition. $V(\boldsymbol{r})$ supplies momentum only in multiples of the reciprocal lattice vector, $\boldsymbol{G}$, mapping equivalent points in k-space across Brillouin zones. Therefore, for K to k mapping in the extended zone scheme, the momentum of the excited electron inside the crystal, k_f, must be related to the initial electron momentum, k_i, by a multiple of $\boldsymbol{G}$. That is, $k_f - k_i = n\boldsymbol{G}$, allowing only 'vertical' transitions (i.e. the position in the Brillouin zone of the excited electron must be equivalent to its position before excitation, Fig. 3.1(b)).

The sample surface is conserving of translational symmetry and therefore the component of momentum parallel to the x-y plane is conserved during the photoemission process. Therefore $K_{\|} = k_{\|}$, and a direct relation between the in-plane component of momentum inside a solid, $k_{\|}$, and the polar angle, θ, can be written:

$$K_{\|} = k_{\|} = \frac{\sqrt{2mE_{\mathrm{kin}}}}{\hbar}\sin\theta, \tag{3.4}$$

where m is the electron mass. Here, $k_{\|} = \sqrt{k_x^2 + k_y^2}$ is defined within the extended zone scheme. If a sample is rotated in the θ-axis sufficiently to pass the Brillouin zone boundary of the first zone, the second zone will be probed directly. The band structure probed between zones is equivalent other than a linear offset in $k_{\|}$ of some multiple of the crystal momentum, $\boldsymbol{G}$. Photoemission matrix elements can vary across Brillouin zones, however.

For the perpendicular component of momentum, $k_{\perp} = k_z$, translational symmetry is not conserved due to the presence of the sample surface[1], and so an assumption needs to be made

---

[1] For a free-electron gas where there is no crystal potential defining a zone boundary ($V(\boldsymbol{r})$ =0), there are no available transitions to final states possible that conserve momentum in the limit $k_{h\nu} = 0$. Increasing energy must be accompanied by an increase in momentum ($E(k) \propto k^2$) and so no photoelectrons are created from the bulk. However, since momentum is not conserved perpendicular to the surface, the momentum required can be delivered by the surface itself, highlighting the crucial role of the sample surface in photoemission experiments.

regarding the final state in order to relate K_z to k_z. By assuming that the photoelectron final state has a nearly-free electron description,

$$E_f(k) = \frac{\hbar^2 k^2}{2m} - |E_0| = \frac{\hbar^2(k_\parallel^2 + k_z^2)}{2m} - |E_0|, \tag{3.5}$$

where E_0 is the valence band bottom and $E_f = E_{\text{kin}} + \varphi_f$ is the final state energy before photoemission, referenced to the Fermi level, E_F (E_{kin} is referenced to the vacuum energy E_v, see Fig. 3.1(c)). In conjunction with Eqn. 3.4, the following approximation for k_z is obtained:

$$k_z = \frac{1}{\hbar}\sqrt{2m(E_{\text{kin}}\cos^2\theta + V_0)}; \quad V_0 = |E_0| + \varphi_f, \tag{3.6}$$

where V_0 is the *inner potential*. This approximation is most valid when the final state wavefunction, with energy E_f, describes a band that is sufficiently high energy that any electrons occupying it are essentially ‘free’, with the periodic crystal potential only a very weak perturbation. Higher energy photons allow for transitions to higher energy final states, and therefore the validity of Eqn. 3.6 is improved. This approximation complicates the interpretation of experimentally obtained dispersions along the k_z direction, but is just one contributor to the large intrinsic uncertainties in k_z, discussed further in Section 3.6.

Now it is possible to relate the properties of photoelectrons in vacuum to the electronic structure of the crystal being measured. In order to give meaning to the band linewidths, positions and intensities in an ARPES spectrum, a formal description of photoemission is required.

3.1.2 The three-step model

The one-step model outlined earlier is a difficult problem to implement in practice, and so the *three-step model* is often invoked in order to interpret ARPES data. Although it requires many further approximations, it functions very well as a formal description of ARPES. Instead of treating the photoemission event as one coherent process, the three-step model divides it into three independent steps, with the total photoemission intensity simply given by the product of the probabilities associated with each step:

1. Excitation between the initial and final bulk Bloch eigenstates. i.e. the probability of a given transition between an initial and final state within the bulk. All the details of the electronic structure are considered here.
2. Travel of the excited electron to the surface. The finite mean free path of an electron in a solid, λ, must be considered.
3. Escape of electron into the vacuum after transmission through the surface potential barrier. i.e. matching the Bloch eigenstates of the final state inside the sample to free-electron like plane waves in vacuum.

The *sudden approximation* must also be introduced at this point, which assumes that any relaxation of remaining $N-1$ electron system happens after the photoelectron has become decoupled from the system. In other words, the properties of the photoelectron in vacuum are not altered by further interactions with the system. This approximation is most suited to high E_{kin} photoelectrons which move away from the surface with a higher velocity, reducing the interaction time between the photoelectron and the $N-1$ electron system[2]. By invoking this approximation, the transition probability, w_{fi}, of making an optical transition between the N electron initial ground state, ψ_i^N, and some available final state, ψ_f^N, can be approximated with Fermi's golden rule.

$$w_{fi} = \frac{2\pi}{\hbar}|\langle\psi_f^N|\hat{H}_{\text{int}}|\psi_i^N\rangle|^2\delta(E_f^N - E_i^N - h\nu) \tag{3.7}$$

Here, the delta function enforces energy conservation, and both the initial and final state energies, E_i^N and E_f^N, can be written as the sums of the initial or final state energies of the $N-1$ electrons which do not undergo excitation, and the one electron that does:

$$E_i^N = E_i^{N-1} - E_B^k; \quad E_f^N = E_f^{N-1} + E_{\text{kin}} + \varphi_f. \tag{3.8}$$

An electron with binding energy E_B and momentum k is excited to a final state energy E_f^k and overcomes the workfunction, φ_f, to become a photoelectron in vacuum with energy E_{kin}. An $N-1$ electron system is left behind, with energy E_f^{N-1}. The interaction Hamiltonian, $\hat{H}_{\text{int}}$ in Eqn. 3.7 describes the dipole interaction with the photon, and has the following form

$$\hat{H}_{\text{int}} = \frac{e}{2mc}(\boldsymbol{A}\cdot\boldsymbol{p} + \boldsymbol{p}\cdot\boldsymbol{A}) = \frac{e}{mc}\boldsymbol{A}\cdot\boldsymbol{p}; \quad [\boldsymbol{p},\boldsymbol{A}] = -i\hbar\boldsymbol{\nabla}\cdot\boldsymbol{A} = 0, \tag{3.9}$$

where $\boldsymbol{p}$ is the electron momentum and $\boldsymbol{A}$ is the electromagnetic vector potential of the electromagnetic field from the photon. Here, the *dipole approximation* has been used, that $\boldsymbol{\nabla}\cdot\boldsymbol{A} = 0$. This is not a good approximation in systems where there is a strong spatial dependence of the electromagnetic field, including at the surface, for example[3].

The final state wavefunction of the N electron system can also be separated into the product of the photoelectron wavefunction, ϕ_f^k, and the $N-1$ electron wavefunction, ψ_f^{N-1}:

$$\psi_f^N = P\phi_f^k\psi_f^{N-1}, \tag{3.10}$$

---

[2] Experimental photoemission studies utilising low energy light sources have suggested that photoelectrons are still within the sudden limit for kinetic energies as low as 2 eV [112]. Indeed, the time-scale of the photoemission process is thought to be on the timescale of 100s of attoseconds [113, 114] whereas, for few Kelvin temperature scales, the $N-1$ system can be expected to relax on time scales on the order of several 100s of femtoseconds, verified experimentally [115, 116].

[3] Note that in the limit $[\frac{p^2}{2m} + V, \boldsymbol{p}] = i\hbar\nabla V$ and $\boldsymbol{\nabla}\cdot\boldsymbol{A} = 0$, for a free electron gas, the matrix elements $\propto \langle\psi_f^N|A\cdot\nabla V|\psi_i^N\rangle$ are all equal to zero, since $\nabla V = 0$. This again shows that it is only possible to satisfy momentum conservation for electrons photoemitted from the surface, where $dV/dz \neq 0$. This is the surface photoelectric effect, and can result in asymmetric line shapes in ARPES spectra [111].

where P is an operator anti-symmetrising the N electron wavefunction such that the Pauli exclusion principle is satisfied [111]. ψ_f^{N-1} is one of the possible excited states, ψ_m^{N-1} with energy E_m^{N-1}. A similar factorisation can be done for the initial state wavefunction:

$$\psi_i^N = P\phi_i^k \psi_i^{N-1}. \tag{3.11}$$

Then, the integral in Eqn. 3.7 can be reformulated as follows

$$\langle \psi_f^N | \hat{H}_{\text{int}} | \psi_i^N \rangle_m = \overbrace{\langle \phi_f^k | \hat{H}_{\text{int}} | \phi_i^k \rangle}^{M_{f,i}^k} \overbrace{\langle \psi_m^{N-1} | \psi_i^{N-1} \rangle}^{|c_{m,i}|}.$$

$M_{f,i}^k$ is defined as the one electron dipole matrix element, with $|c_{m,i}|$ the probability that the removal of an electron from the initial state leaves the $N-1$ system in the excited state m. In the limit of zero electron interactions, $E_i^{N-1} = E_f^{N-1}$ and the final $N-1$ system is as it was with the photoemitted electron included, and the photohole lifetime is infinite. In general, the more strongly interacting the system, the higher the number of possibilities to annihilate the photohole, and hence the more excited states. The total photoemission intensity can be written over the sum of all m:

$$I(k, E_{\text{kin}}) = \sum_{f,i} |M_{f,i}^k|^2 \sum_m |c_{m,i}|^2 \delta(E_{\text{kin}} + E_m^{N-1} - E_i^N + \varphi_f - h\nu). \tag{3.12}$$

This relation demonstrates that an ARPES spectrum does not simply reflect the electronic structure of the independent particle picture (often referred to as the ‘bare band’, ϵ_k). Instead, each band has an intrinsic linewidth corresponding to the probabilities of the possible final states of the $N-1$ electron system. This intrinsic linewidth is related to the lifetime of the photohole in the final state [111], which can be extracted from experiment in systems without significant additional linewidth broadening from k_z, a point that will be expanded upon in Section 3.1.4.

Moreover, each band can have a k-dependent renormalisation by an amount corresponding to the kinetic energy cost/gain of exciting the $N-1$ electron system from E_i^{N-1} to E_m^{N-1}. Band renormalisations and lifetimes can be related to other lattice properties. For example where there is a strong coupling of electrons to the vibrational modes of the underlying lattice, the band renormalisation will reflect the increase in the effective mass of the phonon-coupled electrons over an energy range related to the relevant phonon energy. Linewidths of bands below the phonon energy will reflect the enhanced scattering rate and therefore the shorter photohole lifetime. Details of electron-phonon coupling and coupling to other bosonic modes can therefore be extracted directly from the deviation of a band from the bare-band solution in an ARPES spectrum.

3.1.3 The one-particle spectral function

The *one-particle spectral function* encapsulates the above description and can be compared directly to an ARPES spectrum. It is obtained from a Green's function approach. The propagation of a single electron in a many body system can be described by a time-ordered one electron Green's function, describing the probability that an electron added to a lattice at position $\boldsymbol{r}$ at time t will still be in the initial state after a time $t - t'$.

Taking the Fourier transform, and considering only the cases where electrons are removed from the system (an opposite but analogous discussion to the one below can be used to describe inverse-photoemission), the *one electron removal Greens function* at temperature $T = 0$ is obtained:

$$G^{-}(k,\omega) = \sum_{m} \frac{|\langle \psi_m^{N-1} | c_k^{-} | \psi_i^N \rangle|^2}{\omega - E_m^{N-1} + E_i^N - i\eta}, \tag{3.13}$$

where $c_k^{-} = c_{k\sigma}$ annihilates an electron with energy ω, momentum k and spin σ from the N particle initial state ψ_i^N. The sum is again over all possible final states of the $N-1$ electron system, ψ_m^{N-1} with eigenvalues E_m^{N-1} and η is a positive infinitesimal.

The associated one-electron removal spectral function can be written as [111]

$$A^{-}(k,\omega) = \sum_{m} |\langle \psi_m^{N-1} | c_k^{-} | \psi_i^N \rangle|^2 \delta(\omega - E_m^{N-1} + E_i^N), \tag{3.14}$$

where $c_k^{-}\psi_i^N = \psi_i^{N-1}$. This describes $|c_{m,i}|$ from previous discussions and enforces energy conservation. By comparing this to Eqn. 3.12 and allowing only for excitations from occupied bands through the inclusion of the Fermi-Dirac distribution, $f(\omega, T)$, the total photoemission intensity can be rewritten as

$$I(k,\omega) = I_0(k,\nu,A) f(\omega) A(k,\omega); \quad I_0 \propto |M_{f,i}|^2; \quad f(\omega) = \Big(\exp\Big(\frac{\omega}{k_B T}\Big) + 1\Big)^{-1}. \tag{3.15}$$

Lifetime and correlation effects characterised by the relative probabilities of possible $N-1$ electron final states in the above discussions are described by the *self-energy*, $\Sigma = \Sigma' + i\Sigma''$. The final full one-particle spectral function for photoemission can then be written as

$$A(k,\omega) = -\frac{1}{\pi} \frac{\Sigma''(k,\omega)}{[\omega - \epsilon_k - \Sigma'(k,\omega)]^2 + [\Sigma''(k,\omega)]^2}. \tag{3.16}$$

In the absence of correlations, $A(k,\omega)$ has non-zero spectral weight only when ω matches the bare band energy ϵ_k and so an 'image' of the band structure is produced. The imaginary part of the self energy, Σ'', acts to increase the linewidths of bands in $A(k,\omega)$, and the real part, Σ', renormalises the band positions, in accordance with the previous discussions. For systems wherein the k_z dispersion of bands is modest, Eqn. 3.15 shares the same properties as an ARPES spectrum, other than extrinsic backgrounds and the effects of experimental resolutions. Extracting the linewidths and peak positions of the bands in an ARPES spectrum can then provide information on photohole lifetimes and electron correlations. For more three-dimensional systems, however, the effect of k_z *broadening* needs to be considered.

3.1.4 The problem with k_z

Eqn. 3.6 shows that the effective k_z probed can be chosen with photon energy. Of course, this is not the only effect of changing the photon energy. Details of the photoelectron final state, experimental energy resolutions and matrix elements also change, acting to complicate the final experimental k_z dispersion. Additionally, the breaking of translational symmetry along the z axis required that this relation was derived under the assumption that all photoelectron final states are free electron like, unlikely to be exactly true in practice, leading to errors when mapping from photon energy to k_z.

More crucially, though, the intrinsic linewidth for the out-of-plane dispersion relation $E(k_z)$ of a three-dimensional electron system does not only reflect the photohole and photoelectron lifetimes, but also the finite probing depth of photoemission.

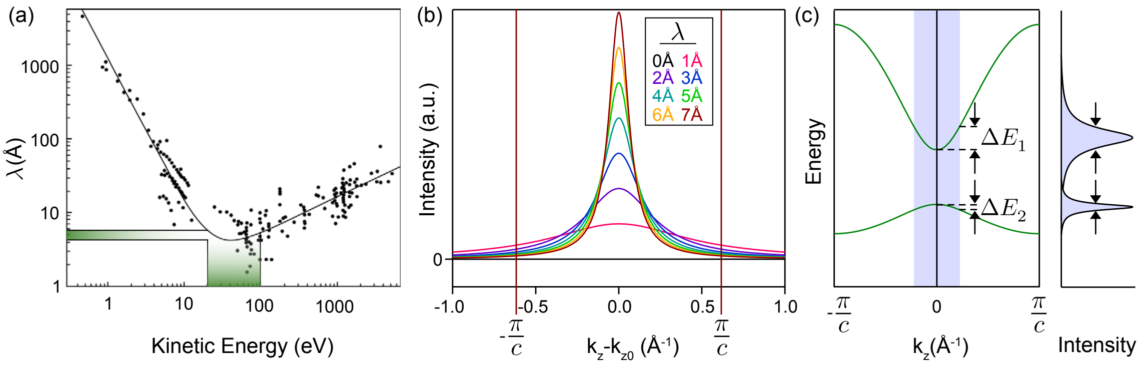

FIGURE 3.2: **Effect of k_z broadening in photoemission.** (a) Electronic mean free path in a solid as a function of kinetic energy [111]. The kinetic energy range relevant to this work is indicated. (b) Envelope of k_z integration ($L(k_z)$) for various mean free paths (λ). The zone boundary of a typical 1T-structured transition metal dichalcogenide is indicated ($c \approx 5.1$Å). (c) Effect of k_z integration (blue shaded area) on an energy distribution curve taken at $k_z = 0$. For the more three-dimensional band (top), the additional broadening is significant. For a more two-dimensional band (bottom), the effects of k_z integration are less significant.

Step two of the three-step model describes the travel of a photoelectron occupying a final state to the surface. Only electrons originating a distance into the bulk material comparable to, or less than, the electron mean-free path can escape into the vacuum and be detected. Therefore, although initial states are infinitely delocalised, the localisation in z of experimentally accessible final state electrons corresponds to a significant wavefunction delocalisation in k_z, thus greatly enhancing the intrinsic uncertainty in k_z[4].

To illustrate this, consider the wavefunction for a photoelectron occupying a final state inside the bulk ($z < 0$). This has the following form [117]:

$$\psi(z) = \frac{1}{\sqrt{\lambda}} \exp(ik_{z0}z) \exp(\frac{z}{2\lambda}). \tag{3.17}$$

The wavefunction amplitude decays exponentially into the bulk on a scale characterised by the electron mean free path, λ. k_{z0} is the nominal k_z-value for a chosen photon energy. The Fourier transform of this is given by

$$\phi(k_z) = \frac{1}{i(k_z - k_{z,0}) - 1/2\lambda}, \tag{3.18}$$

and hence the envelope of k_z integration, centred at k_{z0}, is given by

$$|\phi(k_z)|^2 \propto L(k_z) = \frac{1}{2\pi\lambda} \frac{1}{(k_z - k_{z,0})^2 + (1/2\lambda)^2}. \tag{3.19}$$

The one-particle spectral function, $A(\omega, k)$, has is linewidths limited by Σ'' in the case of 2D systems. For three-dimensional systems, an ARPES spectrum for $k_z = k_{z,0}$ can be described by the sum of one-particle spectral functions for all k_z, with a maximum contribution arising from $k_z = k_{z,0}$ and the width of integration set by the Lorentzian function $L(k_z)$, which has a FWHM given by the inverse of the mean free path. That is:

$$A'(\omega, k_x, k_y, k_{z,0}) = \int_{-\infty}^{\infty} L(k_z) A(\omega, k_x, k_y, k_z) dk_z. \tag{3.20}$$

Fig. 3.2(a) shows the empirically determined electronic mean free path as a function of electron kinetic energy. From this, the following empirical formula is determined [118]:

$$\lambda = \frac{1430}{E_{\mathrm{kin}}^2} + 0.54\sqrt{E_{\mathrm{kin}}} \quad [\text{Å}], \tag{3.21}$$

where E_{kin} is the electron kinetic energy in eV. The kinetic energies corresponding to the core photon energy range used within this work (24-107 eV) is indicated in Fig. 3.2(a), giving a mean free path on the order of 5 Å. Fig. 3.2(b) shows the shape of the $L(k_z)$ for various λ. The Brillouin zone size for a typical trigonally structured (1T) transition-metal dichalcogenide is indicated, demonstrating that k_z integration is significant, with the central 50%, 90% and

---

[4] Similarly, in the one-step model, an electron is excited from a periodic Bloch initial state wavefunction extending infinitely into the bulk, to a final state described by an infinitely propagating plane wave in vacuum decaying exponentially into the bulk. Transitions to the final state are therefore only possible for a finite range of z, increasing the intrinsic uncertainty in k_z.

99% of spectral weight distributed over 0.2, 1.1 and 11.6 Brillouin zones in k_z respectively for $\lambda = 4.47$ Å. This is of course only a problem for three-dimensional systems. If a band structure is entirely two-dimensional then the uncertainty in k_z is inconsequential and the intrinsic linewidths once again becomes limited by the photohole lifetimes. This is schematised in Fig. 3.2(c), the more dispersive a band within the k_z integration window, the larger the energy broadening in the measured spectral function. As a result, surface states are typically much sharper in energy than three-dimensional bands, limited only by Σ'', and not by $L(k_z)$.

3.2 ARPES Experiments

3.2.1 Synchrotrons and beamlines

An ARPES experiment requires a source of monochromatic light. This is typically provided by one of three sources. Gas discharge lamps using the characteristic emission lines of He, Xe or Ne are common place in laboratory environments, providing a well defined source of light, albeit at only a few discrete photon energies. More recently, laser-ARPES systems have gained prominence, typically providing photons at one or more energies between 5 and 11 eV depending on the laser type. Typically, laser sources are significantly more intense and the light spot size incident on the sample is much smaller than lamp sources (tens μm vs. few mm), vastly improving ARPES data quality, particularly for small, non-uniform samples. Laser sources are most suited for the cases where the electronic bands of interest are close to $k_{||} = 0$, however. Eqn. 3.4 is maximal for $\theta = 90$ degrees, demonstrating an intrinsic limit on the k-space available at low photon energies. The third light source is that of synchrotron radiation, as will be discussed below.

Synchrotron Radiation

In this thesis, all of the data collected is from synchrotron sources at one of four beamlines. Spin-integrated data was taken either at the i05 beamline of Diamond Light Source (Oxfordshire) or at the CASSIOPEE beamline of SOLEIL (Paris). Spin-resolved data (discussed in Section 3.2.3) is collected from either the APE beamline of Elettra (Trieste) or the BL9A beamline of HiSOR (Hiroshima).

Synchrotrons offer significant advantages over lamp and laser based light sources. Although the light spot available is larger than a well focussed laser source, the photon energy is variable over a large continuous energy range (~18 eV to >150 eV) with significantly more flux available in the 'core' operating energy range than is typical for a lamp source. This increases the rate at which data can be collected, useful when typically only five days are awarded for a particular 'beamtime'.

The bremsstrahlung radiation emitted from the electrons accelerated by the 'bending' magnets within the synchrotron ring itself does not have a tunable emission peak, and contributes only to energy losses. These energy losses are inversely proportional to the radius of the ring, and so modern synchrotrons are usually extremely large with diameters up to 180 m for the case of Diamond Light Source. Whilst this gain in efficiency is associated with extremely large commissioning and operating costs, limiting the number of synchrotrons worldwide, the large ring diameter allows for many *beamlines* which form linear tangents to the synchrotron ring, allowing many experiments using synchrotron radiation to run in parallel.

The emission peak of the radiation of the electrons around the ring is set entirely by the radius of the ring and the strength of the magnetic fields in the bending magnets. The radiation used by experiments is produced in an *undulator* located at the synchrotron end of each beamline. Undulators allow both for the selection of the beam energy as well as its polarisation. Undulators consist of a pair of parallel arrays of fixed dipole magnets separated by a gap. Each successive pair of magnets applies an alternating transverse force to the electron beam, resulting in a sinusoidally oscillating electron path, emitting radiation of wavelength, λ_u, equal to the wavelength of the electron beam oscillations. The undulator simultaneously acts as a diffraction grating, with each pair of dipole magnets adding coherently to the peak intensity at λ_u, with higher harmonics also produced.

The electrons are retained in the synchrotron ring, leaving only the emitted photons usable for experiments to continue down the beamline axis. The photons have a modified wavelength from λ_u due to the relativistic speed of electrons and the associated Doppler effect [119].

$$\lambda = \lambda_u\Big(\frac{1+\gamma^2\theta^2}{2\gamma^2}\Big) + \lambda_u^3\Big(\frac{eB}{4\gamma\pi mc}\Big)^2 \tag{3.22}$$

Here, γ is the Lorentz factor, B is the magnetic field strength and θ is the angle at which the emitted light cone is centred relative to the beamline axis. The desired photon energy can be selected by changing the gap separation between the parallel magnet arrays, effectively changing the magnetic field strength applied to the electron beam. The desired light polarisation can also be set by the undulator by introducing a phase shift of the two magnet arrays along the axis of the beamline[5].

Whilst centred at the desired photon energy, the bandwidth of light from the undulator is very broad, requiring a monochromator to discard the unwanted wavelengths. The monochromator consists of a diffraction grating with physical orientation chosen such that photons of the desired wavelength are centred along the axis of the beamline. Unwanted photons are filtered out using a variable 'exit slit' further down the beamline, wherein photon flux can be traded for a better defined photon energy. The photon beam is then focussed onto the sample with a final spot size typically between 1 mm and 1 μm depending on the optical path and experimental requirements. A schematic of the 50 m long beamline of the 'high-resolution' branch of the i05

---

[5] Light polarisation dependent ARPES has the ability to inform of band orbital character. The one particle matrix element, $M^k_{f,i} = \langle \phi^k_f | \boldsymbol{A}\cdot\boldsymbol{p} | \phi^k_i \rangle$ is only non-zero when the integrand is an even function, giving well defined selection rules for the excitation of odd or even parity initial states for even (free-electron like) final states. For example, Fig. 3.3(c) depicts light travelling in the y-z plane with wavefronts perpendicular to the sample surface (p-polarised). This corresponds to an even $\boldsymbol{A}\cdot\boldsymbol{p}$ term with respect to the scattering plane and therefore only even initial states will contribute to spectral weight (here p_y and p_z orbitals, but not p_x) [41, 111].

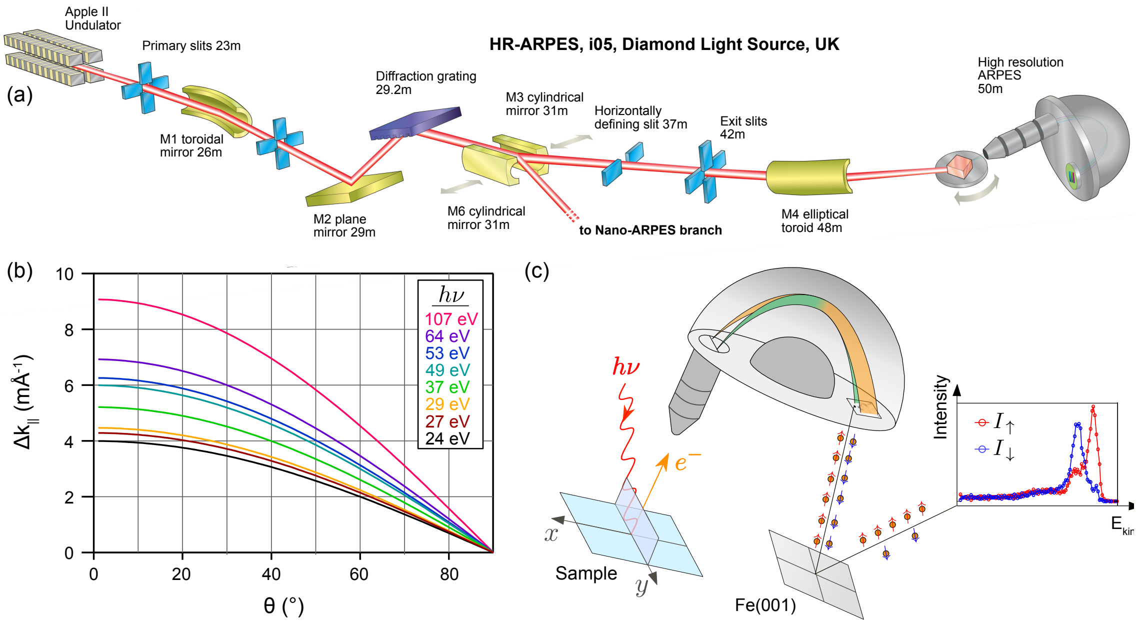

FIGURE 3.3: **Typical (spin-)ARPES beamline and endstation.** (a) The i05 beamline of Diamond Light Source is schematised [120]. Each component is labelled and the distance from the undulator indicated. (b) Momentum resolution, $\Delta k_{\|}$ is given as a function of in-plane emission angle for key photon energies used in this work, with $\Delta\theta = 0.1°$. (c) Typical sample and experimental geometry for an analyser capable of spin-resolved studies. The Fe(001) spin target is selectively magnetised by pairs of Helmholtz coils positioned along the horizontal and vertical axes of the target. A typical pair of spin-resolved EDCs is shown.

beamline at Diamond Light Source, used for the majority of the spin-integrated ARPES results in this work, is shown in Fig. 3.3(a) [120].

3.2.2 ARPES endstation

The final two elements of any ARPES beamline are the sample and the electron analyser. The analyser is made of three key components. A multi-element, electrostatic input lens accelerates or decelerates, as well as focusses photoelectrons into the entrance slit of the analyser, with the position of electron incidence along the entrance slit determined by the in-plane emission angle, θ, from the sample surface. The bulk of the analyser is made up of two concentric hemispheres of radii $R_{1,2}$ with a potential difference ΔV applied across them. Photoelectrons follow curved trajectories around the analyser, with the radius of curvature set by their kinetic energy after the transfer lens section. Only electrons in a narrow energy range will reach the detector without colliding with the analyser walls, centred at the *pass energy*, E_{pass}, defined as follows:

$$E_{\text{pass}} = \frac{e\Delta V}{\frac{R_1}{R_2} - \frac{R_2}{R_1}}. \tag{3.23}$$

The electrostatic lens voltages are tunable, allowing to choose the E_{kin} range which is accelerated sufficiently such that they fall into the acceptance window defined by the pass energy. If the kinetic energy region of interest is larger than is available for a given pass energy, then the input lens voltages need be 'swept' to build up a full dataset. The electrons, now sorted by their kinetic energy, are incident on a position sensitive two-dimensional detector, consisting of multichannel plates (MCP) and a phosphor screen, with a CCD camera providing a live image of the electronic structure.

Energy and momentum resolution

The theoretical energy resolution of an ARPES acquisition is given by [111, 121]

$$\Delta E = \sqrt{\Delta_{h\nu}^2 + E_{\text{analyser}}^2}; \quad \Delta_{h\nu} = \frac{h\nu}{R_m}; \quad E_{\text{analyser}} = E_{\text{pass}}\Big(\frac{w}{\frac{1}{2}(R_1 + R_2)} + \frac{\alpha^2}{4}\Big). \tag{3.24}$$

There are contributions from both the analyser, E_{analyser}, and the monochromator, $\Delta_{h\nu}$. E_{analyser}, is set largely by the pass energy. Higher pass energies allow electrons over a wider kinetic energy to range to reach the detector simultaneously, but with an associated energy resolution penalty related to the finite number of detector channels. In the case of 'swept' scans, the energy information contained within the image is most often binned digitally into a smaller number of pixels corresponding to the step size chosen. In this case, the effective analyser energy resolution is often limited by the energy step size chosen. Data acquisitions for a fixed lens voltage are therefore preferable when interested in the smallest binding energy windows. Other contributing factors to E_{analyser} are the width of the analyser entrance slit, w, and the acceptance angle, α. The latter derives from the fact that only electrons travelling entirely within the scattering plane (y-z plane in Fig. 3.3(c)) will follow the nominal electron trajectories intended for a chosen ΔV.

The component $\Delta_{h\nu}^2$ is determined by the 'resolving power', R_m, of the monochromator, set largely by the width of the beamline exit slit. The wider the photon energy range incident on the sample surface, the larger the uncertainty in the kinetic energy. In the case of i05, the resolving power, R_m is typically on the order of 3000 for the photon energy range 50-200 eV, and can surpass 20000 for lower photon energies. This therefore gives a contribution to ΔE as low as 1 meV [120].

The momentum resolution also is limited by the resolving power of the monochromator, but with a larger contributing term given by the differentiation of Eqn. 3.4. Together, the $k_{\|}$ resolution can be written as follows [121]:

$$\frac{\Delta k_{\|}}{k_{\|}} = \sqrt{(\Delta\theta \cot(\theta))^2 + R_m^{-2}}. \tag{3.25}$$

Here, $\Delta\theta$ is the angular resolution, typically on the order of 0.1° [120]. Fig. 3.3(b) displays the momentum resolution obtained for key photon energies used in this thesis. The higher θ, the better the momentum resolution, providing some incentive to measure outside of the first Brillouin zone. For modern ARPES end stations, the resolution limitations are extremely small, with ARPES even a viable technique to measure sub-meV wide features such as superconducting gaps [122, 123]. The theoretical momentum resolutions for the core photon energy range used in this work are shown in Fig. 3.3(b).

3.2.3 Spin-resolved ARPES

In spin-resolved ARPES systems, the description for ARPES above is largely unchanged from the synchrotron to the detector of the analyser, although light flux is often favoured over absolute resolution. In addition to the photoelectrons collected at the 2D detector, a subset of electrons are taken through an aperture of finite size situated above or below the detector, through a further transfer lens section and reflected off a target. The target is chosen such that there is a spin-dependent scattering asymmetry of the incident photoelectrons.

The spin-resolved ARPES endstations used for the work in this thesis employ a *very low energy electron diffraction* (VLEED) principle [124, 125], where the scattering asymmetry is derived from the exchange interaction. A ferromagnetic target, typically oxygen-passivated Fe(001) on a MgO(001) substrate, is selectively magnetised with Helmholtz coils. An imbalance of spin up and spin down density of states within the target then creates a spin-dependent asymmetry in elastic scattering events [126]. Repeating the procedure with the opposite magnetisation provides a pair of spin-resolved intensity profiles as a function of either kinetic energy or θ depending on whether it is the ARPES lens voltages or the sample position that is varied, with the difference in peak heights informing of the spin-polarisation of the corresponding electronic band in the spin-integrated 2D dataset. A simplified schematic example of this, along with such a dataset, is shown in Fig. 3.3(c).

The spin-resolved intensity profiles, $I_i^{\uparrow,\downarrow}$, for a given spin component, $i \in \{x, y, z\}$, are given by

$$I_i^{\uparrow,\downarrow} = \frac{I_i^{\text{tot}}(1 \pm P_i)}{2}. \tag{3.26}$$

$I_i^{\text{tot}} = I_i^+ + I_i^-$, where $I_i^\pm$ is the measured intensity for a chosen detector magnetisation, often corrected with a relative efficiency calibration determined from the measurement regions corresponding to unpolarised, diffuse background intensity. The spin polarisation, P_i, is determined according to

$$P_i = \frac{I_i^+ - I_i^-}{S I_i^{\text{tot}}}, \tag{3.27}$$

where S is the detector *Sherman function*, a measure of the spin asymmetry in elastic scattering events, determined by spin-resolved measurements of a electronic state with a known spin-polarisation, often the Rashba surface state of Au(111). For the work in this thesis, the

Sherman functions vary between $S = 0.2$ and $S = 0.43$, with a larger Sherman function thought to correspond to a flatter, cleaner and more ordered target [124]. More reliably, spin-polarisations of a given band can be determined by fitting the uncorrected intensity profiles to Gaussian-Broadened Lorentzians, incorporating a Shirley background[6] as well as the Fermi-Dirac distribution where required. The extracted peak areas can then be inputted into Eqn. 3.27 as an alternative to the raw intensity profiles.

The component of spin that a VLEED detector is sensitive to is determined by the geometry of the experimental set up. In practice, twin VLEED chambers, each with their own target and detector, are positioned orthogonal to each-other, such that each can be sensitive to the out-of-plane spin component and opposite in-plane spin-components. Standard VLEED systems only provide a single point in $E_{\text{kin}}(\theta)$, requiring either the lens voltages or sample position to be varied to produce one-dimensional distribution curves. Additional contributions to the experimental energy and momentum resolutions are derived largely from the finite aperture size, with the typical energy resolution between 10-100 meV [124].

Both the Sherman function and reflectivity of VLEED targets require low energy incident electrons (few eV). 'Mini-Mott' systems are an earlier developed alternative to VLEED, instead operating at extremely high kinetic energies (keV) using a high Z target (typically gold) with the spin dependent scattering asymmetry derived from the large spin-orbit coupling term. Both Mott and VLEED based spin-systems are very inefficient compared to spin-integrated ARPES. VLEED systems are approximately 100 times more efficient than Mott-based systems [124], owing in part to the smaller Sherman function of the latter (S =0.17 is typical) as well as considerably poorer reflectivity. A high quality sample provides a pair of EDCs similar to those shown in Fig. 3.3 in approximately 30 minutes.

3.2.4 Surface sensitivity and need for ultra-high vacuum

The mean free path of electrons through a solid is on the order of only 5 Å for the photon energy range used within this work, and so it is vital that the top most layers of a sample stay clean during an experiment. Whilst some level of vacuum is clearly needed in order permit a collision-free journey of a photoelectron from sample to detector, the need for *ultra-high vacuum* (UHV) only becomes apparent when considering the build up of adsorbates on the sample surface.

The rate, R, of particles arriving at a sample surface can be approximated by [27]

$$R \approx 4 \times 10^{22} \frac{pS_c}{\sqrt{MT}} [\text{cm}^{-2}\text{s}^{-1}], \tag{3.28}$$

where p is the pressure in mbar, M is the molecular mass, T is the temperature in Kelvin, and $0 < S_c < 1$ is the 'sticking constant'.

---

[6] The Shirley background, first described in [127], accounts for inelastic scattering and other energy loss events of electrons within the sample. The background at some binding energy is proportional to the occupied density of states at shallower binding energies.

Even for a pressure as low as $p = 10^{-9}$ mbar, it takes only ten minutes for a monolayer[7] of nitrogen ($M = 28$) to cover the sample surface at measurement temperatures of $T = 15$ K and assuming a sticking constant $S_c = 0.5$. This is not enough time to align a sample with the desired azimuthal orientation before data collection. A pressure of 3×10^{-11} mbar extends this time period to approximately 6 hours however, sufficient for most ARPES experiments.

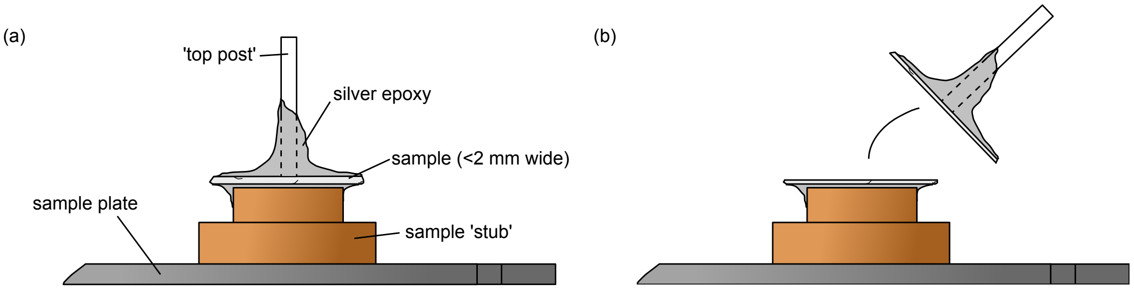

FIGURE 3.4: **Sample cleaving.** (a-b) Cartoon (not to scale) of a 'top-posted' sample before (a) and after (b) the cleave in UHV conditions.

This also requires that the measurement sample surface has not already been exposed to atmosphere before it was loaded into the system. This is achieved by *sample cleaving*: A ceramic or metallic 'top post' is glued to a sample surface with silver epoxy, which is then knocked off at the measurement temperature and pressure. The sample will cleave at the weakest point in the structure, intended to be within the sample itself. The full sample surface is coated in epoxy to ensure that a partial layer is not left after cleaving. This procedure, outlined in Fig. 3.4, works best for van der Waals-bonded, layered structures.

It is not possible to go from atmospheric pressure down to UHV with a single chamber without performing a 'bake-out', where the temperature of the full chamber is greatly increased for a period of days to desorb all molecules from chamber walls. All ARPES end stations are therefore composed of multiple vacuum chambers. In general, the 'loadlock', into which samples are installed, is the only vacuum chamber that is routinely exposed to atmospheric pressure, usually in the form of dry nitrogen. After samples are installed, the loadlock is pumped down to 'rough vacuum' ($\approx 10^{-2}$ mbar) by a scroll pump before being taken down to 'high vacuum' ($\approx 10^{-8}$ mbar) by a turbomolecular pump. The measurement chambers, which often have additional pumping in the form of ion pumps, sublimation pumps and/or non-evaporable getters, are therefore never exposed to higher pressures than the minimum of the loadlock, helping to preserve their pressure to UHV levels. There are usually intermediate chambers acting as further buffer regions between UHV and vacuum, also allowing for processes such as ion sputtering, alkali metal deposition and sample annealing, protecting the measurement chamber from pressure spikes associated with those procedures.

---

[7] 1ML $\approx 6 \times 10^{14}$ particles cm^{-2} [27].

3.3 Density Functional Theory (DFT)

Chapters 4, 5 and 6 will each contain density functional theory (DFT) calculations to complement the ARPES experimental data. A brief overview of the main principles behind DFT will be given below. This section draws heavily from [18].

3.3.1 Moving away from the tight binding model

Exactly solving for the band structure of a $N+ZN$ particle system (where N is the number of nuclei and Z the proton number of the atom involved) requires solving the following many-body Hamiltonian.

$$\hat{H} = -\frac{\hbar^2}{2}\sum_i \frac{\nabla_{\boldsymbol{R}_i}{}^2}{m_i} - \frac{\hbar^2}{2}\sum_i \frac{\nabla_{\boldsymbol{r}_i}{}^2}{m_e} - \frac{1}{4\pi\epsilon_0}\sum_{ij}\frac{e^2 Z_i}{|\boldsymbol{R}_i - \boldsymbol{r}_j|} + \frac{1}{8\pi\epsilon_0}\sum_{i\neq j}\frac{e^2}{|\boldsymbol{r}_i - \boldsymbol{r}_j|} + \frac{1}{8\pi\epsilon_0}\sum_{i\neq j}\frac{e^2 Z_i Z_j}{|\boldsymbol{R}_i - \boldsymbol{R}_j|} \tag{3.29}$$

$\boldsymbol{R}_i$ and $\boldsymbol{r}_i$ are the positions of a nucleus and electron with masses m_i and m_e respectively. The first and second terms on the right hand side describe the kinetic energies of the nuclei and electrons respectively, and the last three describe the Coulomb-derived potential felt from nucleus-electron, electron-electron and nucleus-nucleus interactions. To solve this, some assumptions are needed.

The first of these is the Born-Oppenheimer approximation, made also in the prelude to discussion of the tight-binding model in Chapter 2. This assumes that the motion of the heavy nuclei is slower than that of the electrons, with the electrons finding a instantaneous equilibrium. It is approximated, therefore, that the nuclei do not move, providing only a source of static positive charge. This sets the first term on the right hand side of Eqn. 3.29 to zero, and simplifies the fifth by approximating it to a variational constant.

This Hamiltonian can be decomposed into a sum of other operators

$$\hat{H} = \hat{T} + \hat{V} + \hat{V}_{\text{ext}}, \tag{3.30}$$

where $\hat{T}$ and $\hat{V}$ correspond to the kinetic potential energies of a system of interacting electrons, with specific properties of the periodic crystal structure contained entirely in $\hat{V}_{\text{ext}}$.

This equation is still too difficult to solve. In the discussion of the tight-binding model (and equivalently for the nearly-free-electron model), at this point the problem was simplified by approximating electron-electron interactions as simply a screening of the nuclear charge, incorporating them into the periodic potential, $V(\boldsymbol{r})$. Whilst this reasonable for some simple systems, the many assumptions which followed in that discussion mean that the tight-binding approach is simply not sufficient to provide any novel insight into the electronic structures of complex systems which have non-zero electron-electron interactions.

3.3.2 Hohenberg-Kohn theorems

Modern day DFT calculations avoid making the oversimplification of electron-electron interactions through the exploitation of two theorems by Hohenberg and Kohn [128]. Firstly, their work establishes a one-to-one correspondence between the exact ground state electron density, $\rho(\boldsymbol{r})$, of a many electron system, and the expectation value of any physical observable.

$$\langle\Psi|\hat{O}|\Psi\rangle = O[\rho] \tag{3.31}$$

This means that, in principle, all information about the system can be obtained with only knowledge of the ground state electron density, ρ, as long as the form of the functional that maps the electron density to the expectation value for the operator of interest is known. The second theorem by Hohenberg and Kohn considers the case $\hat{O} = \hat{H}$, and on the form of the functionals mapping the electron density to the energy expectation value, the electronic structure.

$$\begin{aligned} E_{V_{\text{ext}}}[\rho] &= \langle\Psi|\hat{H}|\Psi\rangle \\ &= \langle\Psi|\hat{T} + \hat{V}|\Psi\rangle + \langle\Psi|\hat{V}_{\text{ext}}|\Psi\rangle \\ &= F_{HK}[\rho] + \int \rho(\boldsymbol{r})V_{\text{ext}}(\boldsymbol{r})d\boldsymbol{r} \end{aligned} \tag{3.32}$$

Here, $F_{HK}[\rho]$ is the 'Hohenberg-Kohn density functional' defined as above, and $V_{\text{ext}}(\boldsymbol{r})$ is the form of system specific potential, for example the spatially varying periodic potential of a lattice. Like the first two terms in Eqn. 3.30, $F_{HK}[\rho]$ is entirely separate from system specific properties, and so, in principle, there is an expression for $F_{\text{HK}}[\rho]$ that exactly maps the electron density of any system to the expectation values of $\hat{T}+\hat{V}$. Eqn. 3.32 also provides the functional required to relate the ground state electron density to the energy contribution from $\hat{V}_{\text{ext}}$.

This is already sufficient to demonstrate that full ground state electronic structure given by Eqn. 3.32 can be exactly solved, other than the application of the Born-Oppenheimer approximation. By inputting every possible form of $\rho(\boldsymbol{r})$ into Eqn. 3.32, the one that minimizes $E_{V_{\text{ext}}}$ is the one that corresponds to energy contribution of the actual potential $V_{\text{ext}}(\boldsymbol{r})$ and gives the exact ground state energy of an arbitrarily complicated electronic system.

In practice this is of course not possible. Not only is the form of $F_{HK}[\rho]$ not known, but there are infinite possibilities for the formulation of electron densities. Subsequent work by Kohn and Sham [129] outlines a method by which ρ can be exactly calculated, whist removing the need for an explicit form of $F_{HK}[\rho]$.

3.3.3 Kohn-Sham Hamiltonian

By reformulating Eqn. 3.32 such that $F_{HK}[\rho]$ can be written as the sum of other functionals; $T_0[\rho]$, the kinetic energy contribution of a non-interacting electron gas, $V_H[\rho]$, the 'Hartree' contribution giving the universal potential energy contribution, and $V_{xc}[\rho]$, the exchange and correlation functional, it is possible to rewrite the ground state energy functional as a non-interacting electron gas subject to two external potentials describing the underlying ionic lattice and the exchange and correlation effects, with functionals $V_{\text{ext}}[\rho]$ and $V_{xc}[\rho]$ respectively.

The corresponding Hamiltonian to this reformulated ground state energy functional is the *Kohn-Sham Hamiltonian*, written as follows [18, 129]:

$$\hat{H}_{KS} = -\frac{\hbar^2}{2m_e}\boldsymbol{\nabla}_i^2 + \frac{e^2}{4\pi\epsilon_0}\int \frac{\rho(\boldsymbol{r}')}{|\boldsymbol{r}-\boldsymbol{r}'|}d\boldsymbol{r}' + V_{xc} + V_{\text{ext}}, \tag{3.33}$$

where the first and second terms on the right hand side are the contributions from T_0 and V_H, respectively. Solving for the electronic structure is then returned to a matter of solving a seemingly simple eigenvalue problem:

$$\hat{H}_{KS}\psi_i(\boldsymbol{r}) = \epsilon_i\psi_i(\boldsymbol{r}), \tag{3.34}$$

where the eigenvectors, ψ_i, are single particle wavefunctions, of which the N lowest energy wavefunctions can be used directly to exactly formulate the ground state electron density.

$$\rho(\boldsymbol{r}) = \sum_{i=1}^{N}\psi_i(\boldsymbol{r})^*\psi_i(\boldsymbol{r}) \tag{3.35}$$

The work by Kohn and Sham therefore reformulated the functional approach such that the problem can be treated simply as a non-interacting system with a Schrödinger like Hamiltonian, without any further approximations. The complication is now contained within the wavefunctions, ψ_i. Whilst they can be used to find the exact electron density, individually they are purely mathematical objects which do not have physical meaning. These 'Kohn-Sham' orbitals can be transformed into atomic site localised *Wannier functions* however, which are orthogonal across atomic sites and describe the real space electron probability distribution, centred at a fixed point in real space, usually chosen to be an atomic site. Wannier functions are useful for advanced tight binding models [130].

3.3.4 LDA approximation and the self consistency problem

This is still not sufficient to find the band structure, as the form of the electron exchange-correlation operator $\hat{V}_{xc}$ is not known. The second approximation used by DFT is the local-density approximation (LDA), or some variation thereof, where the functional relating the electron density to the expectation value of $\hat{V}_{xc}$, by the Hohenberg-Kohn theorems, can be written as follows:

$$V_{xc}[\rho] \approx E_{xc}^{LDA} = \int \rho(\boldsymbol{r})\epsilon_{xc}(\rho(\boldsymbol{r}))d\boldsymbol{r}; \quad \hat{V}_{xc} = \frac{\delta V_{xc}[\rho]}{\delta \rho}, \tag{3.36}$$

where $\epsilon_{xc}(\rho(\boldsymbol{r}))$ describes a homogeneous electron gas within a volume, V, which is completely isotropic with density $\rho(\boldsymbol{r}) = N/V$. Each infinitesimally small spatial region with constant density contributes to the total E_{xc} by equal amounts. This approximation is most valid for systems with slowly varying potentials. The generalised gradient approximation (GGA) is one variation of this, accounting for the gradient of the density by considering electron density in neighbouring volumes.

This leads to the 'self-consistency' problem. In order to approximate V_{xc} which allows for the determination of $\hat{H}_{KS}$ and the Kohn-Sham wavefunctions, ψ_i, the electron density, ρ, already needs to be known, which requires ψ_i to already be known. This is circumvented by estimating a starting density ρ_n to find a corresponding $V_{xc,n}$ and $V_{H,n}$ allowing to solve for the single particle wavefunctions ψ_n and hence obtain a ρ_{n+1}. The result is fed iteratively through this system until the electron density converges: $\rho_n = \rho_{n+1}$. The eigenvalues can then be found.

3.3.5 Choosing a basis and solving

The Hamiltonian for a many-body electron system in Eqn. 3.29 is now simplified to a series of single particle eigenvalue problems (Eqn. 3.34) with $i = (n, \boldsymbol{k})$ and the Hamiltonian the Kohn-Sham Hamiltonian in Eqn. 3.33 but with an LDA approximation for V_{xc}.

Like for the tight binding model, the form of the single particle wavefunctions, ψ_i, needs to be chosen such that the Bloch condition is satisfied. This can be done by writing each as a linear combination of plane waves,

$$\psi_i = \sum_{p=1}^{P} c_p^i \phi_p. \tag{3.37}$$

Then, in close analogy to the procedure outlined for the tight binding model in Section 2.1.2, by substituting into Eqn. 3.34, premultiplying by $\langle \phi_p |$ and diagonalising, one can deduce the form of the p coefficients c_p^m, and the ground state energy of a given $i = (n, k)$ can be extracted. The form of the Kohn-Sham orbitals is complicated, and to construct them exactly requires basis set of plane waves of infinite size. It is therefore necessary to find a basis set that is simultaneously accurate enough to provide a good approximation to the electronic structure, whilst being small enough such that it can be run without excessive computational effort.

To do this, a K_{max}, or equivalently a cut off energy, is first chosen to limit the region of $E(k)$ space of interest to make P finite. Even then, approximately 10^8 periodic plane waves are required in order to accurately model the potential which evolves over extremely small spatial scales [18]. In practice, this is simplified further by adapting *muffin-tin potentials*, which divide space into two regions separated by a characteristic *muffin-tin radius*, R_{mt}. The near-nuclear region is approximated to atomic wavefunctions, which are then matched strictly at R_{mt} to freely propagating plane waves. There are many variations of this procedure (APW/LAPW etc.), each requiring iterative procedures to find self-consistent eigenvalues and eigenfunctions. This procedure can be further modified by applying 'local orbital' approximations, which either neglect the tightly bound orbitals not involved in bonding, or use a combination of alternative computational methods depending on the orbital type.

This procedure can provide extremely accurate bulk electronic structure calculations for complex correlated electron systems, although band gaps are often underestimated (an artefact of the LDA approximation [131, 132]). For all DFT calculations within this thesis, the cut off momentum, K_{max}, is chosen such that its product with the radius of the muffin-tin potential is exactly 7. Direct comparison with ARPES experiments require that DFT is also sensitive to the surface electronic structure, however.

3.3.6 Surface-slab calculations

In order to calculate the surface electronic structure, a hypothetical periodic system is constructed which simultaneously mimics the bulk structure of the compound of interest as well as the truncation of periodicity at the surface of the real semi-infinite crystal.

A 'slab' of some thickness is taken, where its crystal structure exactly matches the bulk crystal structure of the compound of interest, but is truncated along the vertical axis. These slabs are stacked periodically with regions of vacuum separating each slab to form an infinite, periodic array of slab and vacuum regions. A band structure calculation is then run for this hypothetical compound, producing layer-resolved full electronic structure calculations which include the surface.

In constructing the slab, both the slab and vacuum regions have to be sufficiently thick that the surface behaves as it would in a semi-infinite crystal. It is also necessary to limit the interaction between the simulated surface of interest, and the 'bottom' surface of a single slab. This is achieved by artificially 'passivating' any dangling bonds with hydrogen, and fixing the atomic positions a few layers down from the top surface to their known bulk values, preventing any relaxation near the bottom surface. In general, the more slabs, the more accurately the surface electronic structure will be captured, but the more computationally expensive it will be. The bulk band structure can be bench marked against DFT calculations for real infinite crystals to determine validity, and the resolution can be set by with the density of the 'k-mesh'. The surface slab calculations presented in this work are obtained through tight-binding calculations of a 100-unit supercell, using localised Wannier orbitals obtained from bulk DFT calculations.

Chapter 4

Topological ladders in the transition metal dichalcogenides

The original research contained within this thesis focusses almost entirely on new realisations of compounds hosting topological phenomena within their electronic structures. The introduction of Dirac cones and non-trivial band topology in Chapter 2 already highlighted the relative abundance of topological phases, as well as the many forms in which they take. Naively, the benefits to finding more instances of essentially the same underlying physics can seem evasive. However, unlike those introduced in Chapter 2, the bulk Dirac cones and topological surface states that will be discussed in this Chapter are formed entirely within a single-orbital manifold, i.e. the band crossings that generate the Dirac cones have the same orbital character. This transition to a single-orbital manifold origin is not just a novelty. Chapter 2 showed that, although the topological surface states in e.g. Bi_2Se_3 do have a topological protection, they are susceptible to small changes in the underlying crystal and electronic structures. This is most readily seen by comparing Bi_2Se_3 with sister compound Sb_2Se_3 [69] where the band inversion and therefore the topological surface state do not survive the reduction in the spin-orbit coupling strength between the two compounds. In stark contrast, any topological phases realised within a single-orbital manifold have an enhanced level of protection, as a relative shift of the energetics of two orbital manifolds following some small perturbation becomes inconsequential. This in turn means that topological phases of this form could be general properties of full material classes rather than isolated compounds.

The purpose of this Chapter is to demonstrate these points in the context of the transition metal dichalcogenide family, a diverse compound class known for its extremely wide array of electronic phases and bulk properties.

4.1 Transition-metal dichalcogenides (TMDs)

The transition-metal dicalcogenides (TMDs) are a class of layered compounds with chemical formula MX_2, where $X \in \{S,Se,Te\}$ and M is almost any transition metal in groups IV through X of the Periodic Table. They are quasi-two dimensional, exhibiting highly anisotropic thermal, chemical and electronic properties arising as a result of the van der Waals gaps separating the

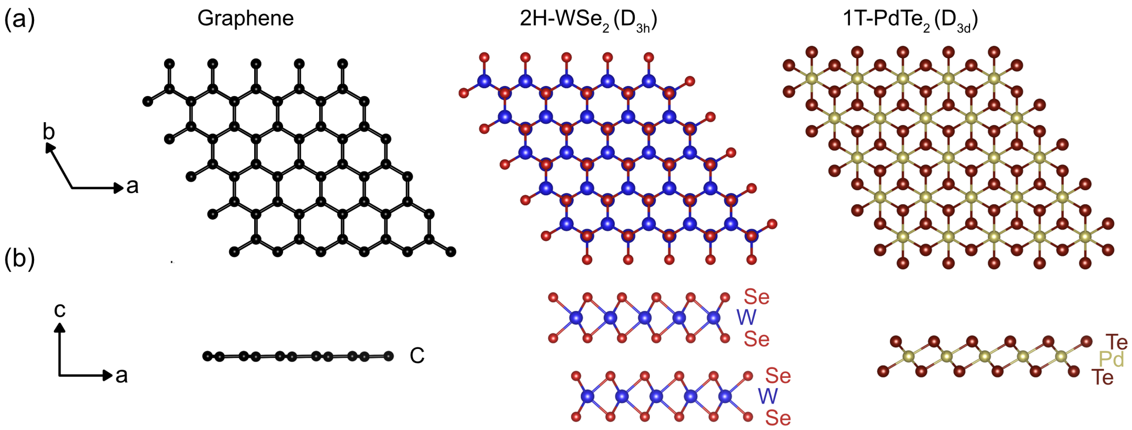

FIGURE 4.1: **Comparison of the crystal structure of graphene with that of the TMD family.** (a) top-view (c-axis projection) structures of graphene, 2H-WSe$_2$ and 1T-PdTe$_2$ from left to right. (b) side-view (b-axis projection) of the same three compounds. The number of layers shown indicates one full repeating unit along the c-axis.

predominantly covalently bonded layers [14, 133]. The 'distorted' 1T'-structured TMDs, 1T'-WTe$_2$ and 1T'-MoTe$_2$ were among the first experimental realisations of Weyl semimetals [134–137], with Fermi arcs in their surface electronic structures. However, the 1T-, 2H- and 3R-structured TMDs (where the number denotes how many layers form one repeating block along the c-axis, and T, H and R indicate the trigonal, hexagonal and rhombohedral structures respectively (see Fig. 4.1)) are not known for their topological phases, but nonetheless have been a cornerstone of condensed-matter physics research for over a decade.

4.1.1 Comparison with graphene

The transition metal dichalcogenides have been studied as early as the 1940s for their applications as machine lubricants [138, 139], but the modern resurgence of interest comes as a direct consequence of the isolation of graphene in 2004 [7, 22]. Graphene, as introduced in Chapter 2, is a single layer of carbon in a honeycomb lattice structure, and is host to Dirac fermions at the K points of its electronic structure. These massless fermions are largely responsible for many of the remarkable properties possessed by graphene, from extremely high electron mobilities [7] to an anomalous integer quantum Hall effect [22].

The Dirac cones in graphene are also an indication of its inherent limitations. The lack of a band gap[1] due to A-B sub-lattice symmetry, coupled with the structure adhering to both time-reversal and inversion symmetries means that controlling charge carriers in any useful way for spintronic applications is extremely difficult.

---

[1] Since graphene is an inversion symmetric two-dimensional material, the Dirac cones here are two dimensional and spin degenerate. The crossing points are therefore unprotected against spin-orbit coupling, which opens small gaps on the order of 10^{-3} meV [56], although this is eclipsed by thermal fluctuations at temperatures above 10^{-2} K.

Figure 4.1 demonstrates how the crystal structures of 2H-structured TMDs (D_{3h} transition metal coordination) share a stark resemblance to graphene, but with some of these symmetry constraints relaxed. Indeed, the electronic structure in the vicinity of the K points of the single-layer variants of the 2H structured TMDs (1H-structure) are well described by the effective Hamiltonian introduced for graphene in Chapter 2.1.3 [52]. Eqn. 4.1 again shows the Hamiltonian derived for the band structure of graphene in the vicinity of the K points, with an additional $\boldsymbol{L}\cdot\boldsymbol{S}$-derived term to approximate the effects of spin-orbit coupling in the 1H-structured TMDs [52].

$$\hat{H} = at(\zeta\sigma_x p_x + \sigma_y p_y) + m\sigma_z - \lambda\zeta\frac{\sigma_z - 1}{2}s^z \tag{4.1}$$

Here, a and t are the lattice spacing and the hopping parameters respectively, with their product proportional to the Fermi velocity. $\zeta = \pm 1$ is again the valley index. λ is the spin-orbit coupling strength, providing a valence band spin splitting of 2λ, and m is the difference in onsite energies for the A and B sub-lattices. The set of Pauli matrices, σ_i, describe electron densities on the A and B sub-lattices.

In graphene, $\lambda \approx 0$ and $m = 0$, leaving only the linear Dirac-like dispersion at the K and K' points. In contrast, the monolayer 1H-structured TMDs do not have an A-B sub-lattice symmetry ($m \neq 0$) and so finite band gaps exist. Moreover, electrons originating form e.g. $6d$-orbitals in W experience a much larger spin-orbit coupling than the electrons deriving from carbon $2p$-orbitals. This acts to simultaneously enhance the size of the band gaps whilst also lifting the spin degeneracy of the valence band maximum (VBM), as permitted by the inversion asymmetric nature of the 1H-structure.

The end result is d-orbital derived conduction and valence bands well described as massive Dirac fermions with strong spin-orbit coupling [14, 52]. There are two copies of the quasi-parabolic valence bands at the K and K' points, offset in energy (Fig. 4.2(b)). The large separation of these valleys in momentum space ensures a robustness against scattering, and therefore the valley index becomes a potentially good information carrier, so long as a process can be identified in which valley carriers respond differently to some external stimulus [52, 140].

Note that the formulation of the spin-orbit coupling term in Eqn. 4.1 indicates a coupling between the spin and valley degrees of freedom. The spin polarisation of the valence bands in monolayer group-VI TMDs is entirely out-of-plane (as indicated by the out-of-plane spin operator, s^z), arising from an effective in-plane electrical dipole inherent to each X-M-X tri-layer block of the crystal structure (see e.g. Fig. 4.1(b)). Time-reversal symmetry relates the valence bands at the K ($\zeta = 1$) and K' ($\zeta = -1$) points, enforcing that the spin-splitting has opposite ordering within each [52]. Much of the resurged interest into transition metal dichalcogenides, especially the monolayer variants of the group-VI semiconducting TMDs, focussed on exploiting this *spin-valley locking* for manipulation of valley carriers.

Several optical absorption and photoluminescence experiments [51, 52, 140, 142, 143] have successfully demonstrated that circularly polarised optical fields can be used to selectively

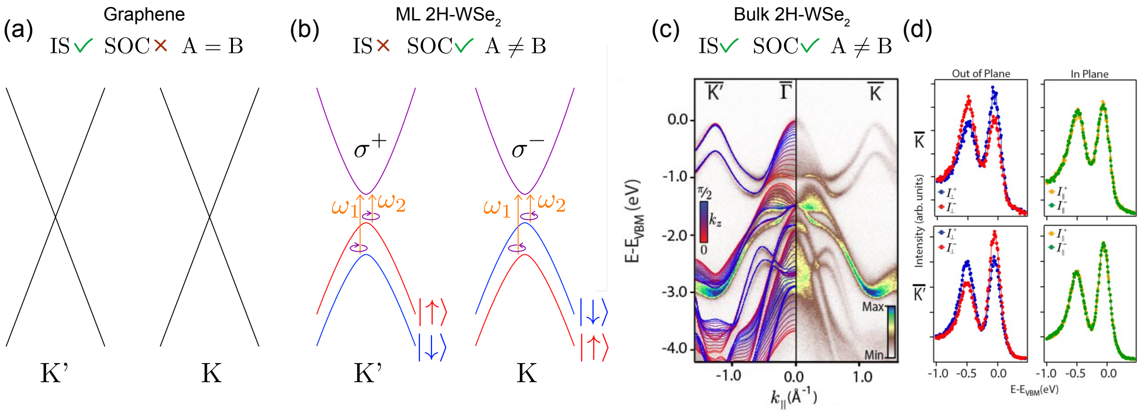

FIGURE 4.2: **Spin-valley locking in group-VI TMDs.** (a) Simplified band structure of graphene. The combination of time-reversal and inversion symmetry (IS) render the band structure spin-degenerate. Sub-lattice symmetry and small spin-orbit coupling results in ungapped crossings at its K points. (b) Simplified band structure for monolayer WSe$_2$. Inversion and sub-lattice symmetries are lost, resulting in a finite band gap with a spin-split VBM. The possible excitations at the K and K' points are indicated. For example, illuminating the sample with fixed energy $h\nu = \omega_1$ circularly-right polarised light (σ^+) will populate the conduction bands at K' with spin-down electrons, with no excitations at K. For σ^-, $h\nu = \omega_1$ photons, the opposite is true. The spin-picture is reversed for $h\nu = \omega_2$. (c) Bulk band structure of 2H-WSe$_2$ as obtained with ARPES and k_z dependent DFT. (d), despite regaining IS, a bulk band polarisation can be observed for the valence band tops at K and K'. (c-d) adapted from [141].

excite only electrons of a single spin species. The matrix elements for an optical transition via the absorption of right (+) or left (−) handed circularly polarised light can be approximated as $|P_{\pm}|^2 \approx A(1 \pm \zeta)^2$, where A is a constant [52].

Fig. 4.2(b) illustrates the consequences of this. For a circularly polarised photons with an energy corresponding to the energetic separation between the deepest binding energy spin-split valence band and the conduction band (ω_1), a choice of right or left hand circular polarisation populates either the conduction band at K with spin up electrons, or the conduction band at K' with spin down electrons. The opposite is true for a photon energy corresponding to the band gap between the top-most valence band and the conduction band (ω_2).

The work in this thesis will focus entirely on bulk transition metal dichalcogenides. For the group-VI family members, their electronic structures stay approximately the same qualitatively when transitioning from monolayer to bulk, with only two notable changes. The valence band maximum is shifted from the K points to the Γ point, giving bulk group-VI TMDs an indirect band gap [51]. The increase in dimensionality in real space also allows for non-zero k_z dispersions in the bulk electronic band structure. The latter change is especially evident near the d_{z^2}-orbital derived VBM at the $\overline{\Gamma}$ point in, for example, WSe$_2$ (Fig. 4.2(c)). The interlayer hopping along the c-axis is significant for these orbitals, resulting in a large k_z dispersion of the corresponding bands in the shallow regions of the valence band structure [14, 83, 141, 144].

More crucially though, the transition from the truncated 1H-structure to the 2H-structures of the bulk compounds restores global inversion symmetry. Surprisingly, the spin-valley locking of their single-layer counterparts partially survives the transition, with spin-sensitive k-resolved probes of electronic structure, such as spin-ARPES, still observing bulk spin polarisations within the valence bands at the K and K' points (Fig. 4.2(d)) [141, 145]. This is possible due to the combination of the extreme surface sensitivity of the experimental probe (discussed in Chapter 3.1.4) and the lack of c-axis hopping between the in-plane d-orbitals from which the bands at the K points are derived from. The electronic wavefunctions in the solid are therefore sufficiently localised that only the local inversion asymmetry of a single X-M-X unit along the c-axis is sampled [146]. Analogous physics has been observed in the metallic TMD $NbSe_2$, [147] and even in chalcogen-derived bands of 1T-TMDs [148, 149].

Modern real world applications for the TMDs are wide ranging. Unlike graphene, they are not chemically inert, making them suitable catalysts for hydrogen production, and their van der Waals gaps are accommodating to alkali metal ions, useful for energy storage devices [14]. Similarly, the 'hidden' spin-valley physics outlined above is just one of many of the bulk electronic properties possessed by this remarkably diverse material family.

4.1.2 Diversity across the TMDs

The TMDs collectively possess a rich array of bulk properties. For example, many TMDs possess *charge-density wave* (CDW) phases [133, 150–155], wherein a small, but long-range, periodic distortion of one or more constituent atoms occurs in reaction to a periodic modulation of the charge density. This enlarges the unit cell, resulting in 'back-folded' copies of bands appearing in the new reduced Brillouin zone, with hybridisation gaps opening in the vicinity of the new zone boundary [156]. These CDW phases are in some cases precursors to superconductivity, intrinsically possessed by a large subset of TMDs.

The disparity in the ground states and properties possessed by the TMDs can be understood only when considering the chemical makeup of these compounds. Although disparate, these properties correlate with both the group of the transition metal and the thermodynamically favoured structural phase [14, 157]. The basic details of the electronic structures of TMDs are the same: In general, the metal d-orbital manifold falls between the anti-bonding and bonding chalogen p-orbital manifolds. Unlike elemental transition metals, the nd-shell is always filled before the $(n+1)s$-shell due to the energetic drop of d-orbital sub-shells in a crystal field [14]. The differences in the compounds then start to arise with progressive filling of the non bonding d-sub shells. Group-VI transition metal dichalcogenides such as $TiSe_2$, have the metal in the d^0 configuration (since the oxidation state of the chalcogen is preferably 2-, leaving the transition metal as 4+), and are hence semiconducting [158]. Naively though, the group-V (d^1) through to group-X TMDs (d^6), should then be metallic.

The deviations from the predictions of this simplified argument can be understood by additionally considering the different structural phases that can be adopted by the TMDs, and, in-particular, the effect of the crystal field on the d-orbital manifold. In the 2H- and 3R- structured TMDs which both possess a trigonal prismatic metallic coordination (D_{3h}), the d-orbital

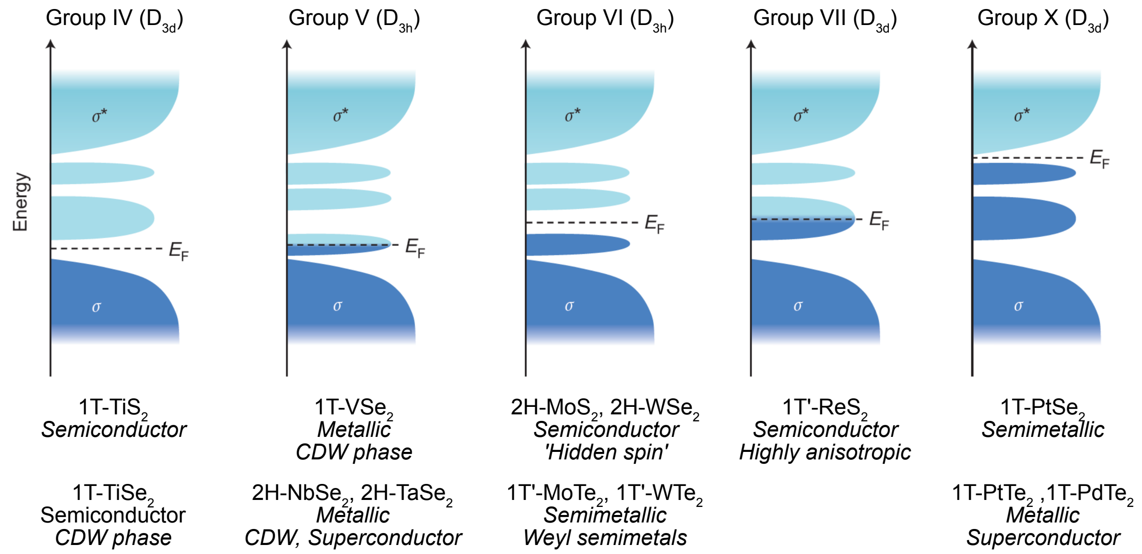

FIGURE 4.3: **Simplified electronic structures of transition-metal dichalcogenides.** Adapted from [14]. Density of states diagrams with the relevant transition metal group and coordination indicated above. Example real compounds and their bulk properties are given in each case. σ and σ^* indicate the bonding and anti-bonding p-orbital manifolds respectively.

manifold is split into a_1 (composed of d_{z^2}), e ($d_{x^2-y^2}$, d_{xy}) and e' (d_{xz}, d_{yz}) orbital subsets from low energy to high. These sub-manifolds can remain energetically separated owing to the M-M bond lengths being up to 25% larger than their elemental counterparts, acting to limit overall orbital overlap in the unit cell [14]. The compounds preferring this structural phase, primarily group-V (d^1) and VI (d^2) TMDs, are therefore metallic and semiconducting respectively. The 1T structured TMDs in the D_{3d} octahedral phase, preferred by group-IV (d_0) and X (d_6) TMDs, have their d-orbital manifold split into two; the higher energy e_g manifold composed of d_{z^2} and $d_{x^2-y^2}$ orbitals, and the lower lying t_{2g} manifold composed of $d_{yz,xz,xy}$ orbitals. The group-X TMDs have an additional complication. By the arguments presented here they should be semiconducting or semimetallic depending on the band gap between e_g and t_{2g} manifolds. In practice however, the group-X (and group-IX) transition metal does not contribute effectively to M-X bonds, instead preferentially forming strong M-M bonds. The electron deficiency of the chalcogen p-orbitals is then partially compensated for by the formation of interlayer and intralayer covalent bonds between p_z and $p_{x,y}$ orbitals respectively [83]. Therefore, both the e_g and t_{2g} manifolds are filled with the chalcogen p-derived anti-bonding manifold only partially filled. (Pt,Pd)Te$_2$ for example, are therefore metallic with the chemical potential lying in the anti-bonding p-orbital manifold [159]. The group-VII TMDs also have a D_{3d} octahedral phase, although these tend to be distorted into a 1T'-structure, leaving them semiconducting with highly anisotropic band structures [160–163].

The above is summarised in Fig. 4.3, where simplified density of states diagrams are presented for several groups of TMDs. For each group, some example bulk compounds are listed with their bulk properties indicated [133, 141, 145, 151–153, 158, 161, 162, 164–168]. Clear parallels can be drawn between TMDs within the same group, or at least across neighbouring groups. Note that whilst this Figure suggests a lack of overlap between chalcogen p-orbital manifolds with the metal d-orbital manifold, this is not true in general. The size of the chalcogen determines the extent of overlap between metal and chalcogen derived bands.

The wide array of emergent phases in these compounds begin to fall into place. For example, the d^0 compound 1T-TiS$_2$ is a small band gap semiconductor owing to the smallest possible choice of both metal and chalcogen [158, 169]. Increasing the degree of overlap of the chalcogen p-orbitals by replacing S with Se results in a smaller indirect-band gap semiconductor, TiSe$_2$. This compound hosts a charge density wave phase, but the hybridisation is extremely k_z dependent owing to the three-dimensional nature of the d-derived conduction bands, unusually resulting in a decrease in the band gap size when cooling through the transition [164].

The group-V, d^1 compounds 1T-VSe$_2$, 2H-NbSe$_2$ and 2H-TaSe$_2$ also have small band gaps or band overlaps between the d-orbital derived conduction and p-orbital derived valence bands. These compounds are metallic, however, with the chemical potential lying towards the minimum of the d-orbital derived conduction bands. This is often a sufficient prerequisite for charge-density wave formation more generally, and indeed the latter two compounds provide very clear CDW signatures in ARPES in the form of large hybridisation gaps between backfolded bands [133, 150–155].

In summary, it is almost solely the role of the transition metal determining the overall structures and properties of the TMDs, while the choice of chalcogen leads only to a decrease (from S to Te) in the band gaps as the larger chalcogen leads, in general, to increased orbital overlap. For the work in this thesis, the roles are somewhat reversed. The focus is on physics derived predominantly from the p-orbital manifold, with the d-orbital manifold playing only a minor, non-crucial, role.

4.2 General mechanism for topological phenomena within a single-orbital manifold

In this Section, a mechanism underpinning the possibility of a simultaneous formation of topological surface states and bulk Dirac cones within the TMDs with undistorted (1T or 2H) structural phases will be overviewed. This mechanism need not be applicable only to the TMDs, although it will be discussed within that context. The toy-model presented in this Section, as well as all density functional theory (DFT) calculations throughout this Chapter were provided by collaborator Dr. M. S. Bahramy at RIKEN and the University of Tokyo.

The unit cell of a 1T-structured TMD (Fig. 4.4(a)) takes the form of an MX$_6$ octahedron. This contains a transition metal in a D_{3d} coordination, and two inequivalent chalcogen atoms, X_1 and X_2. This unit cell has three sub-layers. The central sub-layer is populated solely by the transition metal, M, sitting exactly at the inversion centre ($\boldsymbol{r} = 0$) of the unit cell. The six chalcogen atoms are divided equally between the two sublayers either side, forming triangular planes. These two chalcogen planes have a relative 180° rotation between them, such that a chalcogen X_1 can be mapped onto X_2 by the translation $-\boldsymbol{r} \rightarrow \boldsymbol{r}$, through the inversion centre.

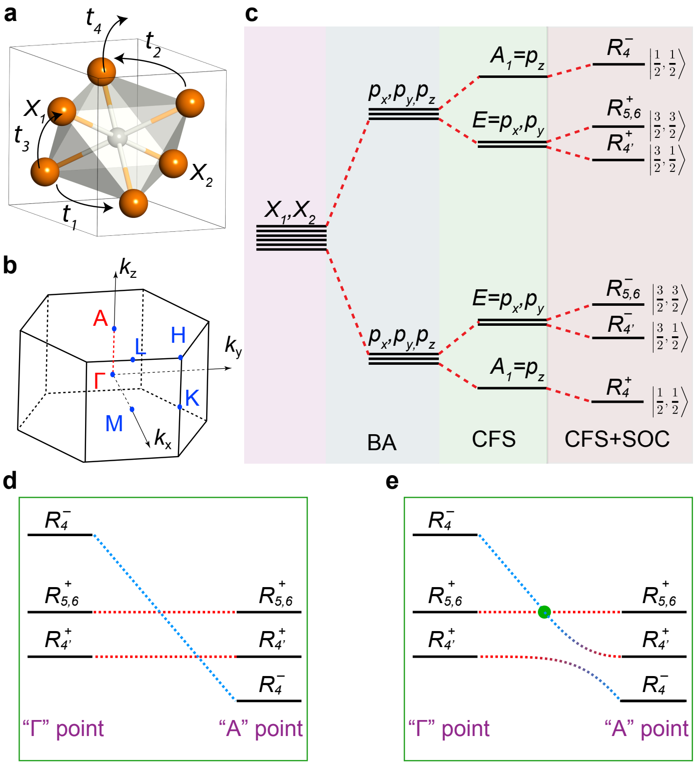

FIGURE 4.4: **Band inversions from p-orbital manifold in the presence of a trigonal crystal field.** (a) Octahedral unit cell of a 1T-TMD. Hopping paths t_1 to t_4 are indicated. The transition metal is neglected. (b) Three-dimensional Brillouin zone of the TMDs without a structural distortion. (c) Three stage degeneracy lifting of six-fold degenerate p-orbital levels from two isolated chalcogen atoms (X_1 and X_2). BA: Formation of bonding and anti-bonding manifolds when bringing two chalcogen atoms (X_1 and X_2) together to form the unit cell. CFS: Trigonal crystal field, C_{3v} separates $p_{x,y}$ and p_z derived bands. SOC: Spin-orbit coupling lifts the remaining degeneracies (neglecting spin). (d) k_z dispersion of the anti-bonding p-orbital manifold in the limit $t_{4\sigma} \gg t_{4\pi} = 0$, neglecting the effect of hybridisation. (e) Hybridisation is additionally considered to the picture in (d).

For the remainder of this Section, the role of the transition metal will be neglected entirely to focus on the p-orbitals of the chalcogen atoms.

The 1T- (D_{3d}) and 2H-(D_{3h}) structured TMDs both possess a C_3 rotational lattice symmetry and three mirror (σ_v) symmetries. Fig. 4.4(c) shows how this combined C_{3v} rotational symmetry, relevant for the p-orbitals, transforms a bonding (B) and anti-bonding (AB) set of triply degenerate (neglecting spin) p_x, p_y and p_z orbitals into A_1 (containing p_z) and E (containing $p_{x,y}$) symmetry subsets. Focussing on the AB manifold, the A_1 subset is at a higher energy than the E subset. Spin-orbit coupling (SOC) lifts the remaining degeneracy of the E subset to produce bands $R^+_{5,6}$ and $R^+_{4'}$, where the superscript ± indicates the parity eigenvalue and the subscript indicates the band symmetry in C_{3v}-space. Additionally, the energy of p_z-derived A_1 is slightly altered and the band is relabelled to R^-_4. This provides the initial relative energy scales for the AB p-orbital manifold. An equivalent picture is formed for the bonding set, although the ordering of A_1 and E is reversed following the application of the crystal-field splitting.

There are two important points to note at this stage. Firstly, the presence of both ± parity eigenvalues here is not necessarily intuitive. Atomic p-orbitals are described always by odd parity wavefunctions. Indeed, if the chalcogen atoms in Fig. 4.4(a) were instead positioned at a centre of inversion symmetry, then all p-orbital derived bands would have negative parity eigenvalues. Instead, the parity eigenvalues are opposite for p_z and $p_{x,y}$-derived bands within the bonding p-orbital manifold, and each band has an opposite parity to its anti-bonding counterpart. This satisfies the requirement for an odd parity total wavefunction for each pair of p-orbitals within the unit cell. It is also clear that, in principle, this parity ordering permits the formation of topologically non-trivial inverted band gaps from crossings of bands both within a single B/AB p-orbital manifold, as well as from the overlap of bands belonging to opposite p-orbital manifolds.

However, there is no change to the relative ordering of these six levels following the inclusion of spin-orbit coupling. This is in contrast to 'conventional' topological insulator phases like that of Bi_2Se_3, wherein band schematics like the one presented here (although also including Bi p-derived bands, see Fig. 2.11) are already sufficient to see that a band inversion between Bi p_z and and Se p_z-orbitals exists at the Γ point of the electronic structure, mediated by spin-orbit coupling [69]. Therefore, any bulk Dirac points and/or topological surface states that form within the chalcogen p-orbital manifolds outlined above must derive from a different mechanism.

The basic details of the band structure of this toy model can be determined by considering the relative hopping strengths within the model unit cell (labeled t_1-t_4 in Fig. 4.4(a)), solely responsible for how each band disperses in the electronic band structure (Chapter 2.1.3). Along the a- and b-axes, intra-layer hopping between X_1 and X_2 in the same a-b plane, labelled $t_{1,2}$, will be higher for p_x and p_y orbitals (π-type hopping) than for p_z orbitals (σ-type hopping), as the extended spatial distribution of the former along the x- and y-axes results in a higher degree of orbital overlap. Conversely, inter-layer hopping can be expected to be larger for p_z-orbitals ($t_{4\sigma}$) than for $p_{x,y}$ orbitals ($t_{4\pi}$), since the wavefunction describing p_z orbitals extends much further into the van der Waals gap than that of the $p_{x,y}$ orbitals.

The bandwidth of p_z-derived bands then ought to be larger than that of the $p_{x,y}$-derived bands along the k_z direction (here the Γ-A line, see Fig. 4.4(b)), with the opposite true for the in-plane $k_{\|}$ directions. If the difference in k_z bandwidths of p_z and $p_{x,y}$ derived bands, owing to the disparity in $t_{4\sigma}$ and $t_{4\pi}$ respectively, is larger than the total energetic separation of p-orbitals imposed by the combination of CFS and SOC, than a pair of crossings between p_z and $p_{x,y}$-derived bands will occur partway along Γ-A in each the B and AB p-orbital manifolds. Fig. 4.4(d) shows the resulting band crossings within the anti-bonding p-orbital manifold when considering k_z dispersion[2]. Note that the simplified model in Fig. 4.4 considers the limit of $t_{4\pi} = 0$, and so $p_{x,y}$-derived bands are completely dispersionless along the k_z direction.

---

[2] Similarly, along the $k_{\|}$ directions, the $p_{x,y}$ bands can cross through the relatively non-dispersive p_z derived bands. For these crossings however, there is no underlying crystal symmetry that can act to protect them as the band crossings will not occur along the rotational axis of the crystal.

The only remaining consideration is possible hybridisations at these crossing points along k_z. The Γ-A line ($k_x = k_y = 0$, changing k_z) is an inclusive set of k-points abiding by the $\hat{C}_{3v}$ rotational lattice symmetry. Following the arguments presented in Chapter 2.2.1, there is therefore a possibility of realising protected crossings (bulk Dirac points) if the wavefunctions describing the crossing bands are orthogonal. Consider the resultant eigenvalues from the operation of the $\hat{C}_{3v}$ rotational symmetry operator on the wavefunctions describing $R_{4'}$, R_4 and $R_{5,6}$, shown in Eqns. 4.2, 4.3 and 4.4 respectively.

$$\hat{C}_{3v}|R^{\pm}_{4'}\rangle = e^{\frac{2\pi i}{3}m_j}|R^{\pm}_{4'}\rangle = e^{\frac{\pi i}{3}}|R^{\pm}_{4'}\rangle \tag{4.2}$$

$$\hat{C}_{3v}|R^{\pm}_{4}\rangle = e^{\frac{2\pi i}{3}m_j}|R^{\pm}_{4}\rangle = e^{\frac{\pi i}{3}}|R^{\pm}_{4}\rangle \tag{4.3}$$

$$\hat{C}_{3v}|R^{\pm}_{5,6}\rangle = e^{\frac{2\pi i}{3}m_j}|R^{\pm}_{5,6}\rangle = -|R^{\pm}_{5,6}\rangle \tag{4.4}$$

$\hat{C}_{3v}$ is a unitary operator as it does not change the magnitude or angle of a vector upon application. Its basis is therefore composed of entirely orthogonal and linearly independent wavefunctions. Wavefunctions which give different eigenvalues under the application of $\hat{C}_{3v}$ must therefore be orthogonal, and the hybridisation matrix between them, $\langle\psi_1|\hat{H}|\psi_2\rangle = E\langle\psi_1|\psi_2\rangle$, must necessarily be zero. Conversely, the eigenfunctions which give the same eigenvalue must be linearly dependent on each other, and therefore the hybridisation matrix element between them non-zero. Table 4.1 can therefore be produced.

$\langle\ \|\ \rangle$	$R^{\pm}_{4}$	$R^{\pm}_{4'}$	$R^{\pm}_{5,6}$
$R^{\pm}_{4}$	$\neq 0$	$\neq 0$	$= 0$
$R^{\pm}_{4'}$	$\neq 0$	$\neq 0$	$= 0$
$R^{\pm}_{5,6}$	$= 0$	$= 0$	$\neq 0$

TABLE 4.1: Hybridisation matrix elements for the crossings of the chalcogen p-derived bands along the k_z direction.

This demonstrates how hybridisation is forbidden for the top crossing point in Fig. 4.4(d), between R_4 and $R_{5,6}$, due to the lack of wavefunction overlap. This crossing point therefore produces a bulk Dirac cone protected by the C_{3v} lattice symmetry. In the cases where the overlap integral is non-zero, such as for the second crossing point in Fig. 4.4(d) between R_4 and $R_{4'}$, a band gap is opened [170]. Although not shown explicitly in Fig. 4.4, a protected crossing and an anti-crossing can also be expected to form within the bonding set of p-derived bands along the k_z axis.

Focussing first on the protected crossings, the enforced degeneracies can be described as three dimensional Dirac fermions, or bulk Dirac points (BDPs). However, unlike the 2D analogues in graphene or the BDPs in, for example, Cd_3As_2 [61, 64], the Dirac cone is tilted along the k_z axis; the magnitudes of group velocities of the two branches making up the Dirac cone are inequivalent along k_z. Tilted Dirac fermions cannot exist in high energy physics as they break Lorentz invariance, and are therefore also known as Lorentz violating Dirac fermions. If the tilt is so severe that the two branches have the same sign of group velocity, then the BDP is referred to as type-II, and in all other cases the BDP is type-I. This is in analogy to the type-II Weyl fermions found to exist in the inversion asymmetric TMDs 1T'-MoTe$_2$ and 1T'-WTe$_2$ [134–137]. In the simple model presented in Fig. 4.4, $t_{4\pi} = 0$, and so the resultant Dirac cone is the at boundary between type-I and type-II. In a real system, the sign of the finite $t_{4\pi}$ will set the type of bulk Dirac cone formed.

Now consider the crossing points between the non-orthogonal R_4 and $R_{4'}$ bands where the hybridisation matrix element is non-zero and so a finite gap can be opened by spin-orbit coupling. For both the bonding and anti-bonding manifolds, these two bands have opposite parities. The resultant anti-crossings therefore have an inversion of parity across them. In a real crystal with a surface, these gaps are required to be populated by topological surface states (Chapter 2.2.2).

In summary, for a given bonding or anti-bonding chalcogen p-orbital manifold in a trigonal crystal field, a bulk Dirac point (BDP), of type-I or type-II, and a parity inverted band gap (IBG) can be simultaneously formed partway along the axis of rotation (here k_z). The topological states will be offset from one another both in energy and k_z. There are only two prerequisites of such a k_z-mediated 'topological ladder'. Firstly, there must be a significant disparity in the hopping strengths, $t_{4\sigma}$ and $t_{4\pi}$, such that the difference in k_z bandwidths of p_z and $p_{x,y}$-derived bands is larger than the combined influence of the crystal-field and spin-orbit coupling strengths. Secondly, C_{3v} rotational symmetry must be present to protect a subset of the subsequent crossing points along k_z.

In the remainder of this Chapter, a combined spin- and angle-resolved photoemission (ARPES) and density functional theory (DFT) study into numerous transition metal dichalcogenides will be presented to assess the validity of model presented above in real systems.

4.3 1T-PdTe$_2$: A model system

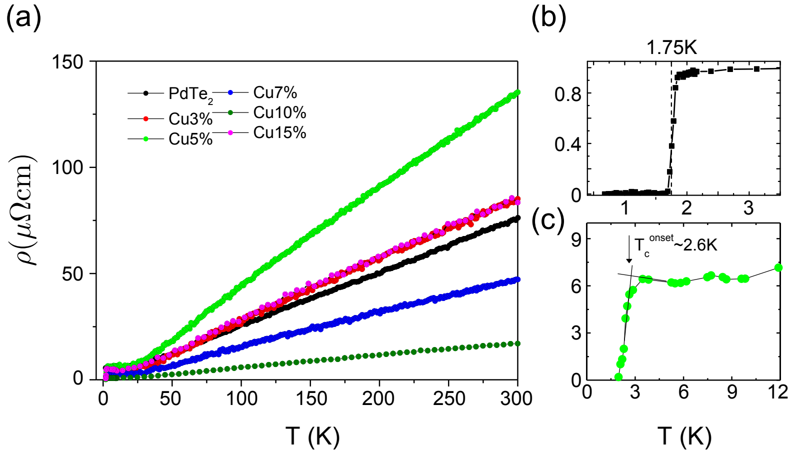

FIGURE 4.5: **Superconductivity in bulk PdTe$_2$.** (a) Transport measurements adapted from [166] for Cu intercalated PdTe$_2$. Similar measurements over a smaller temperature range are presented for (b) pristine PdTe$_2$ from [167] and 5% Cu-intercalated PdTe$_2$ from [166].

The model described in the previous Section entirely neglects the role of the transition metal. The presence of a transition metal atom separating the triangular chalcogen planes is of course an added complexity, and so an ideal testbed is a TMD member wherein the chalcogen p- and transition metal d-orbital manifolds are isolated from one another energetically. As discussed briefly in Section 4.1.2, the group-X TMD $PdTe_2$ fits this description well, as both the t_{2g} and e_g manifolds are filled leaving the AB chalcogen p-derived states electron deficient at the Fermi level. Moreover, the strengthening of interlayer and intralayer bonds between p_z and $p_{x,y}$ bonds respectively acts to enhance the disparity in p-orbital hopping strengths, required for the formation of the BDP and IBG in the toy model presented in Fig. 4.4. $PdTe_2$ also has a large Te-derived spin-orbit coupling strength, which will act to enhance the size of any anti-crossings relative to those in its S and Se containing sister compounds. If the model presented above holds true, then the bulk Dirac points and topological surface states formed should be as apparent in this compound as any other.

$PdTe_2$ is a relatively understudied TMD, even when compared to other metallic TMDs. The group-V metallic TMDs, for example, are well known to exhibit charge-density wave phases [133, 150–153, 165] with an additional superconducting phase emerging at 7.2 K in $NbSe_2$ [157, 171]. $PdTe_2$ does not have a CDW phase but does possess a conventional s-wave superconducting phase with a T_C of 1.7 K [167]. This has been found to be tunable as high as 2.6 K when intercalating Cu between the $PdTe_2$ layers ([166] and Fig. 4.5).

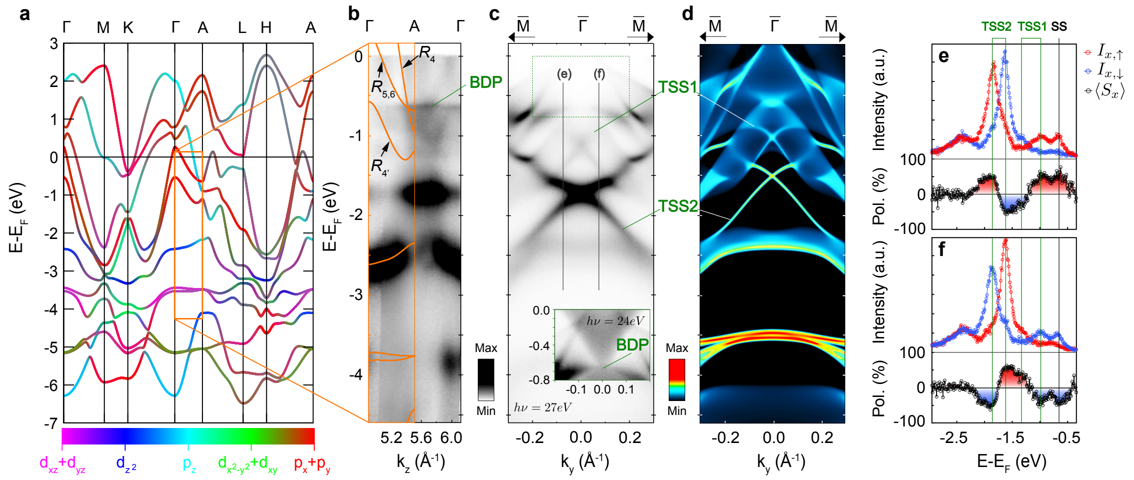

FIGURE 4.6: **Realisation of topological ladders in 1T-$PdTe_2$.** (a) Orbitally projected density functional theory calculations, show the full bulk band structure of $PdTe_2$. (b) Photon energy dependent ARPES (hν=80-132 eV) simulates a k_z dispersion in good agreement with the Γ-A line of the bulk DFT, overlaid and rescaled in energy by a factor of 1.08. (c) ARPES dispersions along the $\overline{\Gamma}-\overline{\mathrm{M}}$ directions at hν=27 eV (24 eV for inset). (d) DFT-based slab calculation covering an equivalent $E(k)$ space as (c) is shown. (e-f), spin-resolved energy distribution curves (EDCs) and the corresponding spin-polarisations (hν=27 eV) are shown for the chiral spin-component $\langle S_x \rangle$ at positions indicated in (c).

Fig. 4.6 serves as an overview of the realisation of the model in this compound, and as a summary of this Section. Orbitally projected density functional theory calculations of the full three-dimensional electronic structure are displayed in Fig. 4.6(a). The chalcogen p-derived

B/AB	label	Γ	A	# crossings
AB	R_4	−	−	5
AB	$R_{5,6}$	+	+	1
AB	$R_{4'}$	+	+	1
B	$R_{5,6}$	−	−	1
B	$R_{4'}$	−	+	2
B	R_4	+	−	2

TABLE 4.2: Band parities, at the Γ and A high symmetry points for the chalcogen p-derived bands in PdTe$_2$, ordered by their binding energy at the Γ point. The number of band crossings that each band is involved inalong the Γ-A line is indicated.

bands, in cyan and red (see colour scale), almost exclusively make up the electronic band structure between $E - E_F = +3$ and -2 eV, with the lower lying metal d-derived bands (in greens and dark blue) gaining dominance only at higher binding energies.

Along the Γ-A line ($k_x = k_y = 0$, changing k_z), the cyan anti-bonding p_z derived band (AB-R_4) forms the conduction band top at the Γ point. It has a significant k_z dispersion, crossing through both the anti-bonding and bonding sets of $p_{x,y}$-derived bands. Focussing on the first two crossings (above E_F), clear parallels can be drawn with the model presented in the previous Section. The first crossing point, with AB-$R_{5,6}$, is ungapped ($E - E_F \approx +1.25$ eV), and the second, with AB-$R_{4'}$, avoided ($E - E_F \approx +1$ eV) consistent with the prediction for an anti-bonding p_z derived state crossing through an anti-bonding $p_{x,y}$ pair (Fig. 4.4(d)). The $p_{x,y}$-derived bands here also show significant k_z dispersion, however, pointing to significant $t_{4\pi}$ in PdTe$_2$. The group velocity of the AB-$p_{x,y}$-derived bands is opposite and almost equal in magnitude to that of the AB p_z-derived band, producing a minimally tilted type-I BDP at their crossing point, protected by the underlying C_{3v} lattice symmetry. The gap opened by the anti-crossing of AB-R_4 with the lowest of the anti-bonding $p_{x,y}$ derived states (AB-$R_{4'}$) does have a parity inversion across it, as can be deduced from the parity eigenvalues of each band calculated for the Γ and A points in Table 4.2. A topological surface state (TSS) should therefore populate the gap.

The situation below the Fermi level is more complex. The total bandwidth of AB-R_4 is sufficiently large that it additionally crosses the bonding set of $p_{x,y}$-derived bands below the Fermi level. The crossing with the highest energy bonding $p_{x,y}$ derived state (B-$R_{5,6}$) ($E - E_F \approx -0.6$ eV) is again protected by the C_{3v} lattice symmetry to give a second BDP, this time of type-II character. Two further inverted band gaps are formed below this. The gap at deeper binding energies is formed from the anti-crossing of the bonding p_z derived state (B-R_4), originating at $E - E_F \approx -2.5$ eV at Γ and dispersing to shallower binding energies to cross the lowest lying bonding $p_{x,y}$ derived state (B-$R_{4'}$). This anti-crossing is large and centred at $E - E_F \approx -1.7$ eV. The remaining anti-crossing, centred at $E - E_F \approx -1$ eV, is an interaction between three bands: A small kink develops in B-$R_{4'}$ towards the A point due to the previously discussed anti-crossing with B-R_4. B-$R_{4'}$, now possessing opposite parity, anti-crosses the AB-R_4 band which approaches from shallower binding energies creating the second inverted band gap below the Fermi level.

In total, therefore, the disparity in bandwidth of p_z and $p_{x,y}$-derived bands is such that the the anti-bonding p_z derived state crosses through all five of the other p-derived bands in this system. The number of bands that a given band crosses through is indicated in Table 4.2.

In summary, a type-I BDP and an inverted band gap are formed above E_F, with a type-II BDP and two further inverted band gaps formed below E_F. Experimentally, probing unoccupied states above the Fermi level is not achievable with conventional spin- and angle-resolved photoemission, and so the type-I BDP and IBG above E_F will be not be verified experimentally in this Chapter. They will, however, be revisited in Chapter 5. First, the type-II BDP will be discussed in full, before moving onto the pair of inverted band gaps below E_F and their associated topological surface states.

4.3.1 Type-II bulk Dirac point in PdTe$_2$

The samples of PdTe$_2$ were grown by chemical vapour transport by the Sasagawa group (Tokyo University of Technology) and cleaved *in situ* at low temperatures. Fig. 4.6(b) displays a E(k_z) dispersion for $k_{||} = 0$, obtained from photon energy dependent ARPES. An inner potential, V_0, of 16 eV best reproduces the periodicity observed within photon energy dependent datasets (see for example Fig. 5.7 in Chapter 5). Despite significant k_z broadening effects, there is general good agreement between the spectral weight and the overlaid DFT calculations when duplicated from Fig. 4.6(a) and rescaled by a factor of 1.08 in energy. Each bulk band within the DFT calculations has a clear companion in the experimental data. Two symmetric BDPs are therefore visible along the A-Γ-A line at a binding energy of $E - E_F = -0.65$ eV in experiment. Note that if Fermi arcs exist between these bulk Dirac points, they would not naively be expected to show signatures in the surface Brillouin zone for the natural (001) cleavage plane, as the two BDPs along A-Γ-A project onto the same point ($\overline{\Gamma}$). However, there is a seemingly non-dispersive state which is pinned to the energy of the bulk Dirac point in Fig. 4.6(b), consistent with a surface localised state dispersing through the BDP. This state will be revisited below.

The tilt of the Lorentz violating type-II bulk Dirac cones along k_z is observed in Fig. 4.6(b), but along in-plane directions, type-I and type-II bulk Dirac cones are indistinguishable. This is demonstrated in Fig 4.7, which shows DFT calculations along a direction parallel to the $\overline{\mathrm{M}}$-$\overline{\Gamma}$-$\overline{\mathrm{K}}$ path for a series of k_z. At $k_z = 0.854\frac{\pi}{c} = k_{z,D}$, the Dirac point is formed, symmetric about the $\overline{\Gamma}$ point. The distinguishability between the two types comes only when tracking the BDP-forming bands when moving away from $k_z = k_{z,D}$. Away from this k_z, the two bands which form this crossing (labelled with *) disperse together to shallower (deeper) binding energies for more positive (negative) k_z. For a type-I BDP formed at the same $k_{z,D}$, the in-plane DFT calculations would look identical at $k_z = k_{z,D}$, but the two branches would disperse in opposite directions away from this, giving a point-like k_x, k_y, k_z constant energy contour, unlike the connected electron and hole pockets observed for this system in Fig. 4.7(e).

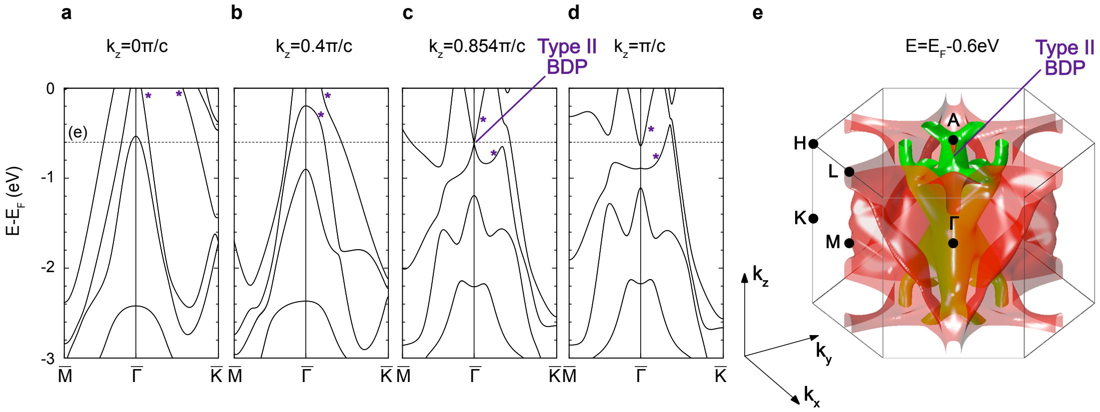

FIGURE 4.7: **Bulk DFT calculations of the type-II Dirac point in PdTe$_2$.** (a-d) in-plane DFT calculations of the bulk Dirac point and neighbouring bulk bands for a series of k_z. The bulk Dirac point is formed in (c). (e) Three-dimensional constant energy contour, at the binding energy of the BDP formation. The type-II BDP is labeled.

The evidence from calculations that this crossing is protected and gives rise to a type-II BDP is compelling, but intrinsic k_z broadening in ARPES means that experimental evidence of protected crossings along k_z is less clear. Indeed, here only the top half of Dirac cone is clearly resolvable (Fig. 4.6(c) inset and Fig. 4.8), partly due to the presence of additional surface surface states, but also due to the more rapidly k_z-dispersing bulk band that forms the lower branch of the Dirac cone relative to the band which forms the upper branch of the Dirac cone (seen by comparing Fig. 4.7(c) and Fig. 4.7(d), for example). Sample dependent factors such as an in-plane uniaxial strain, which would act to break the C_{3v} symmetry and gap these crossing points, would be missed by calculations. These possibilities can be dismissed by considering the resulting form of the bulk Dirac cone following the opening of a hybridisation gap. As when transitioning from Dirac cones in graphene to the CBM and VBM at the K-points of 1H-TMDs, the bands forming Dirac points should lose their linear dispersion, instead adopting a more parabolic description.

The top branch of a bulk Dirac cone, with radius at the Fermi level, k_R, and band minimum, E_{min}, should disperse linearly in accordance with the Dirac equation:

$$(E-E_F)_{\mathrm{Dirac}} = \sqrt{\left(\frac{E_{\mathrm{min}}k_y}{k_R}\right)^2 + \left(\frac{E_{\mathrm{min}}k_x}{k_R}\right)^2} - E_{\mathrm{min}}, \tag{4.5}$$

where the k_x and k_y directions are again taken to be along the $\bar{\Gamma}$-$\bar{\mathrm{K}}$ and $\bar{\Gamma}$-$\bar{\mathrm{M}}$ directions respectively. In contrast, an electron-like band with an equal Fermi level radius and band minimum, will disperse more similarly to that of a paraboloid,

$$(E-E_F)_{\mathrm{Parabola}} = \frac{E_{\mathrm{min}}k_y^2}{k_R^2} + \frac{E_{\mathrm{min}}k_x^2}{k_R^2} - E_{\mathrm{min}}. \tag{4.6}$$

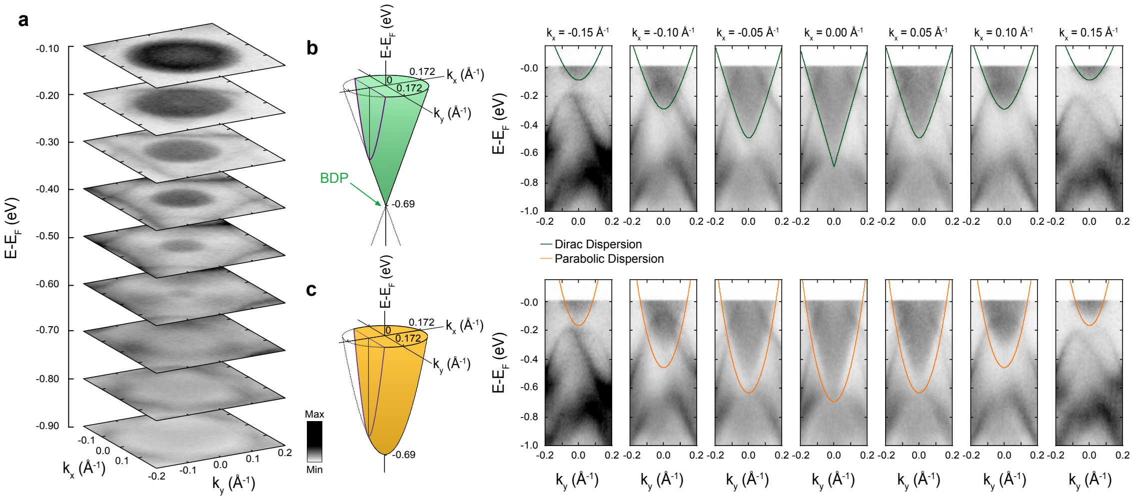

FIGURE 4.8: **Experimental verification of a bulk Dirac fermion in 1T-PdTe$_2$.** (a) Constant energy contours (hν=24 eV) taken over the range of the bulk Dirac cone. (b-c) ARPES dispersions ($E - E_F(k_y)$) where $k_y \parallel \Gamma$-M, moving k_x. Dirac and parabolic dispersions are overlayed in (b) and (c) respectively, where the band minimum is -0.69eV and the radius at E_F is $k_R = 0.172\text{Å}^{-1}$ in each case.

Fig. 4.8 displays in-plane dispersions, ($E - E_F(k_y)$), at a series of k_x as probed by ARPES. Both equations 4.5 and 4.6 are overlaid. It is clear that the former much better matches the observed spectral weight than the latter, validating the Dirac dispersion of the bulk Dirac cone.

Together, these observations provide strong experimental evidence for the presence of type-II bulk Dirac points in 1T-PdTe$_2$. Outside of PdTe$_2$ and the other group-X TMDs PtSe$_2$ and PtTe$_2$ (Chapter 5, [83, 172–177]), very few compounds have been experimentally verified to host type-II Dirac fermions, making these compounds apparently rare platforms in which to study such fermions which cannot exist in high-energy physics.

4.3.2 Topological surface states and resonances in PdTe$_2$

Referring back to the k_z dispersion in Fig. 4.6(b), non-dispersive regions of spectral weight can be seen within the band gaps of the bulk DFT calculations. Most prominent is the two dimensional spectral weight at $E - E_F = -1.74$ eV. This is centred in the larger of the two inverted band gaps formed below the Fermi level, formed from the anti-crossing of the bonding p_z-derived state (B-R_4) and the lowest bonding $p_{x,y}$-derived band (B-$R_{4'}$). The lack of dispersion of this band along k_z, and its absence in the bulk DFT calculations, together provide strong evidence that it is surface derived. Moreover, its location within the inverted band gap strongly suggests a topological origin for this surface state. Indeed, when performing ARPES dispersions along the in-plane directions in which surface states are permitted to disperse, the state exhibits a Dirac dispersion with its Dirac point at at $E - E_F = -1.74$ eV. Fig. 4.9 demonstrates the full conical dispersion of the topological surface state through a series of constant energy $k_x - k_y$ contours over the energy region covered by the TSS. This state, referred to as TSS2 for the rest of this thesis, is captured well by DFT-based slab calculations presented

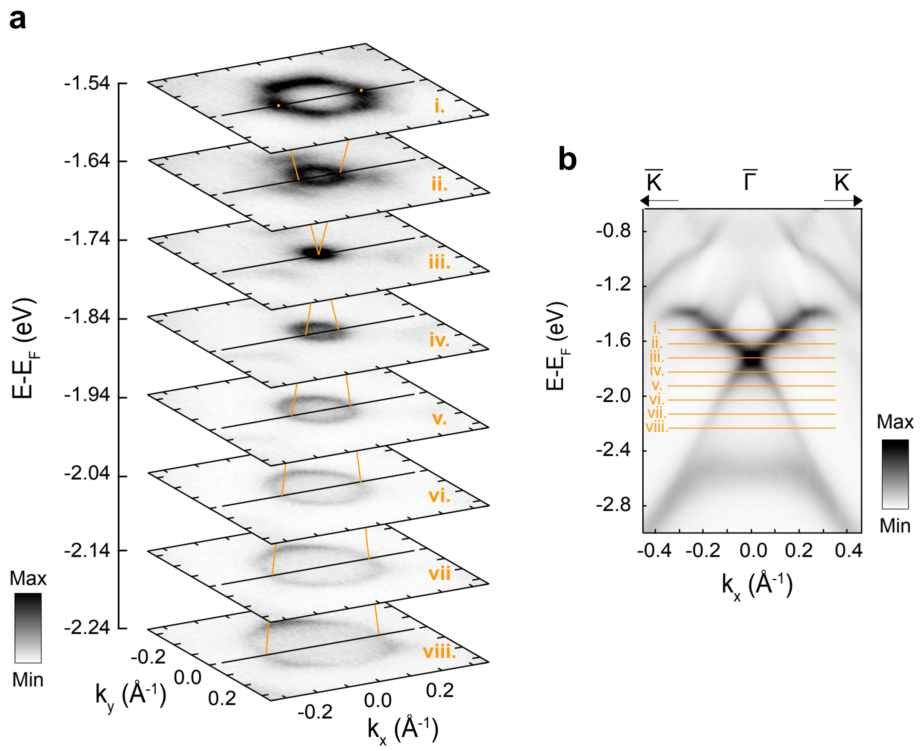

FIGURE 4.9: **Conic dispersion of TSS2.** (a) Constant energy $k_x - k_y$ contours over an energy range covered by TSS2. Energies are indicated in panel (b), which shows the energy dispersion of TSS2 along the $\bar{\Gamma}-\bar{\mathrm{K}}$ direction. A photon energy of $h\nu = 24$eV was used.

in Fig. 4.6(d), again showing a clear Dirac cone dispersion. Altogether, this verifies both the topological nature of the surface state and the topologically non-trivial nature of the highest binding energy inverted band gap. This TSS has been previously identified in [178], although its k_z mediated origin not explored.

Fig. 4.9 also highlights a prominent hexagonal warping of TSS2. Below the Dirac point, this is entirely consistent with that predicted from a higher order $\boldsymbol{k}\cdot\boldsymbol{p}$-derived Rashba Hamiltonian [78], as described in Chapter 2.2.3. The warping is minimal close to the Dirac point, but clear vertices are developed along the $\bar{\Gamma}$-$\bar{\mathrm{M}}$ (here k_y) direction. Above the Dirac point, the hexagonal warping develops over a much smaller energy range, consistent with the reduced group velocity of the bands above the Dirac point. Surprisingly though, the direction of warping has switched, with the vertices instead aligned along the $\bar{\Gamma}$-$\bar{\mathrm{K}}$ (here k_x) direction. A switch of hexagonal warping across a Dirac point cannot be explained by a warping model of the type discussed in Section 2.2.3. Instead, this is a consequence of *small k_z projected bandgaps*, a subject that will be returned to in detail in Chapter 5.

The topological surface state residing in the shallowest of the two inverted band gaps below E_F, henceforth referred to as TSS1, is much more subtle. Again referring to the bulk DFT calculations along the Γ-A direction in Fig. 4.6(a, b), this band gap does not survive the k_z projection to the two dimensional surface Brillouin zone. This means that any topological state residing in this gap will be energy degenerate with bulk bands. It is hence better described as a topological surface resonance (Chapter 2.1.4). Consequently, this state will have a more

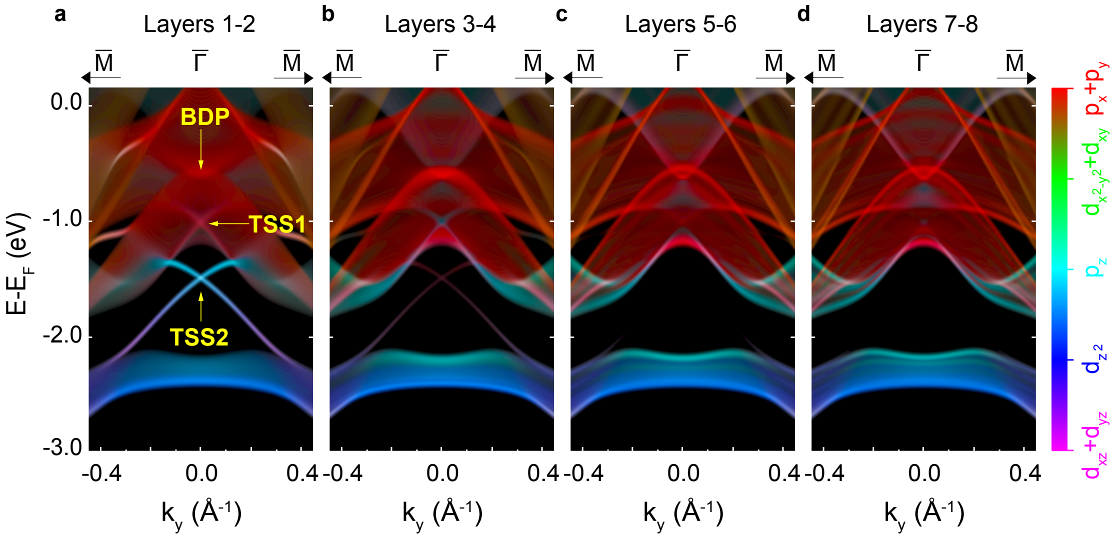

FIGURE 4.10: **Layer-dependent orbitally projected DFT-based surface slab calculations for $PdTe_2$.** The surface state TSS2 is completely absent by layer 5-6 whereas the surface resonance, TSS1, is not.

spatially extended wavefunction than that of a true surface state. Fig. 4.10 demonstrates this explicitly through the presentation of layer-dependent, orbitally-projected DFT-based surface slab calculations. TSS2 has lost almost all intensity by layers 3-4 (Fig. 4.10(b)), but signatures of TSS1 persist through layers 5-6 (Fig. 4.10(c)).

Experimentally, although TSS1 should still be two-dimensional and present for all k_z, its spectral weight can be expected to be at a maximum when the k_z integration has the largest contribution from a k_z value corresponding to the local band gap. For example, at a photon energy hν =27 eV, as in Fig. 4.6(c), the state is clearly resolved, but for $h\nu = 24$ eV (Fig. 4.9), only diffuse bulk bands are visible in its place. Despite this added complexity, both experiment and calculations clearly demonstrate a Dirac like dispersion with the Dirac point centred at the energy of the shallowest energy inverted band gap below the Fermi level.

Chapter 2.2.2 showed how topologically protected surface states need necessarily to carry a chiral spin polarisation, switching both above and below the Dirac point, and with -k to k in accordance with time-reversal symmetry. Spin-resolved ARPES therefore has the capability to provide an additional conformation for the topological nature of TSS1 and TSS2. Fig. 4.6(e,f) present spin-resolved energy distribution curves (EDCs) for the k-points indicated in Fig. 4.6(c), each cutting through two legs of both TSS1 and TSS2. Here, the $\langle S_x \rangle$ (chiral) component of spin is parallel to the $\bar{\Gamma}-\bar{\mathrm{K}}$ direction, as determined by the experimental geometry. Starting at low binding energies and working towards E_F (left to right in Fig. 4.6(e,f)), there is a clear relative up-down-down-up ordering of the four legs of the two topological surface states. TSS2 has a counter-clockwise (CCW) chirality below its Dirac point, switching to clockwise (CW) above. The opposite is true for TSS1. Fitting these EDCs with Gaussian broadened Lorentzian functions to account for experimental resolution, and incorporating a Shirley background, returns magnitudes of 92±14 % and 73±16 % for the chiral-polarisation of the upper and lower legs of TSS2 respectively.

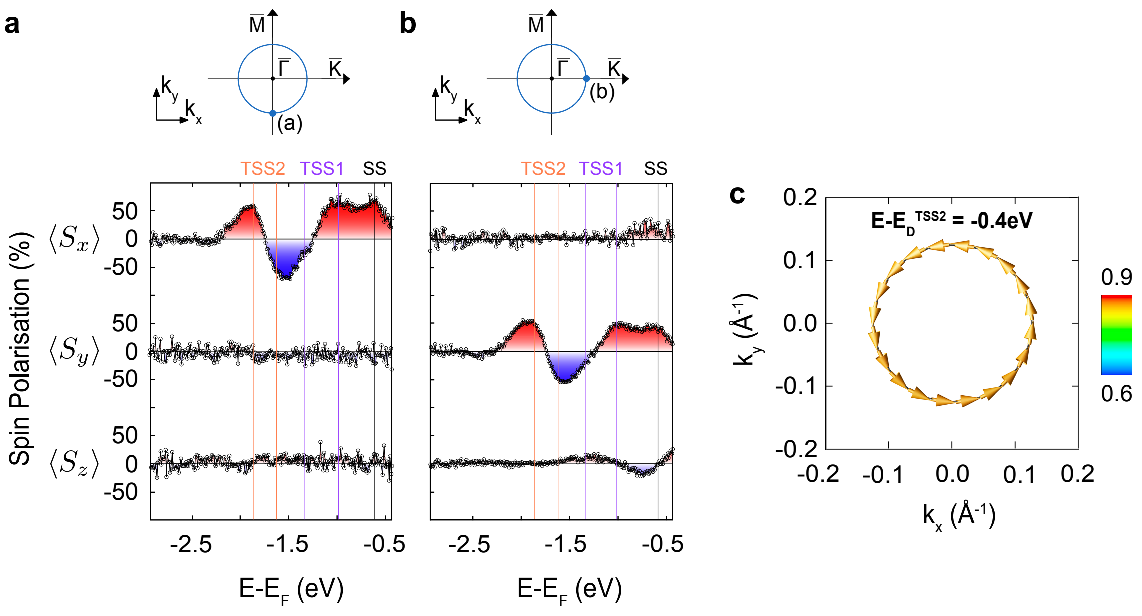

FIGURE 4.11: **Determining the chirality of TSSs in PdTe$_2$ through spin-resolved ARPES and first-principles calculations.** (a-b) Three-component spin polarisations extracted for EDCs measured (a) along the $\overline{\Gamma}-\overline{\mathrm{M}}$ and (b) along the $\overline{\Gamma}-\overline{\mathrm{K}}$ directions of the surface Brillouin zone, at locations (k_x, k_y) = (0, -0.094$\frac{\pi}{a}$) and (0.094$\frac{\pi}{a}$,0) respectively ($h\nu$ =27 eV). (c) CCW chirality of the lower legs of TSS2 as provided by calculations at an energy 0.4 eV below the DP of TSS2.

Fig. 4.11 shows more completely the dominant chirality of these spin textures. Three component spin-EDCs performed at a position $(k_{\overline{\Gamma}-\overline{\mathrm{K}}}, k_{\overline{\Gamma}-\overline{\mathrm{M}}}) = (0, -0.094\frac{\pi}{a})$, again shows a clear non-zero chiral spin component, $\langle S_x \rangle$, as well as additionally demonstrating that the radial (here $\langle S_y \rangle$, parallel to the $\overline{\Gamma}-\overline{\mathrm{M}}$) and out-of-plane, $\langle S_z \rangle$, components are equal to zero. Note that both the radial and out-of-plane components are enforced to be zero for $k_{\overline{\Gamma}-\overline{\mathrm{K}}} = 0$ in accordance with the mirror line defined by the $\overline{\Gamma}$-$\overline{\mathrm{M}}$ direction, consistent with the observation here.

Repeating the measurements for a position $(k_{\overline{\Gamma}-\overline{\mathrm{K}}}, k_{\overline{\Gamma}-\overline{\mathrm{M}}}) = (0.094\frac{\pi}{a}, 0)$, however, shows that whilst the chiral spin-component (now $\langle S_y \rangle$) still dominates, there additionally exists a relatively small out-of-plane spin canting along the $\overline{\Gamma}-\overline{\mathrm{K}}$ direction. As outlined in Chapter 2.2.3, this is consistent with the hexagonal warping of these surface states (see for example Fig. 4.9). The absolute chiralities of these spin textures are consistent with that obtained by calculations. Fig. 4.11(c) for example demonstrates a CCW chirality of the lower legs of TSS2. Together these observations verify the predominantly in-plane momentum-locked chiral spin textures of TSS1 and TSS2. The seemingly non dispersive state at the energy of the BDP mentioned earlier also shows a dominant, CCW chiral spin polarisation in EDCs presented in Fig. 4.6 and Fig. 4.11 at $E-E_F \approx -0.6$ eV. The detailed origin and band dispersion of this surface state will be discussed in Chapter 5.

This work therefore establishes that 1T-PdTe$_2$ is an excellent framework in which to experimentally realise the model presented in the previous Section, containing extremely rich bulk and surface electronic structures owing to a series of k_z mediated band dispersions within its

Te p-orbital manifold. In this compound, the 'topological ladder' centred at $\overline{\Gamma}$ and composed of the type-II BDP, TSS1 and TSS2 is aided by the strong spin-orbit coupling strength of Te and the relative isolation of chalcogen and transition metal-derived orbital manifolds. In the remainder of this Chapter, it will be made clear that the removal of either or both of these factors does not prevent the formation of the topological ladder, although its signatures become more subtle.

In the introduction to this Chapter it was stated that topological phases formed within a single-orbital manifold should persist across entire material families, owing to the added level of protection against changes in the relative energetic separations of orbital manifolds. Indeed, concurrent works have shown that the bulk Dirac cone and two topological surface states below E_F shown above are also present in the group-X TMDs $PtSe_2$ (Chapter 5 and [83, 173, 174]) and $PtTe_2$ [172], despite the changes to the transition metal and/or a reduction of spin-orbit coupling strength. The focus shifts now to TMDs with varied crystal structures, and in-particular to a deviation away from the D_{3h} metallic coordination of both the 1T-TMDs and the toy model presented in Section 4.2. Firstly, the transition to a 2H crystal structure will be discussed.

4.4 2H-WSe_2: Doubling the unit cell

The mechanism outlined at the start of this Chapter uses a single octahedral unit cell as its basis, only appropriate for the 1T-structured TMDs. Evaluating whether or not topological ladders can also exist in the 2H-TMDs first requires the consideration of the changes to mechanism driving the k_z-mediated band inversions imposed by the expansion of the unit cell and the altered transition-metal coordination.

4.4.1 Changes to BDP-TSS pair forming mechanism

The crystal structures of a 1T- and 2H- TMD are compared in Fig. 4.1. The unit cell of a 1T-TMD contains two inequivalent chalcogen atoms which each provide three p-derived bands, giving a total of six chalcogen p-derived bands across the bonding and anti-bonding manifolds. A single unit cell of a 2H-TMD is constructed from similar X-M-X tri-layer blocks, but there are now two such trilayers within the unit cell. Unlike in the 1T-TMDs, there is no relative rotation of the three-fold symmetric chalcogen sub-layers either side of the central transition metal plane within a single X-M-X unit. Instead, the second X-M-X unit has both of its chalcogen planes 180° rotated relative to the chalcogen planes in the first X-M-X unit. The total unit cell is therefore still inversion symmetric, but there are now four inequivalent chalcogen atoms contained within.

In analogy to the discussion of charge density wave phases in Section 4.1.2, a change of the unit cell from 1T to 2H doubles the periodicity of the system along the c-axis, halving the size of the Brillouin zone along k_z. Each of the chalcogen-derived bands can therefore be expected to be effectively back-folded along k_z direction, with respect to a 1T-structure. Although the transition metal in this 2H-structure now has a D_{6h} coordination, the C_{3v} lattice symmetry is retained. The orthogonality relations outlined in Table 4.1 still hold true, and so one can simply expect twice as many inverted band gaps and bulk Dirac cones for sufficiently dispersive p_z-derived bands.

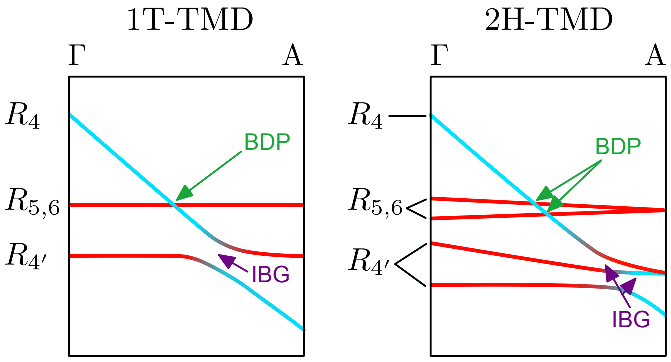

$$\langle R_4 | R_{4'} \rangle \neq 0$$
$$\langle R_4 | R_{5,6} \rangle = 0$$

FIGURE 4.12: **Schematic illustration of BDP and IBG formation in a 2H-TMD.** Illustrated band dispersions are presented for both a 1T- and 2H-structured TMD in the limit $t_{4\pi} = 0$. In the 1T case, a BDP-IBG pair is produced from the anti-bonding chalcogen p-manifold. In the 2H-case, the doubling of $R_{5,6}$ and $R_{4'}$ results in twice as many band crossings.

To see this visually, the schematic diagram in Fig. 4.12 illustrates the k_z dispersion of an anti-bonding set of chalcogen p-bands for both a 1T- and 2H-structured compound. Both $R_{5,6}$ and $R_{4'}$ are back-folded about the A point in the case of the 2H-structure. In the case where the interlayer hopping of p_z-orbitals is larger than that of the $p_{x,y}$-orbitals ($t_{4\sigma} > t_{4\pi} = 0$), and the p_z-derived band has a bandwidth along k_z larger than the combined crystal field and spin-orbit derived degeneracy lifting, band crossings will occur. In a 2H-structure, therefore, there are two crossings of R_4 with $R_{5,6}$ to produce two closely spaced bulk Dirac cones. Recall that in the 1T-case the type of BDPs formed was set by the sign of the interlayer hopping between $p_{x,y}$ orbitals ($t_{4\pi}$). Here, the two closely spaced BDPs here are strictly fixed to be of opposite types due to the requirement of degeneracy of the back-folded bands at the A point: The two bands forming the $R_{5,6}$ pair have opposite group velocities, and so the ordering of BDP types is left dependent on the group-velocity of the R_4 band.

Similarly, the $R_{4'}$ band is duplicated, and two closely spaced inverted band gaps should be created from the crossing of R_4 with the $R_{4'}$ pair, and each should be populated with its own topological surface state. A second major challenge to the model is that, unlike the group-IX and X TMDs, all of the 2H-TMDs have significant d- and p-band overlap (Section 4.1.2 and [14]). This acts to further reduce $t_{4\pi}$, giving the $p_{x,y}$ derived bands a much flatter dispersion along the k_z axis, reducing the size of any band gaps produced. These two complications together provide a test for the robustness of the BDP-TSS forming mechanism outlined in Section 4.2.

4.4.2 Type-I and type-II BDPs and TSSs in WSe$_2$

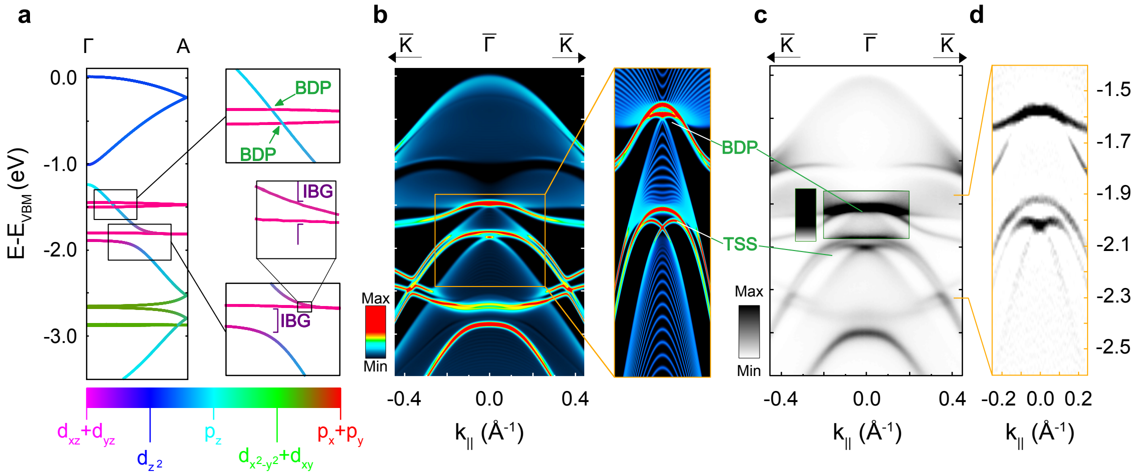

Figure 4.13: **Realisation of two BDPs and two IBGs in 2H-WSe$_2$.** (a) Orbitally projected DFT calculations for the Γ-A direction in WSe$_2$. The band crossings producing BDPs and IBGs are reshown in insets. (b) Surface slab calculations along the $\bar{\Gamma}$-$\bar{\mathrm{K}}$ direction. (c) ARPES ($h\nu$ =49 eV, CL+CR pol.) dispersion over an equivalent range. Inset shows the same data with altered colour contrast only. (d) Curvature analysis of the data shown in (c).

The strongly spin-orbit coupled semiconductor, 2H-WSe$_2$, is chosen as the basis for the study of potential k_z-mediated topological ladders in 2H-structured TMDs. Orbitally projected DFT calculations for the Γ-A line of 2H-WSe$_2$ are shown in Fig. 4.13. Consistent with the simplified TMD electronic structures presented in Fig. 4.3 and [14], the valence band top is composed almost entirely of W d_{z^2} character bands. These persist down to a binding energy of $E - E_F = -1$ eV. The band directly below this, originating at $E - E_{\mathrm{VBM}} \approx -1.2$ eV at the Γ point, is a chalcogen p_z-derived band (R_4). This disperses steeply downwards to cross through two pairs of pink-coloured bands, centred at $E - E_F \approx -1.4$ eV and -1.9 eV. These are the $p_{x,y}$ derived bands, $R_{5,6}$ and $R_{4'}$ respectively, each back-folded along the Γ-A line due to the effective doubling of the unit cell relative to the 1T-structured TMDs. Unlike in PdTe$_2$, they are almost entirely dispersionless, consistent with the significant orbital character contribution from $d_{xz} + d_{yz}$ orbitals. Despite this, the first pair of crossings between R_4 and $R_{5,6}$ produces two closely spaced BDPs of type-II (type-I) character for the upper (lower) protected crossing. Fig. 4.13(b-d) shows both DFT based slab calculations and ARPES dispersions along the $\bar{\Gamma}$-$\bar{\mathrm{K}}$ direction. The close spacing of the two BDPs means that only the linear dispersion forming the lower branch of the type-I Dirac cone is clearly resolvable experimentally.

The second crossing pair in Fig. 4.13(a) produces closely spaced inverted band gaps. The lack of dispersion of the $R_{4'}$ bands means the band gaps are extremely small, with the shallower binding energy anticrossing on the order of 1 meV. The higher binding energy anti-crossing gives a larger gap tens of meV wide, however, centred at $E - E_{\mathrm{VBM}} \approx -1.9$ eV and focussed on below.

Whilst the $p_{x,y}$-derived bands are almost entirely dispersionless along the k_z direction, they have large bandwidths along $k_{||}$, dispersing steeply to higher binding energies away from $\bar{\Gamma}$.

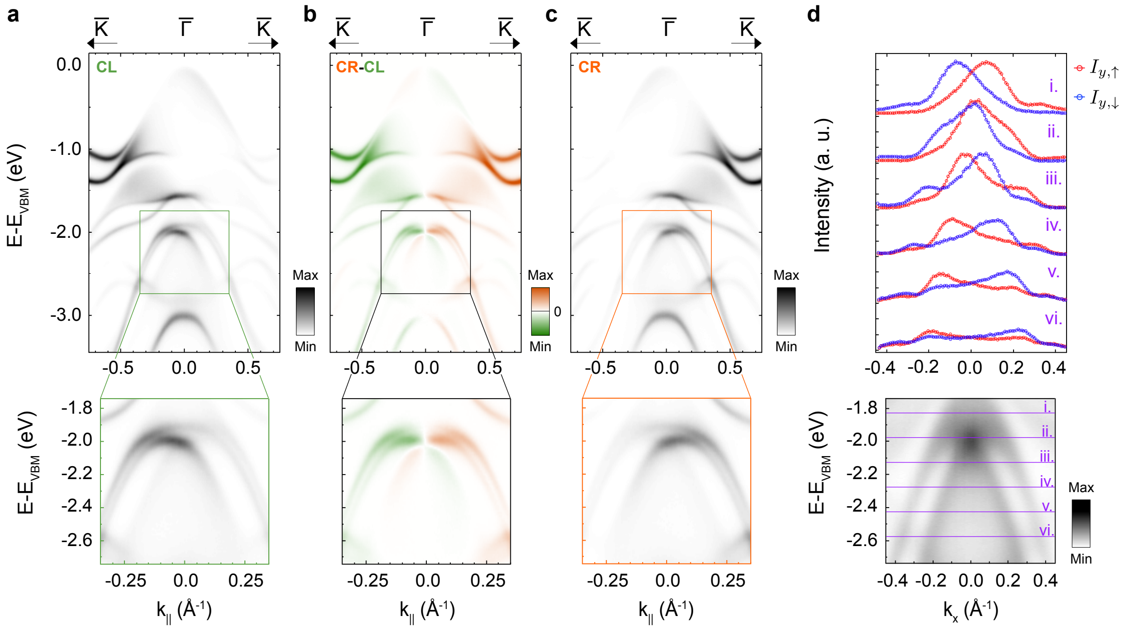

FIGURE 4.14: **Circular dichroism and spin-resolved ARPES of a TSS in WSe$_2$.** ARPES dispersions performed with circularly left (CL, a) and circularly right (CR, c) polarised light ($h\nu$ =49 eV). The resultant dichroism (CR-CL) is shown in panel (b). Insets show the region occupied by the largest TSS. (d) Spin-resolved MDCs for the chiral spin component, over the energy range indicated in the inset.

Therefore, although the inverted band gap is small at $\bar{\Gamma}$, the resultant TSS can bridge the two parity inverted bands at much higher binding energies. The result of this is a TSS with Dirac point centred within the energy of the inverted band gap formed along Γ-A, but with legs that follow the rapid in-plane dispersion of the surrounding bulk bands. Together, this TSS, clearly resolved in DFT based slab calculations and in experiment (Fig. 4.13(b) and Fig. 4.13(c) respectively) appears almost Rashba-like in appearance. Fig. 4.13(d) shows the result of curvature analysis[3] of the data in (c) to improve visibility. The unconventional dispersion here of the TSS is another consequence of the small k_z projected band gaps that inevitably arise in compounds hosting k_z mediated topological ladders. Since surface states typically avoid becoming resonant with bulk bands where possible, the legs of the surface state here instead follow the small k_z projected paths down to higher binding energies.

Experimentally, the spectroscopic signatures of the TSS dwelling in the larger IBG can be enhanced by using circularly polarised light. Fig. 4.14 shows energy dispersions performed with circularly left (CL) and circularly right (CR) polarised light in panels (a) and (c) respectively. This allows for the selective excitation of just one branch of the surface Dirac cone, resulting in strong dichroic signatures when the difference (CR-CL) is taken, shown in Fig. 4.14(b). Circular dichroism is often linked to both the spin- and orbital- angular momentum of electrons, although deducing the exact relation between these and the matrix elements for photoemission is not a trivial problem [180, 181]. Nevertheless, the surface state is clearly resolved, and

---

[3] A slight modification of a two-dimensional second derivative [179].

a clear switch of sign for each branch of the surface state provides supporting evidence for its topological origin, and for its chiral spin texture [180].

The latter can be verified explicitly with spin-polarised momentum distribution curves (spin-MDCs) for the chiral component (here $\langle S_y \rangle$). Spin-MDCs are shown in Fig. 4.14(d) at a series of binding energies in the vicinity of the TSS, indicated in the inset. For the highest binding energies, the spin-MDCs exhibit four clear peaks from the TSS, with a down-up-down-up relative ordering from low momentum to high. When moving to shallower binding energies these signals become clearer, until a degeneracy is reached at the the Dirac point. Above this, the sign is switched. All of this is consistent with a topological surface state with a confined Rashba-like dispersion.

The presence of BDPs and TSSs from the same mechanism in both $PdTe_2$ and WSe_2 is a strong indicator that this physics is indeed a generic property of the transition metal dichalcogenides. Building on the insights developed here, the rest of this Chapter details predictions for TMDs with structural instabilities which can be accessed with temperature. If the C_{3v} symmetry is lost through the reconstruction, then temperature could be potentially used as a switch for any BDPs. If it is not, then the potential for studying the topological phenomena across structural phase transitions is unlocked. Both cases will be overviewed below.

4.5 Outlook: TMDs with structural distortions

The only prerequisites for the formation of bulk Dirac cones and topological surface states in the TMD compounds is a disparity in the bandwidths of the p-orbital derived bands large enough to eclipse crystal field and spin-orbit splittings, and the presence of the C_{3v} symmetry to protect a subset of the subsequent crossings along k_z. 1T-$IrTe_2$ is TMD with an octahedral crystal structure. It too possesses the above prerequisites, and like in $PdTe_2$, it benefits from a large separation of metal and chalcogen derived bands. It has a tunable superconducting phase with Pt doping, with a maximum T_C of 1.7 K for $Ir_{0.9}Pt_{0.1}Te_2$ [182]. Realising a k_z mediated topological ladder in this compound would provide $IrTe_2$ with a greater functionality for practical applications than $PdTe_2$, however. The potential of this compound becomes clear when identifying the bulk Dirac point and two topological surface states that this compound develops from the k_z dispersion of its p-orbital manifold.

4.5.1 1T-$IrTe_2$: Removing C_{3v} symmetry

Fig. 4.15(a) shows the k_z dispersion in the energy window $E-E_F=+1$ eV to -2 eV. The p_z character band which originates midway between the Γ and A points at the top of this energy window is the anti-bonding R_4 band. Its first crossing, centred at approximately $E-E_F=200$ meV is with B-$R_{5,6}$, producing a strongly tilted type-II bulk Dirac cone. The band gaps centred at $E-E_F=-300$ meV and -800 meV are parity inverted band gaps populated by a topological surface resonance and a topological surface state respectively (Fig. 4.15(b)). As in $PdTe_2$, the

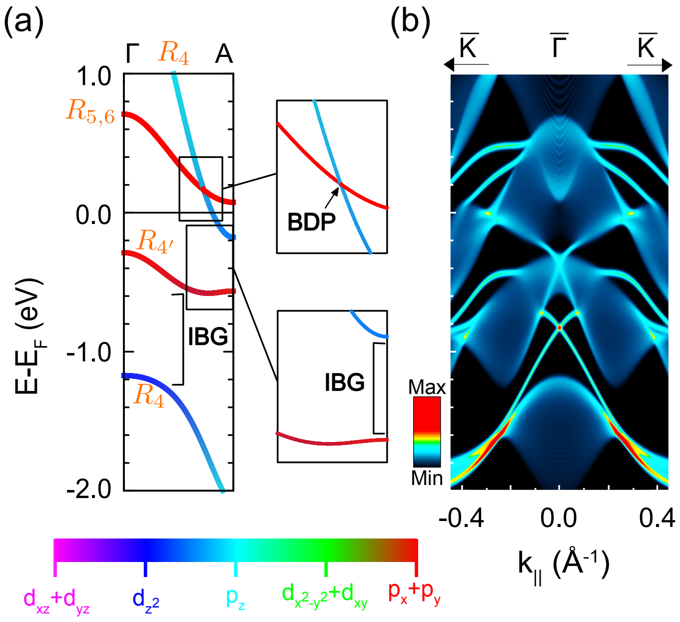

FIGURE 4.15: **Topological ladder in the high-temperature phase of 1T-IrTe$_2$.** (a) Orbitally-projected DFT calculation of the Γ-A line in IrTe$_2$. Insets show the regions in which the type-II BDP and highest-energy inverted band gap are formed. (b) Surface slab calculation demonstrating the formation of a BDP and two topological surface states.

B/AB	label	Γ	A	# crossings
AB	$R_{5,6}$	+	+	0
AB	$R_{4'}$	+	+	0
AB	R_4	−	−	3
B	$R_{5,6}$	−	−	1
B	$R_{4'}$	−	+	2
B	R_4	+	−	2

TABLE 4.3: Predicted band parities at Γ and A for the chalcogen p-derived bands in IrTe$_2$, ordered by their binding energy at the Γ point.

lowest lying of these band gaps is an anti-crossing between B-R_4, dispersing towards shallower binding energies, and B-$R_{4'}$, the highest binding energy bonding $p_{x,y}$ derived state. The shallowest binding energy of the two band gaps is produced from the crossing and subsequent hybridisation of B-R_4, AB-R_4 and B-$R_{5,6}$. A parity table, although not supported by explicit calculations, is presented in Table 4.3.

This compound adopts the same crystal structure as 1T-PdTe$_2$ and has the same peculiarity of the transition metal not donating effectively to M-X bonds. Ir has one less electron than Pd however. The shallowest portions of band structure (chalcogen p-derived) are therefore almost identical to that in PdTe$_2$, but the Fermi level falls lower. The type-II BDP in this compound is therefore located within 200 meV of the Fermi level, and the bands forming it should contribute to transport in this system. Subsequently to this work, Pt dopants in Ir$_{1-x}$Pt$_x$Te$_2$ have been shown to increase the Fermi level, with $x = 0.3$ pining the Fermi level almost exactly to the energy of the BDP [182]. Ir$_{0.7}$Pt$_{0.3}$Te$_2$ retains the superconducting phase

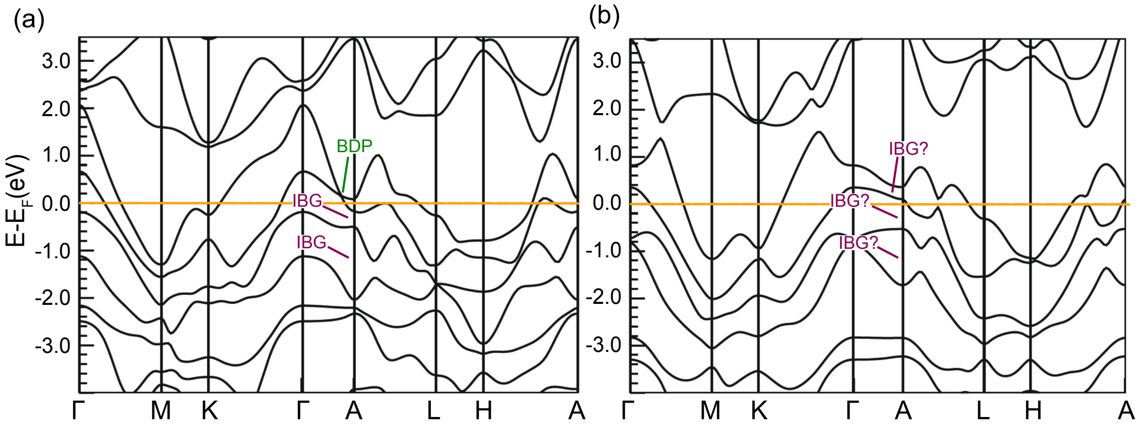

FIGURE 4.16: **High and low temperature DFT calculations of IrTe$_2$.** High- (a) and low-temperature (b) DFT calculations from [183]. The BDP and IBGs are labelled for the high-temperature phase, and the position of three candidate band inversions labelled in (b).

of the pristine compound, albeit with a greatly reduced T_C [182].

Pristine IrTe$_2$ additionally undergoes a structural phase transition with decreasing temperature ($T_C = 240$ K [183]). The origin of this is not well understood. The structural transition itself emerges as a suppression of the IrTe$_6$ octahedra, mainly along the c-axis [183]. Early reports predicted mechanisms including a CDW origin driven by Fermi surface nesting [184], a Peierls transition [185] or an energetic incentive derived from a modified crystal field splitting which acts to decrease the size of the Fermi surface by changing the details of the chalcogen p-orbital manifold splitting [183]. More recently, the formation of Ir dimers through the phase transition have been found to play an important role [186]. Regardless of the mechanism, the C_{3v} symmetry crucial for the protection of any k_z-formed BDPs is lost through this transition. Fig. 4.16(a,b) shows DFT band structure calculations for both the high temperature octahedral phase and the low temperature phase. These demonstrate the transition from a bulk Dirac point to a band gap through the transition. Whether or not the resultant band gap between the otherwise BDP forming bands is parity inverted is unknown, but if it is then this compound presents a unique opportunity to study the transition from protected crossing to an avoided one with temperature. i.e. a compound which has high mobility massless bulk electrons that can be effectively tuned with temperature such that the conductive electrons reside only at the surface following the transition. Additionally, the ability to pin this band gap to the Fermi level through Pt dopants discussed above presents the opportunity to study the interplay of topological surfaces with bulk superconductivity, possibly resulting in emergent Majorana fermions [182].

4.5.2 Charge density wave phases in TaSe$_2$ and NbSe$_2$

As outlined in the introductory Sections, many bulk transition metal dichalcogenides undergo charge density wave (CDW) transitions with reducing temperature. This is another type of structural instability, but, unlike in IrTe$_2$, rotational lattice symmetries are retained through the transition, with only the size of the unit cell changing. 2H-$TaSe_2$ and 2H-$NbSe_2$ are particularly notable examples of CDW compounds. Like all 2H-TMDs, they possess a D_{3h} metallic coordination, and so their d^1 filling renders both compounds metallic. The charge density wave instability derives from the small d-band occupation, as the opening of gaps in such a scenario can often lower the overall energy of the system.

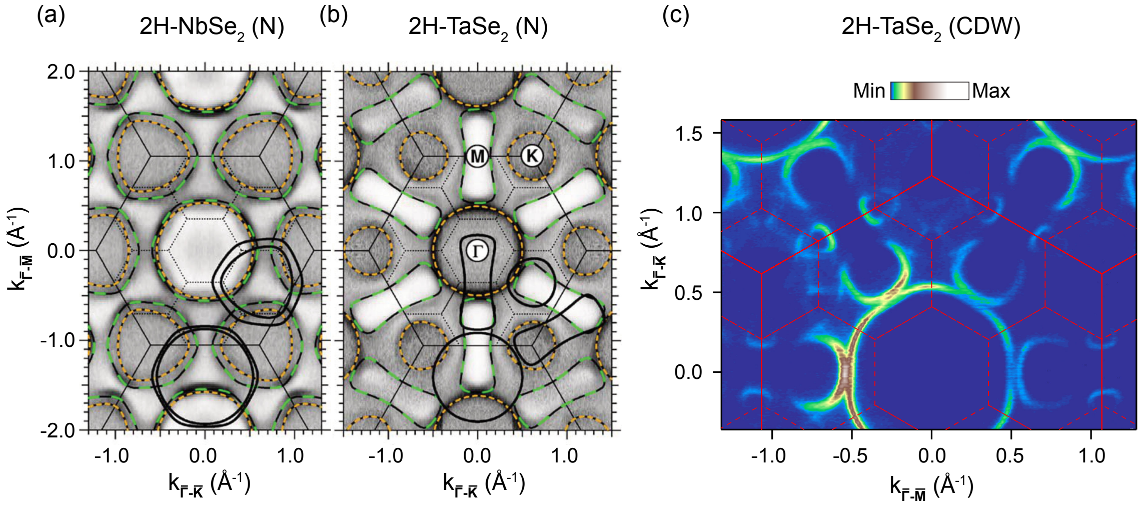

FIGURE 4.17: **Overview of CDW phases in $NbSe_2$ and $TaSe_2$.** (a-b) Normal phase Fermi surface maps for (a) 2H-$NbSe_2$ and (b) 2H-$TaSe_2$. The reconstructed Brillouin zone following the onset of the charge density wave is overlaid, adapted from [151]. (c) Fermi surface map in the CDW phase of 2H-$TaSe_2$, demonstrating the opening of clearly resolved hybridisation gaps from back-folded bands, adapted from [187].

Indeed, prominent band gaps are opened by the hybridisation of bands at the boundaries of the CDW reconstructed Brillouin zone [133, 151–155, 188]. Fig 4.17 shows experimentally obtained Fermi surfaces of both 2H-$NbSe_2$ and 2H-$TaSe_2$ in their normal state ($T >$33 K and $T >$90 K respectively [151, 189]). The surface Brillouin zones before and after reconstruction are overlaid. For $TaSe_2$, an experimentally obtained Fermi surface within the CDW phase is also shown, demonstrating the formation of clear hybridisation gaps at the Fermi level.

The k_z dispersion of the chalcogen p-orbital manifold in the normal phases of each of these compounds is much the same as in 2H-WSe_2, with two BDPs and two IBGs formed below E_F. Fig 4.18 details the DFT prediction for the formation of the topological ladder in each compound. In $NbSe_2$, the type-II and type-I BDPs are centred at $E - E_F \approx -0.8$ eV, increasing to ≈ -0.75 eV in $TaSe_2$. In both cases the BDPs are formed from the C_{3v} protected crossing with a p_z derived band (R_4) dispersing down and crossing through both back-folded pairs of $p_{x,y}$ derived $R_{5,6}$ bands. Inverted band gaps are again formed from the subsequent anti-crossings of R_4 with the back folded $R_{4'}$ pair, centred at $E - E_F = -1.0$ eV and -1.05 eV for $NbSe_2$ and $TaSe_2$ respectively. Like in WSe_2 the deeper binding energy IBG is the larger of the pair. The significant d-orbital mixing into $R_{4'}$ means that the size of the inverted band gaps here is sensitive to the change in the transition metal spin-orbit coupling strength. The inverted band gaps are therefore larger in $TaSe_2$ (5d-orbitals) than $NbSe_2$ (4d-orbitals), resulting in a harder-to-resolve TSS in surface slab calculations for the latter.

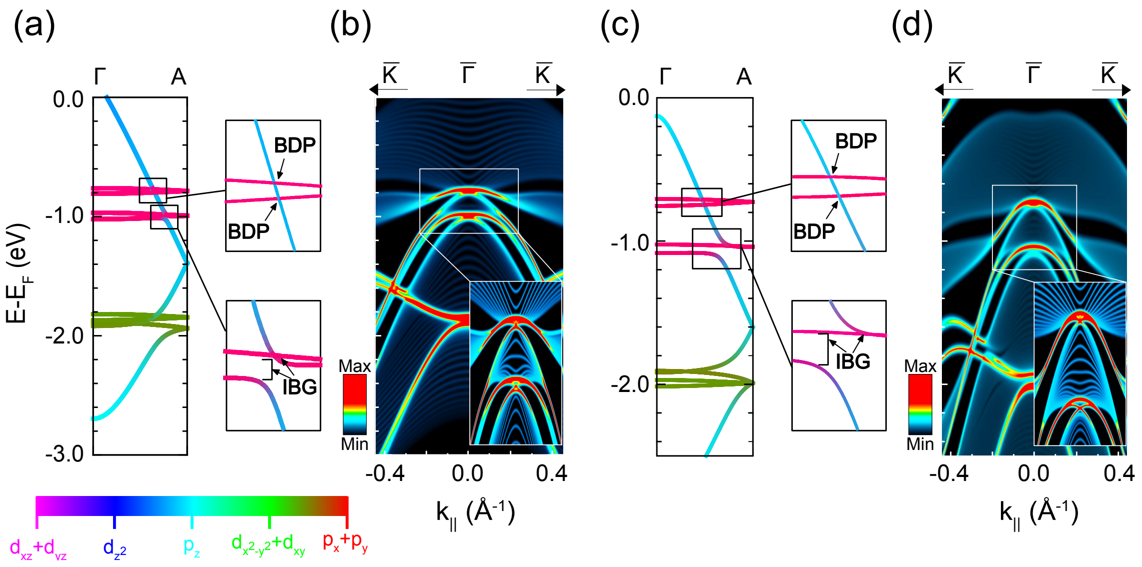

FIGURE 4.18: **Realisation of two BDPs and two IBGs in 2H-TaSe$_2$ and 2H-NbSe$_2$.** (a) Orbitally projected DFT calculations for the Γ-A direction in NbSe$_2$. The band crossings producing BDPs and IBGs are reshown in insets. (b) Surface slab calculations along the $\overline{\Gamma}$-$\overline{\mathrm{K}}$ direction. (c-d) Equivalent calculations for 2H-TaSe$_2$.

The charge density wave transition retains all rotational symmetries. Experimentally obtained ARPES dispersions for TaSe$_2$ within the charge density wave phase, presented in Fig. 4.19, are consistent with the persistence of these BDPs and TSSs through the transition. Although there is an overall energy discrepancy on the order of 200 meV between these experimental observations and the calculations in Fig 4.18(c-d), clear signatures of a bulk Dirac cone and a topological surface state are observed. Fig. 4.19(c) shows how the left and right branches of the observed TSS give opposite circular dichroic signatures, like the equivalent TSS in WSe$_2$.

In summary, k_z mediated topological ladders, entirely contained within the chalcogen p-orbital manifold, exist within several transition metal dichalcogenide compounds. The choice of transition metal changes only the fine details of the ever-present topological surface states and bulk Dirac cones. The small number of prerequisites for this, which many compounds naturally fulfil, suggests that topological states of this new origin are likely to be extremely commonly occurring, despite having being almost completely overlooked prior to this work.

Moreover, the persistence of a k_z-mediated topological ladder through the charge density wave transition of 2H-TaSe$_2$ provides a proof of principle that the study of the interplay between features belonging to a k_z-mediated topological ladder and compound specific bulk properties may be possible. Chapter 2.2.5 showed how topological superconductivity could be one such consequence, for example. However, a 'meaningful coexistence' requires that the two properties exist on the same energy scales. The next Chapter therefore examines the purview for tuning the position and composition of the topological ladders in the TMDs.

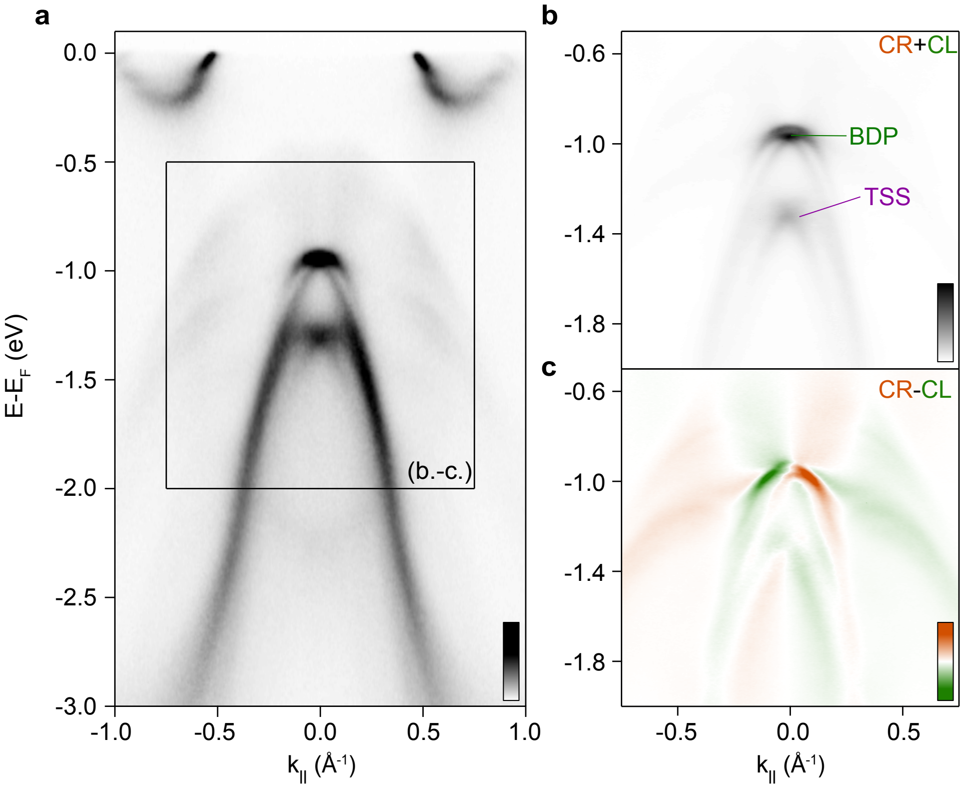

FIGURE 4.19: **Coexistence of bulk Dirac points and topological surface states within the charge density wave phase of $TaSe_2$.** (a) ARPES dispersion (p-polarisation, $h\nu = 77$ eV) of $TaSe_2$ in the charge density wave phase. (b-c) Circular dichroism signatures of the band structure over the region indicated in (a). (b) Unpolarised (CR+CL pol, $h\nu = 77$ eV) dispersion of $TaSe_2$. (c) Circular dichroism (CR-CL pol, $h\nu = 77$ eV) of the dispersion of $TaSe_2$.

Chapter 5

Tunability of topological phases in group-X transition metal dichalcogenides

By comparing the five transition metal dichalcogenides (TMDs) shown to host single-orbital manifold topological phases in Chapter 4, it is clear that, although the mechanism inducing these topological states is constant throughout, the final appearance of the states themselves is strongly dependent on finer details of a compound's specific electronic structure. This strongly suggests an element of tunability to the topological phenomena found in the TMDs. The possibility of tuning between topological phases in $IrTe_2$ by relying on a structural phase transition was already discussed, potentially allowing for the transformation of a bulk Dirac point (BDP) to an inverted band gap (IBG).

Finding a non-binary control parameter for the topological states within the TMDs is important. Whilst surface and bulk Dirac cones are often associated with desirable properties such as high electron mobilities, each of the experimentally verified Dirac cones in the previous Chapter are located energetically far from the Fermi level, meaning that they do not contribute to the transport properties of the TMDs. Moreover, a tuneable parameter allowing for the manipulation of the position of Dirac cones in the electronic band structures could be exploited to engineer an interplay between topological phenomena and properties that affect only the near-E_F density of states, such as superconductivity.

In this Chapter, two related routes for tunability will be discussed; altering inter-layer hoping, and altering the details of p-orbital degeneracy lifting due to the crystal field splitting and spin-orbit coupling (SOC) strength. This Chapter will also further discuss the effect of small k_z-mediated band gaps on the topologically non-trivial surface electronic structures in the TMDs.

5.1 Tunability through altering hopping strengths

The toy model for the k_z dispersion of p-orbital manifold in the presence of a trigonal crystal field in Section 4.2 relies on the disparity of p-derived bandwidths along a rotationally symmetric axis in order to generate the requisite band crossings for bulk Dirac cones and topological surface states. Those bandwidths are set solely by the inter- and intra-layer hopping parameters t_{1-4}, as introduced in Fig. 4.4(a). It follows that by manipulating the relative strengths of these hopping parameters, one can modify the k_z dispersion of the p-orbital derived bands and therefore alter the position of the resultant BDPs and TSSs in the electronic structure.

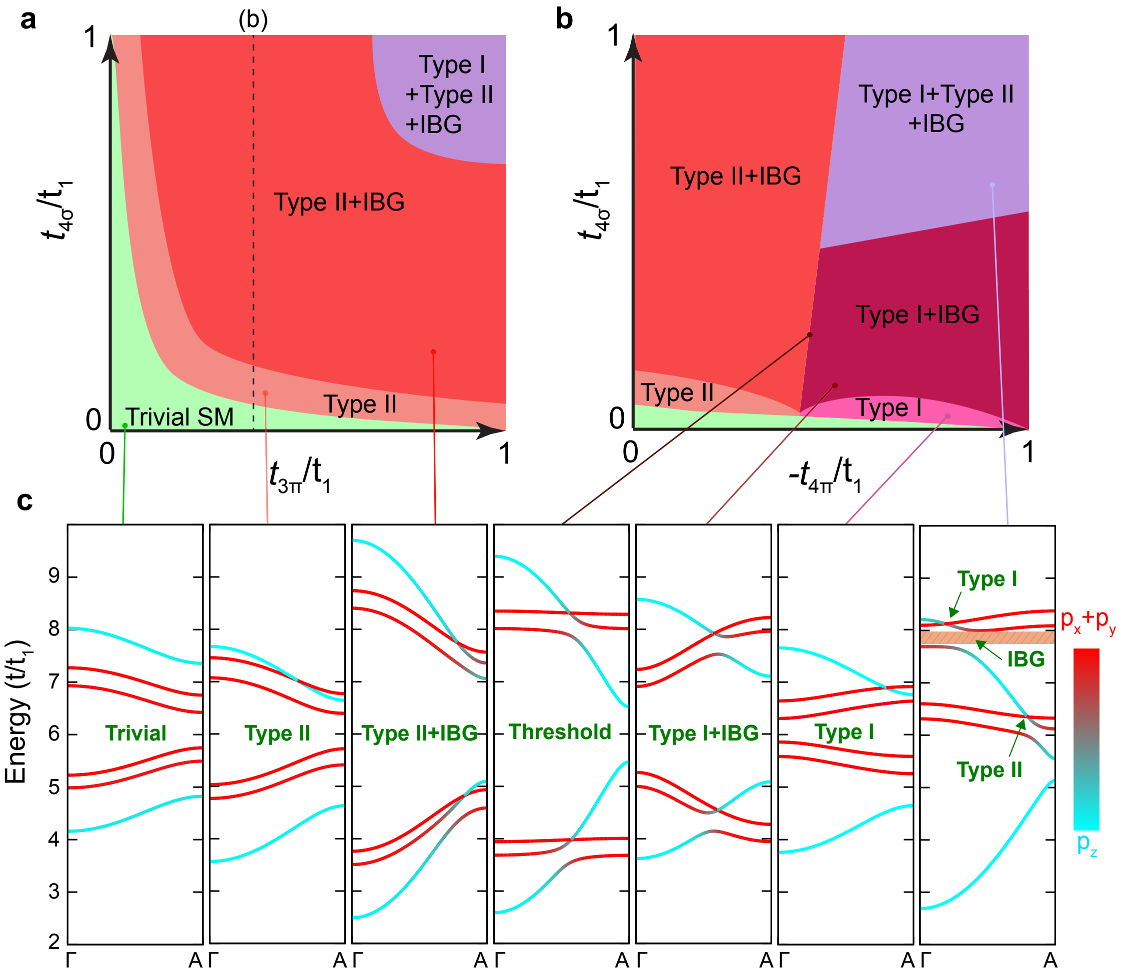

FIGURE 5.1: **Modifying the hopping parameters in the toy model for the chalcogen atoms in a 1T-TMD.** (a) The phase space available by changing the inter-layer p_z hopping term ($t_{4\sigma}$) and the out-of-plane intra-layer $p_{x,y}$ hopping terms ($t_{3\pi}$) (b) Additional phase space opened by tuning the inter-layer hopping of $p_{x,y}$ orbitals ($t_{4\pi}$) (c) Calculated k_z band dispersions for various the combinations of hopping parameters indicated in (a-b).

Fig. 5.1 shows the phase space available by tuning relative hopping strengths within the toy model presented in Chapter 4.2. The large number of different phases in these diagrams demonstrates that there are numerous ways in which k_z-mediated topological ladders can be altered. Experimentally, this rich phase diagram can be traversed by applying c-axis uniaxial strain, carrier-doping or altering dimensionality, all of which can act to change the relative hopping strengths of p-orbitals without removing the rotational lattice symmetry.

The bulk Dirac points (BDPs) and topological surface states (TSSs) that populate topological ladders in the 1T-TMDs are formed from the crossing points of highly dispersive chalcogen p_z-derived bands with $p_{x,y}$-derived bands along the k_z-axis. This difference in k_z bandwidths is achieved naturally from the disparity in c-axis hopping for p_z and $p_{x,y}$-orbitals. It follows that upon reducing $t_{4\sigma}$ (the inter-layer hopping from p_z-orbitals) in Fig. 5.1, the number of crossings between p_z and $p_{x,y}$ type bands reduces sequentially, until only a topologically trivial Γ-A dispersion is left, corresponding to almost completely decoupled monolayers.

Fig. 5.1(b) additionally demonstrates that the type of the BDP can be switched by altering the interplay between inter-layer and intra-layer hopping strengths along the c-axis of $p_{x,y}$ orbitals ($t_{4\pi}$ and $t_{3\pi}$ respectively). Increasing $t_{3\pi}$ for a zero $t_{4\pi}$ (as in Fig. 5.1(a)) acts to increase the bandwidth of the $p_{x,y}$ derived states along k_z, therefore enhancing the tilt of the Dirac cone. This will always produce type-II BDPs. However, a non-zero $t_{4\pi}$ acts to tilt the $p_{x,y}$ derived states in the opposite sense. In principle, this competition between $p_{x,y}$ hopping terms can be exploited to set the type of BDP formed. Changes of this form could be experimentally achieved by altering the van der Waals spacing between layers, whilst leaving the size of the unit cell itself approximately constant. As well as altering the type of a bulk Dirac cone, the unstable intermediate phase at the transition could be realised with fine tuning. These "type-III" Dirac fermions, although inherently unstable, have recently been argued to be a condensed matter analogue of a 'black-hole horizon' [190].

Perturbations of this form would likely be coupled to a change in the p_z derived inter-layer hopping, $t_{4\sigma}$. Increasing $t_{4\sigma}$ will always eventually additionally induce an IBG, regardless of the type of BDP formed by the first crossing. Maximally increasing $t_{4\sigma}$ such that there is an overlap between bonding and anti-bonding manifolds, as in $PdTe_2$, will produce a type-II BDP within the bonding manifold, even for large $-t_{4\pi}$. Schematic k_z dispersions are provided in Fig. 5.1(c) for each of these cases.

Note that the rich phase diagram presented in Fig. 5.1 for the TMDs is in stark contrast to an equivalent phase diagram for a more conventional topological insulator (TI) or Dirac semimetal (DSM) phase of a two-orbital manifold origin. For a TI phase like in Bi_2Se_3, the band inversion is realised at a high symmetry point rather than a high symmetry line. The scope for altering the position of the inverted band gap is therefore less naturally available. Instead, perturbing the crystal structure enough to alter the band structure is likely to simply destroy the state of interest by undoing the corresponding band inversion.

5.1.1 Strain engineering

Experimentally, reducing the van der Waals gap (increasing t_4) to either transform a type-II BDP into a type-I BDP, or induce IBGs or further BDPs, could be achieved via applying uniaxial strain along the c-axis [174]. If surface states are induced, then in principle it could be exploited as a switch for surface localised, high mobility charge carriers. Otherwise, the energetic positions of topological phenomena could be altered, possibly providing routes to move Dirac ones into the vicinity of the Fermi level or to induce a meaningful coexistence of properties in the TMDs. The toy model on which the discussions in the previous Section are based neglects the role of the transition metal. However, recent studies using real crystal and electronic structures of group-X TMDs $PdTe_2$ [191] and $PtSe_2$ [174] verify the potential for strain engineering in the 1T-structured TMDs.

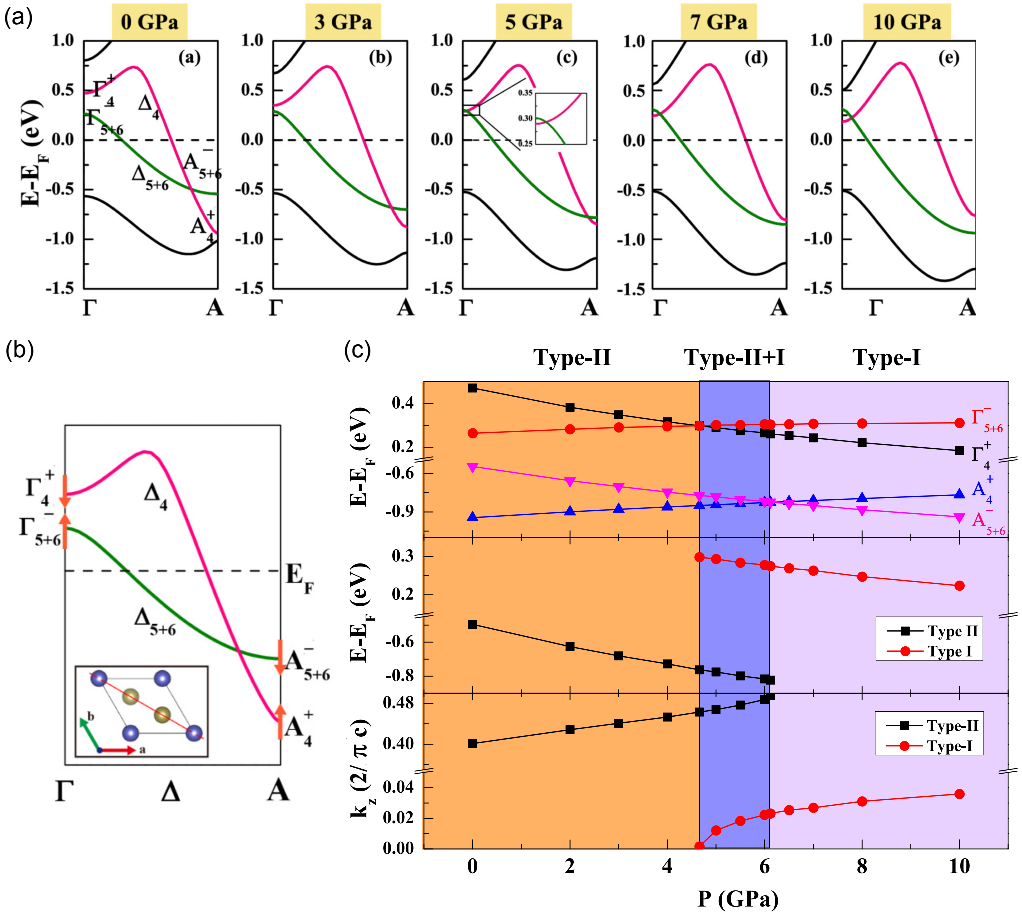

FIGURE 5.2: **Strain engineering in $PdTe_2$.** Adapted from [191]. (a) Evolution of the near-E_F Γ-A dispersion in $PdTe_2$ with applied pressure along the c-axis. (b) The energy shifts of the two bands of interest at both Γ and A with applied pressure are indicated. (c) Energetic shifts of AB-R_4 and B-$R_{5,6}$ (top) and the formed BDPs (middle) are shown as a function of applied pressure. The k_z position where the BDPs are formed is indicated in the bottom panel.

A recent DFT based study by Xiao *et al.* [191] artificially strains $PdTe_2$ to uncover how the bulk Dirac points evolve. Consistent with the phase diagrams above, Fig. 5.2 demonstrates how the type-II BDP formed from the protected crossing of the anti-bonding p_z-derived band, AB-R_4, with the bonding $p_{x,y}$-derived band, B-$R_{5,6}$, along the Γ-A direction below E_F is shifted to lower binding energies with increased applied pressure along the c-axis. Increasing the pressure to >5 GPa unwinds the band crossings forming the type-II BDP and the IBG below it. Surprisingly, however, a new BDP of type-I character is formed close to Γ approximately 300 meV above E_F with continued applied pressure. This demonstrates how both the type and the energetic positioning of BDPs can be changed with applied pressure, with even a small regime existing where both types of BDPs are simultaneously formed from the same two bands along k_z. Similar studies for the same band crossing, but in sister compound PtSe$_2$, show how the BDP formed in the pristine compound can be tuned to much shallower binding energies by increasing the van der Waals spacing, effectively reducing $t_{4\sigma}$ within the context of the model introduced above. The high mobility electrons forming the bulk Dirac cone in PtSe$_2$ can then contribute directly to transport [174].

The pressures required to modify the band structure of PdTe$_2$ are likely too high for this to form the operational principles of a device. However, studies of this form verify both the robustness of topological phenomena formed from a single orbital manifold in the TMDs, as well as the potential offered by tuning hopping parameters in real systems containing k_z-mediated topological ladders.

5.2 1T-PtSe$_2$: Changing the effective crystal field and spin orbit splitting

The above shows that the details of a k_z mediated topological ladder can be altered with changes to the unit cell. This Section furthers that discussion by comparing the ‘model’ system 1T-PdTe$_2$ with a sixth transition-metal dichalcogenide compound, 1T-PtSe$_2$. All DFT calculations in this Chapter are performed by M. S. Bahramy at RIKEN and the University of Tokyo, as part of the publications [83], [173] and [192].

5.2.1 Type-II BDP and two TSSs in 1T-PtSe$_2$

Like in PdTe$_2$ and IrTe$_2$, the transition metal in PtSe$_2$ takes a non-bonding role, placing the Fermi level within the chalcogen AB p-orbital manifold. The ground state of this compound is semimetallic, however, owing to a smaller energetic overlap of chalcogen derived bonding and anti-bonding p-orbital manifolds [193].

When considering the formation of the k_z-mediated topological ladder in this compound, several differences to the ‘model’ system 1T-PdTe$_2$ should be noted. Firstly the atomic spin-orbit coupling strength of the 4p-orbitals in selenium is weaker than that of the 5p-orbitals of tellurium. As a result, PtSe$_2$ will have a smaller energetic separation of the $p_{x,y}$-derived $R_{5,6}$ and $R_{4'}$ bands than in PdTe$_2$, and any hybridisation gaps opened at band crossings between p-derived bands will be of a reduced size, owing to the smaller $\boldsymbol{L}\cdot\boldsymbol{S}$ terms. The smaller atomic size of selenium relative to tellurium will also result in reduced p-orbital overlap within the crystal structure (which stays approximately the same size owing to the larger metal atom) altering relative hopping strengths in line with the discussion above. Together, these changes can be expected to reduce the total energetic extent of any topological ladder formed within the p-orbital manifold.

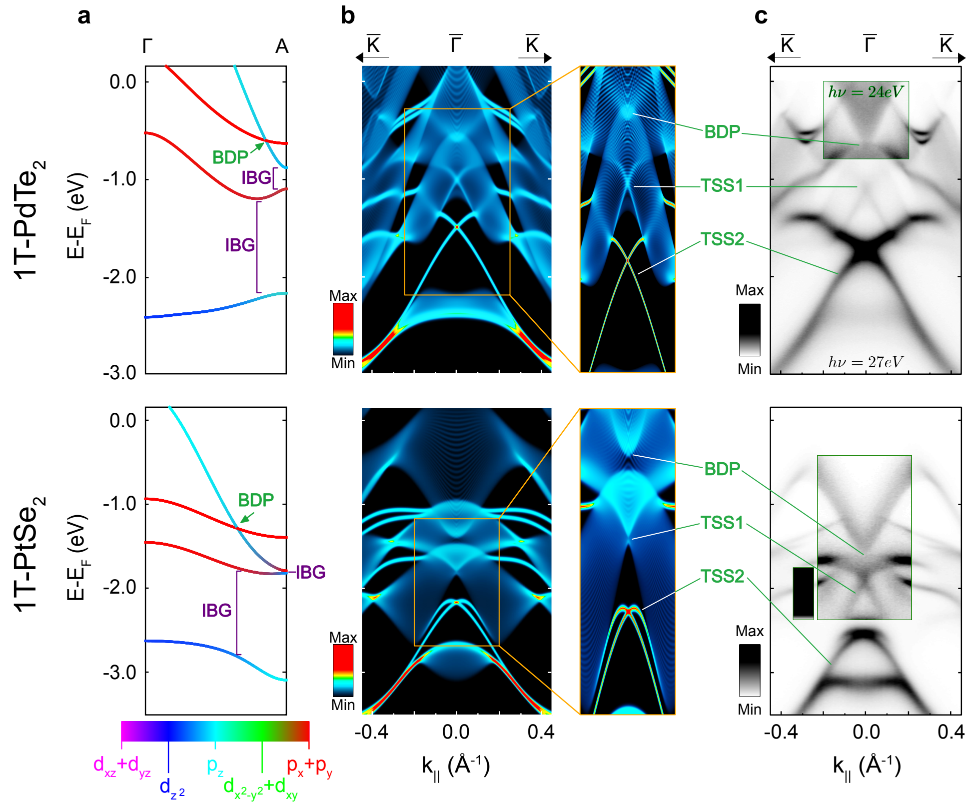

FIGURE 5.3: **Topological ladders below E_F in both PdTe$_2$ and PtSe$_2$.** (a) Orbitally projected DFT calculations along the Γ-A direction. BDPs and IBGs are indicated. (b) DFT based slab calculation of the $\bar{\Gamma}$-$\bar{K}$ dispersions over the same energy range as in (a). Equivalent ARPES dispersions obtained with $h\nu$ =27 eV (24 eV for inset) in PdTe$_2$, and 64 eV in PtSe$_2$.

Despite these changes, a topological ladder does indeed exist in this compound. Fig. 5.3 compares orbitally projected DFT calculations for the Γ-A directions of both PtSe$_2$ and PdTe$_2$ below the Fermi level. A type-II BDP is formed in PtSe$_2$, again from the protected crossing of the antibonding p_z-derived band (AB-R_4) and the shallower energy bonding $p_{x,y}$ derived band (B-$R_{5,6}$). The BDP is formed at a much deeper binding energy ($E - E_F \approx -1.5$ eV) than in PdTe$_2$, however. This Dirac cone is clearly observed in both the DFT based surface slab calculations (Fig. 5.3(b)) and $E(k_{||})$ dispersions obtained via angle-resolved photoemission (ARPES) (Fig. 5.3(c)). Fig. 5.3(b-c) additionally show that this Dirac cone is strongly modified away from $k_{||}$, turning over towards E_F to ensure compensation of electron and hole carriers at the Fermi level, as required by the semi-metallic ground state [168, 193].

As with PdTe$_2$, significant k_z broadening again prohibits irrefutable experimental verification of the ungapped nature of the BDP forming crossing points. However, artificially k_z broadened DFT calculations can be compared directly to experiment. Following the arguments outlined in Chapter 3.1.4 and [117], k_z-dependent DFT calculations at 41 discrete, evenly-spaced $k_{z,0}$ between 0 and π/c were used to produce spectral functions each incorporating a k_z integration over approximately $k_{z,0} \pm 3\frac{\pi}{c}$ in line with Eqn. 3.19 (λ =4.47 Å), where each successive addition would contribute less than 0.5% of the intensity for $k_z = k_{z,0}$. A small imaginary component of the self energy, Σ'', was included to approximate a continuous k_z dispersion from the 41 discrete steps.

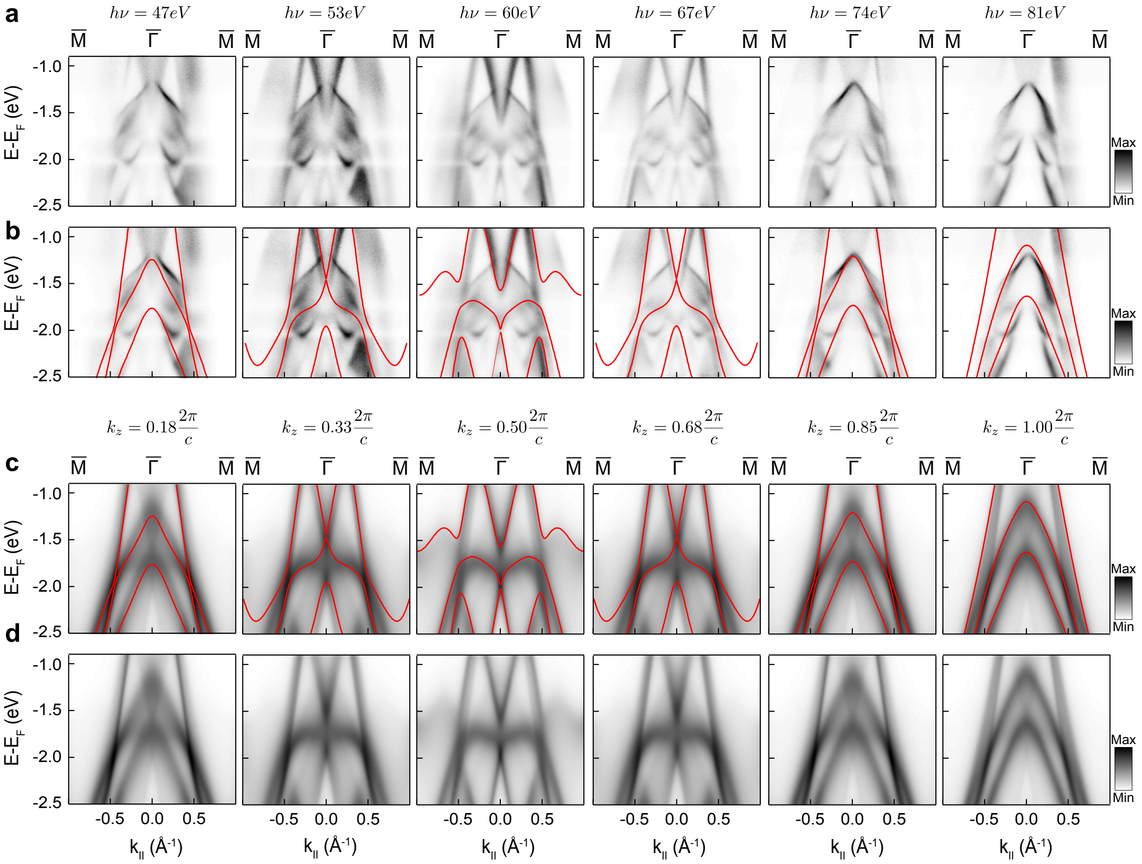

FIGURE 5.4: **Photon energy dependence of the type-II BDP in PtSe$_2$.** (a) ARPES dispersions along the $\overline{\Gamma}$-$\overline{M}$ directions for the photon energies indicated. (b) The data in (a) are reproduced, with overlaid bulk DFT calculations. (c-d) Artificially broadened bulk DFT calculations following the procedure outlined in this section with (c) and without (d) the overlaid unbroadened DFT. An energy offset of −0.1 eV and and an energy scaling of 1.05 is applied to all calculations in (b-d).

Fig. 5.4 displays the end result of this analysis for various $k_{z,0}$ compared to nominally equivalent dispersions from photon energy dependent ARPES dispersions (c =5.09 Å and V_0 = 16 eV). Although the presence of additional surface states in the experimentally obtained dispersions slightly clouds this picture, good agreement is observed between ARPES (Fig. 5.4 (a-b)) and k_z broadened bulk DFT calculations (Fig. 5.4 (c-d)). Like in PdTe$_2$, the bottom branch of the type-II BDP is not clearly observed experimentally, owing to its rapid dispersion in k_z. This is verified here by the apparent absence of this band even in the broadened DFT calculations for $k_{z,BDP} = 0.68\frac{2\pi}{c}$, whilst the crossing is clearly formed in the un-broadened calculations (red traces in Fig. 5.4 (b,c)). This experimentally verifies the presence of type-II Dirac fermions in PtSe$_2$, first predicted in [174], originating from the same mechanism as in PdTe$_2$, WSe$_2$ *et al.* in the previous Chapter.

The topological surface states, TSS1 and TSS2, are also shared by both PdTe$_2$ and PtSe$_2$, with a slightly altered appearance between the two compounds owing to the differing constraints imposed by the corresponding crystal structures. With reference to Fig. 5.3, TSS1 in PtSe$_2$

resides in an almost vanishingly small local band gap formed along Γ-A in this material. This is most clearly seen in the inset of Figure 5.3(b), where a very small Dirac like surface state can be seen bridging the bulk manifolds. Although ARPES cannot clearly resolve the band gap, the surface resonance itself is still clearly resolved (Fig. 5.3(c)), energetically degenerate with the surrounding k_z projected bulk bands. This suggests that the topological surface states formed via the mechanism presented in Chapter 4 are able to survive the reduction of the size of spin-orbit gaps to arbitrarily small values, demonstrating the robustness of these states[1].

It is worth noting once more at this stage that an equivalent reduction in spin orbit strength from Bi_2Se_3 to Sb_2Se_3, like the case here from $PdTe_2$ to $PtSe_2$, renders the latter topologically trivial [69]. In Bi_2Se_3, the band inversions themselves are driven by spin-orbit coupling. Here, spin-orbit coupling, along with the crystal field splitting, merely set the starting energy scales of the p-orbital bands, with the out-of-plane wavevector k_z mediating the band crossings. Small changes to the spin-orbit coupling strength in the TMDs therefore can change the position along k_z where the inverted band gap forms, but cannot destroy the state entirely.

The appearance of TSS2 is also strongly modified from that in $PdTe_2$. Again with reference to Fig. 5.3(b-c), the dispersion below the Dirac point is much the same in between the two compounds, but above the Dirac point the upper legs of TSS2 in $PtSe_2$ rapidly turn over to adopt a more Rashba-like appearance. In analogy to the discussion of the experimentally resolved TSS in WSe_2 (Chapter 4.4), this is a consequence of the surrounding k_z projected bulk bands. The in-plane dispersion of the bulk manifold is larger in $PtSe_2$ than in $PdTe_2$, so TSS2 needs to adopt a more Rashba-like appearance in order to maximise the momentum-space region in which it avoids becoming resonant with the bulk manifold.

This Section establishes the presence of topological ladders in a sixth TMD compound, $PtSe_2$, and again shows that by changing the details of the unit cell, the appearance of the topological surface states and bulk Dirac cones have their appearance modified. This, given the previous Chapter, is not a surprising result. However, whilst the surface band structures are similar below E_F for the two compounds, there are profound consequences above E_F to the change in the unit cell.

Full k_z band dispersions of $PdTe_2$ and $PtSe_2$ are shown in Fig. 5.5. $t_{4\sigma}$ is sufficient in size to enforce a crossing of the anti-bonding p_z derived band (AB-R_4) with the bonding $p_{x,y}$ (B-$R_{5,6}$, B-$R_{4'}$) below the Fermi level in $PtSe_2$ as discussed above and shown again in Fig. 5.5(e). However, AB-R_4 originates at Γ at a deeper binding energy than the anti-bonding $p_{x,y}$ derived states, and so there are no band crossings within the anti-bonding chalcogen manifold. The type-I BDP and inverted band gap above E_F in $PdTe_2$ (Fig. 5.5(a)) are therefore absent in $PtSe_2$. In other words, the changes to the unit cell when transitioning from $PdTe_2$ to $PtSe_2$ modify the relative hopping strengths between p-orbitals sufficiently to reverse the effective

---

[1] However small, the spin-orbit coupling strength needs still to be finite to generate inverted band gaps. Otherwise critical bulk Dirac fermions are formed in their place. See for example Chapter 2.2.1.

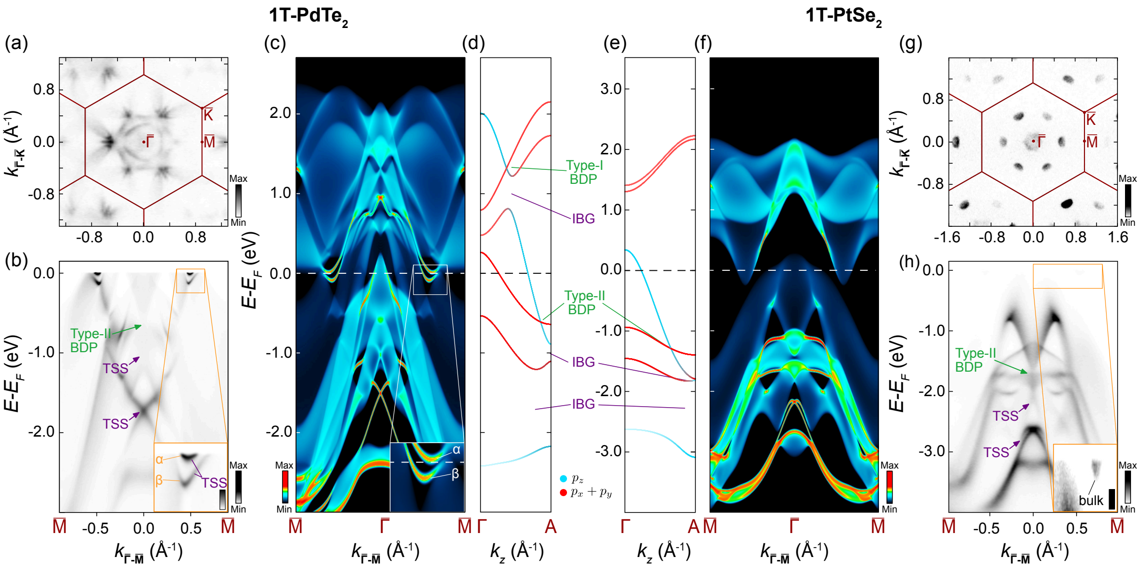

FIGURE 5.5: **Comparing the fermiology of the group-X TMDs.** (a) Fermi surface of PdTe$_2$ ($h\nu$ =107 eV probing close to an A plane) (b) Full $\bar{\Gamma}$-$\bar{\mathrm{M}}$ dispersion ($h\nu$ = 24 eV, probing close to an A plane) of PdTe$_2$. (c) Equivalent DFT based slab calculation to data shown in (b) over an extended energy range. (d) Orbitally projected DFT calculations along the Γ-A direction for the equivalent energy range. (e-h) Equivalent calculations and datasets for PtSe$_2$ ($h\nu$ = 107 eV). IBGs, TSSs and BDPs are indicated.

crystal field splitting of the anti-bonding p-orbital manifold. Equivalently, an extra BDP-TSS pair is effectively induced in PdTe$_2$ by altering details of the unit cell [192][2].

The next Section shows how this extra TSS above the Fermi level in PdTe$_2$, coupled with small k_z projected band gaps, results in a Fermi surface composed in part of topological surface states. This result is significant, as PdTe$_2$ is an intrinsic superconductor.

5.2.2 Fermiology of PdTe$_2$

Exactly how this situation arises is shown in the DFT-based slab calculations along the $\bar{\Gamma}$-$\bar{\mathrm{M}}$ direction in Fig. 5.5(c). The Dirac point of this third topological surface state, referred to as TSS0 from now on, has a Dirac point at $\bar{\Gamma}$, energetically positioned within the inverted band gap at $E - E_F \approx +1$ eV. Away from $\bar{\Gamma}$, the in-plane bandwidths of the surrounding chalcogen $p_{x,y}$-derived bands are extremely large. Therefore, similar to the above discussion for TSS2 in PtSe$_2$, both branches of TSS0 turn over and adopt significant downward dispersion to avoid becoming resonant with the bulk bands.

In fact, the two branches follow the narrow channels left within the k_z-projected bulk band structure down below the Fermi level. TSS0 crosses E_F approximately midway along the $\bar{\Gamma}$-$\bar{\mathrm{M}}$ direction. The dispersion of this state into the occupied region of the band structure allows

---

[2] Note that this is an *effective* CFS reversal only. The ordering of E and A_1 sub-manifolds following the inclusion of CFS is likely unchanged between the two compounds. Rather, the interference of chalcogen wavefunctions, $\psi_X(\boldsymbol{r})$, is altered such that the relative B/AB splittings of p_z and $p_{x,y}$ orbitals result in a reversed final ordering of bands in the AB manifold relative to PdTe$_2$ [192].

it to be probed experimentally (Fig. 5.5(b)). The upper branch of this surface state, labelled α in the inset in Fig. 5.5(b) is barely occupied, with a band minimum of <20 meV. The lower band, β, has a band minimum of approximately −130 meV, and becomes resonant with the bulk manifold at high momentum. These two branches together form TSS0.

This topologically non-trivial surface state at the Fermi level of $PdTe_2$ is consistent a recent de Haas van Alphen study of $PdTe_2$ [176], wherein a signature of a band of non-trivial Berry phase was found at the Fermi level. Fig. 5.5(a), shows the full fermiology of $PdTe_2$, including TSS0.

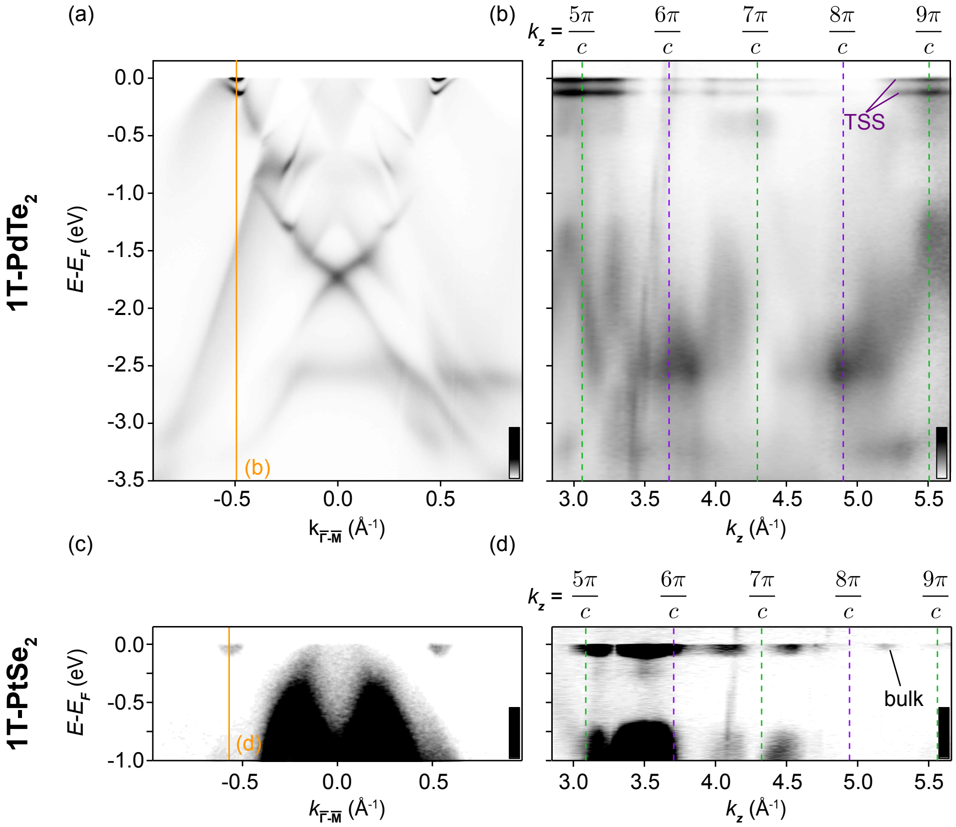

FIGURE 5.6: **Photon energy dependence for TSS0 in $PdTe_2$.** (a) $h\nu$ =24 eV band dispersion along the $\overline{\Gamma}$-$\overline{\mathrm{M}}$ direction of $PdTe_2$. An EDC is indicated, with a k_z dispersion spanning multiple Brillouin zones shown in (b). (c-d) Equivalent datasets for $PtSe_2$ ($h\nu$ =107 eV for the dispersion in (c)) The inner potential, V_0, was taken to be 16 eV for both compounds.

The absence of the inverted band gap above E_F in $PtSe_2$ can be used to help verify the topologically non-trivial nature of TSS0 in $PdTe_2$. Indeed, TSS0 is absent in equivalent band dispersions for $PtSe_2$ shown in Fig. 5.5(f,h). In contrast to the rich multi-valley Fermi surface of $PdTe_2$, the Fermi surface of 1T-$PtSe_2$, shown in Fig. 5.5(h), hosts only diffuse bulk electron and hole pockets. Although there are bulk electron pockets in approximately the same place within the surface Brillouin zone as the topological surface states in $PdTe_2$, the two are unrelated.

Fig. 5.6 compares photon energy dependent energy-distribution curves performed through approximately the band minima of TSS0 in $PdTe_2$, and of the electron pocket midway along the $\overline{\Gamma}$-$\overline{\mathrm{M}}$ direction in $PtSe_2$. Both the α and β branch of TSS0 have zero k_z dispersion, consistent

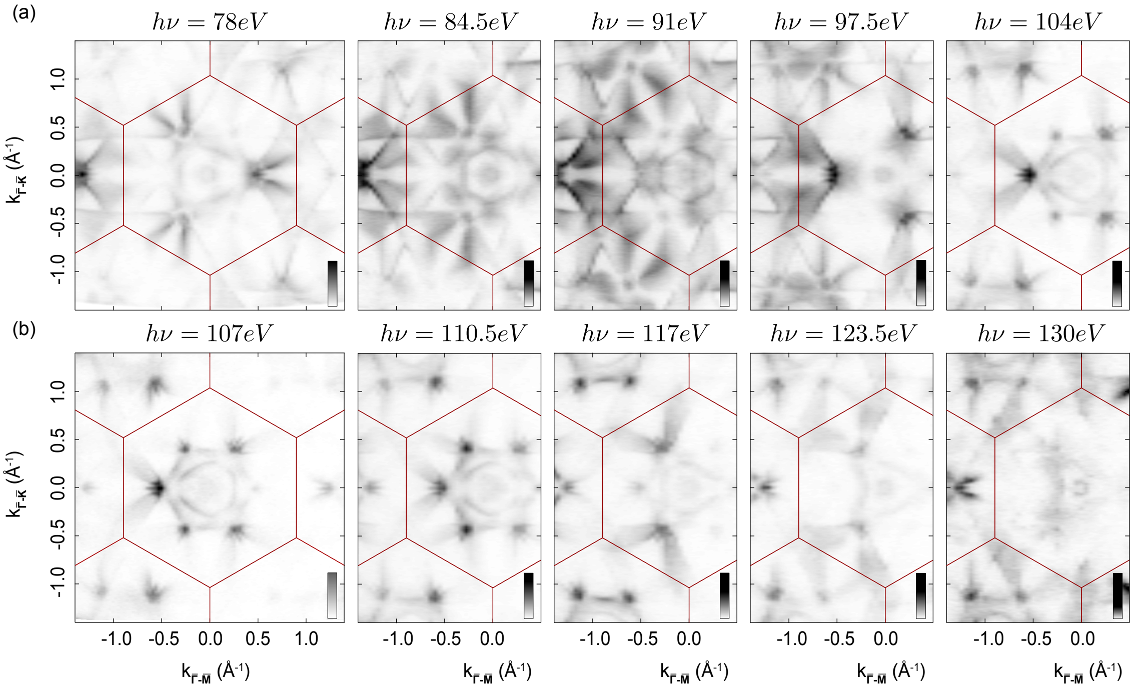

FIGURE 5.7: **Three-dimensional Fermi surface of PdTe$_2$.** A series of Fermi surface slices are displayed for varying photon energy. $h\nu$ =78 eV and $h\nu$ =130 eV correspond approximately to Γ planes in k_z, with $h\nu =$ 107 eV approximately an A-plane.

with their assignment as branches of a surface state. This is in contrast to the three-dimensional bulk bands at deeper binding energies in PdTe$_2$, and to the electron pockets in PtSe$_2$, which both show clear dispersion in k_z. This contrast provides additional evidence for the lack of any surface derived bands at the equivalent k-point in PtSe$_2$ and further supports the topological origin of TSS0 in PdTe$_2$.

Fig. 5.6(b) additionally shows how TSS0 has periodic intensity variations over the range of k_z shown. The spectral weight is generally higher at A planes (odd integer multiples of π/c) than Γ planes (even integer multiples of π/c). These same k_z-dependent matrix elements can be seen more explicitly when probing the full three-dimensional Fermi surface through a series of k_x-k_y Fermi surface slices for various k_z. The result of these measurements is shown in Fig. 5.7. Close to an A plane ($h\nu$ =107 eV), TSS0 has a larger spectral weight at negative $k_{\overline{\Gamma}-\overline{M}}$ than positive $k_{\overline{\Gamma}-\overline{M}}$ for $k_{\overline{\Gamma}-\overline{K}} = 0$. This asymmetry persists in a three-fold rotationally symmetric fashion around the Fermi surface, with the relative ordering maintained in the neighbouring Brillouin zones. At a Γ plane, however (e.g. $h\nu$ =78 eV), although portions of the TSS become resonant with the bulk bands, this threefold rotational symmetry is clearly reversed. The maximum asymmetry of TSS0 at $\pm k_{\overline{\Gamma}-\overline{M}}$ is found at intermediate k_z planes, for example at $h\nu$ =97.5 eV and $h\nu$ =123.5 eV.

Although the surface Brillouin zone is six-fold symmetric, these measurements show how the matrix elements of TSS0 reflect the three-fold rotation symmetry of the bulk band structure. The IBG that forms TSS0 occurs at $\overline{\Gamma}$, but the k_z projected bulk band gap in which it is observed is located partway along the $\bar{\Gamma}$-$\bar{\mathrm{M}}$ direction. Since the regions of $E(k)$ related by $(k_{\parallel}, \pm k_z)$ are not equivalent for $k_{\parallel} \neq 0$, TSS0 has maximum spectral weight along either $\pm k_{\parallel}$ for a given k_z.

The fermiology of TSS0, shown in Fig. 5.7 and Fig. 5.5(a), is clearly far removed from the quasi-circular appearance of TSS1 and TSS2 in the constant energy contours presented previously. Although severe, this warping away from circular geometry can be well explained by considering the details of the small k_z projected band gaps in the surface Brillouin zone. The relationship between the k_z projected band gaps and the dispersion of TSS0 is demonstrated in Fig. 5.8, which directly compares the detailed experimental band dispersion of TSS0 to bulk, k_z-resolved DFT calculations.

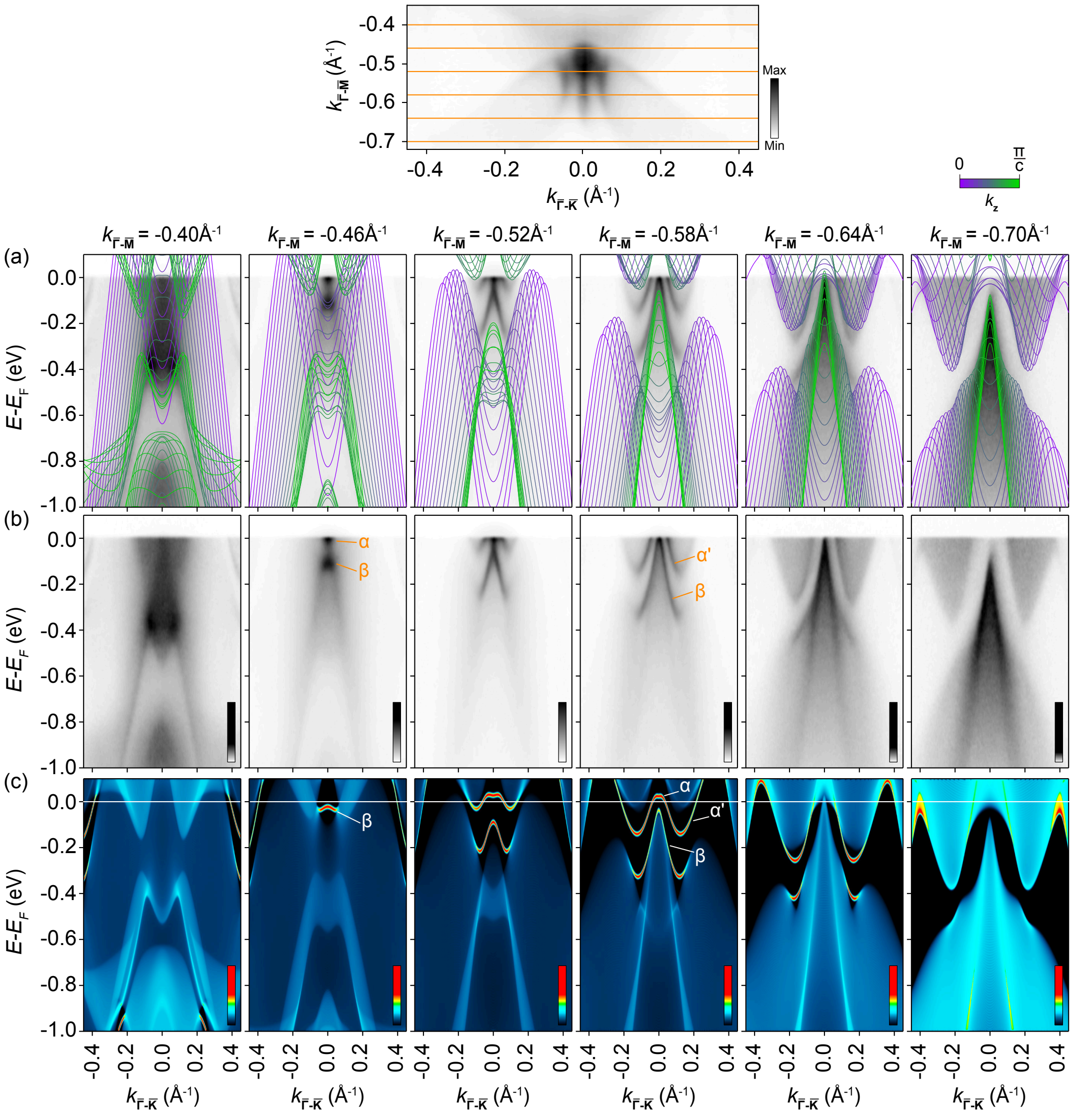

FIGURE 5.8: **Detailed band dispersion of TSS0.** (a-b) Experimental band dispersions ($h\nu = 24$ eV) parallel to the $\bar{\Gamma}$-$\bar{\mathrm{K}}$ direction for various $k_{\bar{\Gamma}-\bar{\mathrm{M}}}$ indicated in the inset (top). k_z resolved bulk DFT calculations are overlaid in (a) with an energy scaling of 1.08 applied. (c) Equivalent dispersions from DFT based surface slab calculations.

The topmost panel in Fig. 5.8 shows the region of the Fermi surface occupied by TSS0, probed at a photon energy corresponding approximately to an A plane. The orange lines indicate the positions of experimentally obtained $E(k_{\overline{\Gamma}-\overline{\mathrm{K}}})$ dispersions shown in Fig. 5.8(a-b). On the low momentum side of the $\overline{\Gamma}$-$\overline{\mathrm{M}}$ line ($k_{\overline{\Gamma}-\overline{\mathrm{M}}} = -0.4$ Å^{-1}), there is no k_z projected band gap and so the branches of TSS0 remain above E_F. Upon moving to higher momenta, small projected band gaps begin to open and the surface state disperses down below E_F to occupy them ($k_{\overline{\Gamma}-\overline{\mathrm{M}}} = -0.46$ Å^{-1}). The 'wing'-like features that exist just off the $\overline{\Gamma}$-$\overline{\mathrm{M}}$ line in the Fermi surface maps (Figs. 5.5, 5.7 and 5.8) can be understood within this framework. The $E(k_{\overline{\Gamma}-\overline{\mathrm{K}}})$ band dispersions at higher momenta ($k_{\overline{\Gamma}-\overline{\mathrm{M}}} = -0.52$ to -0.64 Å^{-1}) reveal how the band minimum of the shallowest branch, α, as viewed along the $\overline{\Gamma}$-$\overline{\mathrm{M}}$ direction is only a local minimum. The state finds a much deeper band minimum at non-zero $k_{\overline{\Gamma}-\overline{\mathrm{K}}}$, taking an overall W-like shape. By doing this, TSS0 avoids becoming resonant with the bulk-derived hole band maximum at ($k_{\overline{\Gamma}-\overline{\mathrm{K}}}$, $k_{\overline{\Gamma}-\overline{\mathrm{M}}}$)= (0, -0.64) Å^{-1}. In summary, by adopting this band dispersion, TSS0 can stay non-resonant with the bulk until very high momenta ($k_{\overline{\Gamma}-\overline{\mathrm{M}}} = -0.7$ Å^{-1}). DFT based surface slab calculations, shown in Fig. 5.8(c) are in excellent agreement with these experimental observations.

As outlined in Chapter 2, even a modest hexagonal warping of a TSS allows for an out-of-plane component to the spin texture. Here, TSS0 can be considered as an extreme case of warping away from circular geometry, and so the complexity of its spin texture can be expected to be commensurate to that of the band dispersion outlined above. Fig. 5.9 provides a summary of the spin texture of TSS0 through three-component spin-resolved constant energy k_x-k_y contours at E_F.

The spin-resolved measurements in Fig. 5.9(a) are displayed on a two-dimensional colour scale. On one axis, the spin polarisation is shown, determined in the usual way according to Eqn. 3.27. The other axis corresponds to the total intensity, I_i^{tot}, defined in Eqn. 3.26 and overlaid as a transparency filter to suppress large spurious polarisation occurring due to the low background intensity.

Regions corresponding to α and β branches have a clear opposite chiral component of spin polarisation, here $\langle S_x \rangle$ (parallel to $\overline{\Gamma}$-$\overline{\mathrm{K}}$), consistent with the expected opposing in-plane momentum locked branches of a conventional TSS.

Their unusual dispersion additionally permits a significant radial component, $\langle S_y \rangle$ (parallel to $\overline{\Gamma}$-$\overline{\mathrm{M}}$), however. This radial spin component switches sign about the $\overline{\Gamma}$-$\overline{\mathrm{M}}$ line in accordance with the $\overline{\Gamma}$-$\overline{\mathrm{M}}$ mirror symmetry. The out-of-plane component $\langle S_z \rangle$ remains small in comparison to the in-plane components. The clarity of this complex spin texture is improved by extracting an in-plane vector schematic directly from the $\langle S_x \rangle$ and $\langle S_y \rangle$ resolved Fermi surface maps in Fig. 5.9(a).

This is shown in Fig. 5.9(d), compiled using the following procedure. Arrows are centred at k-points corresponding to the positions of bands from spin-integrated ARPES. Their magnitudes are determined according to

$$I_x^{\mathrm{tot}} \sqrt{P_x^2 + P_y^2}, \tag{5.1}$$

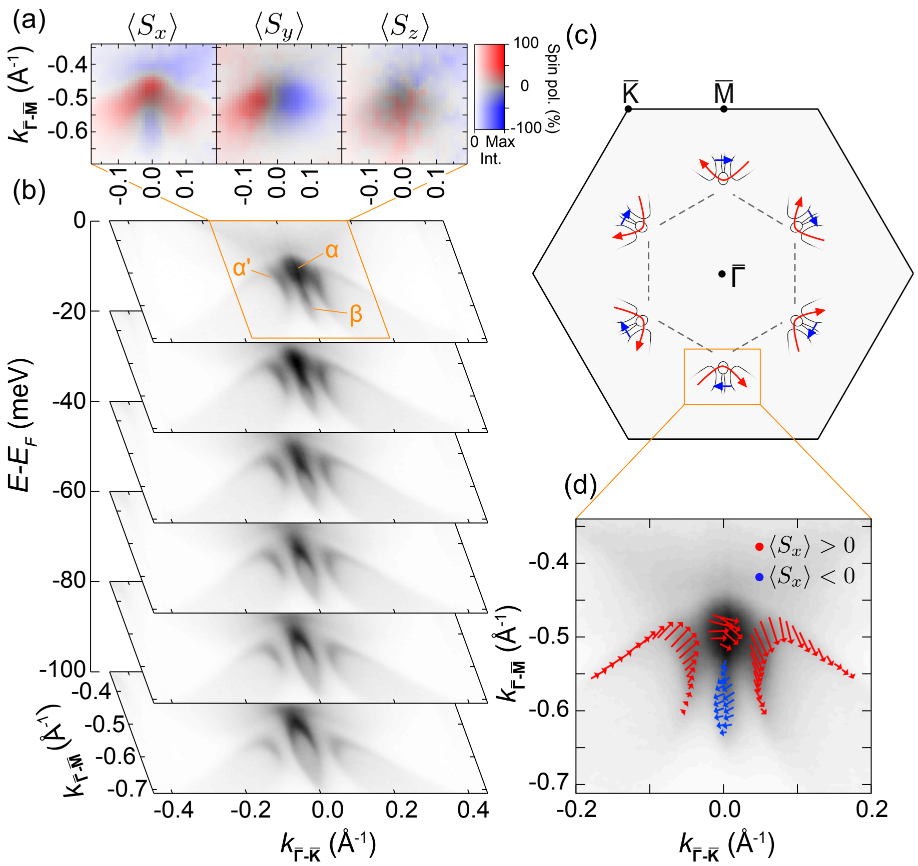

FIGURE 5.9: **Spin texture of TSS0 at the Fermi level.** (a) Three component spin-resolved Fermi surface maps ($h\nu$ =24 eV, APE beamline of Elettra, S=0.26 for $\langle S_{x,z} \rangle$ and 0.43 for $\langle y \rangle$). (b) Near E_F constant energy contours of TSS0 over the region of the Brillouin zone which it occupies. (c) Schematic global spin texture extrapolated from the extracted in-plane vector field shown in (d), created following the procedure in the text.

and their directions determined according to

$$\tan^{-1}\frac{P_y}{P_x} \quad \text{or} \quad \pi + \tan^{-1}\frac{P_y}{P_x}, \tag{5.2}$$

for positive and negative signs of P_x respectively.

Fig. 5.9(d) demonstrates an opposite, fully momentum-locked, spin texture along the $\bar{\Gamma}$-$\bar{\mathrm{M}}$ direction of the α and β branches. Radial warping is developed only for non-zero $k_{\bar{\Gamma}-\bar{\mathrm{K}}}$. The spin vector winds up along α' for negative momenta, through α and back down α' for positive momenta. Whilst complex, the schematised global spin texture shown in Fig. 5.9(c) is still clearly reminiscent of a topological or a Rashba surface state, with counter rotating, predominantly in-plane and momentum-locked branches.

Fig. 5.9(b) additionally provides details of the band dispersion of TSS0 at deeper binding energies. Both the central, approximately circular α band, and its associated 'wing' features, α', shrink in size with binding energy, consistent with their electron-like nature. The former is quickly lost owing to its small band minimum along the $\bar{\Gamma}$-$\bar{\mathrm{M}}$ direction. The β band energetically below it along the $\bar{\Gamma}$-$\bar{\mathrm{M}}$ direction, behaves as a hole band however, growing in size.

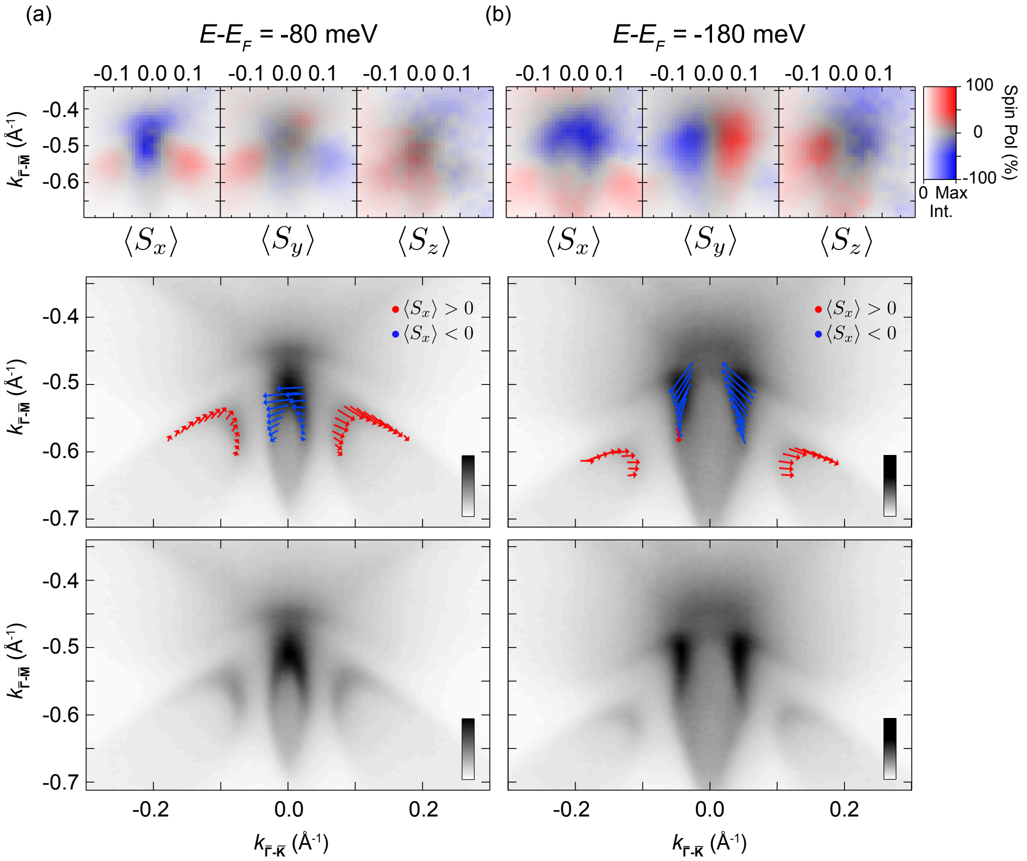

FIGURE 5.10: **Spin texture of TSS0 below the Fermi level.** (a-b) Three component spin-resolved Fermi surface maps ($h\nu$ =24 eV, APE beamline of Elettra, S=0.26 for x,z and 0.43 for y) are shown for two separate binding energies. In each case, an in-plane vector field diagram is shown below atop a $h\nu$ =24 eV constant energy contour for the appropriate binding energy.

Fig. 5.10 demonstrates how the growth of the β band is associated with an enhancement of the $\langle S_y \rangle$ component, as well as a development of a non-zero $\langle S_z \rangle$ spin polarisation at the deepest binding energies probed ($E - E_F = -180$ meV). The opposite chirality of the α and β branches is retained throughout this range of binding energy.

The above description of the spin texture can be substantiated with a more conventional, quantitative approach. Performing three-component spin-resolved energy-distribution curves, shown in Fig. 5.11 at the k-points indicated in Fig. 5.11(a), again clearly demonstrate the opposing chirality of α and β. Fig. 5.11(b) shows how the spin-polarisation of the β band, still present at the largest momentum probed ($-k_5$), becomes suppressed as the state merges into the bulk manifold. Fig. 5.11(b) additionally establishes that time-reversal symmetry is obeyed by these states with the EDCs in Fig. 5.11(b) performed at the opposite side of the Brillouin zone to the spin-resolved constant energy contours in Fig. 5.9(a) and Fig. 5.10, as well as the EDCs in Fig. 5.11(c). EDCs in Fig. 5.11(c) verify the switch in sign of the radial spin component at $\pm k_{\bar{\Gamma}-\bar{K}}$, as well as demonstrating the negligible $\langle S_z \rangle$ component.

Fitting the EDC corresponding to the $\langle S_x \rangle$ (chiral) spin component at position $k = k_7$ (Fig. 5.11)

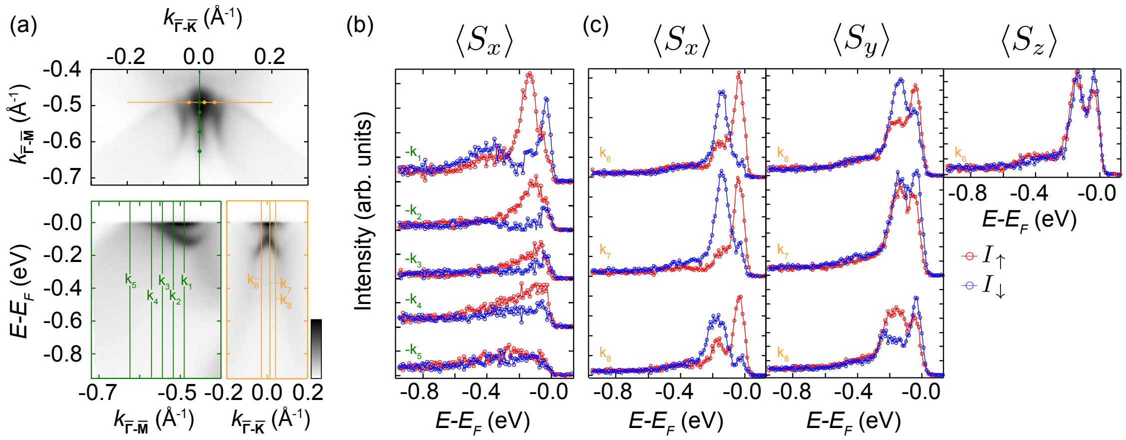

FIGURE 5.11: **Spin-resolved EDCs through TSS0.** (a) ARPES dispersions indicating the position where spin-resolved EDCs labelled k_{1-8} are performed. (b-c) Spin-resolved EDCs ($h\nu$ =24 eV, APE beamline of Elettra, S=0.2) for the positions indicated in (a). Note that the spin-resolved EDCs in (b) are taken at the opposite side of the Brillouin zone to those in (c).

to Gaussian broadened Lorentizians with a Shirley background, returns spin polarisation magnitudes of 73% and −72% for the α and β branches respectively. k_7 is close the mirror-line defined by $k_{\bar{\Gamma}-\bar{K}}$ =0, and so $\langle S_y \rangle$ and $\langle S_z \rangle$, odd under this mirror operator, must be near zero. The spin polarisation magnitude of TSS0 is therefore comparable to that of TSS2 (Chapter 4.3.2).

TSS0 in PdTe$_2$ is the first experimentally verified topological surface state in this work to cross the Fermi level. PdTe$_2$ is known to be an s-wave bulk superconductor, affecting the density of states in the immediate vicinity of E_F. It is possible, therefore, that the superconducting surface of this compound is host to Majorana zero modes [94].

5.3 Surface superconductivity of topologically non-trivial PdTe$_2$

This Section will provide an overview of scanning-tunnelling microscopy/spectroscopy (STM/STS) measurements on the surface of PdTe$_2$, motivated by the work presented in the previous Section and performed entirely by collaborator M. J. Neat in the group of P. Wahl at the University of St Andrews [173].

A summary of the results and conclusions is presented in Fig. 5.12. Fig. 5.12(a) shows a surface topography with atomic resolution, demonstrating the high quality samples of the crystal grown by the group of T. Sasagawa at the Tokyo Institute of Technology. The spin- and angle-resolved photoemission results in the previous Sections are performed above the superconducting critical temperature of 1.7 K [166, 167], limited by the boiling point of Helium in conventional liquid Helium cryostats. The home-built ultra-low vibration laboratories in St Andrews can achieve a base temperature of 10 mK using a dilution refrigerator, however [194]. It is therefore important to first verify that the topological surface states do indeed survive the superconducting transition. Fig. 5.12(b) shows an angle-integrated (±$\overline{\text{M}}$) dispersion, provided by ARPES measurements, above T_C. The two peaks, corresponding to the α and β branches of TSS0, are well recaptured by the STS tunnelling spectrum at 8 K. Upon cooling down to 40 mK, the two peaks persist, demonstrating a true coexistence of topological surface states and superconductivity. The change in the background between the 8 K and 40 mK spectra is an artefact of the measurement tip only, and is not indicative of a real physical change [173].

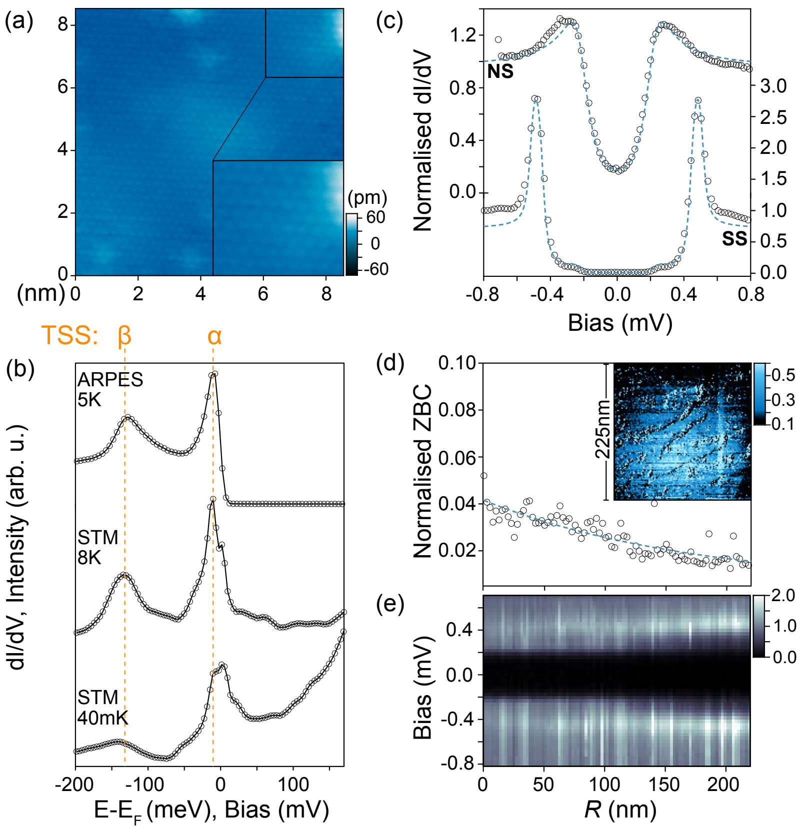

FIGURE 5.12: **STM/STS study of PdTe$_2$.** (a) Surface topography of PdTe$_2$ measured at T =8 K. (b) ARPES spectra (top; T = 5 K, $h\nu = 24$ eV, integrated along the $\overline{\Gamma}$-$\overline{M}$ direction of the Brillouin zone) and differential conductance spectra measured using STM at T = 8 K (middle) and T = 40 mK (bottom). (c) Low-energy spectra measured at 40 mK and performed with a normal (N, top) and superconducting (S, bottom) tip, normalised to the conductance at 0.6 mV. The dashed lines show the result of BSC-Dynes fits [173]. (d) Radially averaged decay of zero bias conductance (ZBC) with distance (*R*) from the centre of a vortex core, measured with a superconducting tip in a magnetic field of 7±2 mT. The inset shows the real-space image of the vortex via its enhanced ZBC. (e) The radial dependence of the full superconducting gap structure with distance from the centre of the vortex core.

Experimentally probed superconducting gap functions are displayed in Fig. 5.12(c) for both a normal tip (NS junction) and a ‘superconducting tip’ (SS-junction), the latter achieved by making brief direct contact to the sample surface, coating the tip in a finite amount of the superconducting bulk material. PdTe$_2$ is known to be a bulk *s*-wave superconductor. However, as discussed in Chapter 2.2.5, superconducting pairing at the surface of 3D topological insulators provides the possibility of a odd-parity pairing mechanism between the spin-polarised branches of a topological surface state [91], which in turn enforces Majorana zero modes to exist in vortex cores. However, the conductance spectra shown in Fig. 5.12(c) unambiguously indicates surface *s*-wave surface superconductivity with both spectra well fit to a BCS-Dynes models (dashed lines) [173]. Note also that there are no features at zero bias, again indicating nodeless, conventional superconductivity. This finding clearly demonstrates that the existence of topological surface states at the Fermi level of an intrinsic superconductor is not a sufficient criterion to realise topological superconductivity.

Moreover, a vortex was found on the sample surface in an applied magnetic field at ≈7 mT, shown in Fig. 5.12(d). Vortices occur at the surface of type-II BCS superconductors under non-zero applied magnetic field strengths, and can be described as regions of the sample surface which are not in a superconducting state; they do not expel all magnetic flux but instead each contain exactly one flux quantum. Consistent with the findings of the bias spectra in Fig. 5.12(c), additional spectra taken with a superconducting tip as a function of distance (R) away from the vortex core show no in-gap states, strongly indicating the absence of Majorana zero modes.

Note that there are mechanisms whereby Majorana zero modes could be missed in $\mathrm{d}I/\mathrm{d}V$ curves. In the tunnelling-limit, $\mathrm{d}I/\mathrm{d}V$ curves can exhibit a dip at zero bias, even in the presence of zero-bias modes [91]. However, given the quality of BCS-Dynes fits to each spectrum, this is an unlikely explanation here. In fact, the presence of vortices at all is puzzling. The bulk superconducting phase of $\mathrm{PdTe_2}$ has been shown to be be type-I [195]. A type-I bulk superconductor with type-II surface superconductivity has not been previously found, nor is the coexistence of the two types easily understood. This requires further study.

5.4 Further implications of small k_z-projected band gaps

At several points within Chapters 4 and 5, unusual appearances of topological surface states within the surface electronic structures of various compounds were explained in terms of small k_z-projected band gaps. These include, TSS2 in $\mathrm{PtSe_2}$ and the experimentally observed TSS in $\mathrm{WSe_2}$, wherein each case the upper legs of the surface state turn over away from $k_{||} = 0$ to avoid becoming degenerate with the surrounding k_z-projected bulk manifold.

The discussion of TSS0 in Section 5.2.2 also clearly fits this description. Although the Dirac point of TSS0 is centred at $k_{||} = 0$ and approximately 1 eV above E_F, both the upper and lower legs follow narrow k_z-projected band below the Fermi level, experimentally observable only approximately midway along the $\overline{\Gamma}$-$\overline{\mathrm{M}}$ direction. When probed at high $k_{||}$, the state is severely modified away from circular geometry, instead forming complex multi-valley pockets in the Fermi surface with significant radial spin canting. This is most easily seen with reference to Fig. 5.8, wherein TSS0 closely mimics the shape of the k_z-projected band gaps. TSS1 and TSS2 an be expected to become similarly increasingly warped with distance from $\overline{\Gamma}$, moulded by the surrounding k_z-projected band gaps.

These small k_z projected band gaps are a natural consequence of forming k_z-mediated topological ladders. The formation of the band inversions and protected crossings along the k_z direction occurs when the bandwidth of p_z-derived bands is much greater than $p_{x,y}$-derived

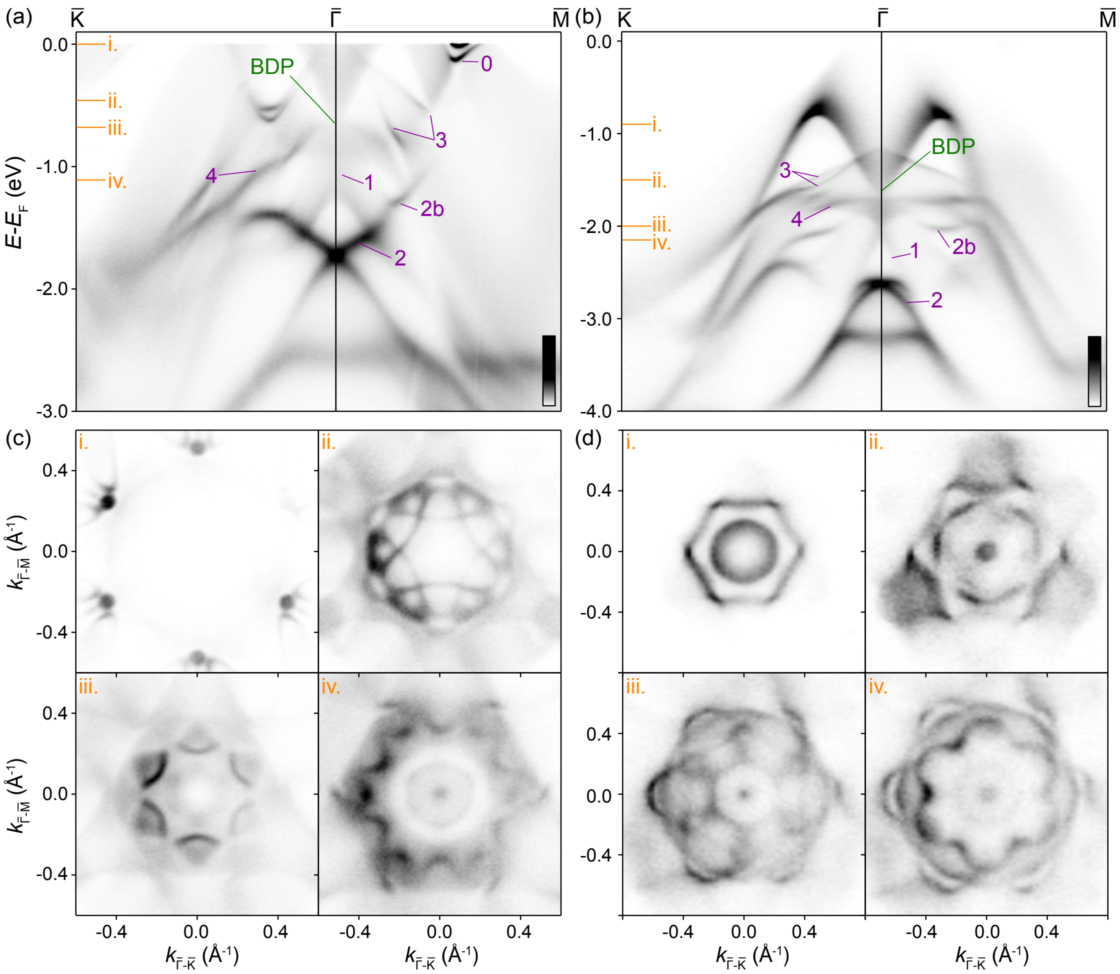

FIGURE 5.13: **Experimentally determined surface electronic structures of $\mathbf{PdTe_2}$ and $\mathbf{PtSe_2}$.** (a) Dispersions of $PdTe_2$ as obtained by ARPES ($h\nu$ =24 eV, probing close to an A plane) along the $\overline{\mathrm{K}}$-$\overline{\Gamma}$-$\overline{\mathrm{M}}$ direction of the surface BZ. Surface states and the bulk Dirac point (BDP) are labelled. (b) An equivalent dataset for $PtSe_2$ ($h\nu$ =107 eV, probing close to an A plane). (c) Selected constant energy contours (±10 meV) of $PdTe_2$ ($h\nu$ =27 eV) at the energies indicated in (a). (d) Selected constant energy contours (±10 meV) of $PtSe_2$ ($h\nu$ =107 eV) at the energies indicated in (b).

bands (since, in principle, $t_{4\sigma} \gg t_{4\pi}$). In practice, although the $p_{x,y}$-derived bands are relatively non-dispersive when compared to the p_z-derived band, Fig. 5.5(d,e) shows how they still have significant k_z dispersion, at least in $PdTe_2$ and $PtSe_2$. In addition to this, bandwidths of $p_{x,y}$-derived bands are generally larger than p_z-derived bands along $k_{\parallel}$ (since $t_{1,2\sigma} \ll t_{1,2\pi}$). The inherent three-dimensionality of the chalcogen p-orbital manifold then results in only very small channels in $E(k_{\parallel})$ left unexplored by the k_z-projected bulk manifold. Topological surface states necessarily must thread through these small channels in order to connect between TRIM points [67] (here Γ, A, L, M), greatly confining the paths that these surface states can take.

This Section will provide an overview of other features within the experimentally probed surface electronic structures of the group-X TMDs. Three more surface states, either created from additional band crossings between the $p_{x,y}$ and p_z derived bands away from the Γ-A line, or simply remnant signatures of TSS0-2 at higher momenta, will be overviewed.

Fig. 5.13 provides a complete overview of the electronic band structures of $PdTe_2$ and $PtSe_2$ through ARPES measurements using photon energies corresponding to A planes. Surface states along with the type-II BDP are indicated. As well as the topological ladder, composed of the BDP, TSS1 and TSS2 in each case, there are several common surface states (SS) at non-zero $k_{||}$ with unusual band band dispersions.

These are labelled 2b, 3 and 4 in Fig. 5.13. TSS2b is a continuation of TSS2 as it disperses through the bulk manifold. This is most obvious in $PdTe_2$, although the spin-resolved data presented below will demonstrate that this also the case in $PtSe_2$. SS3 has a more complex dispersion. In $PdTe_2$, its two branches have a turning point part-way along the $\overline{\Gamma}$-$\overline{\mathrm{K}}$ direction, but monotonic downward dispersions along $\overline{\Gamma}$-$\overline{\mathrm{M}}$. Together, this produces a strongly hexagonaly warped, interlocking constant energy contour (Fig. 5.13(c ii.)), evolving to arc like-features when probing below the band minima along $\overline{\Gamma}$-$\overline{\mathrm{K}}$ (Fig. 5.13(c iii)).

SS4 is the seemingly single-branch state dispersing exactly through the bulk Dirac point, mentioned previously in Chapter 4.3.1, present in both compounds. In $PdTe_2$, its signatures are clearest along the $\overline{\Gamma}$-$\overline{\mathrm{K}}$ direction where its dispersion can be traced almost to $\overline{\mathrm{K}}$. It appears to hybridise with TSS2b, forming a pronounced anticrossing gap. Along $\overline{\Gamma}$-$\overline{\mathrm{M}}$ SS4 is less pronounced, apparently crossing with TSS2b. Fig. 5.13(c iv) shows a constant energy contour for a binding energy between the band maximum of TSS2b along the $\overline{\Gamma}$-$\overline{\mathrm{K}}$ and $\overline{\Gamma}$-$\overline{\mathrm{M}}$ directions. This shows how TSS2b and SS4 together make an almost 12-fold symmetric pattern, again highlighting the complexity in band dispersions of surface states populating the narrow projected band gaps here.

In $PtSe_2$, each of surface states 2b, 3 and 4 have qualitative differences to their appearance in $PdTe_2$. In particular, each has a shallower band dispersion than in $PdTe_2$ (Fig. 5.13). This can again be attributed to the details of the k_z projected bulk manifolds. Whilst the c-axis lattice constants of the two compounds are similar (5.13 vs 5.08 Å for $PdTe_2$ and $PtSe_2$ respectively [196, 197]), Pt is more electronegative than Pd, and Se is physically smaller than Te. This combination can be expected to modify relative hopping strengths of in- and out-of-plane p-orbitals whilst also changing the degree of absolute band-overlap between the two compounds. Therefore, whilst these states still show significant hexagonal warping in $PtSe_2$(Fig. 5.13(d)), they are different. Specifically, they do not exhibit local band minima like SS3 in $PdTe_2$.

Like TSS2b, SS3 and SS4 are not necessarily distinct from TSS1 and TSS2. In the case of SS4, its apparent relationship with the BDP, dispersing exactly through it, prompts the consideration of a Fermi arc origin. Whilst Fermi arcs commonly occur between BDPs separated in $k_{||}$, the pair of BDPs formed along the k_z axis in the TMDs project onto the same $k_{||}$ point in the surface Brillouin zone. Despite this, some credence can be given to a Fermi arc interpretation through a series of surface slab calculations of $PdTe_2$ where strain fields of various sizes are applied along the crystallographic c-axis. These are presented in Fig. 5.14.

Although discrepancies in the details of the surface electronic structure between experiment and calculations makes a direct comparison difficult, as shown in Section 5.1.1 applying strain to $PdTe_2$ leads to the creation and annihilation of bulk Dirac points. By tracking the evolution

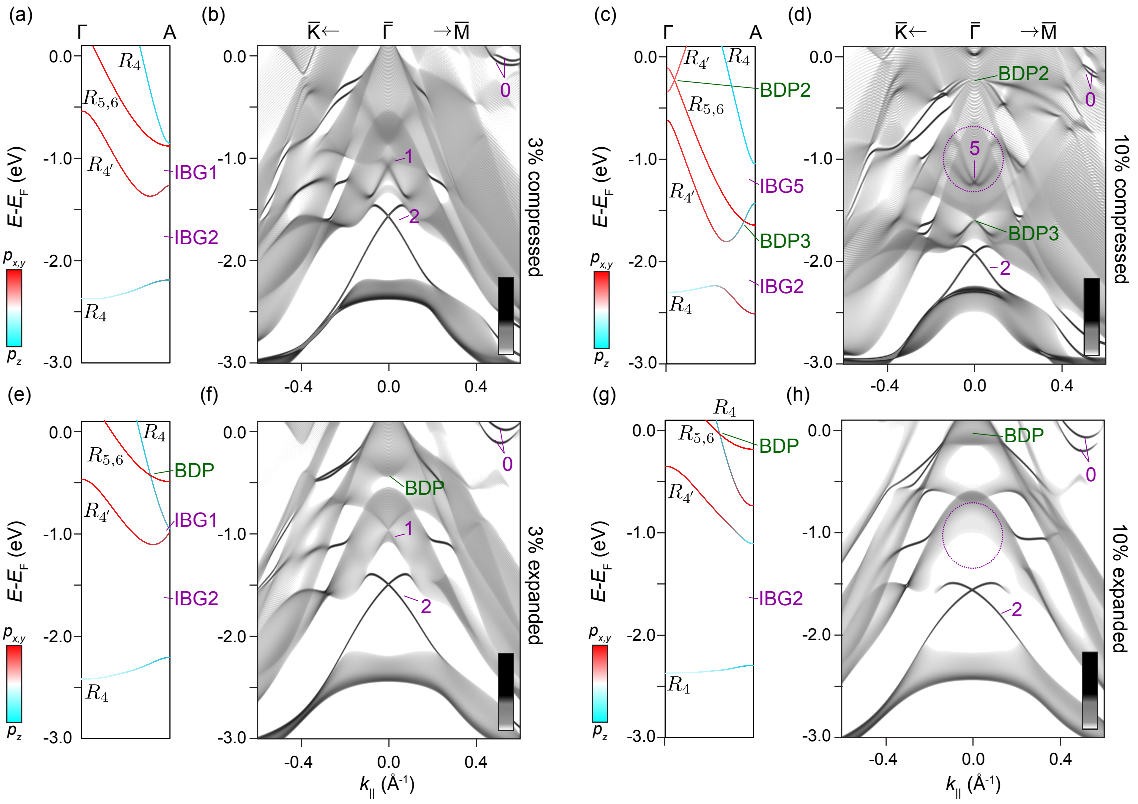

FIGURE 5.14: **Deducing the origin of SS4 through strain.** (a,b) Bulk (a) and surface (b) calculations for the case where 3% strain has been applied in compression. (c,d) Equivalent calculations for 10% compressive strain. (e-h) Equivalent calculations for 3% and 10% strain in expansion.

of the overall surface electronic structure with strain, one can infer the origin of the experimentally observed surface state, SS4.

Fig. 5.14(a-d) show calculations where a strain field is applied in compression, i.e. where the Pd-Te bond lengths remain unchanged but the interlayer gap decreases in size. The increased inter-layer hopping in this case enhances the size of the B-AB separation of a given pair of p-orbitals. This leads to a shifting of the AB-p_z derived band to lower binding energies, and hence an opposite shifting of the B-$p_{x,y}$ derived bands is required in order to maintain charge neutrality of the system. Accordingly, for the case of a 3% strain (Fig. 5.14(a-b)), the type-II BDP formed from the crossing of AB-R_4 and B-$R_{5,6}$ is lost. With continued applied strain in compression (10%) (Fig. 5.14(c-d)), the picture changes substantially. The band inversion forming TSS1 is lost, but a new IBG (IBG5) as well as two additional BDPs are created, each centred at $\bar{\Gamma}$. The new IBG, positioned at $E-E_F \approx -1.2$ eV, produces a further TSS (here TSS5) in Fig. 5.14(d), formed from the anticrossing of the B and AB p_z-derived R_4 bands.

The type-I bulk Dirac point labelled BDP2 in Fig. 5.14(d) is formed from the crossing of AB-$R_{4'}$ and B-$R_{5,6}$, both of which have $p_{x,y}$ orbital character. BDP2 is located within 250 meV of E_F. BDP3, again of type-I, is formed from the p_z-derived B-R_4 with the $p_{x,y}$-derived B-$R_{5,6}$. Whilst these observed changes to the bulk band structure are largely consistent with those of Xiao *et al* in [191] and Fig. 5.2, the surface slab calculations additionally reveal how new sharp surface states unambiguously disperse through both BDP2 and BDP3. This can be interpreted as evidence that SS4, observed clearly only in experiment, is indeed likely connected to the type-II BDP below E_F in the unstrained compound.

Similarly, Fig. 5.14(e-h) show the case where the strain is applied in expansion. Here, the AB-p_z derived band shifts to a higher binding energies with the B-$p_{x,y}$ derived bands moving to lower binding energies. Whilst AB-R_4 still anticrosses B-$R_{4'}$, the anticrossing between B-R_4 and B-$R_{4'}$ no longer occurs. There is therefore no longer a parity exchange across the resultant band gap, and so TSS1 is lost. Surface states likely corresponding to SS3 in these calculations seem to be largely unaffected by this change, again suggesting a distinct origin of SS3 and SS4 to the topological states populating the $\overline{\Gamma}$-centred topological ladder discussed in Chapter 4.

More generally, the calculations in Fig. 5.14 are again an indication of the extreme resilience of topological surface states formed from k_z-mediated band inversions within a single-orbital manifold. TSS0 and TSS2 each survive both 10% compression and expansion, and whilst the type-II BDP and TSS1 can be destroyed, further BDPs and TSSs are produced in their place with continued perturbation.

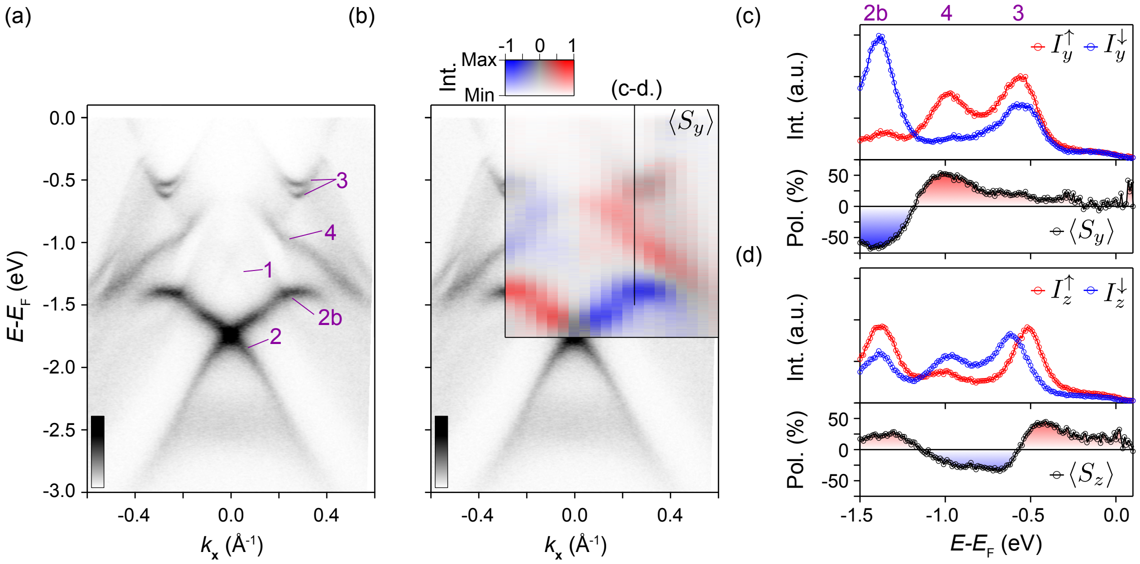

FIGURE 5.15: **Spin-polarisations of surface states 2b, 3 and 4 in PdTe$_2$.** (a) ARPES dispersion along the $\overline{\Gamma}$-$\overline{\text{K}}$ direction (hν =29 eV). (b) The dispersion in (a) is duplicated, with a spin-resolved dispersion (hν =29 eV) overlaid for the chiral spin component ($\langle S_y \rangle$). This spin-resolved dispersion utilises a 2D colour scale (see text). (c-d) Spin-resolved constant energy-distribution curves (EDCs) (hν =27 eV) at the position indicated in (b) for the chiral ($\langle S_y \rangle$) (c) and out-of-plane ($\langle S_z \rangle$) (d) spin components.

Returning to the experimental observations of the pristine compounds, the complexity of the spin textures of these states can be expected to be significant, in-line with the band dispersions presented above. Fig. 5.15 shows spin-integrated (a) and spin-resolved (b) $\overline{\Gamma}$-$\overline{\text{K}}$ dispersions of PdTe$_2$, with the surface states again indicated. The spin-dispersion shows the 'chiral' component (here $\langle S_y \rangle$), expected to be dominant for topological and Rashba surface states. Like in the spin-resolved constant energy contours shown in Section 5.2.2, this dispersion utilises a 2D colour scale: The total intensity, I_i^{tot} is included as a transparency filter over the determined

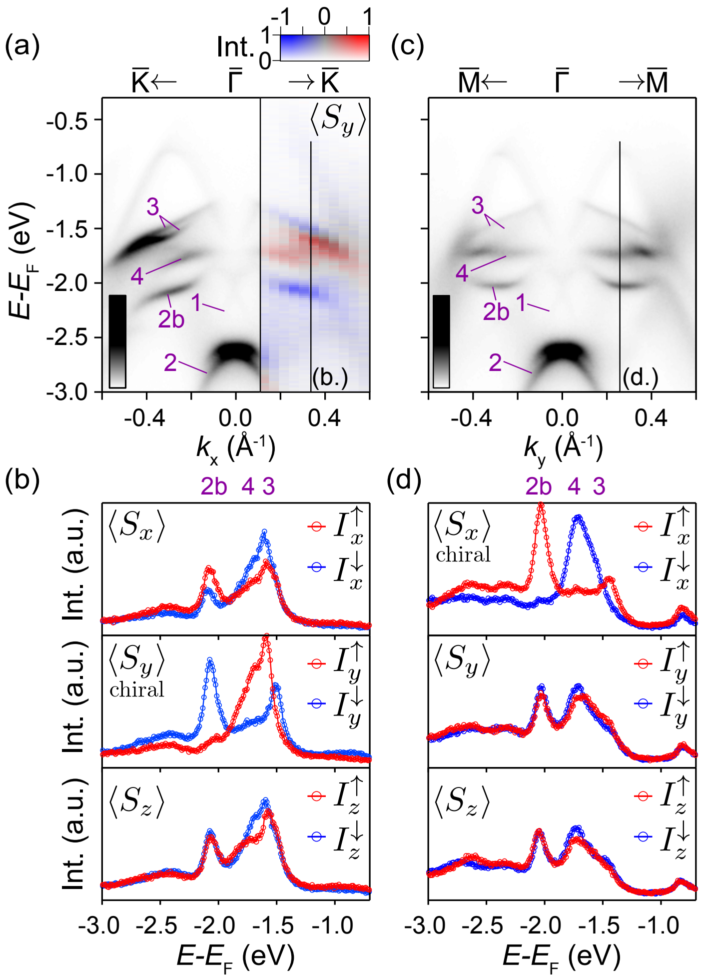

FIGURE 5.16: **Spin-polarisations of surface states 2b, 3 and 4 in PtSe$_2$.** (a) ARPES dispersion along the $\bar{\Gamma}$-$\bar{K}$ direction (hν =29 eV) overlaid with a spin-resolved dispersion (hν =29 eV) overlaid for the chiral spin component ($\langle S_y \rangle$). This spin-resolved dispersion utilises a 2D colour scale (see text). (b) Spin-resolved EDCs (hν =29 eV) for the radial (x), chiral (y) and out-of-plane (z) spin components, for the position indicated in (a). (c) ARPES dispersion along the $\bar{\Gamma}$-$\bar{M}$ direction (hν =29 eV). (d) Spin-resolved EDCs (hν =29 eV) for the radial (y), chiral (x) and out-of-plane (z) spin components, for the position indicated in (c).

spin-polarisation, P_i, to suppress spurious polarisation arising from low background spectral weight intensity.

This reveals how the clockwise chirality of TSS2 is inherited by TSS2b, with the spin-polarisation non-zero even over the region of $k_{||}$ where the state becomes resonant with the bulk manifold. SS4, the seemingly single branch state (Fig. 5.13(a)), finds a CCW chirality which persists over the full momentum range shown. The chiral spin polarisation of SS3 is small in comparison. Each of these surface states exhibit a switch of spin-polarisation from $-k$ to $+k$, in accordance with time-reversal symmetry.

In line with the discussions above, spin-resolved energy distribution curves shown in Fig. 5.15(c-d) demonstrate that each of these surface states has non-zero out-of-plane spin polarisation.

For TSS2b and SS4, which disperse monotonically along both in-plane high symmetry directions, this out-of-plane spin component is much smaller in magnitude than the chiral component. For SS3 however, the out-of-plane component of SS3 is significant, with a Zeeman-like ordering of the local band minima formed partway along the $\overline{\Gamma}$-$\overline{\mathrm{K}}$ direction. Although not shown explicitly here, there is negligible radial (here $\langle S_x \rangle$) warping in $PdTe_2$ for any of the surface states discussed in this Section.

Fig. 5.16 details the spin textures of each of these states in $PtSe_2$. Whilst the relative chiralities of each of these surface states is retained from that in $PdTe_2$, the details of the warping paths are altered. Consistent with with their monotonic dispersions, the chiral component, $\langle S_y \rangle$ ($\langle S_x \rangle$) for Fig. 5.16(a) (Fig. 5.16(b)), is dominant for all surface states, with even an opposite ordering of the two branches of SS3 being resolvable here. There is still spin canting of each of these states, however, with both a non-zero radial ($\langle S_x \rangle$ in Fig. 5.16(a)) and out-of-plane ($\langle S_z \rangle$) component observed along the $\overline{\Gamma}$-$\overline{\mathrm{K}}$ direction. Along the $\overline{\Gamma}$-$\overline{\mathrm{M}}$ direction, both the radial and out-of-plane components are symmetry enforced to be zero, consistent with the experimental observations here.

Table 5.1 summarises the chiral components of each surface state discussed in this section in each of these compounds. In summary, the chiralities of all surface states discussed here have the same sign between compounds, and in general the total deviation from a chiral spin texture is higher for $PdTe_2$ than $PtSe_2$, likely linked to the stronger deviation from linear band dispersions. The warping in $PtSe_2$ tends to be predominantly radial for these states, whereas the warping in $PdTe_2$ is entirely out-of-plane.

TABLE 5.1: Chiral components of spin for surface states in $PtSe_2$ and $PdTe_2$. (U)pper and (L)ower correspond to shallow and high binding energies respectively.

SS	TSS2L	TSS2U	TSS2b	SS4	SS3L	SS3U
$\langle S_{\text{chiral}} \rangle$	CCW	CW	CW	CCW	CCW	CW

It is important to note that this warping is not a natural result of higher order terms to the $\boldsymbol{k} \cdot \boldsymbol{p}$ Rashba Hamiltonian discussed in Chapter 2.2.3 [78]. Instead, the warping here is due to the shape of the underlying k_z-projected band manifold, and in fact an inherent competition exists between these two warping mechanisms.

By focussing once more on TSS2 in $PdTe_2$, this point can be well illustrated. Below the Dirac point of TSS2 where the lower branch populates a large k_z-projected band gap, constant-energy contours shown in Fig. 5.17 grow increasingly hexagonally warped with distance from the Dirac point, with hexagon corners positioned along the $\overline{\Gamma}$-$\overline{\mathrm{M}}$ directions. As noted previously in Chapter 4.3.2, this is entirely consistent with a Fu type model [78] derived from higher order $\boldsymbol{k} \cdot \boldsymbol{p}$ terms to the Rashba Hamiltonian, commonplace in topological insulators and systems with Rashba surface states [80]. However, above the Dirac point where the momentum-space extent of the k_z-projected band gap becomes smaller, the sign of the warping switches, with apexes now formed along the $\overline{\Gamma}$-$\overline{\mathrm{K}}$ direction.

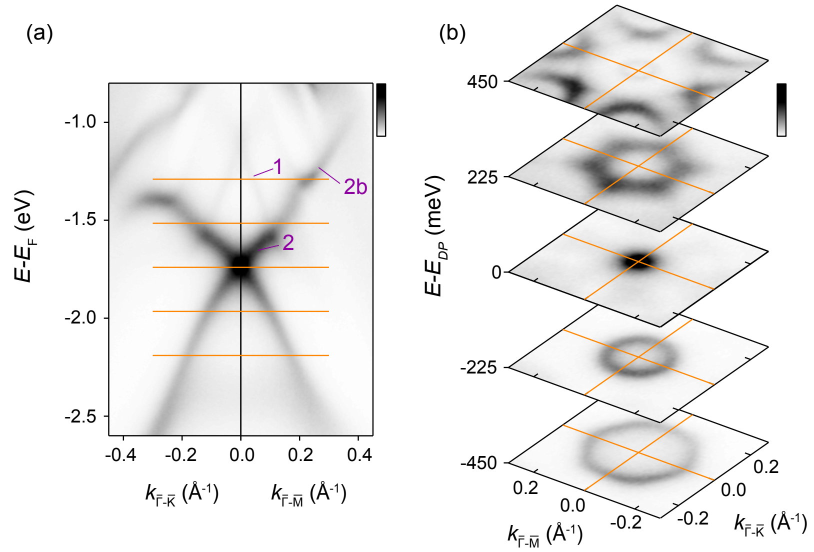

FIGURE 5.17: **Competition of hexagonal warping in PdTe$_2$.** (a) ARPES dispersions ($h\nu$ =27 eV) in the vicinity of TSS2. Orange lines correspond to the energy and momentum ranges of the constant energy contours in (b). (b) Constant energy contours (±15 meV) ($h\nu$ =27 eV) for the energies indicated in (a).

This switch of warping is inconsistent with a Fu Hamiltonian for a C_3 system, but can again be explained in terms of the small k_z-projected band gaps. TSS2b has its warping direction set by the relative energetics of the local band gap in which it disperses into along the two azimuthal directions ($\bar{\Gamma}$-$\bar{K}$ or $\bar{\Gamma}$-$\bar{M}$). With reference to Fig. 5.13(a), TSS2b disperses into a band gap which is at a shallower binding energy when viewed along the $\bar{\Gamma}$-$\bar{M}$ direction than along the $\bar{\Gamma}$-$\bar{K}$ direction. Resultantly, the direction of warping of TSS2b ought to be such that its apexes are orientated along the $\bar{\Gamma}$-$\bar{K}$ direction. TSS2 follows suit to ensure good continuity to TSS2b.

In PtSe$_2$ a switch of warping across the Dirac point of TSS2 does likely not occur, although the small energy range over which the upper legs of TSS2 turn over make this difficult to verify. In PdTe$_2$, TSS2b is approximately dispersionless along $\bar{\Gamma}$-$\bar{K}$, and has positive group velocity along $\bar{\Gamma}$-$\bar{M}$. However, in PtSe$_2$ the state is dispersionless along $\bar{\Gamma}$-$\bar{M}$ and has negative velocity along $\bar{\Gamma}$-$\bar{K}$. This results in an opposite warping direction to TSS2b in PdTe$_2$, with apexes now formed along the $\bar{\Gamma}$-$\bar{M}$ direction Fig. 5.13(diii.-iv.)). There is therefore no incentive for a switch in the warping direction of TSS2 in PtSe$_2$.

Overall, this Section illustrates that $\bar{\Gamma}$ centred topological ladders are likely not the only generic property of systems hosting a series of band inversions along a rotationally symmetric axis within a single orbital manifold. Small k_z projected band gaps have a significant influence over both the band dispersions and spin textures of the surface electronic structures. The group-X TMDs, relatively understudied relative to the group-VI semiconductors for example, therefore host as many as five topologically non-trivial surface states and two bulk Dirac cones within their electronic structures. The next Chapter does not focus on k_z-mediated topological phenomena, but instead further establishes the potential of these compounds by demonstrating several unusual properties possessed by two-dimensional electron gases induced at the surface of $PtSe_2$.

Chapter 6

Rb dosed 1T-PtSe$_2$: A model gated semimetal

Chapter 5 demonstrated how a discrepancy in the interlayer hopping and spin-orbit coupling strengths between PdTe$_2$ and PtSe$_2$ is sufficient to drive an effective crystal field sign reversal in the anti-bonding p-orbital manifold. As a result, the Fermi surface of PdTe$_2$ is composed in part of topological surface states but the Fermi surface of PtSe$_2$ is entirely bulk derived. This Chapter focusses on the latter, and in particularly how its multi-valley composition can support an unconventional two-dimensional electron gas (2DEG) when electronically gated. This result provides insight into the added potential of semimetallic systems as hosts for induced 2DEGs relative to their more traditional semiconducting counterparts. The Chapter will begin with an brief overview of electrical gating in semiconducting systems.

6.1 Gated Semiconductors

6.1.1 Solution to Poisson's equation for a single charge carrier type

Chapter 2 provided a simple argument for how the application of an electrostatic potential normal to a completely lattice-decoupled quasi two-dimensional electron gas (2DEG), produces a band structure of the form $E(k) \propto k_{\parallel}^2 + k_z^2 + \alpha_R k_{\parallel}$. The term in $k_z \propto n_z/L_z$, where $L_z \ll L_x, L_y$, demonstrates the possibility of realising an energetic ladder of sub-bands, one for each accessible n_z. Each sub-band mimics the bulk in-plane band structure $E(k_{\parallel})$, but without the constraints imposed by inversion symmetry. In that simplified discussion, the 2DEGs were confined by an effective quantum well imposed by the applied electric field $E(\boldsymbol{r}) = E_0\hat{\boldsymbol{z}}$.

In a real system, the form of any band banding potential acting to quantum confine subbands has to obey Poisson's equation [198]:

$$\nabla^2 V(z) = -\frac{1}{\epsilon_b \epsilon_0}\rho(z); \quad \rho = e_0[\rho_e(z) - \rho_{e,\text{bulk}} - \rho_h(z) + \rho_{h,\text{bulk}}], \tag{6.1}$$

where $V(z)$ is the potential describing electronic band bending near the surface and ϵ_b is the static permeability of the crystal relative to the vacuum permeability, ϵ_0. $\rho(z)$ describes the space charge profile as function of depth into a sample surface, and is the sum the hole (h) and electron (e) charge densities, $\rho_e(z)$ and $\rho_h(z)$, and the total number of bulk ions, $\rho_{e,\mathrm{bulk}}$ and $\rho_{h,\mathrm{bulk}}$.

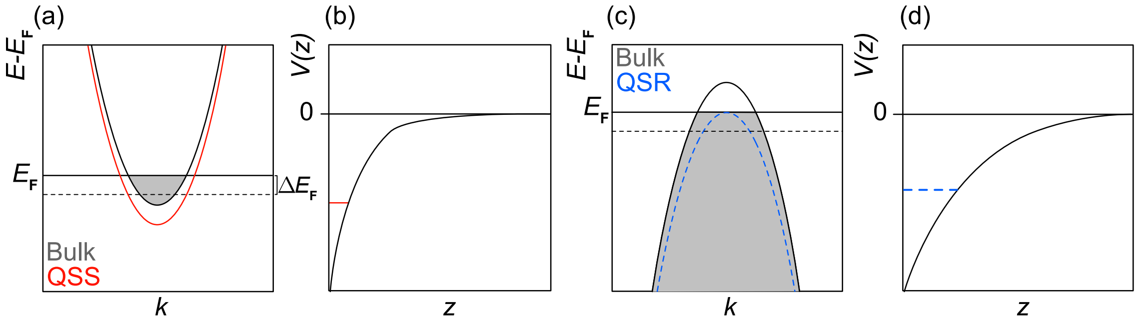

FIGURE 6.1: **Adding electrons to electron and hole systems.** (a) Schematic of chemical potential shift (ΔE_F) and formation of a quantised surface localised state (QSS) following the addition of electrons. (b) Corresponding schematic of the potential $V(z)$ for the case outlined in (a). (c-d) Equivalent diagrams for the case of a hole system, where any quantised sub bands would be better described as a surface resonances (QSR).

A non-trivial solution requires a deviation of $\rho_{e,h}(z)$ from the bulk values in the near surface region, either achieved naturally on, e.g. a cleaved compound with residual surface charge, or induced from an extrinsic electrical gating. In ARPES experiments the latter is mimicked through the deposition of a dilute concentration of an electropositive alkali metal, which readily donates electrons to the sample surface.

The following boundary conditions must be met:

$$V(z \to \infty) = 0; \quad \frac{dV(z=0)}{dz} = \frac{eN_{\mathrm{SS}}}{\epsilon_b \epsilon_0}. \tag{6.2}$$

For a charge neutral system, the total space charge in the bulk, $\rho(z \to \infty)$ must become zero, enforcing the former condition presented in Eqn. 6.2. The latter requires that the divergence of the potential at the surface ($z = 0$), is equal to the deposited total charge, given by eN_{SS}.

The potential typically finds a solution of the form $V(z) \propto -[\exp(-z/r_{TF})]/z$, where $r_{TF} \propto 1/k_F$ is the Thomas-Fermi screening length [198]. This sets the spatial extent of the quantum well, and hence the delocalisation of any confined sub-bands within. The larger k_F, the shallower the potential well and so the higher the zero point energy. Metallic systems which have a large k_F are therefore typically incapable of hosting quantised 2DEGs, whereas semiconductors provide an ideal platform on which to stabilise 2DEGs.

Fig. 6.1 shows schematic band structures and $V(z)$ profiles the case where electrons are added to the system and there there is only a single bulk conduction or valence band near E_F. For both an electron (Fig. 6.1(a-b)) and hole (Fig. 6.1(c-d)) system, the Fermi level is shifted upwards with the addition of electrons, and therefore the charge profile, $\rho(z)$, is in both cases more electron rich at the surface than in the bulk. The potential, $V(z)$, necessarily finds a monotonic downward band bending as its solution, driven in both cases by the negative space charge build up in the sub-surface layers, screening the positive surface ions. This downwards band bending provides the effective quantum well required for confining quantised versions of the bulk electron pockets within the electronic structure. Note, however, that this form of band-bending is only confining for electron bands. If a quantised two-dimensional hole gas was to form here from electron deposition, then it would necessarily become resonant with the three-dimensional bulk hole band and adopt a wavefunction delocalised over a spatial scale exceeding r_{TF}.

6.1.2 Applications from gated semiconductors

Band bending in semiconducting systems has been exploited for decades, and forms the basis of all modern day electronics [199]. Many potential 'next-generation' applications additionally require the formation of 2DEGs within the band-bending potential, occurring naturally both at the interface between certain oxide materials (e.g. between ABO_3-type perovskite oxides) [42, 43], or in systems developing residual surface charge, either naturally upon cleaving, or by developing vacancies with air exposure [36, 38–41].

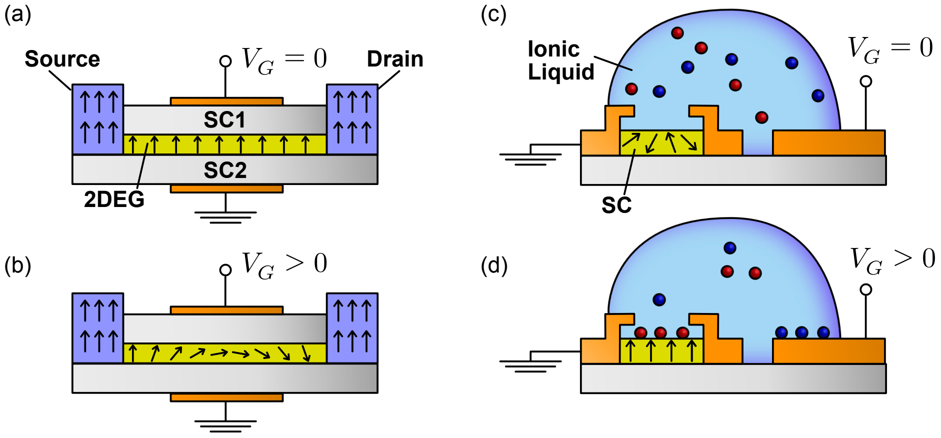

FIGURE 6.2: **Controlling spin with electric fields.** (a-b) Operational principal of a Datta-Das style spin FET [32]. When $V_G = 0$, there is a negligible Rashba effect in the 2DEG at the interface of the two semiconductors (SC) and so the measured spin orientation at the drain is the same as injected at the source. (b) When $V_G \neq 0$, spin degeneracy in the 2DEG is lifted enforcing a spin precession across the 2D sheet. (c-d) Inducing ferromagnetism with ionic liquid gating [200]. A non-zero V_G creates layer of single-charge ions, inducing ferromagnetism in TiO_2.

A sample surface or interface is inherently inversion asymmetric and so, as introduced in Chapter 2, the band structure of the 2DEG induced by any of the mechanisms listed above needs not be spin degenerate. Low-dimensional electron systems are therefore potentially useful for 'spintronic' based applications. Any functional spintronic device would require a tuning parameter for the size of the spin-splitting within the 2DEG, however. Inducing and controlling 2DEGs on charge-neutral systems by electrical gating is therefore of current interest [44, 45]. In these systems, tuning the applied gate voltage provides direct control over the shape and depth of the confining potential profile, changing the scale of inversion symmetry breaking and hence directly altering the degree of spin-splitting in the 2DEG [36, 38–40, 45].

'Datta-Das' style spin-FETs, mentioned briefly in Chapters 2 and 4 operate using this mechanism [32–34]. A 2DEG is realised at the interface of two zinc-blende structured metal pnictides, (Al, Ga, In)(As, Sb). As illustrated in Fig. 6.2(a-b), a gate voltage is applied normal to the 2DEG plane to control the coefficient of the spin-splitting term, α_R. A 'source' ferromagnet is placed at one end of the 2DEG, acting to proximity polarise electrons within. In the presence of the Rashba effect, the spins must naturally precess across the 2DEG; the rate of precession measured by a 'drain' ferromagnet at the other side [32, 34]. The rate of spin precession can be written as

$$\Delta\theta = \Delta k_F L = \frac{2m^*\alpha_R(V_G)L}{\hbar^2}, \tag{6.3}$$

where $\Delta\theta$ is the change in spin orientation across the 2DEG , L is the length of the 2DEG, m^* is the effective mass, and Δk_F is the momentum separation of the spin-split pair at the Fermi level [32, 34], controlled by the applied potential V_G. When V_G is zero, the degree of inversion asymmetry is minimal with the Rashba coefficient, α_R, near zero and so the spin precession is negligible.

More recently, similar operational principles have been used to create electrically controlled room-temperature ferromagnetism in TiO$_2$/LaAsO$_3$ interfaces using *ionic liquid gating* [200]. Fig. 6.2(c-d) demonstrates the general principle [201, 202]: A liquid electrolyte forms a contact between the gate electrode and the compound. When the gate voltage is non-zero, ions of a single-charge species form a ≈ 1 nm thick charge carrier sheet, forming an effective electric field normal to the system on the order of 10 MVcm^{-1}. This mediates a ferromagnetic coupling in that case [200]. Similar manipulation of magnetic order in two dimensions has been demonstrated on Gd-doped GaN [203] and in the LaTiO$_3$/SrTiO$_3$ interface [204].

The transition metal dichalcogenide (TMD) family is also known to produce novel low- dimensional properties when electrically gated. As discussed in Chapter 4, although globally inversion symmetric, the group-VI semiconducting TMDs have an intrinsic spin-valley locking which, when layer degeneracy is lifted, enforces a strong out-of-plane (Zeeman-like) spin splitting at the K point valence bands due to the layer-localised in-plane electric dipole [142, 205]. Electrically gating these compounds lifts the layer degeneracy whilst providing a tuning paremeter for the degree of the resultant Zeeman-like spin splitting [44, 143]. The additional carriers are sufficient to create a superconducting state, also accessed via pressure [206], here manifesting as 'Zeeman-protected' two-dimensional Ising superconductivity [207–209].

Despite the long-lasting, intense research effort into quantum confined quasi-2DEGs, studies almost exclusively use semiconducting material systems as their basis, warranting analogous studies in systems with other ground state structures and properties.

6.2 Rb dosed PtSe$_2$

The Ising superconducting state realised in 2H-MoS$_2$ discussed above is a direct consequence of symmetry breaking in a TMD. By electrically gating, a competition between the in-plane electrical dipole inherent to the 2H-structure, and the effective out-of-plane dipole provided by the quantum well itself is created, producing a complex spin-texture of the confined 2DEG and permitting the formation of the aforementioned two-dimensional superconducting state.

Symmetry breaking in 1T-PtSe$_2$ can also be expected to give rise to emergent low-dimensional physics. Although inversion symmetry is maintained down to single monolayer in a 1T structure, there is a local inversion asymmetry within each chalcogen (X) sublayer of the X-M-X formula unit along the c-axis. Here, though, the effective sublayer-locked dipole is out-of-plane, providing the potential for unlocking an in-plane spin-splitting, if the electronic wavefunctions are sufficiently localised. Indeed, in analogy to the 'hidden' out-of-plane spin polarisation observed in spin-resolved ARPES measurements of bulk 2H-MoS$_2$ [145], 2H-WSe$_2$ [141] and 2H-NbSe$_2$ [147], an in-plane spin signal has been obtained in monolayer PtSe$_2$, despite global inversion symmetry [148]. Therefore, in contrast to the 2H-TMDs, the intrinsic local inversion asymmetry to the topmost Se layer can act to enhance the magnitude of a Rashba-like spin splitting in any confined 2DEGs stabilised on the surface of the bulk compound.

PtSe$_2$ is not semiconducting, however. The shorter Thomas-Fermi screening length is an added complication when attempting to confine a 2DEG at the surface of its semimetallic bulk. This semimetallic ground state will be overviewed next. Once again, all DFT calculations within this Chapter are provided by M. S. Bahramy at RIKEN and the University of Tokyo.

6.2.1 The semimetallic ground state of PtSe$_2$

The near-E_F three dimensional band structure of PtSe$_2$ is overviewed in Fig. 6.3. There are three separate bands contributing to transport in this system [193]. Firstly, there is a hole band centred at $\bar{\Gamma}$. This is the chalcogen p_z derived valence band which plays a role in the formation of the type-II bulk Dirac point and an inverted band gap below the Fermi level, as discussed in Chapter 5. Its diffuse appearance in ARPES measurements is consistent with its three-dimensional nature, necessary for the formation of the topological states. The other two pockets are electron-like bands. These are similarly three-dimensional with each pocket localised to only a small k_z region (see e.g. Fig. 6.3(a)).

One set of electron pockets are situated approximately midway along the $\bar{\Gamma}$-$\bar{\mathrm{M}}$ directions of the surface Brillouin zone (henceforth referred to as the $\bar{\mathrm{S}}$ points). The constant energy k_x-k_y cuts in Fig. 6.3(a) (corresponding to $k_z \approx \pm 0.6\pi/c$) show how there are three such pockets each side of the Γ plane in k_z, with their triangular coordination switching about $k_z = 0$, reminiscent of the chalcogen sublayers in the real-space crystal structure (e.g. Fig. 4.4). There is excellent agreement between theory and experiment, although the k_z broadening here is sufficiently large (Chapter 5 and [173]) that signatures of the Γ centred hole bands are also present in the experimentally obtained constant energy contours in Fig. 6.3(a).

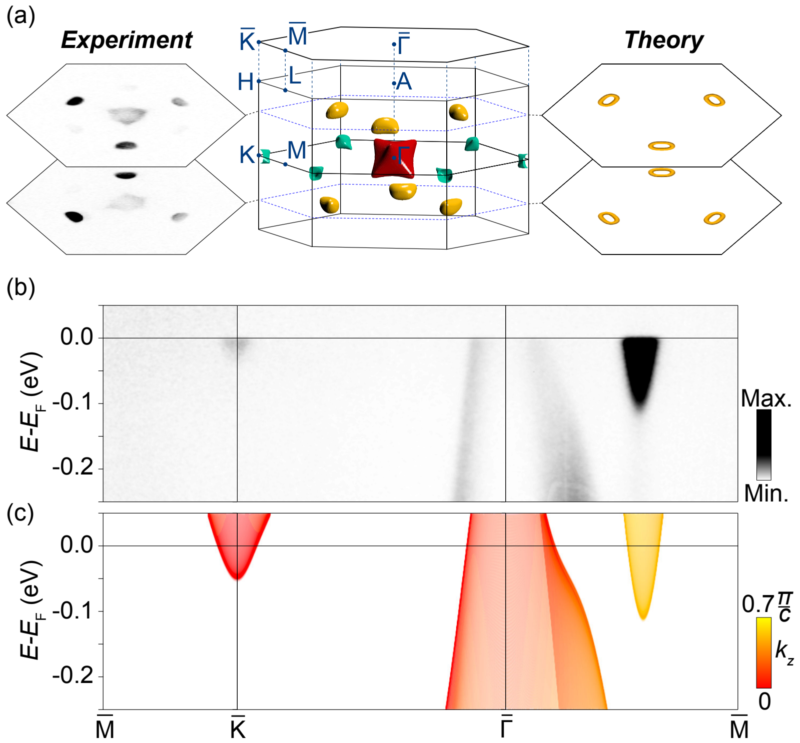

FIGURE 6.3: **Semimetallic ground state of 1T-PtSe$_2$.** (a) Three-dimensional Fermi surface (middle) provided by bulk DFT calculations, with insets at $\approx \pm 0.6\ \frac{\pi}{c}$ from ARPES (left, $h\nu$ =99 eV (left, top) and 120 eV (left, bottom), $E_F \pm$ 30 meV) and DFT (right). (b) $\overline{\mathrm{M}}$-$\overline{\mathrm{K}}$-$\overline{\Gamma}$-$\overline{\mathrm{M}}$ ARPES dispersions ($h\nu$ =53 eV). (c) Corresponding k_z resolved bulk DFT calculations.

The second set of electron pockets are situated exactly at the K points of the bulk Brillouin zone, apparent in electronic dispersions shown in Fig. 6.3(b). These are barely occupied, with only a tail of spectral weight falling below the Fermi level experimentally. Fig. 6.3(c) additionally shows k_z projected bulk DFT calculations of the pristine compound, which can be used to verify that the electron and hole carriers in the bulk of PtSe$_2$ are exactly compensated, verifying the semimetallic ground state.

Despite this, this multi-band Fermi surface has a k_F sufficiently small that the Thomas-Fermi screening length, r_{TF}, remains modest in size and small enough that a bend bending potential can still confine quasi two-dimensional electron gases, as will be demonstrated below.

6.2.2 Stabilising a 2DEG at the surface of 1T-PtSe$_2$

Electrical gating of PtSe$_2$ was simulated in ARPES by the deposition of Rb atoms from a well-degassed SAES getter operated at 5.6 A for 8 minutes, immediately following the sample cleave.

Fig. 6.4 provides an overview of the changes to the near-E_F electronic structure following Rb deposition. A schematic representation of the surface charge accumulation is provided in Fig. 6.4(a). Rb is highly electropositive and therefore readily donates its electrons to the near-surface layers of PtSe$_2$. There is a build up of negative charge in the near surface region,

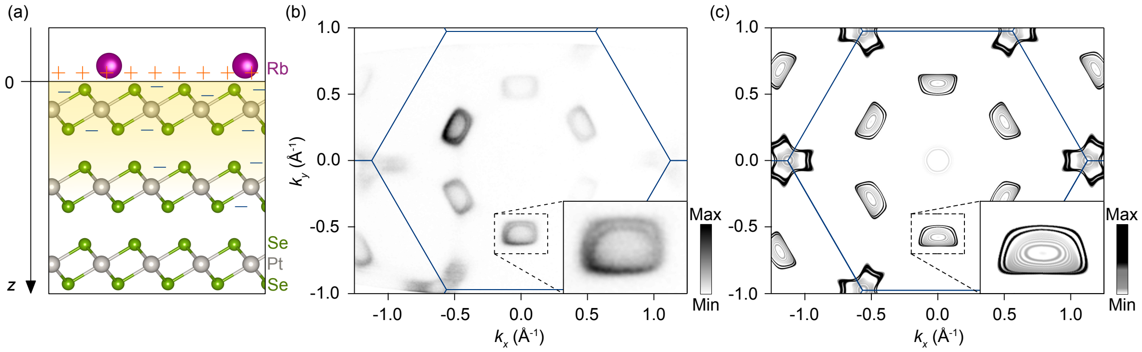

FIGURE 6.4: **Fermiology of Rb dosed PtSe$_2$.** (a) Schematic diagram of Rb deposition onto PtSe$_2$. (b) Fermi surface map (E_F±12 meV, $h\nu$ =37 eV) as obtained by APRES following Rb deposition. (c) Equivalent Fermi surface map as provided by DFT based surface slab calculations.

acting to screen the positive charge of the Rb ions. This creates a band bending effect, acting to push all electronic bands to a higher binding energy, whilst being sufficiently deep to quantum confine a copy of the bulk electronic structure, as shown below.

Fig. 6.4(b) shows the Fermi surface of PtSe$_2$ following Rb deposition. The shift of chemical potential leads to an increase in size of both the $\overline{\mathrm{S}}$ and K pockets relative to the Fermi surface maps shown in Fig. 6.3. In addition, Fig. 6.4(b) clearly shows how sharp regions of spectral weight develop around the perimeter of the bulk $\overline{\mathrm{S}}$ pockets. This sharpening signifies a deviation from the three-dimensional nature of the bulk electronic structure and as such, these intense rims can be attributed as quantum confined sub-bands of the underlying bulk electron pockets, still visible as a shading within the area enclosed by the new sharp spectral weight.

The two-dimensionality of the new sharp spectral weight at $\overline{\mathrm{S}}$ can be verified through photon energy dependent ARPES measurements, shown in Fig. 6.5(b). In contrast to equivalent measurements on the pristine sample, shown in Fig. 5.6(a) and the previous Chapter (Fig. 5.6), the bands at $\overline{\mathrm{S}}$ do not disperse in momentum over more than two full Brillouin zones in k_z, unlike the bulk valence bands at deeper binding energies.

Fig. 6.4(c) shows an equivalent Fermi surface map to that presented in Fig. 6.4(b), as provided by DFT-based slab calculations with an additional on-site band bending potential, solved self-consistently in line with Eqn. 6.1. The $\overline{\mathrm{S}}$ point pockets are again shown to take on a near-rectangular appearance, in excellent agreement to experiment. Both this and the experimental equivalent in Fig. 6.4(b) clearly show a band splitting on the low momentum side of this pocket, suggesting the presence of either multiple sub-bands or a spin-splitting within a single subband. However, the DFT calculations also predict quantum confined versions of the bulk K pockets, again with an apparent band splitting, maximum along the $\overline{\Gamma}$-$\overline{\mathrm{K}}$ direction. This band splitting is not clearly resolved in experiment, with the pocket at K remaining diffuse, taking on a triangular appearance with extended regions of spectral weight along the $\overline{\Gamma}$-$\overline{\mathrm{K}}$ directions.

A more detailed electronic structure in the vicinity of the K points following deposition is outlined in Fig 6.6. Along the $\overline{\mathrm{M}}$-$\overline{\mathrm{K}}$ directions, the pockets are relatively sharp, but along $\overline{\Gamma}$-$\overline{\mathrm{K}}$, there is an additional intense region of spectral weight that develops, with a sudden increase

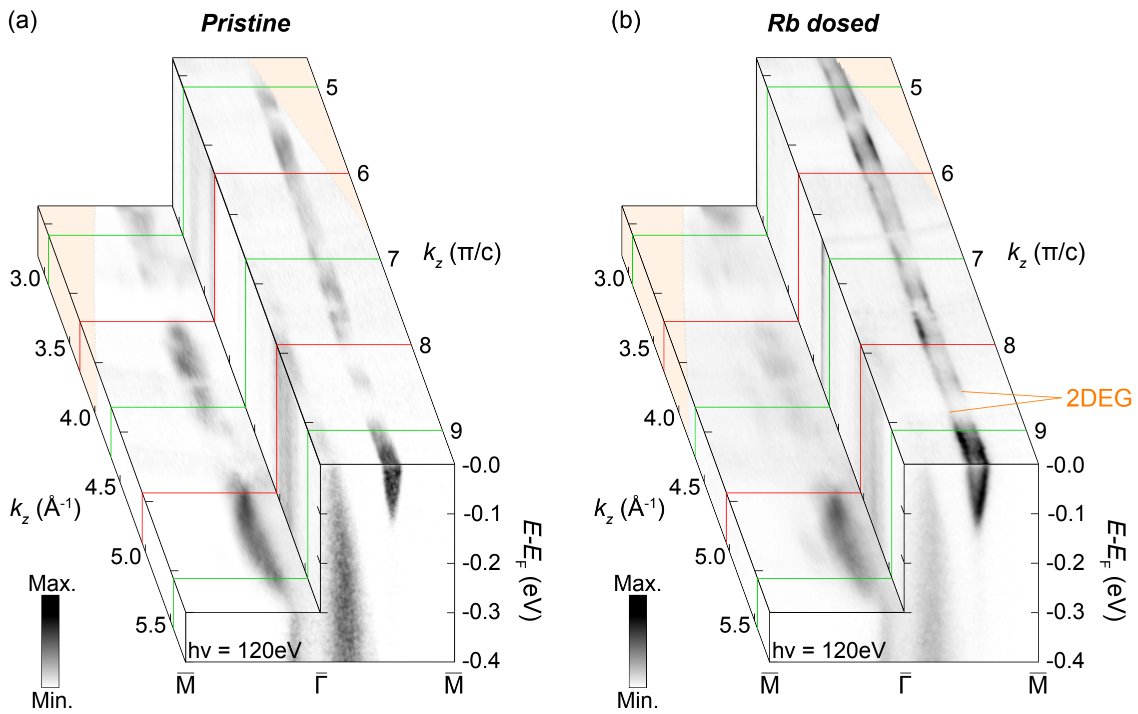

FIGURE 6.5: **Establishing the dimensionality of the quantised subband states at $\bar{S}$.** Photon energy dependent ($h\nu$=20-120 eV) ARPES measurements of (a) pristine and (b) Rb dosed PtSe$_2$. Constant energy k_z-$k_{||}$ cuts are integrated within an energy window of 24 meV, centred at E_F and -0.3 eV.

in effective mass in the band dispersion approximately 10 meV below E_F. The reduced band gradient towards the $\bar{\Gamma}$ point results in the extended tail towards the zone centre as seen in the Fermi surface maps in Fig. 6.4(b) and Fig. 6.6(a). At the time of writing, the band dispersion in the vicinity of $\bar{K}$ is not well understood. It is possible that a second, heavier, electron pocket does exist at K, but lies just above the Fermi level in DFT, but below E_F in experiment. This could sufficiently complicate the experimental picture such that the band splitting predicted by DFT at K is not resolved.

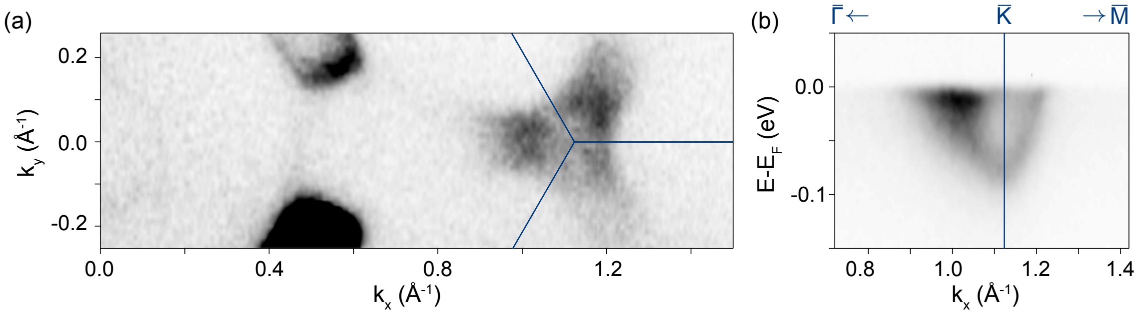

FIGURE 6.6: **Evolution of K point in Rb dosed PtSe$_2$.** (a) Fermi surface map ($h\nu$ =37 eV, E_F±12 meV, p-pol) and (b) $\bar{\Gamma}$-$\bar{K}$-$\bar{M}$ dispersion ($h\nu$ =37 eV, p-pol + s-pol) of Rb dosed PtSe$_2$.

Extracting the 2DEG carrier density

For the DFT-based calculations shown in Fig. 6.4, two free parameters needed to be fixed in order to recreate the experimental condition. These are the dielectric constant of the solid, required for the static permeability in Eqn. 6.1, and the total amount of band bending. The former is taken form first-principles calculations presented in [210]. The latter can be varied until the experimentally realised surface sheet carrier density is obtained. The carrier density can be extracted directly from the Fermi surface map presented in Fig. 6.4(b).

Luttinger's theorem states that the number of charge carriers obeys the following condition [211],

$$n = g \int \frac{d^D k}{(2\pi)^D}, \tag{6.4}$$

where n is the number of charge carriers, D is the dimensionality of the system, and g is the spin and valley degeneracy, characterising how many equivalent bands exist within the first Brillouin zone. Only the deposited carriers which populate the surface localised 2DEG are of interest, and therefore D =2.

A good estimate of the pocket areas can be obtained by transforming the Fermi surface map from $k_x - k_y$ coordinates to k_r-α, where k_r is the radial $k_{||}$-point and α is the azimuthal angle. The Fermi surface can be approximated as slices each of area $\frac{\Delta\alpha}{2\pi}\pi k_r^2$, where $\Delta\alpha$ is a chosen azimuthal resolution. The sum over such slices over the region of the Brillouin zone which a pocket occupies provides an approximation to the area of the pocket. This procedure is shown schematically in Fig 6.7.

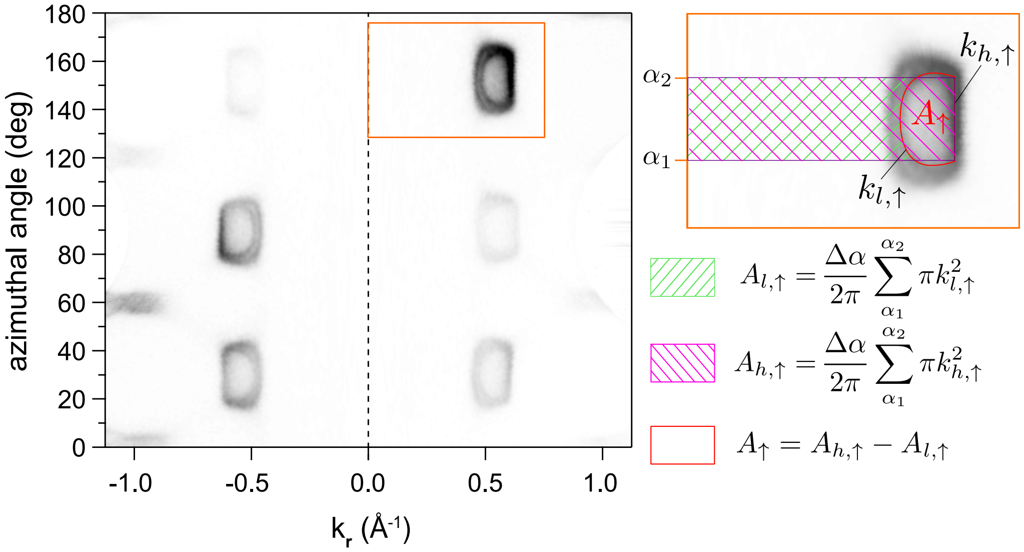

FIGURE 6.7: **Extracting the surface sheet carrier density.** The Fermi surface map in Fig. 6.4(b) is transformed into a polar coordinate system. A schematic diagram showing the extraction of pocket areas is shown in the inset (the pocket refered to as $A_{\overline{S},\uparrow}$ in the text is used here as an example). k_h and k_l are the high and low momentum sides of a pocket for at a given azimuthal angle. $\Delta\alpha$ is the chosen step size for the summation over α.

Assuming that there is negligible change to the hole pockets at Γ, the surface sheet density is made up of the $\overline{\mathrm{S}}$ and K point pockets, of which there are six and two per Brillouin zone respectively. The spin degeneracy of the K point pockets is assumed to be 2, since there is no band splitting resolvable in Fig. 6.6 and Fig. 6.4(b). The spin degeneracy of the $\overline{\mathrm{S}}$ pockets was assumed to be 1, with the two separated rims of spectral weight assigned as two halves of an oppositely spin-polarised Rashba-split single sub-band. Note that this assumption is not robust at this stage, but it will be justified below. The electron count can then be expressed as areas in k-space of each pocket type, $A_{\overline{S},K}$:

$$n = \frac{6}{(2\pi)^2}(A_{\overline{S},\uparrow} + A_{\overline{S},\downarrow}) + \frac{4}{(2\pi)^2}(A_K). \tag{6.5}$$

From this, a surface carrier concentration of approximately $n = 10^{14}$ cm^{-2} is obtained, similar in magnitude to what is typically induced in heavily dosed semiconducting systems via alkali-metal deposition [44]. Using this sheet carrier density, the resultant Fermi surface presented in Fig. 6.4(c) is produced, with excellent agreement to experiment.

Large spin anisotropy from orbital character

A spin-splitting of the quantised $\overline{\mathrm{S}}$ pocket is just one possible origin for the observed band-splitting. Although all quantised 2DEG states should exhibit Rashba-type spin splitting (for non-zero $\boldsymbol{L}\cdot\boldsymbol{S}$), this is often much less than the resolution of experiment (see for example [39]). Instead, the two branches surrounding the $\overline{\mathrm{S}}$ pocket could be explained as two spin degenerate sub-bands with different n_z values. In addition, the Fermi surface maps in Fig. 6.4 demonstrate a significant anisotropy in the magnitude of band splitting. Whilst a large splitting is observed on the low momentum side of the quantised $\overline{\mathrm{S}}$ pocket, the splitting reduces to near degeneracy on the high momentum side.

Fig. 6.8(a) shows experimentally obtained band dispersions of pristine and Rb-dosed PtSe$_2$ along the $\overline{\Gamma}$-$\overline{\mathrm{M}}$ direction. Once again, the anisotropy of band splitting on the low and high momentum sides of the pocket following Rb deposition is clear, with the splitting resolvable down to the band minimum. Orbitally-resolved surface slab-based calculations are shown over the same region of $E(k)$ in Fig. 6.8(b). In addition, spin-resolved calculations projected onto the chiral component are shown in the inset of Fig. 6.8(b). This verifies that that the band splitting discussed above is indeed a spin splitting of the Rashba-type, rather than two near-degenerate discrete sub band copies.

The anisotropy in the size of the spin splitting can be understood as a natural consequence of an orbital character switch across the underlying bulk $\overline{\mathrm{S}}$ pocket. The orbitally projected DFT calculations for the pristine compound in Fig. 6.8(b) show how the low momentum side of the pocket has mixed p-character with a significant $p_{x,y}$ contribution, whereas the high momentum side of the pocket is almost entirely of p_z character. The $\boldsymbol{L}\cdot\boldsymbol{S}$ contribution for a predominantly p_z-derived band can be expected to be small ($l_z = m_l\hbar; m_l = 0$), growing in magnitude only with significant orbital mixing. The 2DEG inherits the orbital character of

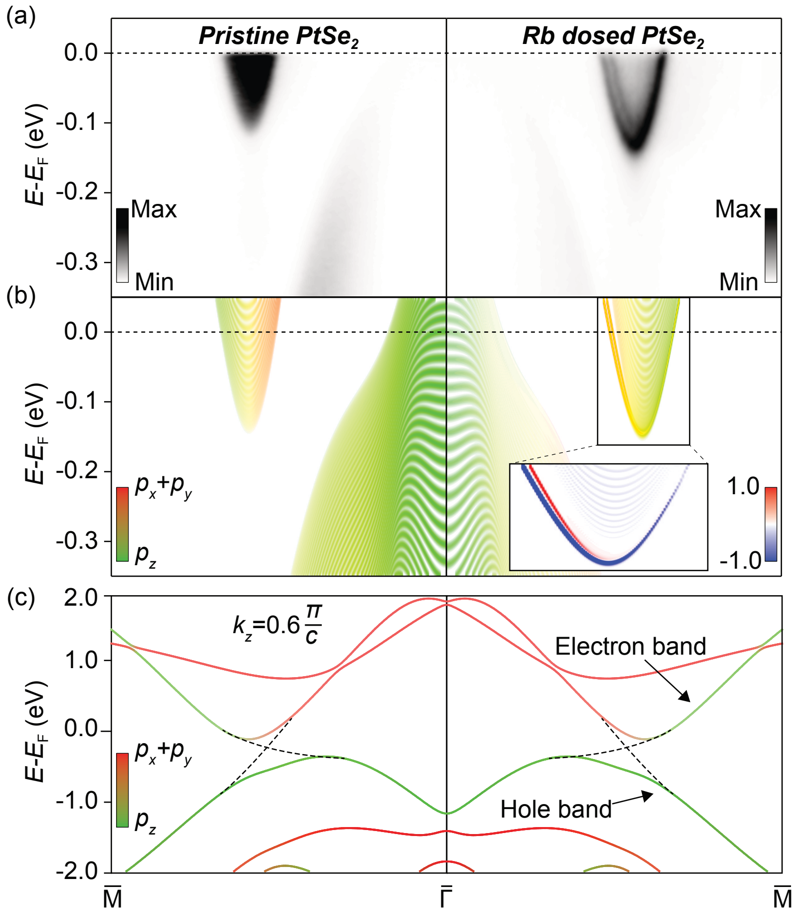

FIGURE 6.8: **Orbital character dependent spin-splitting in Rb-dosed PtSe$_2$.** (a) Pristine (left) and Rb-dosed (right) ARPES dispersions ($h\nu$ =37 eV) along the $\bar{\Gamma}$-$\bar{M}$ direction. (b) Orbitally projected DFT based surface slab calculations over an equivalent range of the electronic structure as in (a). The inset in (b) shows the spin-projection of the confined 2DEG at $\bar{S}$ for the chiral component. (c) Orbitally projected bulk DFT calculations for k_z =0.6 $\frac{\pi}{c}$. The dashed lines indicate the case for zero hopping between $p_{x,y}$ and p_z orbitals.

the underlying bulk band structure, and hence the spin-splitting within is found to be non-negligible only on the low momentum side of the pocket where there is significant $p_{x,y}$-orbital character contribution.

The origin of the orbital character switch is made clear by Fig. 6.8(c), demonstrating how the bulk $\bar{S}$ point pocket is formed from the hybridisation of a hole-like and electron-like band, with $p_{x,y}$ and p_z characters respectively. Such a spin anisotropy can therefore expected to be common place in strongly hybridised multi-band semimetallic systems.

Anomaly in the Rashba coefficient

Although highly anisotropic, the size of the maximum magnitude of the spin splitting here is very large compared to 2DEGs in other systems. Along the $\bar{\Gamma}$-$\bar{M}$ direction, the spin-splitting on the low momentum side of the $\bar{S}$ pocket is $\Delta k_F = 25 \pm 1$ mÅ^{-1}. To put this into context, one can extract the same measure of splitting from the InAs 2DEGs induced in the first operational spin-FETs of the Datta-Das type [34] using Eqn. 6.3. In that case, the effective mass, $m^* = 0.05m_0$ [34] and the largest Rashba coefficient recorded is $\alpha_{R,\max} = 13 \times 10^{-12}$ eVm [34]. This gives a maximum $\Delta k_F = 1.7$ mÅ^{-1}, fifteen times smaller than the observation in PtSe$_2$ here.

TABLE 6.1: Approximate spin splitting magnitudes at the Fermi level (Δk_F) extracted from the literature.

Compound	Δk_F (mÅ^{-1})	Reference
InAs	1.7	[32, 34]
Cu(111)	6	[212]
Ag(111)	<10	[213]
CO dosed Bi$_2$Se$_3$	15	[45]
KTaO$_3$	<20	[39]
Au(111)	23	[37, 213]
Rb dosed PtSe$_2$	25	[168], here
Rb dosed Bi$_2$Se$_3$	37	[45]
BiTeI	130	[48]
PtCoO$_2$	130	[214]
Bi/Ag alloy	130	[215]
PtRhO$_2$	160	[214]

Estimates for Δk_F values in other systems hosting Rashba-split bands at the Fermi level are shown in Table 6.1. It should be noted that the 'delafossite oxides' are the current record holders for Rashba splittings, with their AO$_2$ (A= Co, Rh, Cr) derived surface electronic structures limited only by atomic spin-orbit coupling strength, rather than the degree of inversion asymmetry [214].

The Rashba-split bands in PtSe$_2$ have a larger splitting than the p- and d- derived Rashba surface state of Au(111) [216]. Gold has an very large atomic mass in comparison to Se, and therefore the $\boldsymbol{L} \cdot \boldsymbol{S}$ term is large. This suggests that the spin-splitting seen here for the Se p-derived bands is anomalously large. Indeed, from the dispersion in Fig. 6.8(a) an energetic splitting of approximately 40 meV near the Fermi level can be extracted. This is ≈20% of the atomic spin-orbit coupling strength of Se (0.22 eV [217]). This can be compared to an equivalent value in the 'giant Rashba system' BiTeI, in which the Rashba splitting of the Bi character quantum well states is ≈0.3 eV, 24% of the atomic spin-orbit coupling (Bi ASOC: 1.25 eV [48, 217]).

The spin-splitting in BiTeI is not limited by the degree of inversion asymmetry imposed by the surface potential, but is instead possessed intrinsically within its bulk structure. To have a comparable spitting in PtSe$_2$ strongly suggests an enhancement of inversion symmetry breaking from an anomalously steep quantum well relative to what is typically achieved in gated systems. Some insight is provided by considering the resultant quantum well profile, $V(z)$, obtained from the self consistent solution to Poisson's equation and applied in the DFT-based slab calculations presented above. This will be discussed next, in the broader context of the potential of semimetallic systems for the basis for two-dimensional spin transport in devices.

6.2.3 Outlook: PtSe$_2$ devices

Fig. 6.9(a) shows the resultant potential profile, $V(z)$, obtained in conjunction with the DFT calculations shown in this Chapter. Unusually, this potential is non-monotonic, exhibiting a hole accumulation region ($V(z) > 0$) in the sub-surface layers beneath the more conventional electron accumulation layer ($V(z) < 0$). $V(z)$ can only deviate from a monotonic form for an electron doped system if at some z there is a sign reversal in the space charge density, $\rho(z)$. Fig. 6.9(b) shows how that is achieved here. The hole-space charge function, $\rho_h(z)$, is peaked at approximately 25 Å where it simultaneously becomes larger in magnitude than its bulk value as well as $\rho_e(z)$. This requires an undamped exchange of electron and hole-like carriers in the near surface region, not possible in a single carrier system.

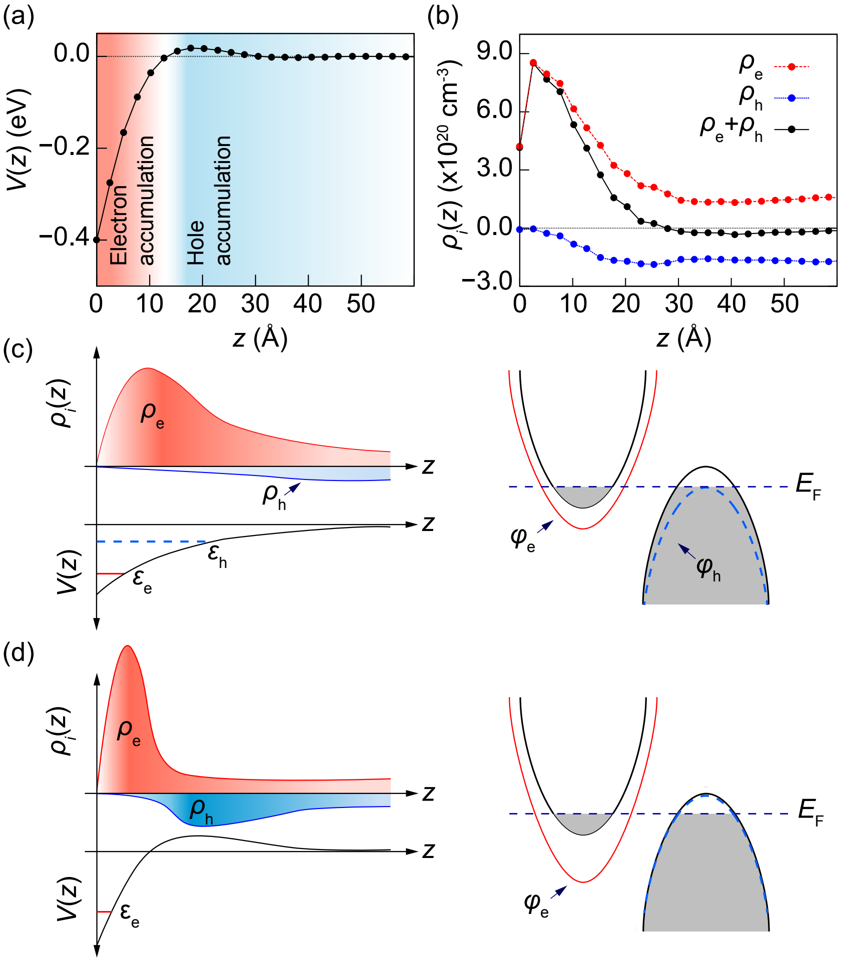

FIGURE 6.9: **Dual quantum confinement in Rb-dosed PtSe$_2$.** (a-b) Calculated potential profile, $V(z)$, (a) and charge density profile, ρ', (b) for $N_{SS} \approx 10^{-14}$ cm^{-2}. (c-d) Schematic diagrams of potential profiles, charge density profiles, and surface electronic structures for the case where the quantum confinement is 'conventional' (c) (as in Fig. 6.1) and when charge pumping is allowed, 'dual confinement' (d).

Section 6.1.1 demonstrated that quantised hole bands from electron deposition typically do not form, as they would necessarily adopt wavefunctions spatially delocalised over a region exceeding r_{TF} due to becoming resonant with the bulk bands. In the case where there is a coexistence of both electron and hole pockets at the Fermi level, a quantised sub-band copy of either pocket cannot form in isolation. Instead, the 2DEG electronic structure must include quantised versions of both the electron and hole bands, and so this energetically unfavourable scenario, displayed again schematically in Fig. 6.9(c), must be circumvented if a quantised two-dimensional electron gas is to form.

This can be achieved by pumping charge between two spatially separated regions, forming a hole accumulation layer. This acts to significantly reduce the depth over which the potential first recovers to its bulk value, minimising the effect of band bending on the hole bands at the cost of steepening the electron accumulation region. This scenario, schematised in Fig. 6.9(d) and verified by calculations for PtSe$_2$ in Fig. 6.9(a-b), is inherently coupled to an increase of inversion symmetry breaking in the immediate sub-surface region, helping to explain the anomaly in the sign of the Rashba spin-splitting discussed in the previous Section.

This 'dual' form of quantum confinement can also explain the presence of only a single sub-band state. The steepening of the electron accumulation region results in a 2DEG which has a smaller spatial extent in the bulk, then it would have done otherwise. L_z is thus sufficiently small as per the discussions in Section 6.1.1 that only a single n_z can be accessed energetically. In other words, the potential profile in the immediate surface region becomes more akin to the case of the surface potential step following the formation of the hole accumulation layer. Similarly, there is no evidence of any hole bands quantised by the hole accumulation regions in the sub-surface layers.

The findings here should be generic to semimetallic systems capable of hosting 2DEGs. The steepening of the potential profile gives semimetallic hosts of 2DEGs potential advantages over their semiconducting counterparts in the design and functionality of spintronic devices. Not only is the Rashba-splitting enhanced, but the hole accumulation region increases the spatial separation between the quasi-2DEG and the bulk charge carriers. This could be exploited as an 'surface-bulk barrier', screening the spin-polarised charge carriers of the 2DEG from the spin-degenerate bulk carriers. In principle, barriers of this form could provide an intrinsic protection against spin decoherence events, for example. Moreover, this crossover from multi-type to single-type carriers at the surface could be exploited as a new form of rectification [168].

It should be noted that the enhanced degree of inversion symmetry breaking in PtSe$_2$ could be additionally aided by the local inversion asymmetry of the Se sub-layers. As discussed in Section 6.2, the Se sub-layers possess an effective out-of-plane electrical dipole, contributing to an in-plane 'hidden' spin-polarisation in PtSe$_2$ monolayers [148]. The electron accumulation region in Fig. 6.9(c) is only 10 Å deep, less than two 1T formula units along the c-axis, and so the top-most Se-layer could contribute to the anomalously large Rashba spin-splittings observed here.

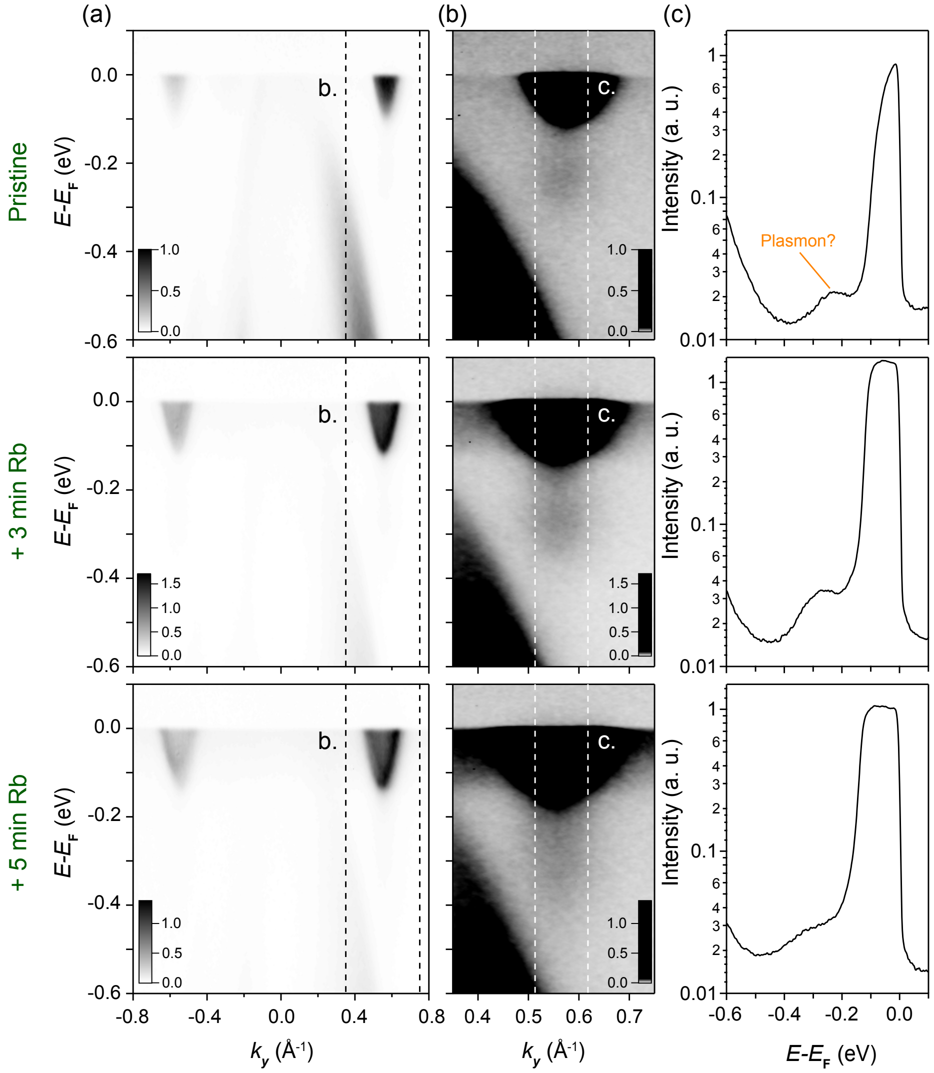

FIGURE 6.10: **Plasmonic signatures in pristine and Rb-dosed PtSe$_2$.** (a) ARPES dispersions ($h\nu$ =37 eV, p-pol) along the $\overline{\Gamma}$-$\overline{M}$ direction for three different quantities of deposited Rb. Pristine (top), 3 minutes, 5.6 A (middle) and a further 5 minutes, 5.6 A (bottom). (b) The data is duplicated over a range indicated in (a) with a strongly enhanced contrast. (c) Angle-integrated EDCs over the range indicated in (b).

6.2.4 Outlook: Plasmonic signatures in PtSe$_2$

The presence of a two-dimensional electron gas at the surface of PtSe$_2$ means that signatures of *electron-plasmon coupling* could be present within an ARPES spectrum. Plasmons are collective oscillations of electron gas density bound to light oscillations, with signatures of electronic coupling in ARPES manifesting as broadened copies of a valence band, renormalised in binding energy by the Plasmon energy [218]. Plasmonic materials can be used to 'trap' light and transmit it into the bulk structure. They are therefore of potential interest for sensing and solar cell applications [219].

Fig. 6.10(a) shows that PtSe$_2$ hosts plasmonic-like signatures even in its pristine form. Band dispersions along the $\overline{\Gamma}$-$\overline{M}$ direction for a pristine compound and two stages of Rb deposition are shown. Significantly over-saturating these datasets, as in Fig. 6.10(b), exposes a region of spectral weight directly below the $\overline{\mathrm{S}}$ point pockets, apparently decoupled from all other bands. Angle-integrated energy distribution curves in Fig. 6.10(c) show a clear peak of spectral weight below the main conduction band.

The energy of a plasmon is approximated by the following equation [220]:

$$E_p = \hbar\omega_p = \hbar\sqrt{\frac{4\pi ne^2}{m\epsilon_0}}, \tag{6.6}$$

where ω_p is the plasma frequency. In order to verify that these enhanced regions of spectral weight are indeed plasmonic signatures, the dependence on the carrier density, n, can be verified by extracting the plasmon position relative to the bulk conduction band for multiple deposited Rb concentrations. This procedure is complicated both by the extremely weak intensity of the candidate plasmonic signature, and by the diffuse nature of the bulk electron pocket, limiting the ability to extract peak positions reliably from distribution curves. Between the dispersions for the pristine compound and following 3 minutes of Rb deposition (5.6A, SAES getter), a shift of ≈ 6 meV is found for the separation of the plasmon mode relative to the leading edge midpoint of the $\overline{\mathrm{S}}$ point pocket. Whilst this shift is consistent with the plasmon assignment, it is within the experimental uncertainties here.

To verify this conclusively, one could utilise *high resolution electron energy loss spectroscopy*, or 'HREELS', in which a low energy electron beam is scattered from a sample target. The resultant 'energy loss' spectrum can inform of vibrational modes, substrate interactions and, importantly, plasmonic response [221, 222]. Very recently, HREELS has been used to find three plasmonic signatures in the group-X TMD PtTe$_2$ [223], of which one corresponds to a three-dimensional 'Dirac plasmon' originating from the bands forming the type-II Dirac cone in that compound. This supports the tentative assignment of plasmon coupling in PtSe$_2$, and it is possible that the more metallic Te-derived equivalent of the bulk $\overline{\mathrm{S}}$ pockets here could contribute to the plasmonic signatures in that study.

6.2.5 Outlook: Changes to the valence band structure

Chapters 4 and 5 show how the group-X TMDs each exhibit at least two topological surface states below the Fermi level, and so it is natural to ask the question of how this surface electronic structure is modified following such a strong surface perturbation offered by Rb deposition.

Figure 6.11(a) again provides an overview of the surface states present in the pristine compound. TSS1 and TSS2 are formed from the anti-crossing of the bonding and anti-bonding chalcogen p_z derived bands with the bonding $p_{x,y}$ derived bands, as discussed extensively in Chapters 4 and 5. The origin of SS3 and SS4 is not exactly known. As discussed in Chapter 5, they are likely distinct from TSS1 and TSS2 and topological in nature, as trivial surface states can not naively expected to occur in van der Waals systems. TSS2b is an extension of TSS2,

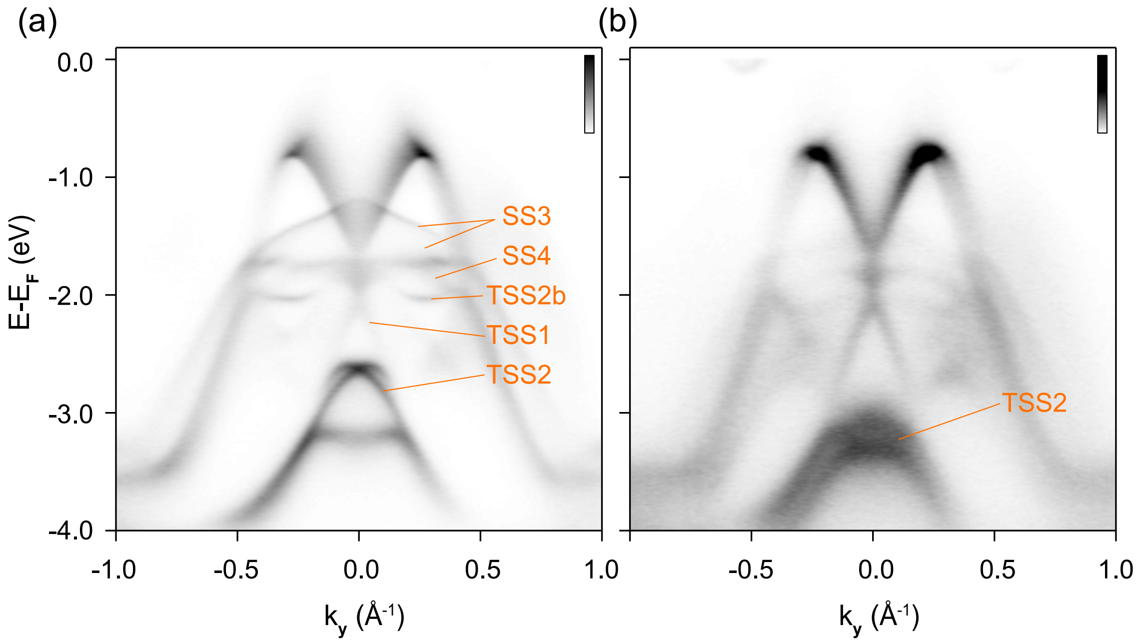

FIGURE 6.11: **Changes to the valence surface electronic structure with Rb deposition.** Pristine (a) and dosed (8 minutes Rb, 5.6A on fresh cleave) (b) ARPES dispersions along the $\overline{\Gamma}$-$\overline{\mathrm{M}}$ direction ($h\nu$ =107 eV). Surface states are indicated, with notation following from Chapter 5.

apparently disconnected form the main state due to the significant in-plane bandwidth of the surrounding bulk bands.

Following Rb deposition, this picture changes significantly. TSS2 is shifted to a higher binding energy by approximately 420 meV, almost merging into the bulk band on which it sits. Whilst this energy shift is consistent with the depth of the quantum well found in calculations (Fig. 6.9(a)), TSS2 becomes significantly broader, developing spectral weight which can be traced out to $k_y \approx 0.5$ Å^{-1}. Its Dirac point is no longer well resolved, although there is some connection between the two ∩-shaped bands centred just below $E - E_F = -3$ eV.

It is possible that the topological interface shifts further into the bulk, with the Rb deposited topmost layers topologically trivial and the bulk topologically non-trivial. The TSS would then exist on a 2D plane further into the bulk, explaining its diffuse nature in ARPES spectra. Consistent with this, TSS2b also becomes broader, losing significant intensity following Rb deposition. However, this would require the unwinding the k_z-mediated inverted band gaps in the near-surface region. Whilst intercalating alkali atoms within a crystal structure is in general able to decouple the topmost layers of the structure and remove the k_z dispersion, the large size of Rb and the low deposition and measurement temperatures (<14 K) make this an unlikely scenario.

The changes to TSS1 are complex. Whilst it appears that it becomes more pronounced, the underlying bulk band structure on which this surface state sits is not easily distinguishable from the topological surface state (see for example, Fig. 5.4). SS3 and SS4 become much weaker, becoming almost unresolvable in the former case. This could be taken an argument for a topologically trivial nature, since the surface states are apparently destroyed by the surface perturbation caused by Rb deposition here. Further datasets with improved statistics and resolution for sequential Rb depositions could shed light on the origin of the changes seen here.

Chapter 7

Conclusions and Outlook

In this thesis, a mechanism for stabilising arrays of type-I and type-II bulk Dirac points (BDPs), multiple topological surface states (TSS) and topological surface resonances was identified and verified in multiple transition-metal dichalcogenides (TMDs). The group-X TMDs, 1T-$PtSe_2$ and 1T-$PdTe_2$ were the focus, each hosting a type-II bulk Dirac cone and at least two topological surface states below the Fermi level. k_z mediated topological ladders were found to persist through the effective doubling of the unit cell to the 2H-structured TMDs, with the 'strong spin-orbit coupled' semiconductor WSe_2 found to host two bulk Dirac points of opposite types, and two topological surface states below the Fermi level. Density functional theory calculations predicted topological ladders in a further three TMDs; 2H-$TaSe_2$, 2H-$NbSe_2$ and 1T-$IrTe_2$, which all undergo structural transitions with cooling temperature. The former two have charge density wave transitions leaving the C_{3v}-protected BDPs in tact, but the latter undergoes a transition to a C_2-symmetric system, wherein the lattice protection of the bulk Dirac points is lost.

The ubiquitous nature of the topological phenomena within the transition metal dichalcogenide material class is largely due to the single-orbital manifold origin. Simply, each TMD member contains a chalcogen p-orbital manifold subject to the same rotational lattice symmetries, and so the topological ladder formed within is retained across the family. Moreover, this same robustness allows broad possibilities for tuning these states. By altering interlayer hopping strengths [83], for example by strain [191] or by chemical substitutions [182, 224], the number, types, and energetic positions of bulk and surface Dirac cones can be altered. This was demonstrated in part by the detailed comparison of the group-X TMDs $PtSe_2$ and $PdTe_2$ wherein slight changes of the unit cell dimensions modifies relative hopping strengths sufficiently to switch the sign of the effective crystal field for the anti-bonding p-orbital manifold, effectively resulting in an extra induced BDP-TSS pair in $PdTe_2$. The additional TSS in $PdTe_2$ is the only topological surface state identified in any of the six TMDs to cross the Fermi level. $PdTe_2$ possesses a bulk superconducting phase intrinsically, and as such this identification provided an opportunity to study the interplay of bulk superconductivity with the topologically non-trivial surface electronic structure. This, along with the possibility of inducing a two-dimensional electron gas in $PtSe_2$ confined by an unconventional band bending profile and exhibiting an enhanced spin-splitting, demonstrates the versatility and promise of the relatively understudied 1T-structured group-X TMDs.

The number of prerequisites for the formation of the topological ladders discussed in this thesis is minimal, and each is commonly occurring. Firstly, the crystal structure must be such that there is a natural disparity in bandwidths along a direction in the Brillouin zone adhering to the rotational symmetry of the lattice. Secondly, this bandwidth disparity must be larger than the energetic separation of these bands imposed by the combination of the crystal field splitting (CFS) and the spin-orbit interaction. The combination of these two factors ensures multiple band crossings occur along a rotationally symmetric axis, wherein bulk Dirac points, protected by the rotational lattice symmetry, and parity inverted band gaps can be produced simultaneously. As a final discussion within this thesis, the question of whether or not analogous physics can occur in systems outside of the TMD family will be addressed, and if so, of the additional properties that such systems may possess.

7.1 p-orbital manifold topological ladders away from the TMDs

The simplicity of the underlying model presented in Chapter 4 makes finding instances of topological ladders outside the TMD family relatively simple. If a band crossing in a bulk band structure calculation can be described in the following way, then k mediated bulk Dirac cones and inverted band gaps are likely commonplace within the corresponding compound family:

1. In the absence of spin-orbit coupling (SOC), there is a (usually asymmetric) band crossing at a low-symmetry k-point.
2. Both branches are (usually) derived from the same orbital character.
3. When SOC is included, one of the two branches becomes doubled.
4. One of the doubled branches retains a gapless crossing, whereas the other produces an anticrossing.

Fig. 7.1 provides two examples of band structure calculations from the literature which show the above signatures. A recent DFT study into the bulk band structure of β-CuI (D_{3d}) predicted the presence of a parity inverted band gap formed at Γ, as well as a type-I BDP at the Fermi level formed along the Γ-Z direction [225]. Calculations of this system (Fig. 7.1(a-b)), however, reveal a second type-I BDP and an anti-crossing gap is formed along this same axis approximately 1 eV below E_F. This latter pair of crossings can be understood as a consequence of the same mechanism as outlined in Chapter 4: The crystal field lifts the degeneracy of the iodine p-orbital manifold. The inclusion of spin-orbit coupling lifts the remaining degeneracy of the $p_{x,y}$-derived states (seen explicitly by comparing Fig. 7.1(a) and Fig. 7.1(b)), and a natural bandwidth disparity along the C_3-symmetric Γ-Z direction of iodine-derived p-bands produces the symmetry protected crossing and an hybridisation gap, exactly as for the mechanism introduced for the TMDs. It is not clear from these calculations whether or not the k_z mediated anti-crossing is topologically non-trivial, however.

Fig. 7.1(c-d) show how a similar situation unfolds in band structure calculations of $Zn_2In_2S_5$. Recently verified in [190], this compound hosts k_z (Γ-A) mediated bulk Dirac cones and an

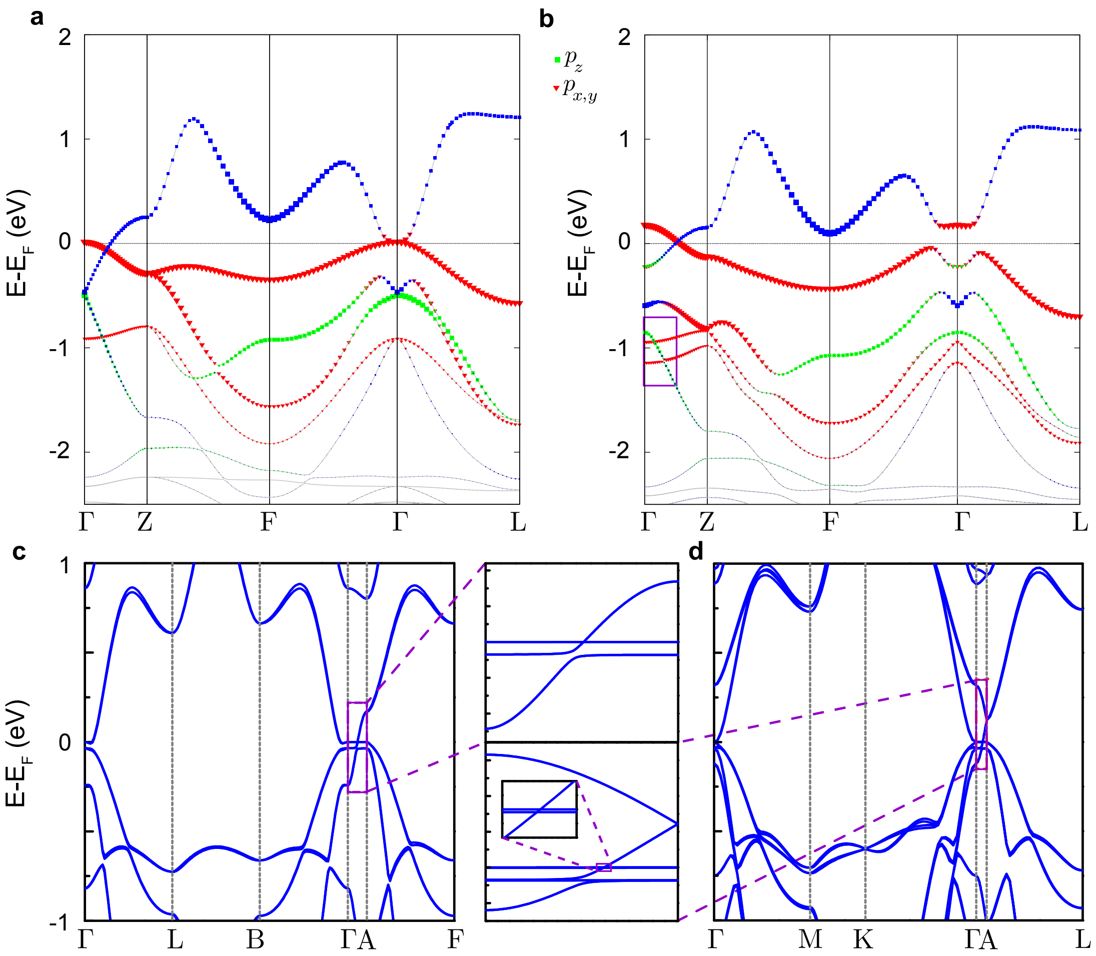

FIGURE 7.1: **DFT calculations of trigonal systems hosting k_z-mediated BDPs and/or TSSs.** (a-b) β-CuI (D_{3d}) with (b) and without (a) SOC [225]. (c-d) $Zn_2In_2S_5$ in the $R3m$ (c) and $P6_3mc$ (d) space groups, with insets enhancing the regions of BDP formation [190]. The regions of interest are indicated with a purple box.

inverted band gap in both its $R3m$ and $P6_3mc$ forms. Like in the transition from the 1T- to the 2H-structured TMDs, each band becomes effectively back-folded along k_z with this change of structure, transforming each BDP into two closely spaced BDPs, and similarly for the band gaps. Intriguingly, the DFT for this system predicts that the bulk Dirac cones in the $R3m$ phase are exactly on the border between type-I and type-II bulk Dirac cones (coined type-III in [190]), although this is unlikely to hold in any real system. In both these examples, the C_{3v} symmetry is again ultimately responsible for protecting the bulk Dirac points.

7.1.1 Type-II bulk Dirac cones and giant Fermi arcs in SnTe

One compound that will be discussed in some detail is SnTe, a carbon group monocalchogenide. Sn and Pb monocalcogenides are most well known for their ferroelectric and topological crystalline insulator phases [226–228][1]. Unlike the TMDs and the examples mentioned above, these compounds do not possess C_{3v} symmetry, but instead have cubic crystal structures. In addition, finding k_z mediated bulk Dirac cones in their 'rock-salt' type Brillouin zones may allow for the experimental detection of Fermi arc surface states for the natural cleavage plane.

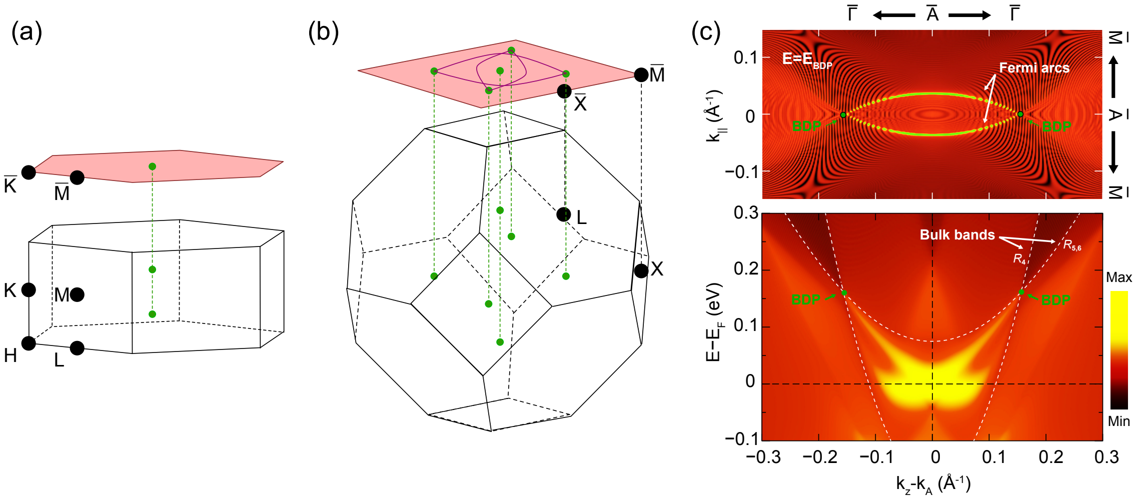

FIGURE 7.2: **Fermi arcs from a single orbital manifold.** (a-b) Bulk and surface Brillouin zones for a hexagonal (a) and cubic (b) system. In both cases, BDPs are indicated in green, demonstrating that BDPs formed along the k_z direction in the hexagonal systems do not remain separated in the surface zone. The four-fold symmetry of the rock-salt zone in (b) requires BDPs formed along k_z to also exist along k_x and k_y, producing three pairs of BDPs in the surface zone, two of which remain separated. (c) Surface slab calculations for a constant energy contour (above, energy indicated by dashed line below) and a Γ-A dispersion (below) for $IrTe_2$ cleaved along the unnatural (100) direction. Bulk Dirac points and Fermi arcs are indicated. (c) is adapted from [83].

To illustrate this, Fig. 7.2(a-b) presents the bulk and surface Brillouin zones for a TMD (Fig. 7.2(a)) and for a rock-salt compound (Fig. 7.2(b)). In the former, the bulk Dirac points formed symmetrically along A-Γ-A both project onto $\overline{\Gamma}$ in the surface Brillouin zone. A pair of BDPs formed along the k_z axis in a rock-salt Brillouin zone also project onto $\overline{\Gamma}$, but here each of the $k_{x,y,z}$ directions are symmetrically equivalent. The pairs of BDPs formed along the k_x and k_y directions therefore do remain separated in $k_{||}$, with Fermi arcs possibly connecting them. As a verification that Fermi arcs can indeed exist between BDPs formed formed via the mechanism outlined in Chapter 4, Fig. 7.2(c) shows a DFT-based surface slab calculation of $IrTe_2$ 'cleaved' along the unnatural (100) plane, with Fermi arcs clearly resolved connecting the BDPs formed along A-Γ-A. An ongoing experimental study into possible Fermi arcs between k_z-mediated type-II BDPs in a rock-salt structured system will be presented below.

---

[1] A topological crystalline insulator exhibits a band inversion at a high symmetry point of the lattice, stabilised by the combination of TRS and a lattice symmetry. The resulting surface states are not considered to be topologically protected [229].

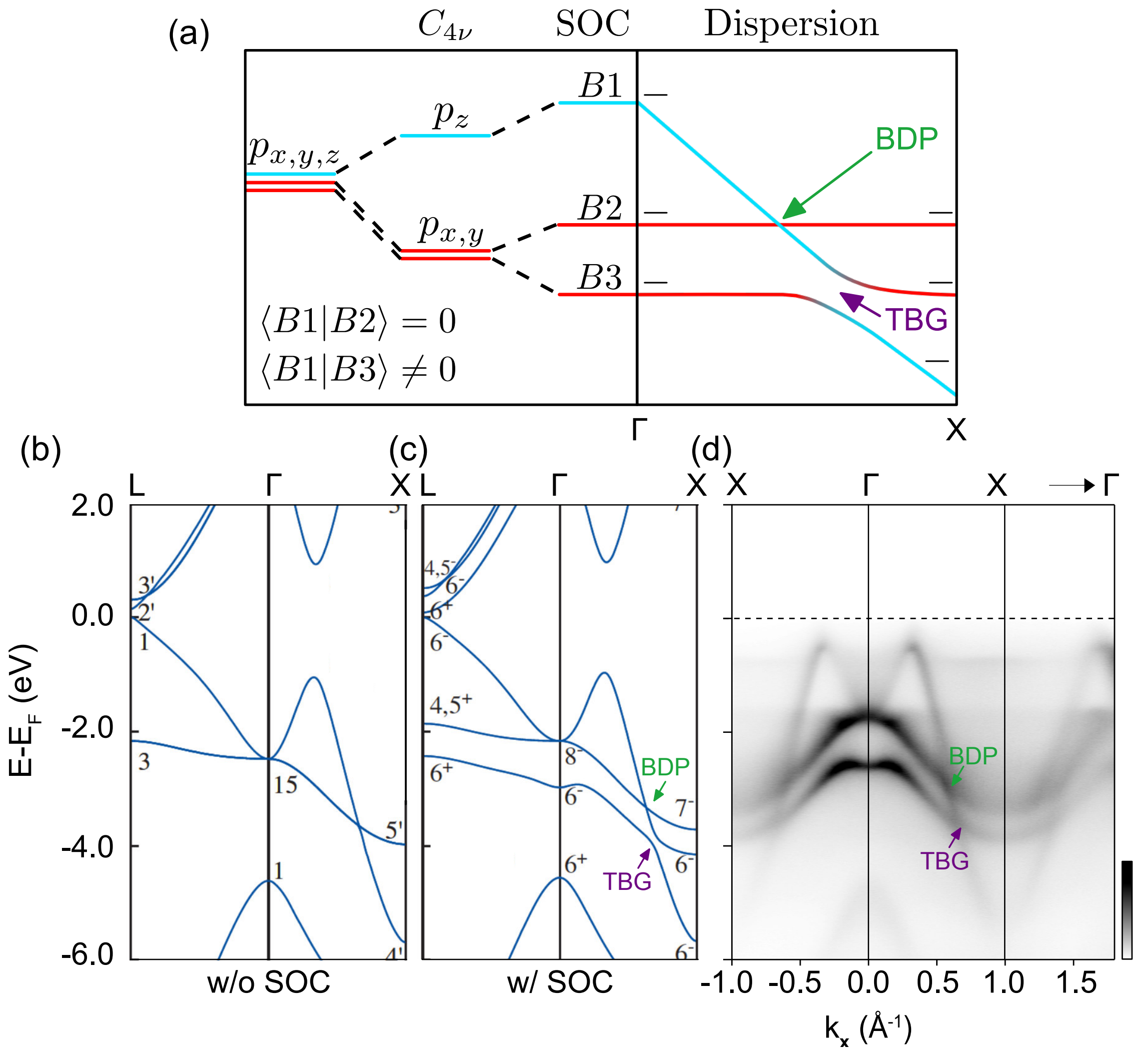

FIGURE 7.3: **Type-II BDPs in SnTe.** (a) Schematic representation of the Te p-orbital manifold under the influence of the crystal field and spin-orbit coupling (left), and a schematic dispersion along a C_{4v} axis shown in the limit of dispersionless $p_{x,y}$-derived bands (right). (b-c) Bulk DFT calculations, from [230] without (b) and with (c) spin-orbit coupling (SOC) included. (d) ARPES dispersion ($h\nu$=135 eV, probing close to a Γ plane) of SnTe, obtained from the CASSIOPEE beamline of SOLEIL.

Fig. 7.3(a) schematises the BDP-IBG forming mechanism in the context of SnTe. The, now-cubic, crystal field lifts the degeneracy of the $p_{x,y}$ and p_z derived bands, with spin-orbit coupling again lifting the remaining band degeneracy between the $p_{x,y}$-derived pair. As with the TMDs, this alone is not sufficient to drive the formation of bulk Dirac points or hybridised band gaps. Instead, their formation is again mediated by band dispersions along the rotationally symmetric axes. The band crossing of the Te p_z derived band with the pair of Te $p_{x,y}$ derived states should create a bulk Dirac point, protected by C_{4v}-symmetry, and a hybridised band gap.

Bulk-DFT calculations from the literature [230] are entirely consistent with this mechanism. In the absence of SOC (Fig. 7.3(b)), there is a single crossing between a likely-p_z derived band and a degenerate $p_{x,y}$ pair along the bulk Γ-X direction. When SOC is included (Fig. 7.3(c)), the degeneracy of the latter is lifted, to produce one crossing which stays protected, and one that does not. Note that since Te and Sn each lie on an inversion centre within the unit cell, each p-derived band is enforced to hold an odd parity eigenvalue. Indeed, explicit parity calculations do *not* predict that the hybridised crossing is an inverted band gap, but instead that it is trivial, as indicated in Fig. 7.3(c).

High quality single crystals were grown by C. O'Niell in the group of A. Huxley at the University of Edinburgh by sealing equal molar weights of Sn and Te in Mo foil and heating [227]. As is typical in SnTe single crystals, these crystals are Te rich, acting to slightly hole dope the system [227].

An ARPES dispersion performed with photon energy nominally probing $k_z = 0$ (for $k_{\|} = 0$) is shown in Fig. 7.3(d). Along the in-plane directions, these measurements are in excellent agreement with the DFT calculations, with a type-II bulk Dirac point formed at approximately $E - E_F = -2.9$ eV. The added benefit of the in-plane formation is that the crossing is not obscured by uncertainties associated with photon energy to k_z mapping, placing this observation firmly among the best-resolved type-II bulk Dirac cones in any compound. Small discrepancies between the band dispersions in the first and second Brillouin zone here can be explained by a changing effective k_z with increasing emission angle ($k_{\|}$), seen explicitly in e.g. Eqn. 3.6.

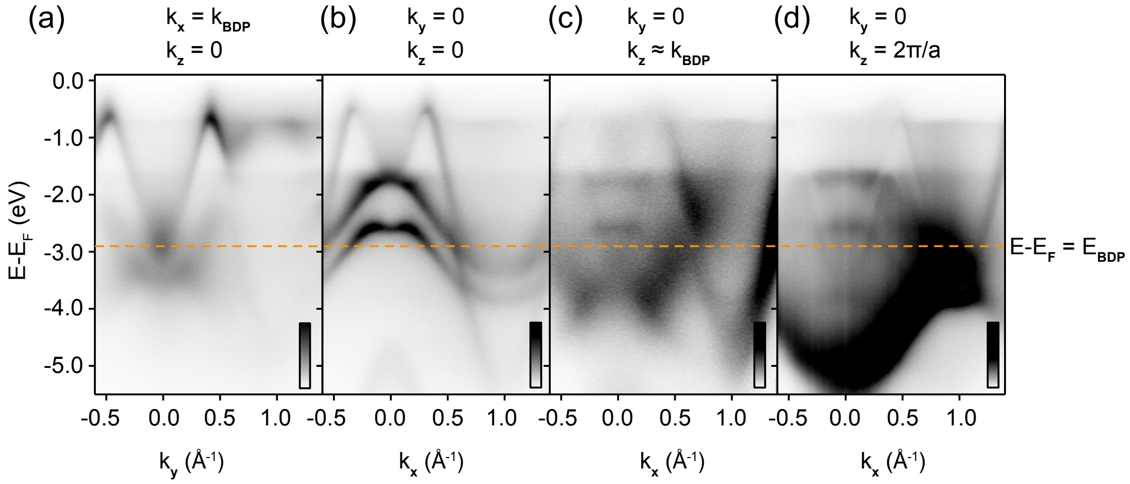

FIGURE 7.4: **Bulk Dirac points along the $x-$ and $z-$ directions in SnTe.** (a-b) Dispersions at the coordinates indicated at a photon energy probing close to a Γ plane (hν =135 eV). (c) Dispersion at photon energy nominally corresponding to a k_z-point where a BDP is formed (hν =83 eV). (d) Dispersion at a photon energy corresponding to an X plane. The approximate binding energies of the bulk Dirac points is indicated with a dashed line. A free-electron final state assumption, with inner potential $V_0 = 2$ eV, was employed for the photon energy mapping here.

In line with the discussions above, there should also be bulk Dirac points formed along the k_y and k_z axes. Fig. 7.4(a-b) reshows the type-II BDP formed along the k_x direction, cutting perpendicular ((k_x,k_y)=(k_{BDP}, k_y)) and parallel ((k_x,k_y)=(k_x, 0)) to the k-point where the BDP is formed, respectively. The shallowest, almost-linear cone feature in Fig. 7.4(b) centred at $\bar{\Gamma}$ is the band which will disperse downwards with changing k_z to form the BDPs centred at $k_{\|}$ =0. Indeed, by changing the photon energy to approach the low symmetry plane where this BDP is formed (at a point $k_z = k_{\mathrm{BDP}}$), the electron like band at $\overline{\Gamma}$ disperses down to form a point at approximately $E - E_F = -2.9$ eV, with a linearly dispersing band rising from below to complete the bulk Dirac cone. Upon moving to a photon energy probing a bulk X plane ($k_z = 2\pi/a$), the three p-orbital derived sates are at their minimum. In addition to the BDPs, there are clear pronounced regions of spectral weight centred at $\overline{\Gamma}$ at binding energies of approximately -1.7 eV and -2.6 eV. These are present in each of panels Fig. 7.4(b-d), suggesting a surface derived origin of these states. These surface states are likely topologically trivial, common in systems with strong three-axial bonding (Chapter 2.1.4).

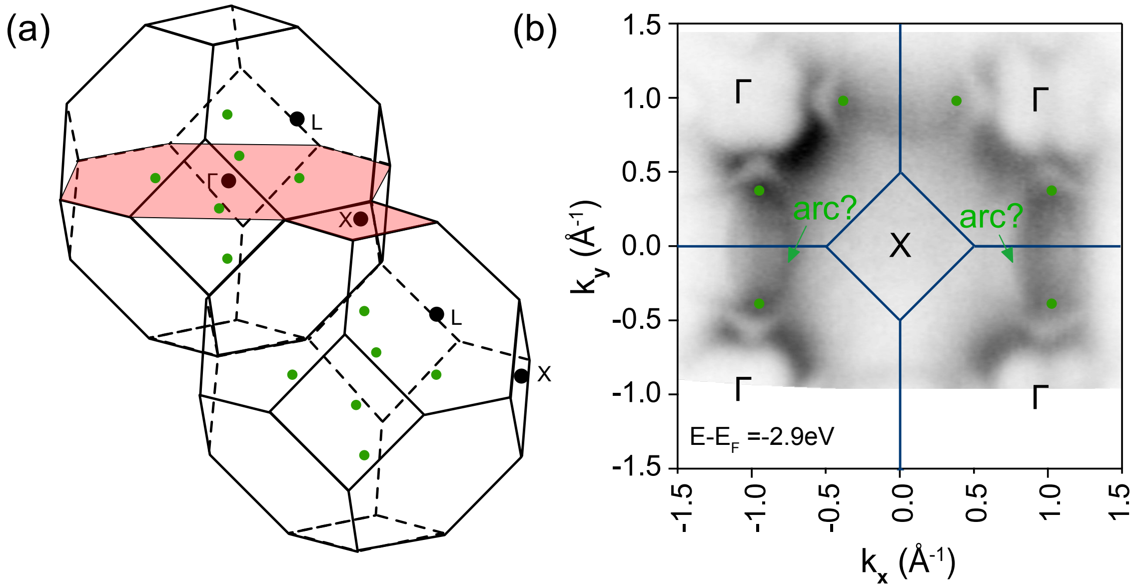

FIGURE 7.5: **Possible Fermi arcs in SnTe.** (a) Schematic of the nominal k_z plane probed with the photon energy choice for the constant energy contour in (b). Four BDPs should be observable outside of the first zone. (b) $h\nu = 98$ eV constant energy contour at the binding energy of the BDP formation ($E - E_F = -2.9 \pm 15$ eV). Approximate positions of BDPs are indicated. Candidate Fermi arcs are indicated.

The experimental data is consistent with the presence of type-II BDPs formed along the three equivalent bulk Γ-X lines within the rock salt Brillouin zone, and therefore Fermi arcs should in principle be observable for this (or any) cleavage plane, originating and terminating at the bulk Dirac nodes. Fig. 7.5(a) shows three pairs of BDPs drawn schematically within the rock-salt Brillouin zone of SnTe. For a photon energy probing close to an X plane (red shaded area), the four BDPs formed along the k_x and k_y directions should be probed directly in the second Brillouin zone. Fig. 7.5(b) shows such a constant energy contour at the binding energy of the BDP formation. Approximate positions of the BDPs are shown with green markers.

There are regions of spectral weight which connect the BDPs across equivalent Brillouin zones. However, they are sufficiently diffuse that it becomes difficult to conclude definitively that these are indeed Fermi arc surface states, and not simply quasi two-dimensional bulk states appearing sharp relative to the background of dispersive, k_z-broadened intensity. This, with the likely presence of topologically trivial surface states in this system means that further experimental evidence is required to verify their assignment as Fermi arcs.

This system has the added complication of a ferroelectric phase at low temperature (T_C =75 K) [226, 227], wherein the unit cell is distorted such that an effective electric dipole along the [111] direction is created. Such a dipole will lift the degeneracies of all six type-II BDPs here, as C_4 symmetry is not retained along any axis. Whilst this could prove an effective way in practice to switch on and off spin-polarised surface states with temperature or pressure by destroying the bulk Dirac cones which they bridge, it should be noted that the data presented in this Section were collected at temperatures below this ferroelectric transition, and so the protection of the BDPs should already have been lost, possibly explaining the lack of obvious Fermi arc candidates. A more limited dataset obtained at high temperature (not shown) does not show any qualitative change to this picture however. Nevertheless, the presence of BDPs in a naturally occurring rock-salt is strong evidence for topological phenomena from a single orbital manifold being prevalent in nature.

7.1.2 Further instances of topological ladders in rock-salt compounds

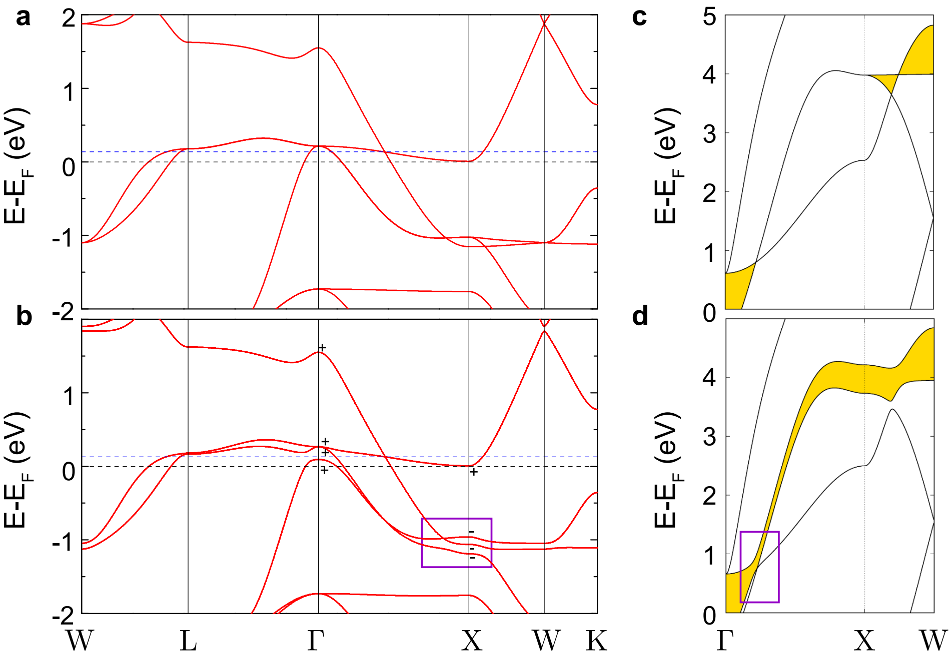

FIGURE 7.6: **DFT calculations of rock-salt systems hosting k_z-mediated BDPs and/or TSSs.** (a-b) YPd$_2$Sn (O_h) with (b) and without (a) SOC [231]. (c-d) TaC (O_h) with (d) and without (c) SOC [232]. The region of interest is indicated with a purple box.

Fig. 7.6 shows two more examples of rock-salt compounds which host BDPs and anti-crossings from within a single-orbital manifold. The 'Heusler' alloys (O_h) ({Y, Sc,}Pd$_2$Sn), ({Zr, Hf,}Pd$_2$Al) and ({Zr, Hf,}Ni$_2$Al), have been recently verified to host type-II bulk Dirac cones at the Fermi level [231]. At higher energies (approximately 1 eV below the Fermi level in YPd$_2$Sn), however, calculations (Fig. 7.6(a-b)) again reveal an additional topological ladder, in this case forming an almost maximally-tilted type-I bulk Dirac cone and a gapped band crossing forming along the Γ-X direction. Again, the $p_{x,y}$-derived bands are degenerate in the absence of spin-orbit coupling [231]. As in SnTe, explicit parity calculations do not predict the formation of inverted band gaps due to the location of the p-orbitals within the unit cell. Nevertheless, these BDP-gap pairs in rock-salt systems can be considered to be cubic analogues to the topological ladders within the TMDs, β-CuI and $Zn_2In_2S_5$.

7.2 *d*-orbital manifold topological ladders in the Fe-based superconductors

In all of the compounds discussed in this thesis so far, the k_z-mediated topological ladders were formed within the chalcogen p-orbital manifold. Indeed, the model outlined in Chapter 4 for the 1T-TMDs completely neglects the role of transition metal d-bands. In the group-X TMDs, there is a large energetic separation of d- and p-derived bands, and so this omission is inconsequential for the understanding of the underlying physics. However, it was shown in Chapter 4.4 that the formation of topological ladders is not limited to isolated p-orbital manifolds. Each 2H-structured TMD considered in this work contains two bulk Dirac points (one of type-I, the other of type-II), and two inverted band gaps below the Fermi level along the Γ-A direction, despite significant $d_{xz,yz}$-orbital character mixing into the otherwise $p_{x,y}$-character bands [83]. Not only, though, does the mixing of d- and p-orbital character not hinder BDP-TSS formation, but analogous physics can be realised from bands with 'pure' d-orbital character. Below it will be shown how the recent experimental realization of bulk Dirac points and topological surface states in the iron based superconductors [224, 233] fits this description.

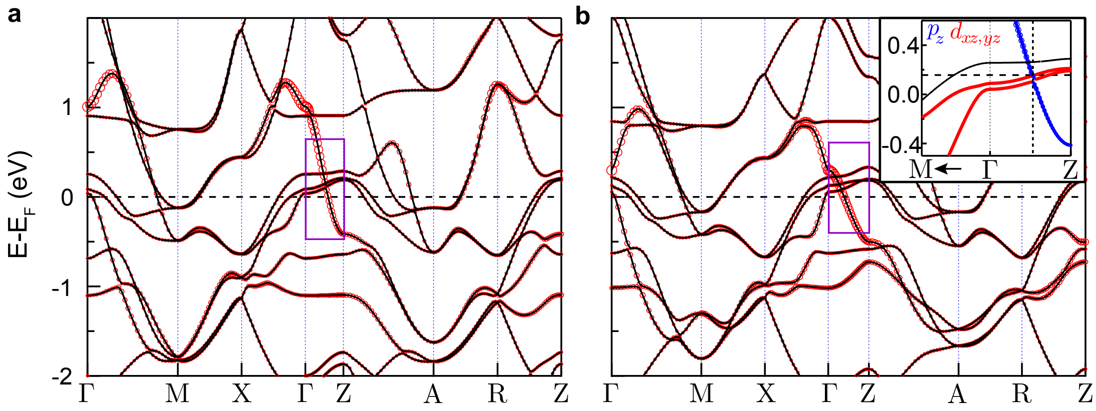

FIGURE 7.7: **DFT calculations of Fe-based superconductors hosting k_z-mediated BDPs and TSSs.** (a) LiFeAs (D_{4h}) with SOC [233]. (b) $FeSe_{0.5}Te_{0.5}$ (D_{4h}) with SOC [233]. Inset shows BDP-IBG formation.

$FeSe_xTe_{1-x}$ forms part of the iron-based superconductor classification, recently verified to host BDPs and parity inverted band gaps [224, 233]. These compounds have a highly tuneable superconducting phase, as low as 8 K in bulk single-crystals of FeSe, but increasing above 40 K when under pressure [234]. Moreover, FeSe has a 'nematic' phase wherein the C_4 rotational symmetry is lost, but translational symmetry is preserved [235, 236]. Therefore, with reducing temperature, a regime wherein the lattice symmetry protection of BDPs is altered is passed en route to a regime where topological surface states coexist with, and possibly interplay with, superconductivity. As a result, Majorana zero modes are predicted to exist at the surfaces of these compounds when the TSSs are tuned to E_F [224]. Although the topological surface states and bulk Dirac point have been discussed in several publications [224, 233, 237], their k_z-mediated origin and its significance has been largely overlooked.

Fig. 7.7(b) outlines the formation of a topological ladders in $FeSe_{0.5}Te_{0.5}$. As with the TMDs, the combination of crystal field splitting and the spin-orbit interaction alone is insufficient to drive the requisite band inversions, instead additionally requiring disparate bandwidths along the k_z direction. The inset in Fig. 7.7(b) shows how a chalcogen p_z-derived band forms C_{4v} protected bulk Dirac points from the crossing points of the highest energy Fe d-derived bands, of predominantly d_{xy} and d_{yz} character (top most and middle bands in the inset of Fig. 7.7(b) respectively) [224]. A non-trivial inverted band gap is then formed with the bottom-most, predominantly d_{xz}-character, band.

More widely, the crystal structure of the iron-based superconductors is such that the p_z band always has a bandwidth large enough to cross through the entirety of the Fe t_{2g} d-orbital submanifold, regardless of its atomic origin. These same states therefore exist even in the similarly structured Fe-based superconductors which do not contain a chalcogen, such as LiFeAs, LaOFeAs and $BaFe_2As_2$. Fig. 7.7(a) shows the realisation of bulk Dirac points and an inverted band gap in LiFeAs. Here the electronic structure is very similar, with the p_z band now deriving from As rather than a chalcogen.

The additional systems presented in this Chapter show that k-mediated topological ladders, ubiquitous across a material family, can arise along one or multiple C_n-symmetric axes from the crossing of bands which may or may not derive from the same orbital manifold. Whilst this greatly diversifies the catalogue of classes to which the underlying mechanism outlined in Chapter 4 has shown to be applicable for, all of compounds considered thus far possess both inversion and time-reversal symmetries in their bulk. As a final discussion, the possibility of realising k-mediated topological ladders in systems which do not host both of these symmetries will be briefly discussed.

7.3 Novel Weyl phases through removing global lattice symmetries

A bulk Dirac cone can be considered as the superposition of two spin-polarised Weyl cones with opposite chiralities, with the degeneracy deriving from the combination of time-reversal and inversion symmetries. Each of the six TMDs considered in this thesis are inversion symmetric in their bulk band structure and so only surface derived states are permitted to be spin-polarised. The *Janus* TMDs are variants of the TMD family where one chalcogen sub-layer in the X-M-X formula unit is switched for another. These compounds retain the C_{3v} symmetry relevant for the chalcogen layers, but they do not posses inversion symmetry in their bulk [238]. Naively, a Janus TMDs should naturally contain the same k_z-mediated topological ladders as in the TMDs, but without the restriction of four-fold Dirac point degeneracies imposed by an inversion symmetric environment.

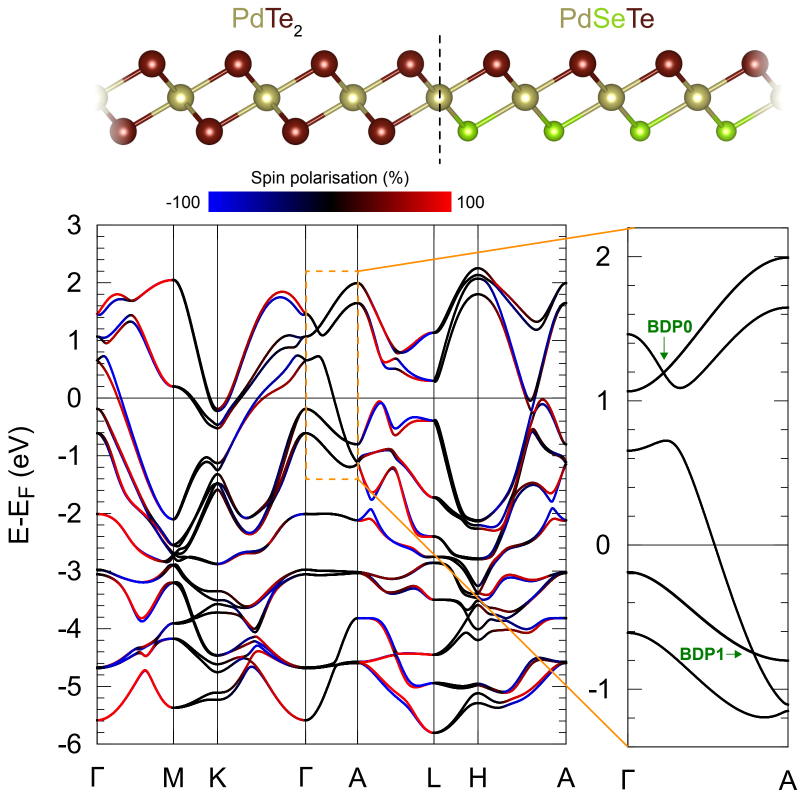

FIGURE 7.8: **Bulk band structure of PdSeTe.** Spin-resolved bulk DFT calculations are shown from the Janus TMD PdTeSe. The crystal structure (top) of PdSeTe is compared to PdTe$_2$. An inset (right) of the Γ-A line is included, which shows that spin degeneracy is maintained along k_z despite the global inversion asymmetry. Rashba-like splittings are found for non-zero $k_{x,y}$. DFT calculations adapted from [83].

Fig. 7.8 compares the crystal structures of PdTe$_2$ and the Janus TMD PdSeTe. In the latter, one tellurium sub-layer is replaced with a selenium sub-layer, breaking bulk inversion symmetry and therefore reducing the global point group symmetry from D_{3h} to C_{3v} [170]. Strikingly, spin-sensitive DFT calculations presented in Fig. 7.8 suggest that the degeneracy of bulk Dirac points, formed along the Γ-A line, centred at $\approx +1.5$ and -0.5 eV, are retained, with spin degeneracy lifting only along the in-plane directions. This implies that C_{3v} can take on the responsibility of enforcing spin degeneracy along the axis where it applies.

A more recent DFT-study [170] demonstrates the persistence of the BDP-TSS forming mechanism in the other group-X Janus TMDs, PtSeTe and PtSTe, as well as the PdSeTe compound presented here. They, however, do report a small energetic splitting of the $R_{5,6}$ bands along the Γ-A line on the order of 1 meV, but Weyl points are still not formed. Instead, each bulk Dirac point is transformed into a *triply degenerate point* (TDP), midway between the two-fold and four-fold degeneracies of Weyl and Dirac points respectively. Fermions of this sort, like type-II Dirac and Weyl points, break Lorentz invariance and are therefore not permitted solutions of

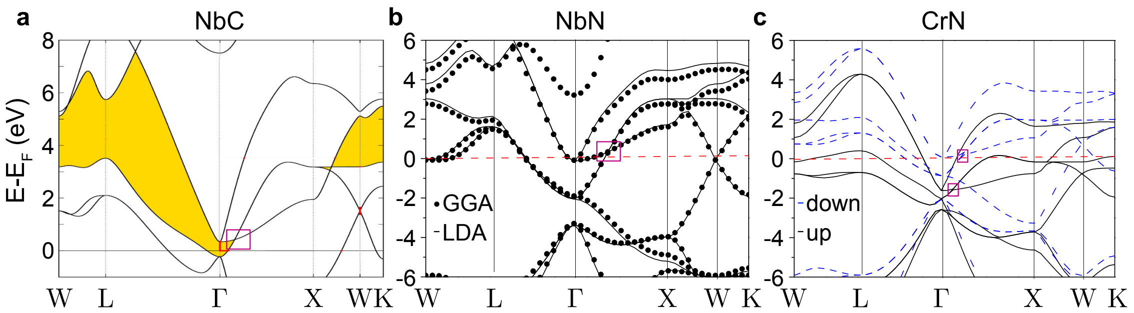

FIGURE 7.9: **Band structure calculations of NbC, NbN and CrN in the absence of spin-orbit coupling.** (a) Band structure of NbC adapted from [232]. (b-c) Band structures of NbN (b) and CrN (c) adapted from [239].

the Dirac equation. This again shows the potential to study of emergent fermions which can only exist in crystalline systems.

Whilst some single-layers of select Janus TMDs have been successfully synthesised [238, 247], only single crystal alloys of bulk group-X TMDs (for example $PtSe_{2-x}Te_x$) have been synthesised successfully [248]. In their few-layer forms the TDP formed along the k_z direction will not exist. These single-orbital manifold triple points may also exist in other systems, however. DFT calculations of bulk, inversion asymmetric, $PbTaSe_2$ presented in [246] show a remarkably similar Γ-A dispersion to that presented above, providing a route to study TDPs and their associated surface states in a bulk system which can be more easily synthesised. Moreover, the 'cone' running into the triple point in PdTeSe in Fig. 7.8 exhibits a band splitting along the A-L direction at the band maximum. This is not dissimilar to the appearance of the type-II BDP in $PtSe_2$ following Rb deposition at the end of the previous Chapter (Fig. 6.11) possibly hinting that an inversion asymmetric near-surface potential well is sufficient to create near-surface localised TDPs in these systems.

The scope for studying the evolution of bulk Dirac points, topological surface states and even Fermi arcs with time-reversal symmetry breaking is presented in Fig. 7.9 for the rock-salt structured transition metal carbides and nitrides (formula MX). The transition metal carbides, {Nb, Ta, V, Cr}C (O_h), have been recently verified to host k_z mediated bulk Dirac cones within their metal d-orbital manifolds (note that the restriction of odd parity eigenstates in rock-salt systems discussed above does not hold for d-orbitals) [232], with the case of TaC shown in Fig. 7.1(c-d). Whilst these are all non-magnetic, analogous physics can be expected to occur in the similarly structured transition metal nitride compounds, {Sc, Ti, V, Cr, Zr, Nb}N. These share remarkably similar band structures to the carbides [239], but CrN has a ferromagnetic ground state. To illustrate this potential, Fig. 7.9 compares the band structures of NbC, NbN and CrN *without* spin-orbit coupling. For the case of NbC, the crossing verified to separate into a protected crossing/anticrossing pair when spin-orbit coupling is included is indicated [232]. DFT calculations of NbN shown in Fig. 7.9(b) [239] are qualitatively very similar. It follows that the indicated band crossing in NbN would also produce a k-mediated topological ladder when spin-orbit coupling is considered. Whilst these two compounds are non-magnetic, CrN shown in Fig. 7.9(c) is not. As a result d-derived band structure is effectively doubled

TABLE 7.1: Systems wherein lattice protected BDPs and anti-crossings are simultaneously formed along a rotationally symmetric axis. Sections separate the trigonal, cubic, tetragonal and hexagonal lattice symmetries. Citations either correspond to bulk DFT calculations which closely resemble the framework outlined in Chapter 4 or works in which the single-orbital manifold has been explicitly verified. The sections separate trigonal, cubic, tetragonal and hexagonal systems. An * indicates that relevant crossing points are between bands originating from two orbital-manifolds.

Compound	**Point group**	**Reference**
PdSeTe, PtSSe, PtSeTe	C_{3v}	Chapter 7([83]), [170]
$Zn_2In_2S_5$	C_{3v}	[190]
(Ni, Pd, Pt)Te_2	D_{3d}	Chapter 4 ([83, 173]), [172, 174, 175, 178, 240]
$PtSe_2$	D_{3d}	Chapter 5 ([83]), [174]
$Pt_xIr_{1-x}Te_2$, $IrTe_2$	D_{3d}	Chapter 4 ([83]), [182]
$PtBi_2$	D_{3d}	[174, 241]
β-CuI	D_{3d}	[225]
(Ge, Sn)Te	O_h	Chapter 7, [230]
(Ge, Sn, Pb)Se	O_h	[242]
PbPo	O_h	[243]
(Sc, Ti, V, Cr, Zr, Nb)N	O_h	[232, 239]
(Cr, Ta, Nb, V)C	O_h	[232]
(Y, Sn) Pd_2Sn	O_h	[231]
(Zr, Hf) Pd_2Al	O_h	[231]
(Zr, Hf) Ni_2Sn	O_h	[231]
Cu(F, Cl, Br, I)	T_d	[244]
Cu(Li, Na, K, Rb)O	T_d	[244]
VAl_3, $NbAl_3$, $TaAl_3$	C_{4v}	[177]
$FeSe_xTe_{1-x}$*	D_{4h}	[224, 233]
LiFeAs, LaOFeAs, $BaFe_2As_2$*	D_{4h}	[233]
$Zn_2In_2S_5$	C_{6v}	[190]
MoP	D_{3h}	[245]
$PbTaSe_2$	D_{3h}	[246]
WSe_2	D_{6h}	Chapter 4 ([83])
(Nb, Ta)Se_2	D_{6h}	Chapter 4 ([83])

with respect to that of NbN. CrN could therefore be host to novel type-II Weyl or triple points stabilised within a time-reversal asymmetric environment, or an intrinsic ‘topological magnetoelectric effect’ could be observed, wherein the Kramer’s degeneracy of topological surface states is lifted [249].

As a summary, Table 7.1 consolidates more than fifty compounds hosting k_z-mediated topological phenomena across nine different point group symmetries. These compounds either satisfy the criteria outlined in the opening discussion to this Chapter based on bulk DFT calculations available in the literature, or they have been verified explicitly by theory and/or experiment.

7.4 Outlook

The ubiquitous nature of highly-tunable, k_z-mediated topological phenomena provides many opportunities to study the interplay of non-trivial topology with other properties. For example, the effort towards robust realisations of Majorana fermions is aided by expansion of the number of verified intrinsic superconductors hosting topological surface states at the Fermi level. $PdTe_2$ (Chapter 5 and [173]) and $FeSe_{0.45}Te_{0.55}$ [237] are two such examples, with their topological surface states arising as a direct consequence of the general mechanism outlined in Chapter 4. This motivated analogous STM/STS studies into these two compounds despite their otherwise disparate crystal and electronic structures. Similarly, the coexistence of single-orbital manifold topological phenomena with magnetism, possible in CrN [239], is yet to be explored.

2008 saw the first prediction and experimental verification of a three-dimensional topological insulator [250, 251], demonstrating that topologically protected spin-polarised Dirac cones can exist at the surfaces of compounds. A decade on, the intensity of the research effort into these systems still continues to grow. The number of articles per year with the word “topological” in the title uploaded to the condensed matter section of arXiv has increased tenfold since 2007, with over one thousand such articles uploaded in each of 2017 and 2018.

By demonstrating explicitly that the same physics persists across the diverse family of transition metal dichalcogenides simply because each of them contain a chalcogen and a layered rotationally-symmetric structure, the works in this thesis are very suggestive that non-trivial band topology is likely just a generic feature of the electronic structures of solids. Although it is genuinely potentially very useful for electronic and spintronic devices, it is not special.

Indeed, a very recent data-mining project [252] into all possible electronic structures predicts that one quarter of existing solids have within them a topological band inversion. The focus now must shift towards the development of the operational principles by which devices can exploit non-trivial band topology, rather then simply adding to the hundreds of compounds that could form their basis.

Bibliography

1. Schelling, P. K., Shi, L. & Goodson, K. E. *Materials Today* **8, 6,** 30–35 (2005).
2. Rosner, M. & Ritchie, H. Technological Progress (2018) [Online], https://ourworldindata.org/technological-progress, [Accessed 26/10/2018].
3. Kamerlingh Onnes, H. Further experiments with Liquid Helium. D. On the change of Electrical Resistance of Pure Metals at very low Temperatures, etc. V. The Disappearance of the resistance of mercury. *KNAW, Proceedings* **14 I,** 113–115 (1911).
4. Drozdov, A. P., Eremets, M. I., Troyan, I. A., Ksenofontov, V. & Shylin, S. I. Conventional superconductivity at 203 kelvin at high pressures in the sulfur hydride system. *Nature* **525,** 73–76 (2015).
5. Schilling, A., Cantoni, M., Guo, J. D. & Ott, H. R. Superconductivity above 130 K in the Hg-Ba-Ca-Cu-O system. *Nature* **363,** 56–58 (1993).
6. OSHA. Hydrogen Sulfide [Online], https://www.osha.gov/SLTC/hydrogensulfide/ hazards.html, [Accessed 26/10/2018].
7. Novoselov, K. S. *et al.* Electric Field Effect in Atomically Thin Carbon Films. *Science* **306,** 666–669 (2004).
8. Akturk, A. & Goldsman, N. Electron transport and full-band electron-phonon interactions in graphene. *Journal of Applied Physics* **103,** 053702 (2008).
9. Chen, J.-H., Jang, C., Xiao, S., Ishigami, M. & Fuhrer, M. S. Intrinsic and extrinsic performance limits of graphene devices on SiO_2. *Nature Nanotechnology* **3,** 206–209 (2008).
10. Mackenzie, A. P. The properties of ultrapure delafossite metals. *Reports on Progress in Physics* **80,** 3 (2017).
11. Young, S. M. *et al.* Dirac Semimetal in Three Dimensions. *Physical Review Letters* **108,** 140405 (2012).
12. Hasan, M. Z. & Kane, C. L. Colloquium: Topological insulators. *Reviews of Modern Physics* **82,** 3045–3067 (2010).
13. Kato, Y. K., Myers, R. C., Gossard, A. C. & Awschalom, D. D. Observation of the Spin Hall Effect in Semiconductors. *Science* **306,** 5703, 1910 (2004).
14. Chhowalla, M. *et al.* The chemistry of two-dimensional layered transition metal dichalcogenide nanosheets. *Nature Chemistry* **5,** 263–275 (2013).
15. Blundell, S. Magnetism in Condensed Matter (Oxford University Press, 2001).
16. Ibach, H. & Lüth, H. An Introduction to Principles of Materials Science (Springer, 2009).
17. Simon, S. H. The Oxford Solid State Basics (Oxford, 2013).
18. Cottenier, S. Density Functional Theory and the Family of (L)APW-methods: a step-by-step introduction (Instituut voor Kern- en Stralingsfysica, K.U.Leuven, Belgium, 2004).
19. Raza, H. Graphene Nanoelectronics (Springer, 2012).

20. Hrostowski, H. J., Morin, F. J., Geballe, T. H. & Wheatley, G. H. Hall Effect and Conductivity of InSb. *Physical Review* **100,** 1672–1676 (1955).
21. Xu, X. *et al.* Length-dependent thermal conductivity in suspended single-layer graphene. *Nature Communications* **5,** 3689 (2014).
22. Novoselov, K. S. *et al.* Two-dimensional gas of massless Dirac fermions in graphene. *Nature* **438,** 197–200 (2005).
23. Gusynin, V. P. & Sharapov, S. G. Unconventional Integer Quantum Hall Effect in Graphene. *Physical Review Letters* **95,** 146801 (2005).
24. Zhong, M. *et al.* Interface coupling in graphene/fluorographene heterostructure for high-performance graphene/silicon solar cells. *Nano Energy* **28,** 12–18 (2016).
25. Ooi, N., Rairkar, A., Lindsey, L. & Adams, J. B. Electronic structure and bonding in hexagonal boron nitride. *Journal of Physics: Condensed Matter* **18,** 1 (2005).
26. Lüth, H. Solid Surfaces, Interfaces and Thin Films, 6th Edition (Springer, 2015).
27. Hufner, S. Photoelectron Spectroscopy: Principals and Applications, 3rd Ed. (Springer, 2003).
28. Foldy, L. L. & Wouthuysen, S. A. On the Dirac Theory of Spin 1/2 Particles and Its Non-Relativistic Limit. *Physical Review* **78,** 29–36 (1950).
29. Winkler, R. Spin-Orbit Coupling Effects in Two-Dimensional Electron and Hole Systems (Springer, 2003).
30. Schiff, L. I. Quantum Mechanics, 3rd Ed. (McGraw, 1968).
31. Bychov, Y. A. & Rashba, E. I. Oscillatory effects and the magnetic susceptibility of carriers in inversion layers. *Journal of Physics. C: Solid State Physics* **17,** 6039 (1984).
32. Datta, S. & Das, B. Electronic analog of the electro-optic modulator. *Applied Physics Letters* **56,** 665 (1990).
33. Koga, T., Nitta, J. & Takayangi, H. Spin-Filter Device Based on the Rashba Effect Using a Nonmagnetic Resonant Tunneling Diode. *Physical Review Letters* **88,** 126601 (2002).
34. Koo, H. C. Control of Spin Precession in a Spin-Injected Field Effect Transistor. *Science* **325,** 1515 (2009).
35. Lee, H., Im, J. & Jin, H. Harnessing the giant out-of-plane Rashba effect and the nanoscale persistent spin helix via ferroelectricity in SnTe thin films. *arXiv:1712.06112.*
36. Michiardi, M. *et al.* Strongly anisotropic spin-orbit splitting in a two-dimensional electron gas. *Physical Review B* **91,** 035445 (2015).
37. Lashell, S., McDougall, B. A. & Jensen, E. Spin Splitting of an Au(111) Surface State Band Observed with Angle Resolved Photoelectron Spectroscopy. *Physical Review Letters* **77,** 3419 (1996).
38. Bianchi, M. *et al.* Coexistence of the topological state and a two-dimensional electron gas on the surface of Bi_2Se_3. *Nature Communications* **1,** 128 (2010).
39. King, P. D. C. *et al.* Subband Structure of a Two-Dimensional Electron Gas Formed at the Polar Surface of the Strong Spin-Orbit Perovskite $KTaO_3$. *Physical Review Letters* **108,** 117602 (2012).
40. Santander-Syro, A. F. *et al.* Two-dimensional electron gas with universal subbands at the surface of $SrTiO_3$. *Nature* **469,** 189–193 (2011).

41. Bawden, L. *et al.* Hierarchical spin-orbital polarization of a giant Rashba system. *Science Advances* **1,** 8 (2015).
42. Ohtomo, A. & Hwang, H. Y. A high-mobility electron gas at the $LaAlO_3/SrTiO_3$ heterointerface. *Nature* **427,** 423–426 (2004).
43. Hotta, Y., Susaki, T. & Hwang, H. Y. Polar Discontinuity Doping of the $LaVO_3/SrTiO_3$ Interface. *Physical Review Letters* **99,** 236805 (2007).
44. Riley, J. M. *et al.* Negative electronic compressibility and tunable spin splitting in WSe_2. *Nature Nanotechnology* **10,** 1043–1047 (2015).
45. King, P. D. C. *et al.* Large Tunable Rashba Spin Splitting of a Two-Dimensional Electron Gas in Bi_2Se_3. *Physical Review Letters* **107,** 096802 (2011).
46. Nicolay, G., Reinert, F., Hüfner & Blaha, P. Spin-orbit splitting of the L-gap surface state on Au(111) and Ag(111). *Physical Review B* **65,** 033407 (2001).
47. Tamai, W. A. Meevasana *et al.* Spin-orbit splitting of the Shockley surface state on Cu(111). *Physical Review B* **87,** 075113 (2013).
48. Ishizaka, K. *et al.* Giant Rashba-type spin splitting in bulk BiTeI. *Nature Materials* **10,** 521–526 (2011).
49. Bahramy, M. S., Yang, B.-J., Arita, R. & Nagaosa, N. Emergence of non-centrosymmetric topological insulating phase in BiTeI under pressure. *Nature Communications* **3,** 679 (2012).
50. Crepaldi, A. *et al.* Giant Ambipolar Rashba Effect in the Semiconductor BiTeI. *Physical Review Letters* **109,** 096803 (2012).
51. Mak, K. F., Lee, C., Hone, J., Shan, J. & Heinz, T. F. Atomically thin MoS_2: A new direct gap semiconductor. *Physical Review Letters* **105,** 136805 (2010).
52. Xiao, D., Liu, G.-B., Feng, W., Xu, X. & Yao, W. Coupled Spin and Valley Physics in Monolayers of MoS_2 and Other Group-VI Dichalcogenides. *Physical Review Letters* **108,** 196802 (2012).
53. Dresselhaus, G. Spin-Orbit Coupling Effects in Zinc Blende Structures. *Physical Review* **100,** 580 (1955).
54. Tao, L. L & Tsymbal, E. Y. Persistent spin texture enforced by symmetry. *Nature Communications* **9,** 2763 (2018).
55. Kane, C. L. & Mele, E. J. Quantum Spin Hall Effect in Graphene. *Physical Review Letters* **95,** 226801 (2005).
56. Yao, Y., Ye, F., Qi, X.-L., Zhang, S.-C. & Fang, Z. Spin-orbit gap of graphene: First-principles calculations. *Physical Review B* **75,** 041401(R) (2007).
57. Ohta, T., Bostwick, A., Seyller, T., Horn, K. & Rotenberg, E. Controlling the Electronic Structure of Bilayer Graphene. *Science* **313,** 951–953 (2006).
58. Sato, T. *et al.* Unexpected mass acquisition of Dirac fermions at the quantum phase transition of a topological insulator. *Nature Physics* **7,** 840–844 (2011).
59. Zu, S. Y. *et al.* Topological phase transition and texture inversion in a tunable topological insulator. *Science* **322,** 540–564 (2011).
60. Yang, B.-J. & Nagoasa, N. Classification of stable three-dimensional Dirac semimetals with nontrivial topology. *Nature Communications* **5,** 4898 (2014).

61. Neupane, M. *et al.* Observation of a three-dimensional topological Dirac semimetal phase in high-mobility Cd_3As_2. *Nature Communications* **5,** 3786 (2014).
62. Wang, Z. *et al.* Dirac semimetal and topological phase transitions in A_3Bi ($A =$ Na, K, Rb). *Physical Review B* **85,** 195320 (2012).
63. Wang, Z., Weng, H., Wu, Q., Dai, X. & Fang, Z. Three-dimensional Dirac semimetal and quantum transport in Cd_3As_2. *Physical Review B* **88,** 125427 (2013).
64. Borisenko, S. *et al.* Experimental Realization of a Three-Dimensional Dirac Semimetal. *Physical Review Letters* **113,** 027603 (2014).
65. Bansil, A., Lin, H. & Das, T. Colloquium: Topological band theory. *Reviews of Modern Physics* **88,** 021004 (2016).
66. Hosur, P. & Qi, X. Recent developments in transport phenomena in Weyl semimetals. *Comptes Rendus Physique* **14,** 857 (2013).
67. Fu, L. & Kane, C. L. Topological insulators with inversion symmetry. *Physical Review B* **76,** 045302 (2007).
68. Bianchi, M. *et al.* The electronic structure of clean and adsorbate-covered Bi_2Se_3: an angle-resolved photoemission study. *Semiconductor Science and Technology* **27,** 12 (2012).
69. Zhang, H. *et al.* Topological insulators in Bi_2Se_3, Bi_2Te_3 and Sb_2Te_3 with a single Dirac cone on the surface. *Nature Physics* **5,** 438–442 (2009).
70. Qu, D.-X., Hor, Y. S., Xiong, J., Cava, R. J. & Ong, N. P. Quantum Oscillations and Hall Anomaly of Surface States in the Topological Insulator Bi_2Te_3. *Science* **329,** 821–824 (2010).
71. Pielmeier, F. *et al.* Response of the topological surface state to surface disorder in $TlBiSe_2$. *New Journal of Physics* **17,** 023067 (2015).
72. Chen, C. *et al.* Robustness of topological order and formation of quantum well states in topological insulators exposed to ambient environment. *Proceedings of the National Academy of Sciences* **109,** 3694–3698 (2012).
73. Lee, C.-K. *et al.* Robustness of a Topologically Protected Surface State in a Sb_2Te_2Se Single Crystal. *Scientific Reports* **6,** 36538 (2016).
74. Zhang, Y. N. Communication: Surface stability and topological surface states of cleaved Bi_2Se_3: First-principles studies. *The Journal of Chemical Physics* **143,** 151101 (2015).
75. Pesin, D. & MacDonald, A. H. Spintronics and pseudospintronics in graphene and topological insulators. *Nature Materials* **11,** 409–416 (2012).
76. Roushan, P. *et al.* Topological surface states protected from backscattering by chiral spin texture. *Nature* **460,** 1106–1109 (2009).
77. Xu, L., Li, X.-Q. & Sun, Q.-f. Revisit the spin-FET: Multiple reflection, inelastic scattering, and lateral size effects. *Scientific Reports* **4,** 7527 (2014).
78. Fu, L. Hexagonal Warping Effects in the Surface States of the Topological Insulator Bi_2Te_3. *Physical Review Letters* **103,** 266801 (2009).
79. Basak, S. *et al.* Spin texture on the warped Dirac-cone surface states in topological insulators. *Physical Review B* **84,** 121401 (2011).

80. Frantzeskakis, E. & Grioni, M. Anisotropy effects on Rashba and topological insulator spin-polarized surface states: A unified phenomenological description. *Physical Review B* **84,** 155453 (2011).
81. Callaway, J. Energy Band Theory (Academic Press, 1964).
82. Bahramy, M. S., Arita, R. & Nagaosa, N. Origin of giant bulk Rashba splitting: Application to BiTeI. *Physical Review B* **84,** 041202 (2011).
83. Bahramy, M. S. *et al.* Ubiquitous formation of bulk dirac cones and topological surface states from a single orbital manifold in transition-metal dichalcogenides. *Nature Materials* **17,** 23–27 (2018).
84. Kargarian, M., Randeria, M. & Lu, Y.-M. Are the surface Fermi arcs in Dirac semimetals topologically protected? *PNAS* **113,** (31) 8648–8652 (2016).
85. Fang, Z. *et al.* The Anomalous Hall Effect and Magnetic Monopoles in Momentum Space. *Science* **302,** 92–95 (2003).
86. Dirac, P. A. M. Quantised singularities in the electromagnetic field, **133,** 60–72 (1931).
87. Castelnovo, C., Moessner, R. & Sondhi, L. Magnetic monopoles in spin ice. *Nature* **451,** 42–45 (2008).
88. Lv, B. Q. *et al.* Observation of Weyl nodes in TaAs. *Nature Physics* **11,** 724–727 (2015).
89. Xu, S.-Y. *et al.* Discovery of a Weyl fermion semimetal and topological Fermi arcs. *Science* **349,** 6248 (2015).
90. Xu, N. *et al.* Observation of Weyl nodes and Fermi arcs in tantalum phosphide. *Nature Communications* **7,** 11006 (2016).
91. Sato, M. & Fujimoto, S. Topological phases of noncentrosymmetric superconductors: Edge states, Majorana fermions, and non-Abelian statistics. *Physical Review B* **79,** 094504 (2009).
92. Elliott, S. R. & Franz, M. Colloquium: Majorana fermions in nuclear, particle, and solid-state physics. *Reviews of Modern Physics* **87,** 137–163 (2015).
93. Fossheim, K. & Sudboe, A. Superconductivity: Physics and Applications (Wiley, 2004).
94. Sato, M. & Ando, Y. Topological superconductors: a review. *Reports on Progress in Physics* **80,** 076501 (2017).
95. Alicea, J., Oreg, Y., Refael, G., von Oppen, F. & Fisher, M. A. P. Non-Abelian statistics and topological quantum information processing in 1D wire networks. *Nature Physics* **7,** 412–417 (2011).
96. Kitaev, A. Y. Unpaired Majorana fermions in quantum wires. *Physics-Uspekhi* **44** (2001).
97. Read, N. & Green, D. Paired states of fermions in two dimensions with breaking of parity and time-reversal symmetries and the fractional quantum Hall effect. *Physical Review B* **61,** 10267 (2000).
98. Gorkov, L. P. & Rashba, E. I. Superconducting 2D System with Lifted Spin Degeneracy: Mixed Singlet-Triplet State. *Physical Review Letters* **87,** 037004 (2001).
99. P., S. A., Ryu, S., Furusaki, A. & Ludwig, A. W. W. Classification of topological insulators and superconductors in three spatial dimensions. *Physical Review B* **78,** 195125 (2008).
100. Sun, Z. *et al.* Dirac surface states and nature of superconductivity in Noncentrosymmetric BiPd. *Nature Communications* **6,** 6633 (2015).

101. Mourik, V. *et al.* Signatures of Majorana Fermions in Hybrid Superconductor- Semiconductor Nanowire Devices. *Science* **336,** 6084, 1103–1007 (2012).
102. Liu, J., Potter, A. C., Law, K. T. & Lee, P. A. Zero-Bias Peaks in the Tunneling Conductance of Spin-Orbit-Coupled Superconducting Wires with and without Majorana End-States. *Physical Review Letters* **109,** 267002 (2012).
103. Maier, L. *et al.* Induced Superconductivity in the Three-Dimensional Topological Insulator HgTe. *Physical Review Letters* **109,** 186806 (2012).
104. Deacon, R. S. *et al.* Josephson Radiation from Gapless Andreev Bound States in HgTe-Based Topological Junctions. *Physical Review X* **7,** 021011 (2017).
105. Zareapour, P. *et al.* Proximity-induced high-temperature superconductivity in the topological insulators Bi_2Se_3 and Bi_2Te_3. *Nature Communications* **3,** 1056 (2012).
106. Yang, F. *et al.* Proximity-effect-induced superconducting phase in the topological insulator Bi_2Se_3. *Physical Review B* **86,** 134504 (2012).
107. Wang, E. *et al.* Fully gapped topological surface states in Bi_2Se_3 films induced by a d-wave high-temperature superconductor. *Nature Physics* **9,** 621–625 (2013).
108. Hor, Y. S. *et al.* Superconductivity in $Cu_xBi_2Se_3$ and its Implications for Pairing in the Undoped Topological Insulator. *Physical Review Letters* **104,** 057001 (2010).
109. Schneeloch, J. A., Zhong, R. D., Xu, Z. J., Gu, G. D. & Tranquada, J. M. Dependence of superconductivity in $Cu_xBi_2Se_3$ on quenching conditions. *Physical Review B* **91,** 114506 (2015).
110. Matano, K., Kriener, M., Segawa, K., Ando, Y. & Zheng, G.-q. Spin-rotation symmetry breaking in the superconducting state of $Cu_xBi_2Se_3$. *Nature Physics* **12,** 852–854 (2016).
111. Damascelli, A. Probing the Electronic Structure of Complex Systems by ARPES. *Physica Scripta* **T109,** 61–74 (2004).
112. Korelek, J. D. Experimental setup for low-energy laser-based angle resolved photoemission spectroscopy. *Review of Scientific Instruments* **78,** 053905 (2007).
113. Gallmann, L. *et al.* Photoemission and photoionization time delays and rates. *Structural Dynamics* **4,** 061502 (2017).
114. Cavalieri, A. L. *et al.* Attosecond spectroscopy in condensed matter. *Nature* **449,** 1029–1032 (2007).
115. Fritz, D. M. *et al.* Ultrafast Bond Softening in Bismuth: Mapping a Solid's Interatomic Potential with X-rays. *Science* **315,** 633–636 (2007).
116. Papalazarou, E. *et al.* Coherent Phonon Coupling to Individual Bloch States in Photoexcited Bismuth. *Physical Review Letters* **108,** 256808 (2012).
117. Wadati, H. *et al.* Angle-resolved photoemission spectroscopy of perovskite-type transition-metal oxides and their analyses using tight-binding band structure. *Phase Transitions* **79,** 617–635 (2006).
118. Oura, K., Lifshits, V. G., Saranin, A. A., Zotov, A. V. & Katayama, M. Surface Science - An Introduction (Springer-Verlag, 2004).
119. Mobillo, S., Boscherini, F. & Meneghini, C. Synchrotron Radiation: Basics, Methods and Applications (Springer, 2015).

120. Hoesch, M. *et al.* A facility for the analysis of the electronic structures of solids and their surfaces by synchrotron radiation photoelectron spectroscopy. *Review of Scientific Instruments* **88,** 013106 (2017).
121. Levy, G., Nettke, W., Ludbrook, B. M., Veenstra, C. N. & Damascelli, A. Deconstruction of resolution effects in angle-resolved photoemission. *Physical Review B* **90,** 045150 (4 2014).
122. Rhodes, L. C. *et al.* Scaling of the superconducting gap with orbital character in FeSe. *arXiv:1804.01436.*
123. Kushnirenko, Y. S. *et al.* Three-dimensional superconducting gap in FeSe from angle-resolved photoemission spectroscopy. *Physical Review B* **97,** 180501 (2018).
124. K., Y. *et al.* High-resolution three-dimensional spin- and angle-resolved photoelectron spectrometer using vacuum ultraviolet laser light. *Review of Scientific Instruments* **87,** 053111 (2016).
125. Okuda, T. *et al.* A new spin-polarized photoemission spectrometer with very high efficiency and energy resolution. *Review of Scientific Instruments* **79,** 123117 (2008).
126. Okuda, T., Miyamoto, K., Kimura, A., Namatame, H. & Taniguchi, M. A double VLEED spin detector for high-resolution three dimensional spin vectorial analysis of anisotropic Rashba spin splitting. *Journal of Electron Spectroscopy and Related Phenomena* **201,** 23–29 (2014).
127. Shirley, D. A. High-Resolution X-Ray Photoemission Spectrum of the Valence Bands of Gold. *Physical Review B* **5,** 4709–4714 (1972).
128. Hohenberg, P. & Kohn, W. Inhomogeneous Electron Gas. *Physical Review* **136,** B864–B871 (1964).
129. Kohn, W. & Sham, L. J. Self-Consistent Equations Including Exchange and Correlation Effects. *Physical Review* **140,** A1133–A1138 (1965).
130. Buth, C. A priori Wannier functions from modified Hartree-Fock and Kohn-Sham equations. *Physical Review B* **75,** 125121 (2007).
131. Sham, L. J. & Schlüter, M. Density-Functional Theory of the Energy Gap. *Physical Review Letters* **51,** 1888–1891 (1983).
132. Perdew, J. P. & Levy, M. Physical Content of the Exact Kohn-Sham Orbital Energies: Band Gaps and Derivative Discontinuities. *Physical Review Letters* **51,** 1884–1887 (1983).
133. Wilson, J. A., Di Salvo, F. J. & Mahajan, S. Charge-density waves and superlattices in the metallic layered transition metal dichalcogenides. *Advances in Physics* **24,** 117–201 (1975).
134. Soluyanov, A. A. *et al.* Type-II Weyl semimetals. *Nature* **527,** 495–498 (2015).
135. Huang, L. *et al.* Spectroscopic evidence for a type II Weyl semimetallic state in $MoTe_2$. *Nature Materials* **15,** 1155–1160 (2016).
136. Deng, K. *et al.* Experimental observation of topological Fermi arcs in type-II Weyl semimetal $MoTe_2$. *Nature Physics* **12,** 1105–1110 (2016).
137. Tamai, A. *et al.* Fermi Arcs and Their Topological Character in the Candidate Type-II Weyl Semimetal $MoTe_2$. *Physical Review X* **6,** 031021 (2016).
138. Bell, M. & Findlay, J. Molybdenite as a New Lubricant. *Physical Review* **59,** 922 (1941).

139. Lansdown, A. R. Molybdenum Disulphide Lubrication (Elesevier, 1999).
140. Zeng, H., Dai, J., Yao, W., Xiao, D. & Cui, X. Valley polarisation in MoS_2 monolayers by optical pumping. *Nature Nanotechnology* **7,** 490 (2012).
141. Riley, J. M. *et al.* Direct observation of spin-polarized bulk bands in an inversion-symmetric semiconductor. *Nature Physics* **10,** 835–839 (2014).
142. Mak, K. F., He, K., Shan, J. & Heinz, T. F. Control of valley polarisation on monolayer MoS_2 by optical helicity. *Nature Nanotechnology* **7,** 494 (2012).
143. Yuan, H. *et al.* Zeeman type spin splitting controlled by an external electric field. *Nature Physics* **9,** 563 (2013).
144. Mattheiss, L. F. Band Structures of Transition-Metal-Dichalcogenide Layer Compounds. *Physical Review B* **8,** 8 (1973).
145. Razzoli, E. *et al.* Selective Probing of Hidden Spin-Polarized States in Inversion-Symmetric Bulk MoS_2. *Physical Review Letters* **118,** 086402 (2017).
146. Zhang, X., Liu, Q., Luo, J.-W., Freeman, A. & Zunger, A. Hidden spin polarization in inversion-symmetric bulk crystals. *Nature Physics* **10,** 387–393 (2014).
147. Bawden, L. *et al.* Spin-valley locking in the normal state of a transition-metal dichalcogenide superconductor. *Nature Communications* **7,** 11711 (2016).
148. Yao, W. *et al.* Direct observation of spin-layer locking by local Rashba effect in monolayer semiconducting $PtSe_2$ film. *Nature Communications* **8,** 14216 (2017).
149. C., C., Sun, J.-T., Chen, X.-R. & Meng, S. Hidden spin polarization in the 1T-phase layered transition-metal dichalcogenides MX_2 (M=Zr, Hf; X=S,Se,Te). *Science Bulletin* **63,** 85–91 (2018).
150. Feng, J. *et al.* Electronic structure and enhanced charge-density wave order of monolayer VSe_2. *Nano Letters* **18,** (7) 4493–4499 (2018).
151. Rossnagel, K., Rotenberg, E., Koh, H., Smith, N. V. & Kipp, L. Fermi surface, charge-density-wave gap, and kinks in 2H-$TaSe_2$. *Physical Review B* **72,** 121103(R) (2005).
152. Terashima, K., Sato, T., Komatsu, H. & Takahashi, T. Charge-density wave transition of 1T-VSe_2 studied by angle-resolved photoemission spectroscopy. *Physical Review B* **68,** 155108 (2003).
153. Eaglesham, D. J., Withers, R. L. & Bird, D. M. Charge-density-wave transitions in 1T-VSe_2. *Journal of Physics C: Solid State Physics* **19,** 3 (1986).
154. Borisenko, S. V. *et al.* Two Energy Gaps and Fermi-Surface “Arcs” in $NbSe_2$. *Physical Review Letters* **102,** 166402 (2009).
155. Borisenko, S. V. *et al.* Pseudogap and Charge Density Waves in Two Dimensions. *Physical Review Letters* **100,** 196402 (2008).
156. Grüner, G. Frontiers in Physics: Density Waves in Solids (Perseus, 1994).
157. Wilson, J. A. & Yoffe, A. D. The transition metal dichalcogenides discussion and interpretation of the observed optical, electrical and structural properties. *Advances in Physics* **18,** 193–335 (1969).
158. Allan, D. R., Kelsey, A. A., Clark, S. J., Angel, R. J. & Ackland, G. J. High-pressure semiconductor-semimetal transition in TiS_2. *Physical Review B* **57,** 5106 (1998).

159. Guo, G. Y. & Liang, W. Y. The electronic structures of platinum dichalcogenides: PtS_2, $PtSe_2$ and $PtTe_2$. *Journal of Physics C: Solid State Physics* **19,** 995 (1986).
160. Friemelt, K., Lux-Steiner, M.-C. & Bucher, E. Optical properties of the layered transition-metal-dichalcogenide ReS_2: Anisotropy in the van der Waals plane. *Journal of Applied Physics* **74,** 5266 (1993).
161. Biswas, D. *et al.* Narrow-band anisotropic electronic structure of ReS_2. *Physical Review B* **96,** 085205 (2017).
162. Webb, J. L. *et al.* Electronic bandstructure of ReS_2 by high resolution angle resolved photoemission spectroscopy. *Physical Review B* **96,** 115205 (2017).
163. McCreary, A. *et al.* Intricate Resonant Raman Response in Anisotropic ReS_2. *Nano Letters* **17,** 10, 5897–5907 (2017).
164. Watson, M. D. *et al.* Orbital- and k_z-selective hybridisation of Se 4p and Ti 3d states in the charge density wave phase of $TiSe_2$. *Physical Review Letters* **122,** 076404 (2019).
165. Arguello, C. K. *et al.* Visualizing the charge density wave transition in 2H-$NbSe_2$ in real space. *Physical Review B* **89,** 235115 (2014).
166. Ryu, G. Superconductivity in Cu-Intercalated CdI_2-Type $PdTe_2$. *Journal of Superconductivity and Novel Magnetism* **28,** 3275–3280 (2015).
167. Singh, A. & Singh, Y. Heat capacity evidence for conventional superconductivity in the type-II Dirac semimetal $PdTe_2$. *Physical Review B* **97,** 054515 (2018).
168. Clark, O. J. *et al.* Dual quantum confinement and anisotropic spin splitting in the multivalley semimetal $PtSe_2$. *Physical Review B* **99,** 045438 (2019).
169. Rasch, J. C. E., Stemmler, T., Müller, B., Dudy, L. & Manzke, R. $1T-TiSe_2$: Semimetal or Semiconductor? *Physical Review Letters* **101,** 237602 (2008).
170. Xiao, R. C. *et al.* Inversion symmetry breaking induced triply degenerate points in orderly arranged PtSeTe family materials. *Journal of Physics: Condensed Matter* **30,** 245502 (2018).
171. Dvir, T. *et al.* Spectroscopy of bulk and few-layer superconducting $NbSe_2$ with van der Waals tunnel junctions. *Nature Communications* **9,** 598 (2018).
172. Yan, M. *et al.* Lorentz-violating type-II Dirac fermions in transition metal dichalcogenide $PtTe_2$. *Nature Communications* **8,** 257 (2017).
173. Clark, O. J. *et al.* Fermiology and Superconductivity of Topological Surface States in $PdTe_2$. *Physical Review Letters* **120,** 156401 (2018).
174. Huang, Z. S. H. & Duan, W. Type-II Dirac fermions in the $PtSe_2$ class of transition metal dichalcogenides. *Physical Review B* **94,** 121117 (2016).
175. Noh, H.-J. *et al.* Experimental Realization of Type-II Dirac Fermions in a $PdTe_2$ Superconductor. *Physical Review Letters* **119,** 016401 (2017).
176. Fei, F. *et al.* Nontrivial Berry phase and type-II Dirac transport in the layered material $PdTe_2$. *Physical Review B* **96,** 041201(R) (2017).
177. Chang, T.-R. *et al.* Type-II Symmetry-Protected Topological Dirac Semimetals. *Physical Review Letters* **119,** 026404 (2017).
178. Yan, L. *et al.* Identification of Topological Surface State in $PdTe_2$ Superconductor by Angle-Resolved Photoemission Spectroscopy. *Chinese Physics Letters* **32,** 067303 (2015).

179. Zhang, P. *et al.* A precise method for visualizing dispersive features in image plots. *Review of Scientific Instruments* **82,** 4 (2011).
180. Xu, C.-Z. *et al.* Photoemission Circular Dichroism and Spin Polarization of the Topological Surface States in Ultrathin Bi_2Te_3 Films. *Physical Review Letters* **115,** 016801 (2015).
181. Wang, Y. & Gedik, N. Circular dichroism in angle-resolved photoemission spectroscopy of topological insulators. *Physica Status Solidi* **7,** 64–71 (2013).
182. Fei, F. *et al.* Band Structure Perfection and Superconductivity in Type-II Dirac Semimetal $Ir_{1-x}Pt_xTe_2$. *Advanced Materials* **30,** 35 (2018).
183. Fang, A. F., Xu, G., Dong, T., Zheng, P. & Wang, N. L. Structural phase transition in $IrTe_2$: A combined study of optical spectroscopy and band structure calculations. *Scientific Reports* **3,** 1153 (2013).
184. Yang, J. J. *et al.* Charge-Orbital Density Wave and Superconductivity in the Strong Spin-Orbit Coupled $IrTe_2$:Pd. *Physical Review Letters* **108,** 116402 (2012).
185. Ootsuki, D. *et al.* Orbital degeneracy and Peierls instability in the triangular-lattice superconductor $Ir_{1-x}Pt_xTe_2$. *Physical Review B* **86,** 014519 (2012).
186. Blake, S. F. *et al.* Fermi surface of $IrTe_2$ in the valence-bond state as determined by quantum oscillations. *Physical Review B* **91,** 121105(R) (2015).
187. Bawden, L. A spin- and angle-resolved photoemission study of coupled spin-orbital textures driven by global an local inversion symmetry breaking. *Doctoral Thesis, University of St Andrews* (2017).
188. Inosov, D. S. *et al.* Fermi surface nesting in several transition metal dichalcogenides. *New Journal of Physics* **10** (2008).
189. Leininger, P., Chernyshov, D., Bosak, A., Berger, H. & Inosov, D. S. Competing charge density waves and temperature-dependent nesting in 2H-$TaSe_2$. *Physical Review B* **83,** 233101 (2011).
190. Huang, H., Jin, K.-H. & Liu, F. Black-hole horizon in the Dirac semimetal $Zn_2In_2S_5$. *Physical Review B* **98,** 121110 (2018).
191. Xiao, R. C. *et al.* Manipulation of type-I and type-II Dirac points in $PdTe_2$ superconductor by external pressure. *Physical Review B* **96,** 075101 (2017).
192. Clark, O. J. *et al.* A general route to form topologically-protected surface and bulk Dirac fermions along high-symmetry lines. *Electronic Structure* **1,** 014002 (2019).
193. Yang, H. *et al.* Quantum oscillations in the type-II Dirac semi-metal candidate $PtSe_2$. *New Journal of Physics* **20,** 043008 (2018).
194. Singh, U. R., Enayat, M., White, S. C. & Wahl, P. Construction and performance of a dilution-refrigerator based spectroscopic-imaging scanning tunneling microscope. *Review of Scientific Instruments* **84,** 013708 (2013).
195. Leng, H., Paulsen, C., Huang, Y. K. & de Visser, A. Type-I superconductivity in the Dirac semimetal $PdTe_2$. *Physical Review B* **96,** 220506 (2017).
196. Finlayson, T. R., Reichardt, W. & Smith, H. G. Lattice dynamics of layered-structure compounds: $PdTe_2$. *Physical Review B* **33,** 2473–2480 (1986).

197. Grønvold, F., Haraldsen, H. & Kjekshus, A. On the Sulfides, Selenides, and Tellurides of Platinum. *Acta Chemica Scandinavica* **14,** 1879–1893 (1960).
198. Mönch, W. Semiconductor Surfaces and Interfaces (Springer, 2001).
199. Ando, T., Fowler, A. B. & Stern, F. Electronic properties of two-dimensional systems. *Reviews of Modern Physics* **54,** 437–672 (1982).
200. Yamada, Y. *et al.* Electrically Induced Ferromagnetism at Room Temperature in Cobalt-Doped Titanium Dioxide. *Science* **332,** 1065–1067 (2011).
201. Yuan, H. *et al.* High-Density Carrier Accumulationin ZnO Field Effect Transistors Gated by Electric Double Layers of Ionic Liquids. *Advanced Functional Materials* **19,** 7 (2009).
202. Goldman, A. M. Electrostatic Gating of Ultrathin Films. *Annual Review of Materials Research* **44,** 45–63 (2014).
203. Yang, Z. *et al.* Anisotropic defect-induced ferromagnetism and transport in Gd-doped GaN two-dimensional electron gasses. *Physical Review B* **92,** 224416 (2015).
204. Wen, F. *et al.* Evolution of ferromagnetism in two-dimensional electron gas of $LaTiO_3/SrTiO_3$. *Applied Physics Letters* **112,** 122405 (2018).
205. Mak, K. F., McGill, K. L., Park, J. & McEuen, P. L. The valley Hall effect in MoS_2 transistors. *Science* **344,** 1489 (2014).
206. Chi, Z. *et al.* Superconductivity in Pristine $2H_a$-MoS_2 at Ultrahigh Pressure. *Physical Review Letters* **120,** 037002 (2018).
207. Li, L. J. *et al.* Controlling many-body states by the electric-field effect in a two-dimensional material. *Nature* **534,** 21–22 (2016).
208. Lu, J. M. *et al.* Evidence for two-dimensional Ising superconductivity in gated MoS_2. *Science* **350,** 1353–1357 (2015).
209. Saito, Y. *et al.* Superconductivity protected by spinvalley locking in ion-gated MoS_2. *Nature Physics* **12,** 144–149 (2016).
210. Lei, J.-Q., Ke, L., Sha, H. & Zhou, X.-L. The comparative study on bulk-$PtSe_2$ and 2D 1-Layer-$PtSe_2$ under high pressure via first-principle calculations. *Theoretical Chemistry Accounts* **136,** 97 (2017).
211. Luttinger, J. M. & Ward, J. C. Ground-State Energy of a Many-Fermion System. II. *Physical Review* **118,** 1417 (1960).
212. Tamai, A. *et al.* Spin-orbit splitting of the Shockley surface state on Cu(111). *Physical Review B* **87,** 075113 (2013).
213. Popović, D. *et al.* High-resolution photoemission on Ag/Au(111): Spin-orbit splitting and electronic localization of the surface state. *Physical Review B* **72,** 045419 (2005).
214. Sunko, V. *et al.* Maximal Rashba-like spin splitting via kinetic-energy-coupled inversion-symmetry breaking. *Nature* **549,** 492–496 (2017).
215. Bian, G., Wang, X., Miller, T. & Chiang, T.-C. Origin of giant Rashba spin splitting in Bi/Ag surface alloys. *Physical Review B* **88,** 085427 (2013).
216. Lee, H. & Choi, H. J. Role of *d* orbitals in the Rashba-type spin splitting for noble-metal surfaces. *Physical Review B* **86,** 045437 (2012).
217. Wittel, K. & Manne, R. Atomic spin-orbit interaction parameters from spectral data for 19 elements. *Chim. Acta (Berl.)* **33,** 347–349 (1974).

218. Caruso, F. & Giustino, F. Spectral fingerprints of electron-plasmon coupling. *Physical Review B* **92,** 045123 (2015).
219. Morawiec, S., Mendes, M. J., Priolo, F. & Crupi, I. Plasmonic nanostructures for light trapping in thin-film solar cells. *Materials Science in Semiconductor Processing* **92,** 10–18 (2019).
220. Nguyen, V. H. & Nguyen, B. H. Quantum theory of plasmon energy spectra in electron gases of bulk metal and metallic nanostructures. *Advances in Natural Sciences: Nanoscience and Nanotechnology* **5,** 3 (2014).
221. Kesmodel, L. L. Applications of High-Resolution Electron Energy Loss Spectroscopy to Technical Surfaces. *Langmuir* **14,** 1355–1360 (1998).
222. Raza, S. *et al.* Electron energy-loss spectroscopy of branched gap plasmon resonators. *Nature Communications* **7,** 13790 (2016).
223. Politano, A. *et al.* 3D Dirac Plasmons in the Type-II Dirac Semimetal $PtTe_2$. *Physical Review Letters* **121,** 086804 (2018).
224. Zhang, P. *et al.* Observation of topological superconductivity on the surface of an iron-based superconductor. *Science,* doi:10.1126/science.aan4596 (2018).
225. Le, C. *et al.* Dirac semimetal in β-CuI without surface Fermi arcs. *PNAS* **115,** 8311–8315 (2018).
226. Brillson, L. J., Burstein, E. & Muldawer, L. Raman observation of the ferroelectric phase transition in SnTe. *Physical Review B* **9,** 1547–1551 (1974).
227. O'Neill, C. D. *et al.* Inelastic x-ray investigation of the ferroelectric transition in SnTe. *Physical Review B* **95,** 144101 (2017).
228. Dziawa, P. *et al.* Topological crystalline insulator states in $Pb_{1-x}Sn_xSe$. *Nature Materials* **11,** 1023–1027 (2012).
229. Fu, L. Topological Crystalline Insulators. *Physical Review Letters* **106,** 106802 (2011).
230. Ye, Z.-Y. *et al.* The origin of electronic band structure anomaly in topological crystalline insulator group-IV tellurides. *npj Computational Materials* **1,** 15001 (2015).
231. Guo, P.-J., Yang, H.-C., Liu, K. & Lu, Z.-Y. Type-II Dirac semimetals in the YPd_2Sn class. *Physical Review B* **95,** 155112 (2017).
232. Zhan, R. & Luo, X. Topologically nontrivial phases in superconducting transition metal carbides. *arXiv:1810.11812.*
233. Zhang, P. *et al.* Multiple topological states in iron-based superconductors. *Nature Physics,* https://doi.org/10.1038/s41567–018–0280–z (2018).
234. Böhmer, A. E. & Kreisel, A. Nematicity, magnetism and superconductivity in FeSe. *Journal of Physics: Condensed Matter* **30,** 2 (2017).
235. Fedorov, A. *et al.* Effect of nematic ordering on electronic structure of FeSe. *Scientific Reports* **6,** 36834 (2016).
236. Watson, M. D. *et al.* Emergence of the nematic electronic state in FeSe. *Physical Review B* **91,** 155106 (2015).
237. Wang, D. *et al.* Evidence for Majorana bound states in an iron-based superconductor. *Science,* doi:10.1126/science.aao1797 (2018).

238. Zhang, X., Lai, Z., Ma, Q. & Zhang, H. Novel structured transition metal dichalcogenide nanosheets. *Chemistry Society Review* **47,** 3301 (2018).
239. Brik, M. G. & Ma, C.-G. First-principles studies of the electronic and elastic properties of metal nitrides XN (X = Sc, Ti, V, Cr, Zr, Nb). *Computational Materials Science* **51,** 380–388 (2012).
240. Xu, C. *et al.* Topological Type-II Dirac Fermions Approaching the Fermi Level in a Transition Metal Dichalcogenide $NiTe_2$. *Chemistry of Materials* **30,** 4823–4830 (2018).
241. Thirupathaiah, S. *et al.* Possible origin of linear magnetoresistance: Observation of Dirac surface states in layered $PtBi_2$. *Physical Review B* **97,** 035133 (2018).
242. Ding, G., Li, J. & Gao, G. Band structure engineering of multiple band degeneracy for enhanced thermoelectric power factors in MTe and MSe (M = Pb, Sn, Ge). *RSC Advances* **5,** 91974–91978 (2015).
243. Bencherifab, Y., Boukraab, A., Zaouic, A. & Ferhatb, M. High pressure structural phase transitions of PbPo. *Physica B: Condensed Matter* **407,** 3520–3523 (2012).
244. Du, Y., Kan, E.-j., Xu, H., Savrasov, S. Y. & Wan, X. Turning copper metal into a Weyl semimetal. *Physical Review B* **97,** 245104 (2018).
245. Lv, B. Q. *et al.* Observation of three-component fermions in the topological semimetal molybdenum phosphide. *Nature* **546,** 627–631 (2017).
246. Bian, G. *et al.* Topological nodal-line fermions in spin-orbit metal $PbTaSe_2$. *Nature Communications* **7,** 10556 (2016).
247. Wang, J. *et al.* Intriguing electronic and optical properties of two-dimensional Janus transition metal dichalcogenides. *Physical Chemistry Chemical Physics* **20,** 18571–18578 (2018).
248. Kliche, G. Far-Infrared and X-Ray investigations of the Mixed Platinum Dichalcogenides $PtS_{2-x}Se_x$, $PtSe_{2-x}Te_x$ and $PtS_{2-x}Te_x$. *Journal of Solid State Chemistry* **56,** 26–31 (1985).
249. Luo, W. & Qi, X.-L. Massive Dirac surface states in topological insulator/magnetic insulator heterostructures. *Physical Review B* **87,** 085431 (2013).
250. Teo, J. C. Y., Fu, L. & Kane, C. L. Surface states and topological invariants in three-dimensional topological insulators: Application to $Bi_{1-x}Sb_x$. *Physical Review B* **78,** 045426 (2008).
251. Hsieh, D. *et al.* A topological Dirac insulator in a quantum spin Hall phase. *Nature* **452,** 970–974 (2008).
252. Vergniory, M. G., Elcoro, L., Felser, C., Bernevig, B. A. & Wang, Z. A complete catalogue of high-quality topological materials. *Nature* **566,** 480–485 (2019).